PhD-FSTM-2021-021
The Faculty of Science, Technology and Medicine

DISSERTATION

Presented on 19/04/2021 in Luxembourg

to obtain the degree of

DOCTEUR DE L'UNIVERSITÉ DU LUXEMBOURG

EN *PHYSIQUE*

by

Tai NGUYEN
Born on 11 December 1989 in Bac Ninh, Vietnam

MAGNETOELECTRIC THIN-FILM COMPOSITES FOR ENERGY HARVESTING APPLICATIONS

Dissertation defence committee

Dr Jérôme POLESEL, dissertation supervisor
Luxembourg Institute of Science and Technology

Dr Elisabeth BLANQUET
Laboratoire Science et Ingénierie des Matériaux et Procédés - SIMaP
Professor, Université Grenoble Alpes

Dr Andreas MICHELS, Chairman
Professor, Université du Luxembourg

Dr Ulrich SCHMID
Professor, Technische Universität Wien

Dr Torsten GRANZOW, Vice Chairman
Luxembourg Institute of Science and Technology

Acknowledgements

"No one who achieves success does so without acknowledging the help of others.

The wise and confident acknowledge this help with gratitude"

– Alfred North Whitehead –

I have been working in the LIST for almost the last four years and looking back it was apparently a great roller coaster experience. I feel fortunate I had the chance to pursuit research in such a pleasant working environment. I am very happy and satisfied with the knowledge and skills that I gained and lot of the scientific and fruitful discussion during my thesis work. Besides, I had a lot of fun in travel – summer schools, conferences, and internal events – summer and the year-end parties, team building days etc. So here I would take the opportunity to thank everyone for the memorable moments.

First, I would like to gratefully thank my daily supervisor Dr. HDR. Habil. Jérôme Polesel-Maris, who gave me the chance to join in the TOT group. You were always there for me starting from the day of interview for the PhD position. You always are energetic, motivative, creative and enthusiastic. I learnt a lot from your knowledge and positive attitude. I thank you very much for teaching, guiding, supporting and encouraging me. Undoubtedly, it is my great honor to work with you.

Next, I would like to thank the CET members, Prof. Dr. Andreas Michel and Dr. Tosten Granzow. With your expertise, my PhD progress run smoothly. I appreciated your advice and brainstorming questions by which a lot of rocky issues was solved during my thesis work. I gratefully thank Prof. Dr Andreas Michel for giving me the chance to participate in SANS measurements in ISIS, Oxford, UK. It was a valuable experience with large facilities. I would also thank both of you for carefully reading and correcting my thesis.

Furthermore, I would thank Prof. Elisabeth Blanquet (SIMaP, CNRS) and Prof. Ulrich Schmid (Technical University of Wien) for reading and evaluating my thesis.

Moving next to the technical team, I would like to acknowledge Noureddine Adjeroud for his exceptional expertise in ALD techniques. With your support, the ALD experiments have been run smoothly. I would like to thank Dr. Nathalie Valle and Brahime El Adib for SIMS analysis, Dr. Jérôme Guillot for XPS analysis, Dr. Yves Fleming for XRD characterization, Dr. Sebastjan Glinsek for four-point-bending characterization, Dr. Mael Guennou for photoluminescence measurement, Patrick Grysan for AFM measurement, Dr. Didier Arl for training on FIB-SEM, Dr. Stéphanie Girod for training on photolithography, Dr. Jérôme Bour for ToF-SIMS analysis, Dr. Petru Lunca Popa for optical measurement, Dr. Renaud Leturcq for training on electrical characterizations. I would specially thank Thomas Gaulain for his support on sputtering. We have spent lot of time together to visualize Ni-Mn-Ga thin films.

I would also thank Dr. Philipp Florian Bender (Technical University of Munich) and Dr. Diego Alba Venero (ISIS, UK) for supporting on magnetization measurements and SANS analysis. Thank you, Diego, for training on SANS-2D at ZOOM and for being tour guide in Oxford.

I would like to thank all the TOT members for fruitful discussion during the group meeting. I have learnt a lot from diverse research topics you have been doing at LIST. I have spent time in my office together with amazing PhD friends: Nikhar Khanna, Rutuja Bhusari, Sabrina

Wack, Dr. Divya Balakrishnan, Dr. Hameeda Raja Padmanathan, Raoul Joly, Joao Antunes Afonso, Shiv Bhudia. Thanks for all the office chit chats, delicious sweets and savouries. I would particularly thank Nikhar and Rutuja for making my birthday special.

I would spend special thanks to my friends, Duy-Carol family, their children – Rafael, Tailor, Sofia for helping me at the beginning and giving me a family atmosphere.

I also had a small Vietnamese group in Luxembourg. We have shared lot of beautiful moments together. Thanks to Cuong for violin, Go training and nice talks, Tung-Thao family, Cu-Phuong family, Tuyet family, Lam, Minh, Hanh, Long-Huyen family, Hieu-Huyen family.

From my whole heart, I would thank my parent, sister, and all my family members for their support, encouragement and patience. Without them none of these would have been possible and meaningful.

Tai Nguyen,

Luxembourg, March 2021.

Abstract

In last decades, magnetoelectric (ME) composites have received significant attention due to their capabilities for practical applications, such as energy harvesters and sensors. However, the current ME composites present severe issues, which are related to either bulky composites for miniaturized devices as MEMS or the low-quality interface between the piezoelectric (PE) and magnetostrictive (MS) constituents induced by high-temperature processes and low conformal coating profiles that could degrade the ME coupling in the composites. In this thesis, these issues are addressed by utilizing (plasma-enhanced) atomic layer deposition (ALD and PE-ALD) techniques at low temperatures (below 250 °C) to grow piezoelectric zinc oxide (ZnO) and aluminum nitride (AlN) thin films and ME composites. The highly conformal coating profile and low-temperature processes of ALD produced a good interface between the two layers, thus enhancing the ME coupling effect.

Firstly, an innovative approach, using pulsed gaseous oxygen during the ALD growth of ZnO thin films at temperatures below 180 °C, is introduced in order to surpass the challenge of obtaining preferentially (002)-oriented and resistive films. These requirements are prerequisite for achieving a piezoelectric response in ZnO thin films and for preventing leakage currents. Indeed, the additional presence of gaseous oxygen profoundly effects the structural, electrical and electronic properties of ZnO thin films. The films grown with O_2 have a highly preferred (002) orientation and their resistivity is 3-4 orders of magnitude higher than the film grown without O_2. In addition, the growth mechanisms of the films grown with and without O_2 are also meticulously studied by combining several sophisticated characterization techniques, such as *in situ* quartz crystal microbalance (QCM), x-ray photoelectron spectroscopy (XPS), dynamic secondary-ion mass spectroscopy (D-SIMS), and time-of-flight SIMS (ToF-SIMS). In the ALD process with O_2, it was found that the ethyl ligand of the zinc precursor can react with O_2 to form ethylperoxy radicals. The formation of the ethylperoxy zinc and/or zinc atoms leads to more adsorption of water to form ethylhydroperoxide during the water pulse. The growth mechanisms were elucidated using an isotopic O^{18} tracer in the water precursor H_2O^{18} for the for the first time in ALD growth. The preferred (002) orientation is attributed to the stabilization of polar surfaces in the O_2 environment, while the higher resistivity is ascribed to the reduction of oxygen vacancies in the films grown with O_2. Although a preferentially (002)-oriented ZnO thin film was obtained with an increase of its resistivity from 3 to 4 orders of magnitude, its piezoelectric response cannot be used for energy harvesting purposes due to the presence of a leakage current which is always prohibitive.

Secondly, an AlN thin film is considered as a relevant alternative to ZnO thin film owing to its insulating property and its good piezoelectric response, which do not require a poling stage. The methods of conformal deposition of thin epitaxial layers by chemical means require very high temperatures (around 1000 °C). These high growth temperatures induce atomic interdiffusion at the interfaces of different materials leading to a reduction of magnetoelectric coupling performance. Nevertheless, PE-ALD (Plasma-enhanced ALD) appears to be a promising deposition technique at moderate temperature (<300 °C) for the growth of AlN thin layers thanks to plasma assistance. In fact, the growth of polycrystalline AlN thin film by PE-ALD faces the difficulties of a low crystallinity and a presence of oxide phase. Dealing with several thermodynamic parameters, it demonstrates for the first time that PE-ALD has the ability to grow high-quality AlN thin film at a deposition temperature of 250 °C with a

preferred orientation (002) and a substantial piezoelectric response. A direct piezoelectric coefficient $e_{31,f}$ of 0.37 C/m^2 is reported.

Thirdly, thanks to the conformal coating profile of ALD, transducing high-response ME composites have been obtained in 2-2 layered composites consisting of AlN films coated on magnetostrictive substrates of nickel, iron and cobalt. High-resolution transmission electron microscopy (HR-TEM) was used to study and to optimize the interface between the AlN films and the ferromagnetic substrates, as well as the thin film quality. The maximum magnetoelectric coefficients of AlN/Ni composites were 3.3, 2.8, and 3.1 $V.cm^{-1}.Oe^{-1}$ off-resonance at a frequency of 46 Hz and at a zero-bias DC magnetic field for Ni foil thicknesses of 7.5, 15, and 30 µm, respectively. Furthermore, the magnetoelectric coefficient was measured in composites made of 550nm-thick AlN films grown on 12.5µm-thick Fe and 15µm-thick Co foils. An RMS power density of 75 nW/cm^3 was obtained on a matched load resistance of 200 kΩ for an AlN/Ni composite with Ni foil thickness of 7.5 µm.

To conclude, methods for upgrading the magnetostrictive/piezoelectric coupling and performance of ME composites are proposed. A recent ferromagnetic shape memory alloy, based on Ni-Mn-Ga Heusler alloy film, is chosen due to its excellent magnetoelastic properties with a giant induced strain of up to 1% under a magnetic field. However, the processing of Ni-Mn-Ga thin films is very challenging due to difficulties in controlling the stoichiometry and diffusion of elements in the supporting surface. These difficulties are discussed and dissociated from each other by providing experimental answers. In addition, two other potential approaches are given using the ternary compound AlScN as a replacement for AlN thin films to obtain a higher piezoelectric response and resonance structures.

This work proposes several robust approaches by which to stimulate the design and development of ME composites, as well as their functionalities in device applications, such as MEMS devices on chip equipped for energy harvesters and sensors.

Résumé

Au cours des dernières décennies, les composites magnétoélectriques (ME) ont reçu une attention particulière en raison de leurs potentiels applicatifs pour des dispositifs tels que les récupérateurs d'énergie et les capteurs. Cependant, les composites ME actuels présentent des limitations importantes qui sont liés soit à leur encombrement pour des dispositifs miniaturisés type MEMS, soit à l'interface de faible qualité entre les constituants piézoélectriques (PE) et magnétostrictifs (MS) induits par des processus à haute température et des profils de revêtement conformes faibles qui pourraient dégrader le couplage ME dans les composites. Dans cette thèse, ces problèmes sont abordés en utilisant des techniques de dépôt de couche atomique par ALD (Atomic Layer Deposition) et PE-ALD (Plasma enhanced- ALD) à températures modérées (inférieures ou égales à 250 °C) pour faire croître des films minces piézoélectriques d'oxyde de zinc (ZnO) et de nitrure d'aluminium (AlN) constituants des dispositifs ME. Le revêtement hautement conforme et le dépôt à température modérée de l'ALD permettent une bonne interface entre les deux couches, améliorant ainsi l'effet de couplage ME.

Dans un premier temps, une approche innovante, utilisant de l'oxygène gazeux pulsé est introduite lors de la croissance ALD des couches minces de ZnO à des températures inférieures à 180 °C afin d'obtenir des films préférentiellement orientés (002) et hautement résistifs électriquement. Ces conditions préalables sont nécessaires à l'obtention d'une réponse piézoélectrique dans les couches minces de ZnO tout en évitant les courants de fuite. En effet, la présence supplémentaire d'oxygène gazeux durant la croissance affecte profondément les propriétés structurelles, électriques et électroniques des couches minces de ZnO. Les films développés avec l'oxygène ont une orientation hautement préférentielle (002) et leur résistivité est de 3 à 4 ordres de grandeur plus élevée que le film développé sans oxygène. En outre, les mécanismes de croissance des films réalisés avec et sans oxygène gazeux ont été méticuleusement étudiés en combinant plusieurs techniques de caractérisation telles que la microbalance à cristal de quartz (QCM) *in situ*, la spectroscopie photoélectronique aux rayons X (XPS), la spectroscopie de masse dynamique par ions secondaires (D -SIMS) et SIMS à temps de vol (ToF-SIMS). Au cours du dépôt ALD avec oxygène, nous avons trouvé que le ligand éthylique du précurseur de zinc peut réagir avec l'O_2 pour former des radicaux éthylperoxy. La formation d'éthylperoxy zinc et / ou d'atomes de zinc conduit à une plus grande adsorption d'eau pour former de l'hydroperoxyde d'éthyle lors de l'impulsion d'eau. L'élucidation de ces mécanismes de croissance a été rendu possible par l'utilisation d'un traceur isotopique O^{18} dans le précurseur d'eau H_2O^{18} pour la première fois dans une croissance ALD. L'orientation préférée (002) est attribuée à la stabilisation des surfaces polaires du ZnO dans l'environnement O_2, tandis que la résistivité électrique plus élevée est attribuée à la réduction des lacunes d'oxygène dans les films développés dans cette atmosphère. Bien que nous ayons obtenu une couche mince de ZnO préférentiellement orientée (002) avec une résistivité électrique augmentée de 3 à 4 ordres de grandeurs, sa réponse piézoélectrique n'est pas envisageable à des fins de récupération d'énergie en raison de la présence d'un courant de fuite toujours rédhibitoire.

Dans un deuxième temps, nous avons considéré une couche mince d'AlN comme alternative pertinente à la couche mince de ZnO en raison de ses propriétés d'isolant électrique et de ses bonnes propriétés piézoélectriques qui ne nécessitent pas d'étape supplémentaire de polarisation. Les méthodes de dépôt conforme de couches minces épitaxiales par voie chimique nécessitent des températures très élevées (autour de 1000 °C). Ces hautes températures de croissance induisent une interdiffusion atomique au niveau des interfaces de matériaux

différents avec une perte de performance de couplage magnetoélectrique. Ainsi, la PE-ALD (Plasma Enhanced-ALD) apparaît comme une technique de dépôt prometteuse à température modérée (< 300 °C) pour la croissance de couches minces d'AlN grâce à une assistance de source plasma. Cependant, la croissance de couche mince polycristalline d'AlN par PE-ALD se heurte aux difficultés d'une faible cristallinité et d'une présence de phase oxyde. En ajustant plusieurs paramètres thermodynamiques de dépôt, nous avons démontré pour la première fois que la PE-ALD a la capacité de produire un film mince d'AlN de haute qualité cristalline à une température de dépôt de 250 °C avec une orientation privilégiée (002) et une réponse piézoélectrique substantielle. Un coefficient piézoélectrique direct $e_{31,f}$ de 0,37 C / m^2 a été évalué.

Dans un troisième temps, grâce au revêtement conforme obtenu par l'ALD, des composites magnétoélectriques à haute réponse de transduction ont été obtenus dans des composites 2-2 en couches constituées de films AlN déposées sur des substrats magnétostrictifs de nickel, fer et cobalt. La microscopie électronique à transmission haute résolution (HR-TEM) a été utilisée pour étudier et optimiser l'interface entre les films AlN et les substrats ferromagnétiques, ainsi que la qualité des couches minces. Les coefficients magnétoélectriques maximaux des composites AlN / Ni étaient de 3,3, 2,8 et 3,1 V.cm^{-1}.Oe^{-1} hors résonance à une fréquence de 46 Hz et à un champ magnétique continu de polarisation nul pour des épaisseurs de feuille de Ni de 7.5, 15 et 30 µm, respectivement. En outre, le coefficient magnétoélectrique a été mesuré dans des composites constitués de films AlN de 550 nm d'épaisseur déposés sur des substrats de Fe de 12.5 µm d'épaisseur et de Co de 15 µm d'épaisseur. Une densité de puissance RMS de 75 nW / cm^3 a été obtenue sur une résistance de charge adaptée de 200 kΩ pour un composite AlN / Ni avec une épaisseur de feuille de Ni de 7.5 µm.

Pour conclure, des méthodes sont proposées pour améliorer le couplage magnétostrictif/piézoélectriques et les performances des composites ME. Un alliage à mémoire de forme ferromagnétique récent, basé sur film d'alliage Heusler Ni-Mn-Ga, est choisi en raison de ses excellentes propriétés magnétoélastiques avec une déformation induite géante allant jusqu'à 1% sous un champ magnétique. Cependant, le traitement des couches minces de Ni-Mn-Ga est très difficile en raison des difficultés de contrôle de la stœchiométrie et de la diffusion des éléments dans la surface lors de la croissance. Ces difficultés sont discutées et dissociées les unes des autres en apportant des réponses expérimentales. En outre, deux autres approches potentielles sont proposées pour utiliser le composé ternaire AlScN en remplacement des films minces AlN pour obtenir une réponse piézoélectrique plus élevée et des structures résonantes.

Ce travail propose plusieurs approches robustes pour permettre la conception et le développement de composites ME, ainsi que leurs fonctionnalités dans des applications tels que les dispositifs MEMS sur puce dotés de récupérateurs d'énergie et de capteurs.

Contents

Acknowledgements ………………………………………………………………………iii
Abstract…………………………………………………………………………………vi
Résumé………………………………………………………………………………..viii
Contents……………………………………………………………………………….....x
Abbreviations…………………………………………………………………………xii
Symbols………………………………………………………………………………xiii

1. Introduction…………………………………………………………………………...1
1.1. Piezoelectricity……………………………………………………………………2
1.1.1. Introduction………………………………………………………………..2
1.1.2. Piezoelectric effect in ZnO and AlN………………………...……………4
1.2. Magnetostriction …………………………………………………………………6
1.2.1. Introduction…….…………………………………………………………6
1.2.2. Microscopic origin of magnetostriction……………………………………8
1.3. Magnetoelectric effect and materials……………………………………………10
1.3.1. Introduction ……………………………………………………………...10
1.3.2. Magnetoelectric effect composites ………………………………………16
1.3.2.1. Introduction ……………………………………………………...16
1.3.2.2. Theoretical approach for layer-layer composites.………………...17
1.3.3. Applications of direct magnetoelectric effect…….……………………...20
1.3.3.1. Magnetic field sensors …………………………………………...20
1.3.3.2. Electromagnetic energy harvesters ………………………………21
1.3.4. References ………………………………………………………………………23

2. Motivation and scope of the thesis…………………………………………………..29

3. Experiments and characterizations……………………………………………………33
3.1. Thin film fabrication techniques…………………………………………….......34
3.1.1. Atomic layer deposition…………………………………………………..34
3.1.1.1. Zinc oxide thin-film deposition…………………………………..35
3.1.1.2. Aluminum nitride thin-film growth………………………………37
3.1.2. Magnetron sputtering……………………………………………………..38
3.2. Thin film characterizations………………………………………………………41
3.2.1. X-ray diffraction…………………………………………………………41
3.2.2. Atomic force microscopy………………………………………………...42
3.2.3. Piezoresponse force microscopy…………………………………………43
3.2.4. Scanning electron microscopy……………………………………………44
3.2.5. Transmission electron microscopy………………………………………44
3.2.6. X-ray photoelectron spectrometry………………………………………..45
3.2.7. Secondary ion mass spectrometry………………………………………..46
3.2.8. Piezoelectric characterization……………………………………………46
3.2.9. Magnetization measurement……………………………………………...48
3.2.10. Magnetoelectric measurement…………………………………………...49
3.3. References ………………………………………………………………………51

4. Highly resistive zinc oxide thin films grown by thermal atomic layer deposition…...53

4.1. Controlling electrical and optical properties of zinc oxide thin films grown by thermal atomic layer deposition with oxygen gas……………………………..54
4.2. Elucidating the growth mechanism of ZnO films by Atomic Layer Deposition with Oxygen Gas via isotopic tracking....……………………………………77
4.3. Piezoelectric characterizations of ZnO thin films……………………….....99
4.3.1. Piezoresponse force microscope characterizations………………………99
4.3.2. C-V characteristic…………………………………………………….100
4.3.3. Discussion...………………………………………………………….101

5. Growth of AlN thin film by plasma enhanced atomic layer deposition...…………102

5.1. Optimization growth of AlN thin films…………..………………………103
5.1.1. Effect of plasma power………………………………………………103
5.1.2. Effect of post-annealing processes……………………………………103
5.1.3. Effect of ZnO buffer layers…………………………………………...104
5.1.4. Discussion ……………………………………………………………105
5.1.5. References ..…………………………………………………………107
5.2. A film-texture driven piezoelectricity of AlN thin films grown at low temperatures by plasma-enhanced atomic layer deposition…………………109

6. Magnetoelectric composites made of AlN films and magnetostrictive foils……….118

6.1. Introduction ..…………………………………………………………….121
6.2. Experimental ……………………………………………………………..123
6.3. Results and discussion……………………………………………………124
6.4. Conclusion………………………………………………………………..131
6.5. References ..……………………………………………………………..133

7. Perspectives: ways to improve magnetoelectric effect in thin-film composites……140

7.1. Off-stoichiometric Ni-Mn-Ga films: fabrication and characterizations…….141
7.1.1. Introduction to Heusler alloys………………………………………...141
7.1.1.1. Ferromagnetic shape memory effect……………………………141
7.1.1.2. Structure………………………………………………………... 143
7.1.1.3. Magnetic properties ..……………………………………………..144
7.1.1.4. Composition dependence of structural and magnetic properties...145
7.1.2. Results ..……………………………………………………………..147
7.1.2.1. Effect of post-annealing process………………………………...147
7.1.2.2. Effect of co-sputtering……………………………………………..152
7.1.2.3. Effect of diffusion barrier layers………………………………...155
7.1.2.4. Temperature dependence of X-ray diffraction measurement……159
7.1.3. Conclusion……………………………………………………………162
7.2. ScAlN alloy thin film as a piezoelectric layer……………………………163
7.3. Resonant structures………………………………………………………165
7.4. References ..……………………………………………………………..167

8. Summary and outlooks……………………………………………………………..169

Annexes: ……………………………………………………………………………..174

A1: Estimation of the interface coupling factor k in ME composites…..…………………..175

A2: Materials properties...…………………………………………………………………..178

List of publications…………………………………………………………………180

List of contributions..………………………………………………………………181

Abbreviations

ALD Atomic Layer Deposition
AFM Atomic Force Microscope
AlN Aluminum nitride
BTO $BaTiO_3$
DEZ Diethyl Zinc
D-SIMS Dynamic Second-In Mass Spectroscopy
EELS Electron Energy Loss Spectroscopy
EDX Energy Dispersive X-ray Spectroscopy
FC Field-Cooling
FW Field-Warming
HR-TEM High Resolution Transmission Electron Microscope
MEZ Monoethyl Zinc
ME Magnetoelectric
MS Magnetostriction
PE-ALD Plasma-enhanced Atomic Layer Deposition
PE Piezoelectric
PZT $Pb(ZrTi)O_3$
PMN-PZT $Pb(Mg_{1/3}Nb_{2/3})O_3$-$Pb(ZrTi)O_3$
QCM Quartz Crystal Microbalance
STEM Scanning Transmission Electron Microscope
SEM Scanning Electron Microscope
TMA Trimethyl Aluminum
XRD X-ray Diffraction
TEM Transmission Electron Microscope
ToF-SIMS Time-of-Flight Second-In Mass Spectroscopy
XPS X-ray Photoelectron Spectroscopy
ZnO Zinc Oxide
ZFC Zero Field-Cooling

Symbols

k_p electromechanical coupling coefficient

k_m magnetomechanical coupling coefficient

λ magnetostrictive coefficient

d_{31}, d_{33} converse piezoelectric coefficient

$e_{31,f}$ effective direct piezoelectric coefficient

ε_{33} dielectric constant

α_{ME} magnetoelectric coefficient

τ_{PE} plasma pulse time

$\tau_{purging}$ purging time

M_s saturation magnetization

1

Fundamental background

The focus of this thesis is magnetoelectric composites, which are made up of piezoelectric and magnetostrictive materials. Therefore, this chapter reviews the fundamentals of piezoelectricity and magnetostriction effects. Piezoelectric effects are present in many classes of materials, such as perovskites, pyrochlores, and hexagonal wurtzite structures. Section 1.1 discusses the piezoelectric effect in perovskite materials and hexagonal wurtzite ZnO and AlN. The magnetostriction effect is reviewed in Section 1.2. A significant effort is made to introduce the basic backgrounds of magnetoelectric effects and materials in both single-phase and composite forms.

1.1 Piezoelectricity

1.1.1. Introduction

The piezoelectric effect is a linear relationship between strain and charge in the crystal surface of a material. The creation of an electric charge Q by the applied stress T is called the direct piezoelectric effect, as described in Figure 1.1(a) by following expression [1–3]:

$$D = d.T + \varepsilon^{T}.E \quad (1.1)$$

where D is the dielectric displacement vector, d is the direct piezoelectric coefficient (in C/N), T is the applied stress tensor, E is the electric field vector and ε^{T} is the dielectric permittivity at the constant mechanical stress.

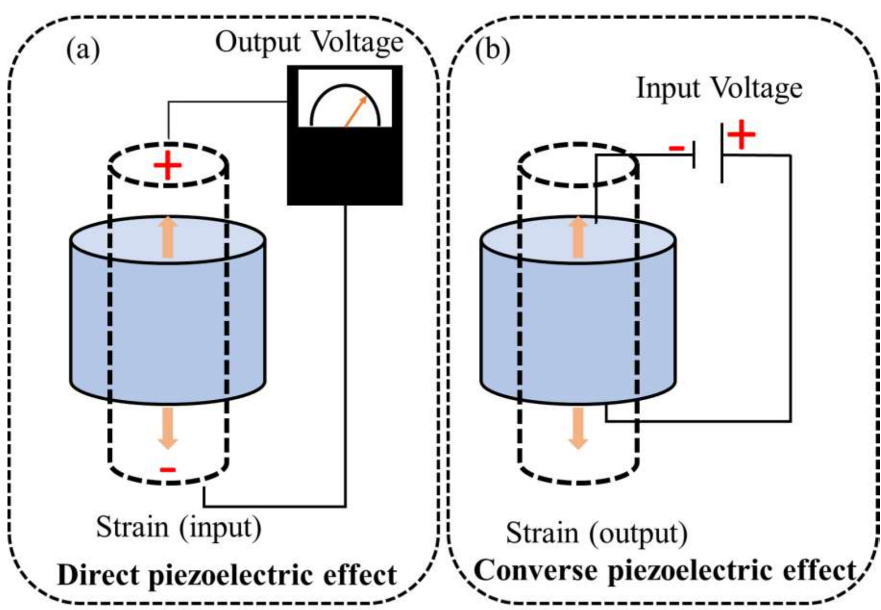

Figure 1.1: *Direct and converse piezoelectric effects.*

Inversely, the development of strain S in a substance produced by the applied field E is called the converse piezoelectric effect, as expressed in Figure 1.1(b) by equation (1.2):

$$S = s^{E}.T + d^{t}.E \quad (1.2)$$

where S is the strain tensor, s^{E} is the elasticity tensor under a constant electric field, and d^{t} is the converse piezoelectric tensor.

The piezoelectric coefficients are defined as follows [3,4]:

$$d_{ij} = (\partial D_i/\partial T_j)_E = (\partial S_i/\partial E_j)_T \quad (1.3)$$

$$e_{ij} = (\partial D_i/\partial S_j)_E = (\partial T_i/\partial E_j)_S \quad (1.4)$$

in which the first terms are related to the direct piezoelectric effect, and the second terms are referred to the converse effect. The *i* and *j* subscriptions are from 1 to 6 in the second-rank tensor.

The electromechanical coupling factor *k* is usually used to evaluate the strength of a piezoelectric effect. When applied to an electric field, it measures the fraction of the mechanical energy converted to electrical energy, and vice versa [2]. The actual relationship is commonly used in term of k^2.

$$k^2 = \frac{\text{mechanical energy converted to electrical energy}}{\text{input mechanical energy}}$$

or

$$k^2 = \frac{\text{electrical energy converted to mechanical energy}}{\text{input electrical energy}}$$

(1.5)

k^2 is always below 1 because of the loss occurring in the conversion of mechanical energy to electrical energy. Some typical examples are quartz, $BaTiO_3$, ZnO and $Pb(ZrTi)O_3$ with *k* values of 0.1, 0.4, 0.27, and 0.5-0.7, respectively [5]. It is noted that other numerical values are possible depending on composition, preparation techniques, etc.

The existence of piezoelectricity strongly depends on material crystallographic symmetries that will only be observed in non-centrosymmetric crystals. Table 1 presents a summary of crystallographic point groups that support piezoelectricity.

Table 1: *The crystallographic point groups that support piezoelectricity.*

Crystal system	Piezoelectricity
Triclinic	1
Monoclinic	2, *m*
Orthorhombic	mm2, 222
Tetragonal	4, $\bar{4}$, 4mm, $\bar{4}$2m, 422
Trigonal	3, 32, 3m
Hexagonal	6, 6mm, 622, $\bar{6}$, $\bar{6}$2m
Cubic	$\bar{4}$3m, 23

1.1.2. Piezoelectric effect in ZnO and AlN

The hexagonal wurtzite ZnO (and AlN) belongs to the non-centrosymmetric space group of C^4_{6v} or $P6_3mc$., as shown in Figure 1.4. Figure 1.5 shows the tetrahedral coordination where a positive atom is surrounded by four anions [6].

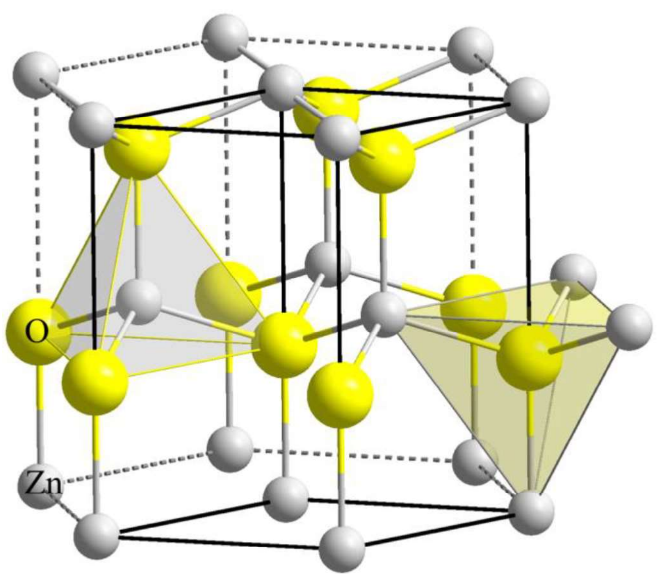

Figure 1.4: *Crystal structure of hexagonal wurtzite ZnO* [7].

In the case of ZnO, the tetrahedral coordination is responsible for the non-centrosymmetric structure, thus the center of negative and positive charges do not overlap, leading to the creation of electric dipoles within the crystal. These dipoles can be modulated by exerting mechanical stress (Figure 1.5(b)). Moreover, ZnO has polar surfaces, which are positively charged $Zn^+(0001)$ and negative charged O-$(000\bar{1})$ surfaces. These polar surfaces created a normal dipole and spontaneous polarization along the c-axis.

Table 2: *Piezoelectric and dielectric constants of piezoelectric materials* [8].

Coefficients	PZT (1 µm thickness)	ZnO (1 µm thickness)	AlN (1 µm thickness)
$e_{31,f}$ (C/m^2)	-8 to -12	-1.0	-1.05
$d_{33,f}$ (pm/V)	60 - 130	5.9	3.9
tan δ (@ 1 to 10 kHz, 10^5 V/m)	0.01 - 0.1	0.01 - 0.03	0.003
ε_{33}	300 - 1300	10.9	10.5

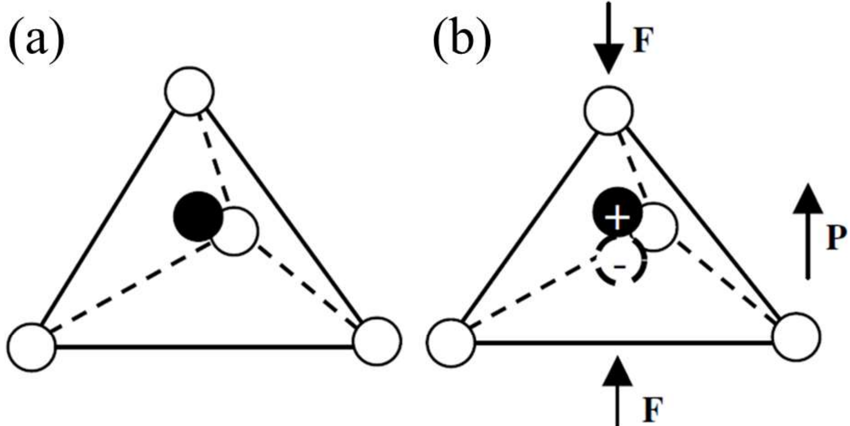

***Figure 1.5**: Schematic diagrams illustrating the piezoelectric effect in ZnO* [6].

The origin of piezoelectricity in the hexagonal wurtzite ZnO (and AlN) is different from ferroelectricity in perovskites such as $BaTiO_3$, which stems from the displacement of the Ti^{4+} cations inducing spontaneous polarization, whereas piezoelectricity originates from the polarization of a tetrahedrally coordinated structure and is a crystal structure-determined effect [6]. The piezoelectric and dielectric constants of some piezoelectric thin films are presented in Table 2.

1.2 Magnetostriction

1.2.1. Introduction

The effect of the change in dimension of a substance by an applied magnetic field is called the magnetostrictive effect [9]. This effect was discovered by Joule in 1842 on an iron rod, the length of which increased when exposed to a weak magnetic field. The magnetostriction effect is illustrated in Figure 1.6. When no magnetic field is applied, spins are randomly oriented. By increasing the magnetic field applied, spins are gradually aligned in the direction of the applied field. In magnetostrictive materials, the alignment of spins causes a change in dimension. The fractional change in length induced by the magnetic field is called the magnetostriction coefficient (or strain).

$$\lambda = \frac{\Delta L}{L} \tag{1.6}$$

The value of λ measured at the saturated field is referred to as the saturation magnetostriction λ_S. The effect described above is the longitudinal effect, also called the Joule magnetostriction effect. There are other magnetostriction effects where the magnetically induced volume changes, and torsion or the bending of a rod is observed, such as volume magnetostriction and the Wiedemann effect. These effects are not in the scope of discussion in this study.

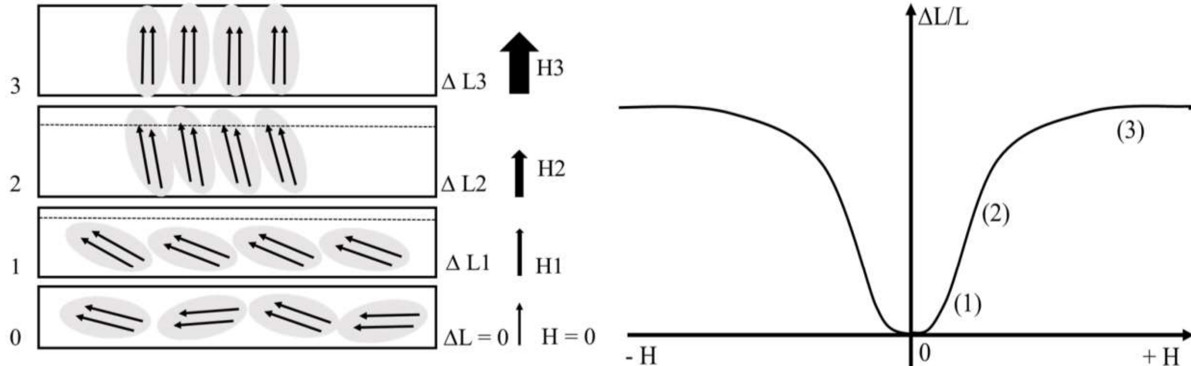

Figure 1.6: *(a) Schematic diagram of the magnetostriction effect; (b) strain versus magnetic field* [9].

There is an inverse effect of the Joule magnetostriction effect, called the Villari effect, which is a strong dependence of material properties such as permeability and the size and shape of the magnetic hysteresis loop on stress [9], as shown in Figure 1.7. The magnetization of a polycrystalline nickel is modified by the application of stress. At a magnetic field of 10 Oe, a compressive stress of about 70 MPa increases the magnetization almost twofold, meanwhile with the same amount of tensile stress, the magnetization is reduced to one-tenth of the zero-stress value.

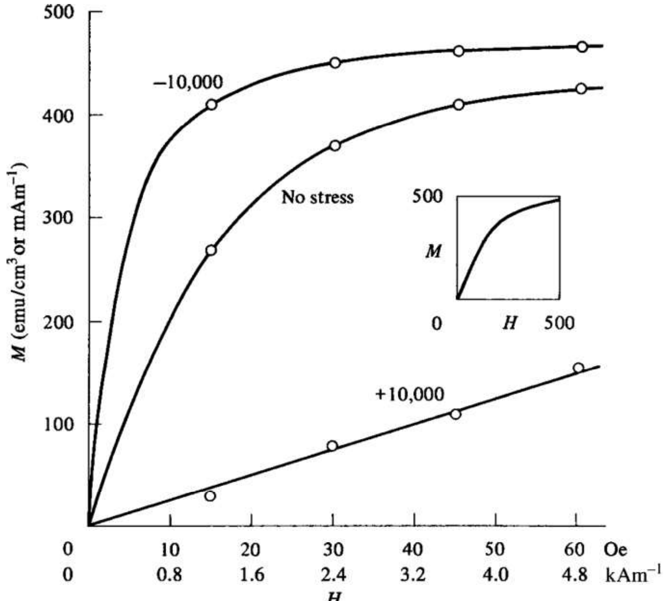

Figure 1.7: *Effect of applied tensile (+) and compressive (-) stress on the magnetic curve of the magnetization M of polycrystalline nickel* [9].

The Joule magnetostriction effect observed in an iron rod is also called anisotropic magnetostriction because of a larger contraction of -36×10^{-6} at 300K parallel to the applied field, which is twice larger than the effect in the plane perpendicular to the applied field [9].

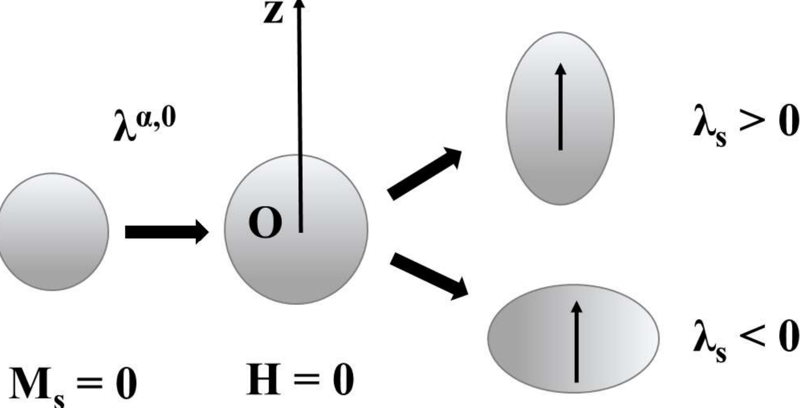

Figure 1.8: *The schematic description of the two magnetostriction effects observed in an isotropic material* [9].

Figure 1.8 illustrates the two magnetostriction effects. An isotropic sample undergoes a relative deformation in volume $\delta V/V = \lambda^{\alpha,0}$ as soon as it is magnetic. $\lambda^{\alpha,0}$ is called the volume magnetostriction coefficient [9]. When the volume change is completed and a magnetic field is applied in the z-axis, an anisotropic deformation occurs at a constant volume. This deformation is induced by the sphere changing into an ellipsoid of evolution along the z-axis. If the sphere deforms into a prolate ellipsoid, it has a positive magnetostriction coefficient ($\lambda_s > 0$). In contrast, the material has a negative magnetostriction coefficient ($\lambda_s < 0$) if it deforms into an oblate ellipsoid.

For many applications such as magnetic sensors, the best materials are not those with giant magnetostriction, but those with a piezomagnetic coefficient $q_{33} = \partial\lambda/\partial H$, and the highest value of the magnetomechanical coupling coefficient. It is defined as below [10,11]:

$$k^2 = 1 - \frac{E_0}{E_S} \quad (1.7)$$

where E_0 is Young's modulus of a substance, which is under zero mechanical stress and where a magnetic field is applied, and E_s is Young's modulus of the sample under magnetically saturated conditions provided either by the application of an extremely high field or extremely high mechanical stress.

Table 3 summarizes the saturation magnetostriction coefficient (λ_S), the magnetomechanical coupling factor (k), the piezomagnetic coefficient (q_{33}^{max}), and the Curie temperature T_C (where the transition of ferromagnetic to paramagnetic behaviors occurs) of several typical magnetostrictive materials. Ni, Fe, and Co are some of the earliest magnetostrictive materials discovered [9], while Terfenol-D ($Tb_{0.3}Dy_{0.7}Fe_2$) shows the highest magnetostriction effect ever observed.

Table 3: *Parameters of selected bulk magnetostrictive materials* [9].

Parameters	Ni	Fe	Co	Metglas	Terfenol-D	FeGaC	FeGaB	FeCoSiB
λ_S (ppm)	-40	-15	-30	30	2000	81.2	70	158
k	0.31	-	-					
q_{33}^{max} (m/A)	-3.1×10^{-9}	-	-		57×10^{-9}			
T_C (°C)	358	770	1115	395	650	-	-	-
References	12	12	12	13	14	15	16	17

1.2.2. Microscopic origin of magnetostriction

To understand the microscopic origin of magnetostriction, a model of the magnetic interaction of a pair of atoms is used, as described in Figure 1.9 [9]. The interaction responsible for magnetism is supposed to depend only on the direction of magnetization and on the distance between the two atoms.

The exchange magnetoelastic coupling energy is a sum of the isotropic exchange term [9]:

$$\mathcal{E}_{ex} = -J_{AB}(r) < S_A . S_B > \quad (1.8)$$

Here, J_{AB} is a Heisenberg exchange integral for a pair of the nearest neighboring atoms. It is negative for antiferromagnetic substances and is positive for ferromagnetic substances.

For deformation in a cubic crystal, the magnetic energy density is defined as [9]:

$$E_{ex} = -Nz\, J_{AB}(r) < S_A . S_B >$$

$$= -Nz\left[(J_{AB})_0 + r_0\left(\frac{\partial J_{AB}}{\partial r}\right)_0 \frac{1}{3}\frac{\delta V}{V_0} + \frac{1}{2}r_0^2\left(\frac{\partial^2 J_{AB}}{\partial^2 r^2}\right)_0 \left(\frac{1}{3}\frac{\delta V}{V_0}\right)^2 < \mathrm{S_A.S_B} >\right] \quad (1.9)$$

where N is the number of atoms per unit volume, z is the number of the nearest neighbors, V_0 is the initial volume of the substance, and r_0 is the interatomic distance measured in the absence of magnetism.

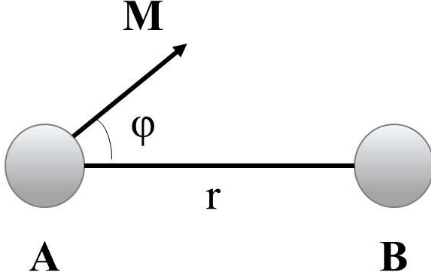

Figure 1.9: *The schematic of magnetic interaction of a pair of atoms* [9].

The elastic energy density is given as [9]:

$$\mathrm{E_{el}} = \frac{1}{2\kappa}\left(\frac{\delta V}{V_0}\right)^2 = \frac{c^\alpha}{6}\left(\frac{\delta V}{V_0}\right)^2 = \frac{c_{11}+2c_{12}}{6}\left(\frac{\delta V}{V_0}\right)^2 \quad (1.10)$$

Here, $\kappa = 3/c^\alpha$ is compressibility of the materials and c_{ij} (c^α) are elastic constants. For cubic symmetry, three independent coefficients are used, c_{11}, c_{12}, and $c_{44} = (c_{11} + c_{12})/2$. The contraction of indices is followed Voigt rule. Details can be found in page 392 in *Magnetism* (Volume 1, Chapter 12 by E. du Trémolet de Lacheisserie) [9].

In cubic symmetry, the volume magnetostriction is calculated by minimizing the sum of the magnetic energy density and the elastic energy density with respect to the relative volume change $\delta V/V_0$.

$$\delta V/V_0 = \lambda^{\alpha,0} = \frac{r_0 Nz}{c^\alpha}\frac{\partial J_{AB}}{\partial r} < \mathrm{S_A.S_B} > \quad (1.11)$$

In the paramagnetic state (above T_C), $< \mathrm{S_A.S_B} >$ vanishes, thus no exchange magnetostriction is observed and a substance does not undergo any deformation by the applied field. At low temperatures, spins are aligned to the applied field and the value of $S_A.S_B$ reaches its saturation value, thus, the exchange magnetostriction saturates.

The descriptions above are used to simply explain the microscopic origin of volume magnetostriction. More details about anisotropic magnetostriction and the effect of symmetry can be found in *Magnetism* (Volume 1, Chapter 12 by E. du Trémolet de Lacheisserie) [9].

Magnetostriction is quite sensitive to the geometry and symmetries of the material. In a thin film case, the problem is complicated by epitaxial stresses. Furthermore, these stresses can generate a strong magnetoelastic anisotropy, which can overcome magnetocrystalline anisotropy, and thus change the easy magnetization directions [9].

1.3
Magnetoelectric effect and materials

"Let us point out two more phenomena, which, in principle, could exist. One is piezomagnetism, which consists of linear coupling between a magnetic field in a solid and a deformation analogous to piezoelectricity. The other is a linear coupling between magnetic and electric fields in a media, which would cause, for example, a magnetization proportional to an electric field. Both these phenomena could exist for certain classes of magnetocrystalline symmetry. We will not however discuss these phenomena in more detail because it seems that till present, presumably, they have not been observed in any substance."

- Landau and Lishitz -

Electrodynamics of continuous media (Fizmatgiz, Moscow, 1959)

1.3.1. Introduction

The coexistence of ferroelectricity (or piezoelectricity) and ferromagnetism (or anti-, ferrimagnetism) has received significant attention for both fundamental and practical purposes where ferroelectric properties can be tailored by an external magnetic field, or magnetic properties can be manipulated by an electric field, or *vice versa* [18–23]. The "multiferroics" term is used for materials possessing two or more such ferroic orderings, as described in Figure 1.10 [24]. However, very few single-phase multiferroic materials exist because of the violation between mechanisms governed by ferroelectricity and ferromagnetism [25,26]. Most ferroelectric materials are transition metal oxides, where the off-centering movement of cations creates a spontaneous electric polarization. An empty d orbital (also called d^0-ness) is required to favor the covalent formation, stabilizing the off-centering displacement [26,27]. In contrast, a partially occupied d orbital is a prerequisite for the occurrence of magnetic exchange interaction between uncompensated spins of different transition-metal cations, which govern long-range magnetic ordering [26,27]. Consequently, the contradiction in the requirement of the occupying level of d orbitals for ferroelectricity and ferromagnetism makes multiferroic materials rare and exclusive.

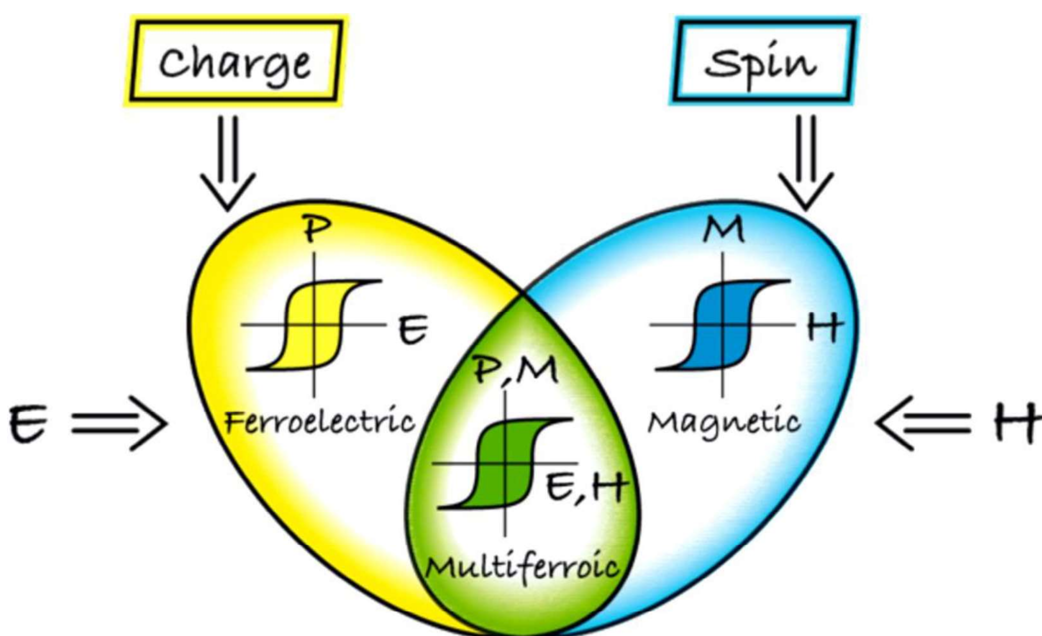

***Figure 1.10**: The schematic diagram of multiferroics materials combining the properties of ferroelectrics and ferromagnetism* [24].

Spaldin and Ramesh [27] presented the multiferroic family tree (Figure 1.11), which clarifies classes and evolution of multiferroic materials into several branches, such as the *"lone pair ferroelectricity, d-electron magnetism"*, *"composite branch"*, *"d^0 ferroelectricity, f-electron magnetism"*, and *"novel ferroelectricity, d-electron magnetism"*, arising from the combination of the interplay between ferroelectric and ferromagnetic mechanisms.

"Lone pair ferroelectricity, d-electron magnetism branch". A typical example of this multiferroic group is $BiFeO_3$. In this compound, the large polarization stems from the stereochemical activity of the Bi^{3+} $6s^2$ "lone pair" of electrons [25,27], and the Fe^{2+}/Fe^{3+} is responsible for the robust antiferromagnetism. Some other compounds, such as $BiCoO_3$, $PbMnO_3$ and $PbFeO_3$ are believed to belong to this multiferroic group [28].

"*d^0 ferroelectricity, f-electron magnetism*". Single component multiferroics, two-cation compounds, an one cation with *f*-electrons is responsible for magnetism and the other one, with d^0-ness electrons, generates ferroelectricity [27]. A well-studied system is the (Eu,Ba)TiO_3 compound, here, magnetic f^7 Eu^{2+} is partially substituted for Ba^{2+} [29].

"*Novel ferroelectricity, d-electron magnetism branch*". In this multiferroic class, magnetic properties originate from d-electrons, and ferroelectricity is induced by phenomena emerging at nano or atomic scales, for example, geometrically driven multiferroics, where rotations of small cations surround coordination polyhedral, which are either polar (in $BaNiFe_4$) or coupled to secondary polar distortion ($YMnO_3$) yielding polarizations [27]; or spin-driven multiferroics, in which inversion symmetry breaking is induced by magnetic ordering. The interaction of spins and charges may transfer the non-centrosymmetry from the magnetic to the electric lattice, leading the formation of polarization [29].

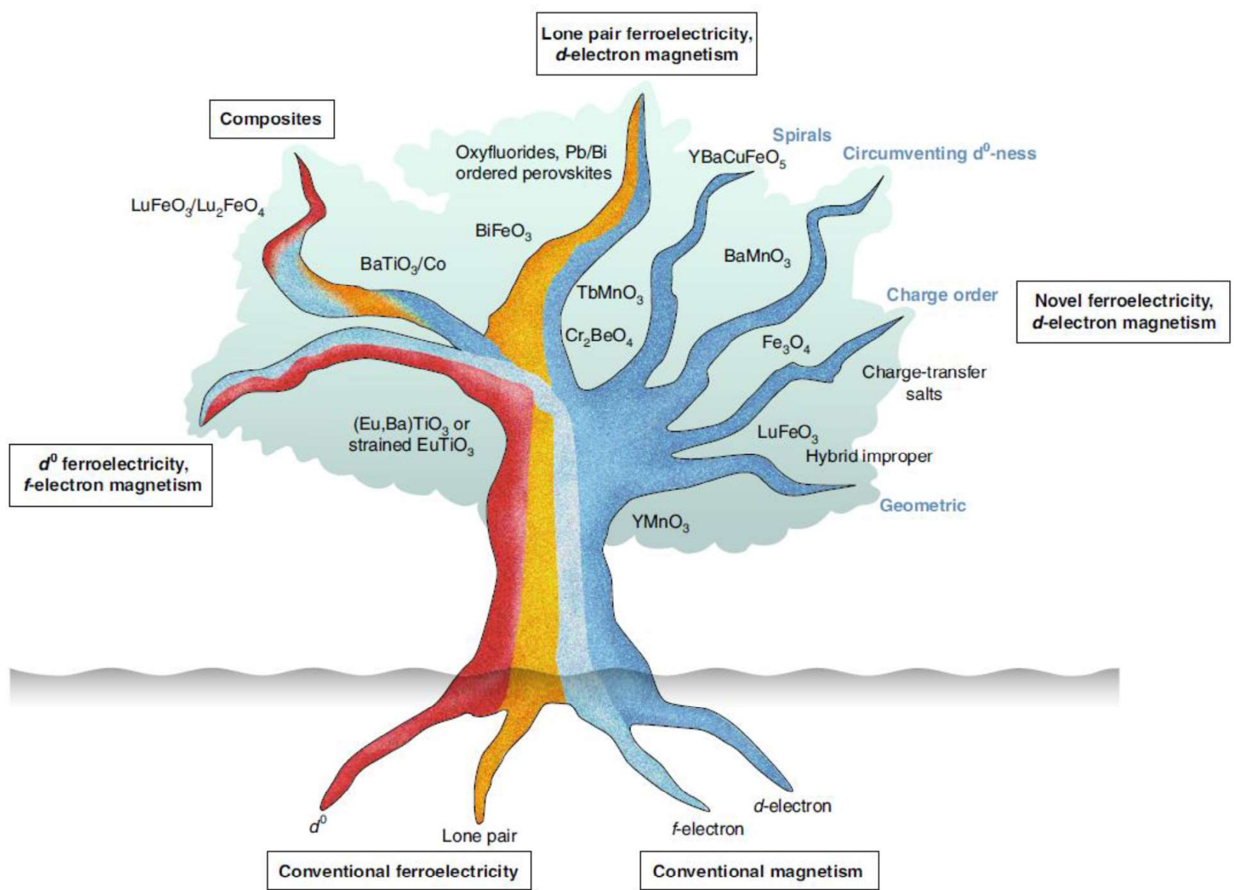

Figure 1.11: *The multiferroic family tree, according to Spaldin and Ramesh* [27].

"*Composites branch*". Composite multiferroics are a combination of a non-magnetic ferroelectric (piezoelectric) compound, and a non-ferroelectric magnetic material. This multiferroic class has received significant attention for both fundamental research and practical applications due to a strong magnetoelectric coupling in single-phase multiferroics, which is usually very weak and/or at low temperatures [30–34]. More details will be discussed in the next section.

Table 1.4: *An exhaustive survey on magnetoelectric multiferroics and composites.*

Author/ Year	Composition	Connectivity	Fabrication method	Magnetic field DC bias /freq.	ME coefficient ($mVcm^{-1}Oe^{-1}$)	Remark
			Single phase			
Astrov, 1961 [35]	Cr_2O_3	Single phase	-	-	4.3 x 10^{-4}	The 1st experimental observation
Wang et al., 2003 [36]	$BiFeO_3$	Epitaxial films on $SrTiO_3$ (100) single crystal substrate	PLD		Ferroelectric and ferromagnetic properties were reported.	
			Bulk/ Layer Laminate			
Van Suchtelen, Van den Boomgaard, 1972, 1974 [37–39]	$(BaTiO_3)_{0.62}(CoFe_2O_4)_{0.38}$ (eutectic composition with 1.5 wt% excess TiO_2	3-0/Particulate	Bridgman	-	50	The first ME composite
Suryanarayana, 1994 [40]	$(CuFe_2O_4)_{0.3}(PbZr_{0.53}Ti_{0.47}O_3)_{0.7}$	3-0/Particulate	Sintered at 1300 °C/24h	460 Oe/ 100 kHz	421	The first resonance type ME composite
Bichurin et al. 1997 [41]	(Ni-Co)-ferrite/PZT ceramics and YIG/$BaTiO_3$	3-0/Particulate	Standard ceramic method	0.8-0.9 kOe	110	The first theoretical approach on the ME effect
Srinivasan et al. 2004 [42]	$Ni_{0.8}Zn_{0.2}Fe_2O_4$-PZT	3-0/Particulate	Hot pressed at 1000 °C	250Oe /100Hz	45	The first hot pressing method
Mathe and Sheikh 2009 [43]	$NiFe_2O_4$ + PMN-PT	3-0/Particulate	Solid-state solution at 1250 °C	Static ME measurement	10.43	

Ryu et al. 2001, 2002 [44,45]	Terfenol-D/PMN-PT/Terfenol-D	2-2/Laminate	Epoxy-glued composite	4000 Oe /1 kHz	5	The first laminate ME composite
Bichurin et al., 2003 [46]	$NiFe_2O_4$ + PZT	2-2/Multilayer	11 layers of 13 µm $NiFe_2O_4$ and 10 layers of 26 µm PZT	1050 Oe /350 kHz at resonance	1.2	The first ME multilayer composite
Dong et al., 2004 [47]	Terfenol-D/PMN-PT	2-2/Laminate		550-800 Oe /1 kHz	430	
Dong et al, 2006 [48]	Metglas/PZT (piezofiber)	2-2/Laminate	Epoxy-glued composites	5 Oe /1 Hz	22’000	
Zhai et al., 2006 [49]	Metglas/PVDF	Layered laminate	Epoxy-glued composites	1 Oe		Thin and flexible ME composites
Gao et al., 2010 [50]	Metglas + PMN-PT and PZN-PT single crystals	Laminated composites	Epoxy-glued composites	1 Oe /1 kHz	8’500	
Chashin et al. 2011 [51]	Metglas/PMN-PT	Laminate composites	Epoxy-glued composites	1 Oe /1 kHz	45’000	
Ryu et al., 2015 [52]	Ni plate + PMN-PZT single crystal fiber composites	Laminate composites	Epoxy-glued composites	5-7 Oe /@ resonance f = 100 Hz	120’000	Resonance cantilever structures
Annapureddy et al., 2018 [53]	Highly textured Fe-Ga alloy + PMN-PZT single crystal macro-fiber composites	Laminate composites	Epoxy-glued composites	2 Oe/ 80-120Hz	26’000 without clamping and proof mass. 1’330’000 with clamping and proof mass	Resonance cantilever structure

Thin-film composites

Park et al., 2009 [54]	PZT-PZN and $(Ni_{0.6}Cu_{0.2}Zn_{0.2})Fe_2O_4$	Nanocomposite thick films	Aerosol-deposition	1 Oe /1 kHz	150	
Xu et al., 2010 [55]	$CoFe_2O_4$/PZT	Nanocomposite thin films	Sol-gel process and spin-coating process	50 kHz /dynamic	273	
Greve et al., 2010 [17]	$(Fe_{90}Co_{10})_{78}Si_{12}B_{10}$-AlN	Thin-film composites	Sputtering at 450 °C	6 Oe /100, 753 Hz	3’100 @ 100 Hz 737’000 @ resonance f = 753 Hz	Resonance cantilever structures
Lage et al. 2012 [56]	AlN film with Ta/Cu/$Mn_{70}Ir_{30}$/$Fe_{70:2}Co_{7:8}Si_{12}B_{10}$	Thin-film composites	Sputtering	10 Oe /	96’700 at resonance f = 1 kHz	Self-bias Hdc = 0 Oe
Gupta et al., 2017 [57]	PZT/Ni	Thin-film composites	PLD at 800 °C	1 Oe /1 kHz	94’500- 130’500	

Table 1.4 presents a survey on magnetoelectric multiferroics and composites and their direct magnetoelectric coefficient. Cr_2O_3 was the first magnetoelectric compound discovered in a single phase and its ME coefficient was as small as 4.3 x 10^{-4} ($mV.cm^{-1}.Oe^{-1}$) [35]. ME laminate composite demonstrated a much greater response with an ME coefficient of 1’330’000 ($mV.cm^{-1}.Oe^{-1}$) for a resonant cantilever structure made of highly textured Fe-Ga alloy and PMN-PZT single crystal macro-fiber composites [53]. Thin-film composites have also attracted significant attention due to their great ability of controlling the interface at the nanoscale and fulfill of requirements for microdevices. The highest response with an ME coefficient of 130’500 ($mVcm^{-1}Oe^{-1}$) was achieved in a PZT/Ni composite fabricated by PLD technique at 800 °C. Here the ME coefficient, α_{ME}, is defined as:

$$\alpha_{ME} = \frac{V_{output}}{tH_{ac}}$$

where V_{output} is the output voltage of the ME substance, t is the thickness, and H_{ac} is a applied AC magnetic field.

1.3.2. Magnetoelectric effect in composites

1.3.2.1.Introduction

As pointed out before, the critical limitations of single-phase ME materials for practical applications are weak coupling and operation at low temperatures, where either ferromagnetic or ferroelectric orders occur. By the 1970s, van Suchtelen [58] had proposed a way to overcome the limitations of single-phase multiferroics by combining ferromagnetic and ferroelectric phases as a two-phase composite. One of the most remarkable advantages of two-phase composites is a significant enhancement of the ME coefficient compared to single-phase materials.

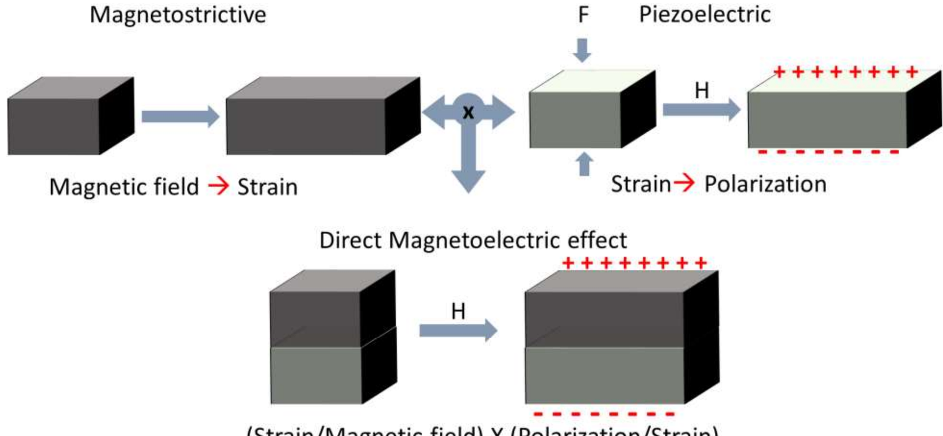

Figure 1.12: *Strain-mediated magnetoelectric effect in composites made of magnetostrictive and piezoelectric (or ferroelectric) materials. Strain/stress induced by an external magnetic field due to a magnetostriction effect transfers to the piezoelectric layer through the interface, and subsequently generates an output voltage due to the direct piezoelectric effect.*

In general, the ME composite consists of a magnetostrictive and a piezoelectric (ferroelectric) layer, as shown in Figure 1.12. The direct ME effect in the ME composite results from the strain/stress coupling between the two layers; i.e. a mechanical stress/strain in the magnetostrictive layer induced by an external magnetic field applied transfers to the piezoelectric layer, producing an output voltage/electric field proportional to the applied magnetic field. In the conserved ME effect, an electric field applied on the piezoelectric layer results in a deformation due to the inverse piezoelectric effect. This deformation is transferred to the magnetostrictive layer through the interface coupling, which then results in a magnetization change due to the Villari effect.

There are three widely used methods of designing ME composites; 0-3 connectivity where magnetic nanoparticles are embedded in a piezoelectric phase, 1-3 composite which are an array of magnetic nanopillars in a piezoelectric phase, and 2-2 connectivity in which a magnetic layer is connected to a piezoelectric layer by epoxy glue (a laminate ME composite) or bilayer films. Here, the indices denote dimensions of the materials. The synthesis of 0-3 particulates and 1-3 composites has been intensively studied by combining a variety of piezoelectric and magnetostrictive materials [34,59]. However, these composites present severe issues [59]: (i) the misfit strain at the interface induced by the thermal expansion mismatch between the two phases, reducing the densification; (ii) the interdiffusion and/or chemical reactions between the two constituents due to high temperature processes, which degrades the piezoelectric and magnetostrictive properties of the two phases; and (iii) the high leakage current arising in the

composites due to the randomly distributed magnetic phase. Compared to the 0-3 and 1-3 composites, the 2-2 composite does not present the above-mentioned issues due to its connectivity method, thus ensuring a high ME response. Ryu et al. [52] reported a giant ME coefficient of 120 $V.cm^{-1}.Oe^{-1}$ in a laminate composite made of PMN-PZT single crystal fiber composites bonded with an Ni plate by epoxy glue. Recently, Gupta *et al.* [57] reported a giant ME coefficient of 130.5 $V.cm^{-1}.Oe^{-1}$ in a PZT/Ni thin-film composite grown by PLD at 800 °C.

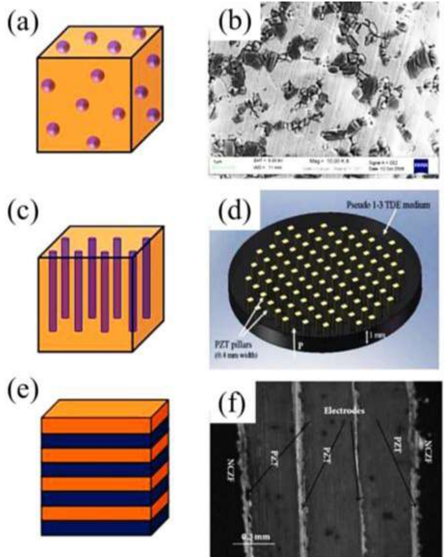

Figure 1.13: *Development of bulk ME composites with different phase connectivity (a)-(b) 0-3 connectivity, $NiFe_{1.9}Mn_{0.1}O_4$ particles in PZT phase; (c)-(d) 1-3 connectivity, Terfenol-D in a matrix of PZT, and (e)-(f) 2-2 connectivity, $NiFe_2O_4$/PZT multilayers* [59].

1.3.2.2. Theoretical approach for layer-layer composites

Several approaches have been introduced in order to formulate the ME effect in the two-phase composite [60–62]. Nan [60] was one of the pioneers in formulating the ME effect in the composite based on Green's function method and perturbation theory. Muchenik [62] further developed this by considering various options of magnetization and induced electric field directions. In the scope of this section, a theory developed by Bichurin and Petrov [61] for a low-frequency ME coupling understanding of the observation of the giant ME effect in the bilayer system will be briefly given.

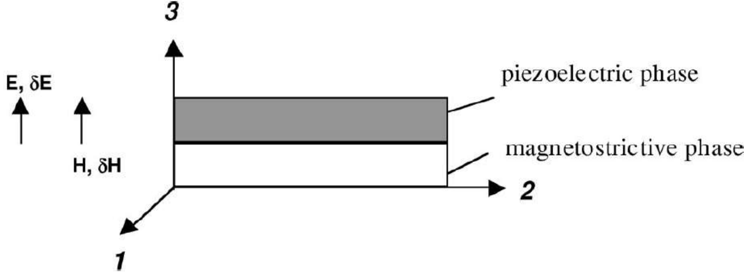

Figure 1.14: *The schematic diagram of a bilayer ME composite made of piezoelectric and magnetostrictive phases in the (1,2) plane* [61].

Figure 1.14 shows the schematic diagram of the bilayer ME composite composed of polycrystalline films. The formalism is established using the two-stage approach, i.e. in the first stage, the composite is considered a bilayer, then as homogeneous in the second stage [61].

In the first stage, the strain and electric displacement in the piezoelectric phase can be written as the following equations [61]:

$$
\begin{aligned}
{}^{p}S_i &= {}^{p}s_{ij}\,{}^{p}T_j + {}^{p}d_{ki}\,{}^{p}E_k \\
{}^{p}D_k &= {}^{p}d_{ki}\,{}^{p}T_i + {}^{p}\varepsilon_{kn}\,{}^{p}E_n
\end{aligned}
\qquad (1.12)
$$

in which, ${}^{p}S$ and ${}^{p}T$ are strain and stress tensors of the piezoelectric layer, ${}^{p}E$ and ${}^{p}D$ are the electric field and electric displacement vectors, ${}^{p}s$ and ${}^{p}d$ are compliance and piezoelectric coefficients and ${}^{p}\varepsilon$ is the permittivity matrix. The i, j and k subscriptions are from 1 to 6 in the second-rank tensor.

For the magnetostrictive layer, which is assumed to have a cubic symmetry, the strain and magnetic induction is described as below [61]:

$$
\begin{aligned}
{}^{m}S_i &= {}^{m}s_{ij}\,{}^{m}T_j + {}^{m}q_{ki}\,{}^{m}H_k \\
{}^{m}B_k &= {}^{m}q_{ki}\,{}^{m}T_i + {}^{m}\mu_{kn}\,{}^{m}H_n
\end{aligned}
\qquad (1.13)
$$

where ${}^{m}S$ and ${}^{m}T$ are strain and stress tensors of the magnetostrictive constituent, ${}^{m}B$ and ${}^{m}H$ are the vector components of magnetic induction and magnetic field, ${}^{m}s$ and ${}^{m}q$ are compliance and piezomagnetic tensors, and ${}^{m}\mu$ is the permeability tensor.

In the second stage, considering the bilayer as a homogeneous composite, the behavior is described as follows [61]:

$$
\begin{aligned}
S_i &= s_{ij}T_j + d_{ki}E_k + q_{ki}H_k \\
D_k &= d_{ki}T_i + \varepsilon_{kn}E_n + \alpha_{kn}H_n \\
B_k &= q_{ki}T_i + \alpha_{kn}E_n + \mu_{kn}H_n
\end{aligned}
\qquad (1.14)
$$

in which S_i and T_j are the strain and stress tensors; E_k, D_k, H_k, and B_k are the vector components of the electric field, electric displacement, magnetic field, and magnetic induction; d_{ki}, q_{ki}, s_{ij} are effective piezoelectric, piezomagnetic and compliance coefficients; and ε_{kn}, α_{kn}, and μ_{kn} are effective permittivity, ME coefficient, and permeability. Effective coefficients of the bilayer composite are obtained by solving Eq. (1.14), accompanied by the solutions of Eqs. (1.12) and (1.13).

For the longitudinal ME effect, in which the directions of the applied magnetic field DC bias and AC component and the direction of induced electric field are along direction 3, Eqs. (1.12) – (1.14) are solved by imposing the following boundary conditions [61]:

$$
\begin{aligned}
{}^{p}S_i &= k\,{}^{m}S_i + (1-\mathrm{k})\,{}^{p}S_{i0} \qquad (i = 1,2), \\
{}^{p}T_i &= -\,{}^{m}T_i\,(1-\upsilon)/\upsilon \qquad (i = 1,2),
\end{aligned}
$$

$$ {}^{p}T_3 = {}^{m}T_3 = T_3 $$
$$ {}^{m}S_i = S_i $$
$$ S_i = \left[{}^{p}S_3 + {}^{m}S_3(1 - \upsilon) \right]/\upsilon \tag{1.15} $$

where $k = \left({}^{p}S_i - {}^{p}S_{i0} \right)/\left({}^{m}S_i - {}^{p}S_{i0} \right)$ is an **interface coupling parameter, which depends on the interface quality and is a measure of the differential deformation of the two layers** [61]. The coupling factor is $k = 0$ for the case with no contact between the two constituents and $k = 1$ for an ideal interface; $\upsilon = {}^{p}\upsilon/\left({}^{p}\upsilon + {}^{m}\upsilon \right)$; ${}^{p}\upsilon$ and ${}^{m}\upsilon$ are the volume of the piezoelectric phase and the magnetostrictive phase, respectively; and ${}^{p}S_{i0}$ are the strain tensor components at $k = 0$ with i=1,2.

At this point, we can highlight that one of the main objectives of this thesis is the experimental optimization of this interface coupling for mechanical energy transfer between the layers by means of thin film deposition methods that we will describe in the next chapter.

Then the longitudinal ME voltage coefficient is then given [61].

$$ \alpha_{33}^{E} = 2\frac{\mu_0 k\upsilon(1-\upsilon)\,{}^{p}d_{31}\,{}^{m}q_{31}}{\left\{2\,{}^{p}d^{2}{}_{31}(1-\upsilon) + {}^{p}\varepsilon_{33}\left[\left({}^{p}s_{11} + {}^{p}s_{12}\right)(\upsilon-1) - \upsilon\left({}^{m}s_{11} + {}^{m}s_{12}\right)\right]\right\}} \times \frac{\left[\left({}^{p}s_{11} + {}^{p}s_{12}\right)(\upsilon-1) - k\upsilon\left({}^{m}s_{11} + {}^{m}s_{12}\right)\right]}{\left\{\left[\mu_0(\upsilon-1) - {}^{m}\mu_{33}\upsilon\right]\left[k\upsilon\left({}^{m}s_{11} + {}^{m}s_{12}\right) - \left({}^{p}s_{11} + {}^{p}s_{12}\right)(\upsilon-1)\right] + 2\,{}^{p}q^{2}{}_{31}k\upsilon^{2}\right\}} \tag{1.16} $$

For a transverse ME effect, the magnetic field is applied along direction 1 (in the sample plane), and the induced electric field is measured along direction 3.

$$ \alpha_{31}^{E} = \frac{-k\upsilon(1-\upsilon)\left({}^{m}q_{11} + {}^{m}q_{21}\right)\,{}^{p}d_{31}}{{}^{p}\varepsilon_{33}\left({}^{m}s_{11} + {}^{m}s_{12}\right)k\upsilon + {}^{p}\varepsilon_{33}\left({}^{p}s_{11} + {}^{p}s_{12}\right)(1-\upsilon) - 2k\,{}^{p}d^{2}{}_{31}(1-\upsilon)} \tag{1.17} $$

1.3.3. Applications of direct magnetoelectric effect

On application of a magnetic field to a ME composite, a strain will be generated on the magnetostrictive layer due to the magnetostriction effect and this will subsequentially be transferred to the piezoelectric layer across the interface, producing an electrical charge on the surface due to the piezoelectric effect. This is called the direct ME effect. Based on this effect, one can use ME composites in various applications such as magnetic field sensors [63–69], transducers [70,71], antennas [72], and energy harvesters [52,53,73]. This section will mainly present two typical applications of the ME effect, in magnetic field sensors and energy harvesters.

1.3.3.1.Magnetic field sensors

Magnetic field sensors based on ME composites have received significant attention because of their simple operation mechanism and the fact that they do not need an external power source [63–69]. Generally, the use of ME composites for magnetic field sensors needs both a DC and an AC field. Maraska et al. [67] demonstrated a magnetic MEMS sensor system using an ME composite consisting of AlN and FeCoSiB, which is functionalized on the micrometer cantilevers with a thickness of 4 µm and a lateral dimension of 0.2 mm × 1.12 mm, as shown in Figure 1.15. The ME cantilever showed a giant ME coefficient of 1000 $(V.m^{-1})/(A.m^{-1})$, measured at a resonance frequency of 2.4 kHz and of 14 $(V.m^{-1})/(A.m^{-1})$, measured at out-of-resonance frequencies. It results in a sensor with a sensibility of 780 $V.T^{-1}$ and a noise level of 100 pT $Hz^{-1/2}$ in the resonance operation.

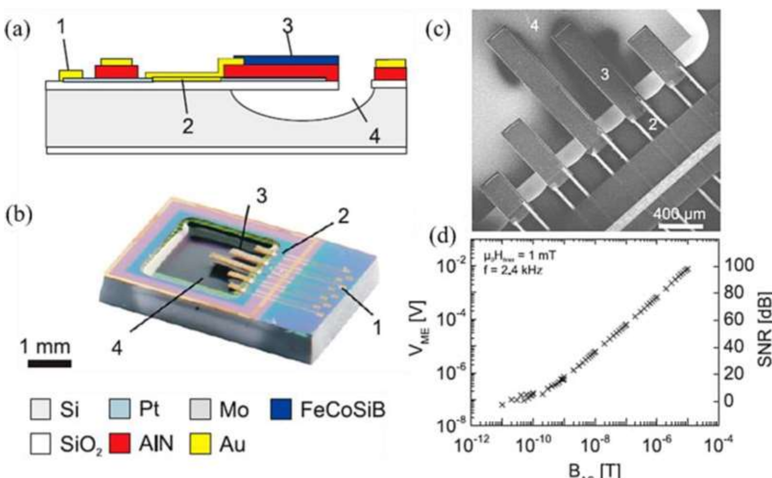

Figure 1.15: *(a) The schematic of a magnetic microsensor based on an ME composite, (b) photograph, (c) SEM micrograph, and (d) sensitivity and signal-to-noise ratio of the MEMS sensor system* [67].

1.3.3.2.Electromagnetic Energy harvester

Another highlighted application of ME composited is for energy harvesting. Ryu and his colleagues showed that using an ME laminate composite composed of a (011)-oriented anisotropic single crystal fiber composite (SFC) bonded to an Ni plate and Nd permanent magnet-proof mass, the ME generator produced a colossal output power density of 46 $mW.cm^{-3}.Oe^{-2}$ under a weak field of 1.6×10^{-4} T at 60 Hz, which is enough to switch on 35 LEDs and drive a wireless sensor network. The schematic diagram of fabrication and demonstration is presented in Figure 1.16.

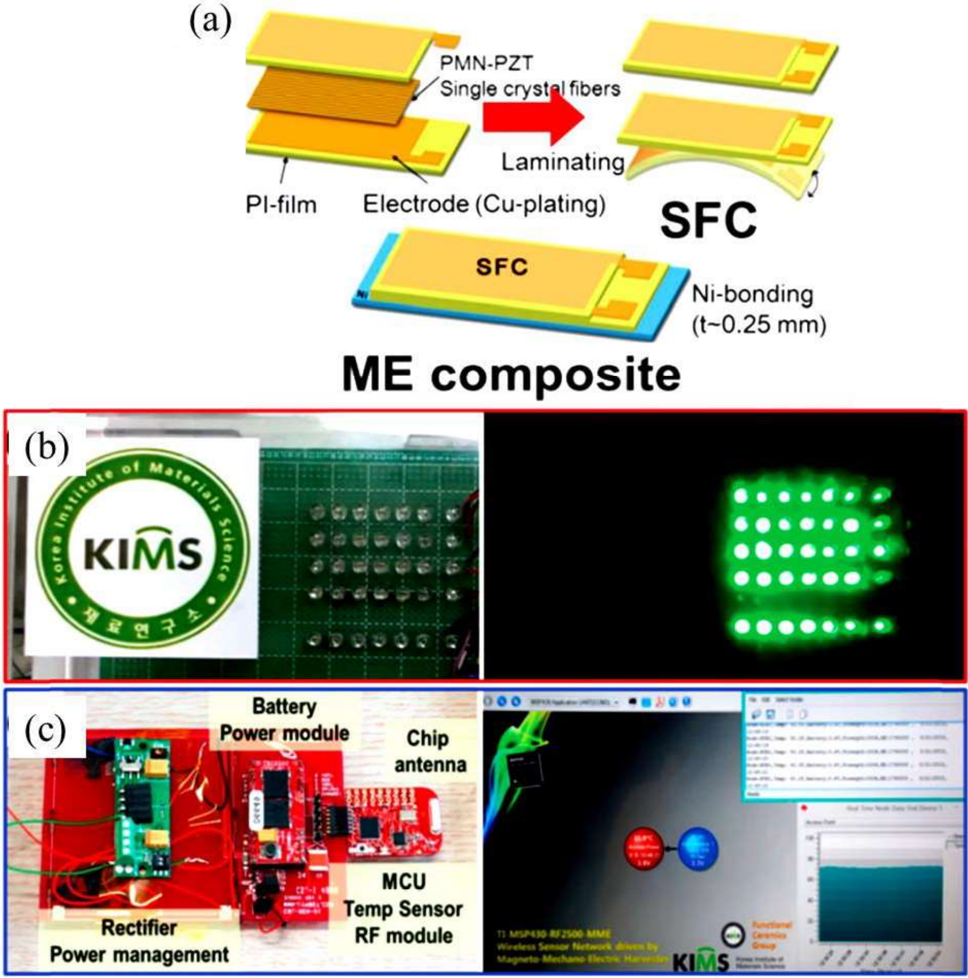

Figure 1.16: *(a) Schematic diagrams of ME laminate structure fabrication, made from SFC and Ni, (b) Demonstration of operation of 35 LEDs powered by the ME generator using a supercapacitor, and (c) a wireless communication system* [53].

Using an ME composite consisting of an Fe-Ga and $Pb(Mg_{1/3}Nb_{2/3})O_3–PbZrO_3–PbTiO_3$ (PMN-PZ-PT) single crystal in macro-fiber form (SCMF), Annapureddy et al. [53] demonstrated the magneto-mechano-electric (MME) generator with an output power density of 3.22 $mW.cm^{-3}Oe^{-2}$, which is able to integrate with wireless sensor networks (WSNs) such as low-power-consumption pressure and temperature sensors, as shown in Figure 1.17.

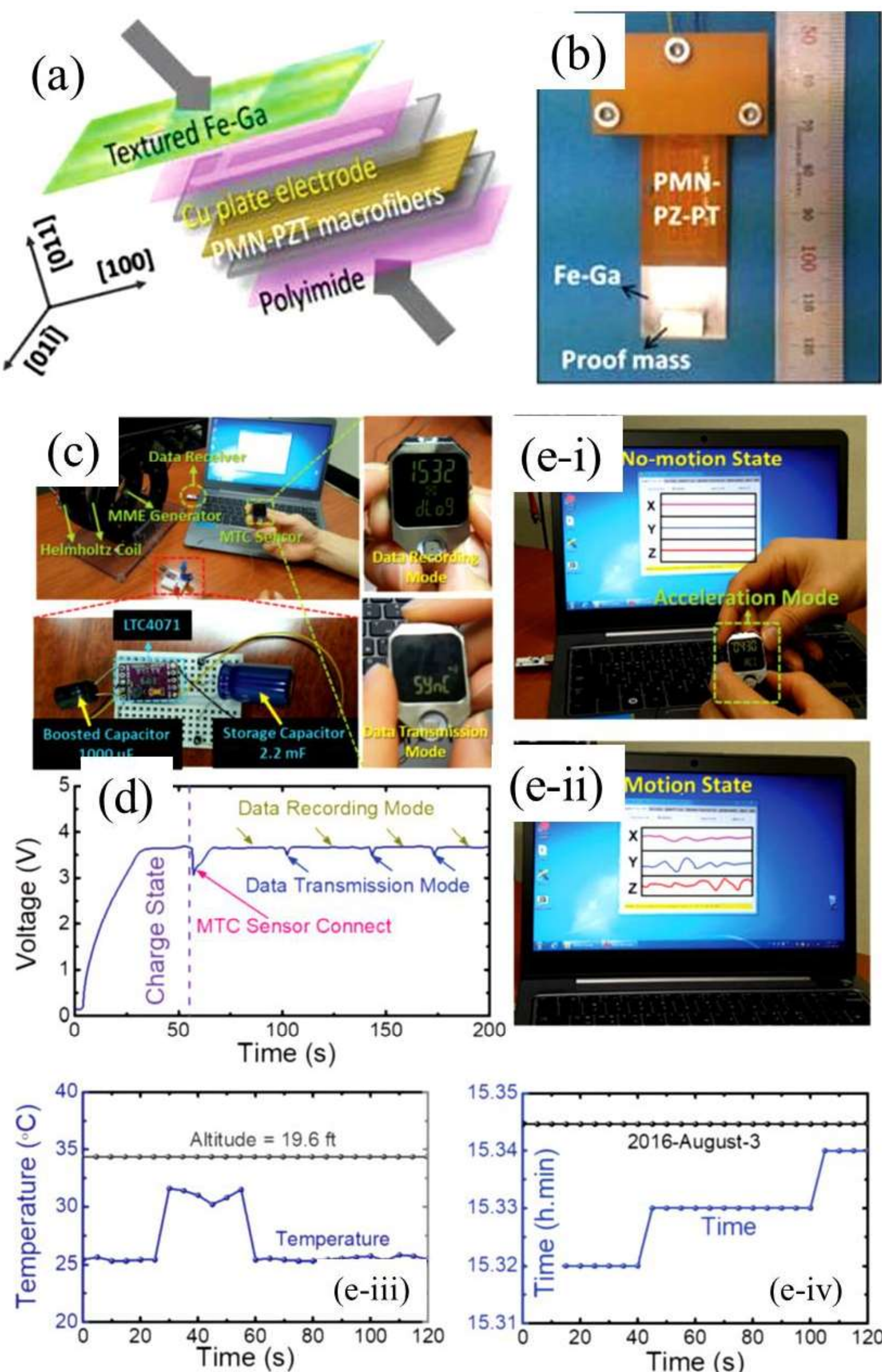

Figure 1.17: *(a) Bonding of textured Fe-Ga and PMN-PZ-PT SCMF, (b) photo of the MME generator designed with the ME composite cantilever structure, (c) photographs of the standalone-powered WSW composed of an MME generator, power management circuit, sensor module, and PE monitoring system, (d) charging and discharging of the storage capacitor, (e-i) to (e-iv) the wireless sensor in stable and operation states* [53].

1.4. References

(1) Ihlefeld, J. F. Chapter 1 - Fundamentals of Ferroelectric and Piezoelectric Properties. In *Ferroelectricity in Doped Hafnium Oxide: Materials, Properties and Devices*; Schroeder, U., Hwang, C. S., Funakubo, H., Eds.; Woodhead Publishing Series in Electronic and Optical Materials; Woodhead Publishing, 2019; pp 1–24. https://doi.org/https://doi.org/10.1016/B978-0-08-102430-0.00001-2.

(2) JAFFE, B.; COOK, W. R.; JAFFE, H. CHAPTER 2 - THE PIEZOELECTRIC EFFECT IN CERAMICS. In *Piezoelectric Ceramics*; JAFFE, B., COOK, W. R., JAFFE, H., Eds.; Academic Press, 1971; pp 7–21. https://doi.org/https://doi.org/10.1016/B978-0-12-379550-2.50006-5.

(3) Leprince-Wang, Y. *Piezoelectric ZnO Nanostructure for Energy Harvesting*; 2015. https://doi.org/10.1002/9781119007425.

(4) The IET. Standard Definitions and Methods of Measurement for Piezoelectric Vibrators, 1966.

(5) Uchino, K. *Advanced Piezoelectric Materials: Science and Technology*; 2010. https://doi.org/10.1533/9781845699758.

(6) Wang, Z. L. Zinc Oxide Nanostructures: Growth, Properties and Applications. *J. Phys. Condens. Matter* **2004**. https://doi.org/10.1088/0953-8984/16/25/R01.

(7) Borysiewicz, M. A. ZnO as a Functional Material, a Review. *Crystals* **2019**, *9* (10), 505. https://doi.org/10.3390/cryst9100505.

(8) Trolier-Mckinstry, S.; Muralt, P. Thin Film Piezoelectrics for MEMS. *Journal of Electroceramics*. 2004. https://doi.org/10.1023/B:JECR.0000033998.72845.51.

(9) Cullity, B. D.; Graham, C. D. *Introduction to Magnetic Materials (Google EBook)*; 2011.

(10) O'Dell, T. H. Measurement of Magnetomechanical Coupling Factor in Amorphous Ribbons. *Phys. status solidi* **1982**. https://doi.org/10.1002/pssa.2210740223.

(11) Squire, P. T. Magnetomechanical Measurements of Magnetically Soft Amorphous Materials. *Meas. Sci. Technol.* **1994**. https://doi.org/10.1088/0957-0233/5/2/001.

(12) du Trémolet de Lacheisserie, E.; Gignoux, D.; Schlenker, M. *Magnetism: Fundamentals, Materials and Applications*; 2002.

(13) Chu, Z.; Shi, H.; Shi, W.; Liu, G.; Wu, J.; Yang, J.; Dong, S. Enhanced Resonance Magnetoelectric Coupling in (1-1) Connectivity Composites. *Adv. Mater.* **2017**. https://doi.org/10.1002/adma.201606022.

(14) Chu, Z.; Pourhosseiniasl, M.; Dong, S. Review of Multi-Layered Magnetoelectric Composite Materials and Devices Applications. *Journal of Physics D: Applied Physics*. 2018. https://doi.org/10.1088/1361-6463/aac29b.

(15) Wang, J.; Dong, C.; Wei, Y.; Lin, X.; Athey, B.; Chen, Y.; Winter, A.; Stephen, G. M.; Heiman, D.; He, Y.; Chen, H.; Liang, X.; Yu, C.; Zhang, Y.; Podlaha-Murphy, E. J.; Zhu,

M.; Wang, X.; Ni, J.; McConney, M.; Jones, J.; Page, M.; Mahalingam, K.; Sun, N. X. Magnetostriction, Soft Magnetism, and Microwave Properties in Co-Fe-C Alloy Films. *Phys. Rev. Appl.* **2019**. https://doi.org/10.1103/PhysRevApplied.12.034011.

(16) Lou, J.; Insignares, R. E.; Cai, Z.; Ziemer, K. S.; Liu, M.; Sun, N. X. Soft Magnetism, Magnetostriction, and Microwave Properties of FeGaB Thin Films. *Appl. Phys. Lett.* **2007**. https://doi.org/10.1063/1.2804123.

(17) Greve, H.; Woltermann, E.; Quenzer, H. J.; Wagner, B.; Quandt, E. Giant Magnetoelectric Coefficients in $(Fe_{90}Co_{10})_{78}Si_{12}B_{10}$-AlN Thin Film Composites. *Appl. Phys. Lett.* **2010**. https://doi.org/10.1063/1.3377908.

(18) Schmid, H. Multi-Ferroic Magnetoelectrics. *Ferroelectrics* **1994**. https://doi.org/10.1080/00150199408245120.

(19) Ramesh, R.; Spaldin, N. A. Multiferroics: Progress and Prospects in Thin Films. *Nature Materials*. 2007. https://doi.org/10.1038/nmat1805.

(20) Wang, K. F.; Liu, J. M.; Ren, Z. F. Multiferroicity: The Coupling between Magnetic and Polarization Orders. *Adv. Phys.* **2009**. https://doi.org/10.1080/00018730902920554.

(21) Dong, S.; Liu, J. M.; Cheong, S. W.; Ren, Z. Multiferroic Materials and Magnetoelectric Physics: Symmetry, Entanglement, Excitation, and Topology. *Adv. Phys.* **2015**. https://doi.org/10.1080/00018732.2015.1114338.

(22) Fiebig, M.; Lottermoser, T.; Meier, D.; Trassin, M. The Evolution of Multiferroics. *Nature Reviews Materials*. 2016. https://doi.org/10.1038/natrevmats.2016.46.

(23) Kimura, T.; Goto, T.; Shintani, H.; Ishizaka, K.; Arima, T.; Tokura, Y. Magnetic Control of Ferroelectric Polarization. *Nature* **2003**. https://doi.org/10.1038/nature02018.

(24) Khomskii, D. Classifying Multiferroics: Mechanisms and Effects. *Physics (College. Park. Md).* **2009**. https://doi.org/10.1103/physics.2.20.

(25) Hill, N. A. Why Are There so Few Magnetic Ferroelectrics? *J. Phys. Chem. B* **2000**. https://doi.org/10.1021/jp000114x.

(26) Ederer, C.; Spaldin, N. A. A New Route to Magnetic Ferroelectrics. *Nat. Mater.* **2004**. https://doi.org/10.1038/nmat1265.

(27) Spaldin, N. A.; Ramesh, R. Advances in Magnetoelectric Multiferroics. *Nature Materials*. 2019. https://doi.org/10.1038/s41563-018-0275-2.

(28) Goodenough, J. B.; Zhou, J. Varied Roles of Pb in Transition-Metal $PbMO_3$ Perovskites (M = Ti, V, Cr, Mn, Fe, Ni, Ru). *Science and Technology of Advanced Materials*. 2015. https://doi.org/10.1088/1468-6996/16/3/036003.

(29) Rushchanskii, K. Z.; Kamba, S.; Goian, V.; Vaněk, P.; Savinov, M.; Prokleška, J.; Nuzhnyy, D.; Knžek, K.; Laufek, F.; Eckel, S.; Lamoreaux, S. K.; Sushkov, A. O.; Ležaić, M.; Spaldin, N. A. A Multiferroic Material to Search for the Permanent Electric Dipole Moment of the Electron. *Nat. Mater.* **2010**. https://doi.org/10.1038/nmat2799.

(30) Ma, J.; Hu, J.; Li, Z.; Nan, C. W. Recent Progress in Multiferroic Magnetoelectric Composites: From Bulk to Thin Films. *Adv. Mater.* **2011**. https://doi.org/10.1002/adma.201003636.

(31) Wang, Y.; Hu, J.; Lin, Y.; Nan, C. W. Multiferroic Magnetoelectric Composite Nanostructures. *NPG Asia Materials*. 2010. https://doi.org/10.1038/asiamat.2010.32.

(32) Premkumar, S.; Varadharajan, E.; Rath, M.; Mathe, V. L.; Ramachandra Rao, M. S. Microstructural Analysis of Co-Sintered PSLZT-NZFO Layered Magnetoelectric Composite. *Ferroelectrics* **2017**. https://doi.org/10.1080/00150193.2017.1362283.

(33) Ryu, J.; Priya, S.; Uchino, K.; Kim, H. E. Magnetoelectric Effect in Composites of Magnetostrictive and Piezoelectric Materials. *Journal of Electroceramics*. 2002. https://doi.org/10.1023/A:1020599728432.

(34) Nan, C. W.; Bichurin, M. I.; Dong, S.; Viehland, D.; Srinivasan, G. Multiferroic Magnetoelectric Composites: Historical Perspective, Status, and Future Directions. *J. Appl. Phys.* **2008**. https://doi.org/10.1063/1.2836410.

(35) Astrov, D. N. Magnetoelectric Effect in Chromium Oxide. *J. Exp. Theor. Phys.* **1961**.

(36) Wang, J.; Neaton, J. B.; Zheng, H.; Nagarajan, V.; Ogale, S. B.; Liu, B.; Viehland, D.; Vaithyanathan, V.; Schlom, D. G.; Waghmare, U. V.; Spaldin, N. A.; Rabe, K. M.; Wuttig, M.; Ramesh, R. Epitaxial $BiFeO_3$ Multiferroic Thin Film Heterostructures. *Science (80-.).* **2003**. https://doi.org/10.1126/science.1080615.

(37) Van Suchtelen, J. *PRODUCT PROPERTIES: A NEW APPLICATION OF COMPOSITE MATERIALS*; 1972.

(38) Van Den Boomgaard, J.; Van Run, A. M. J. G.; Van Suchtelen, J. Magnetoelectricity in Piezoelectric—Magnetostrictive Composites. *Ferroelectrics* **1976**. https://doi.org/10.1080/00150197608241997.

(39) Van Den Boomgaard, J.; Terrell, D. R.; Born, R. A. J.; Giller, H. F. J. I. An in Situ Grown Eutectic Magnetoelectric Composite Material - Part I Composition and Unidirectional Solidification. *J. Mater. Sci.* **1974**. https://doi.org/10.1007/BF00540770.

(40) Suryanarayana, S. V. Magnetoelectric Interaction Phenomena in Materials. *Bull. Mater. Sci.* **1994**. https://doi.org/10.1007/BF02747225.

(41) Bichurin, M. I.; Kornev, I. A.; Petrov, V. M.; Lisnevskaya, I. V. Investigation of Magnetoelectric Interaction in Composite. *Ferroelectrics* **1997**. https://doi.org/10.1080/00150199708222209.

(42) Srinivasan, G.; Devreugd, C. P.; Flattery, C. S.; Laletsin, V. M.; Paddubnaya, N. Magnetoelectric Interactions in Hot-Pressed Nickel Zinc Ferrite and Lead Zirconante Titanate Composites. *Appl. Phys. Lett.* **2004**. https://doi.org/10.1063/1.1795365.

(43) Sheikh, A. D.; Mathe, V. L. Effect of the Piezomagnetic $NiFe_2O_4$ Phase on the Piezoelectric $Pb(Mg_{1/3}Nb_{2/3})_{0.67}Ti_{0.33}O_3$ Phase in Magnetoelectric Composites. *Smart Mater. Struct.* **2009**. https://doi.org/10.1088/0964-1726/18/6/065014.

(44) Ryu, J.; Carazo, A. V.; Uchino, K.; Kim, H. E. Piezoelectric and Magnetoelectric Properties of Lead Zirconate Titanate/Ni-Ferrite Particulate Composites. *J. Electroceramics* **2001**. https://doi.org/10.1023/A:1012210609895.

(45) High Magnetoelectric Properties in $0.68Pb(Mg_{1/3}Nb_{2/3})O_3$-$0.32PbTiO_3$ Single Crystal and Terfenol-D Laminate Composites . *J. Korean Ceram. Soc.* **2002**. https://doi.org/10.4191/kcers.2002.39.9.813.

(46) Bichurin, I.; Filippov, A.; Petrov, M.; Laletsin, M.; Paddubnaya, N.; Srinivasan, G. Resonance Magnetoelectric Effects in Layered Magnetostrictive-Piezoelectric Composites. *Phys. Rev. B - Condens. Matter Mater. Phys.* **2003**. https://doi.org/10.1103/PhysRevB.68.132408.

(47) Dong, S.; Li, J. F.; Viehland, D. A Longitudinal-Longitudinal Mode TERFENOL-D/$Pb(Mg_{1/3}Nb_{2/3})O_3$-$PbTiO_3$ Laminate Composite. *Appl. Phys. Lett.* **2004**. https://doi.org/10.1063/1.1829159.

(48) Dong, S.; Zhai, J.; Li, J.; Viehland, D. Near-Ideal Magnetoelectricity in High-Permeability Magnetostrictive/ Piezofiber Laminates with a (2-1) Connectivity. *Appl. Phys. Lett.* **2006**. https://doi.org/10.1063/1.2420772.

(49) Zhai, J.; Dong, S.; Xing, Z.; Li, J.; Viehland, D. Giant Magnetoelectric Effect in Metglas/Polyvinylidene-Fluoride Laminates. *Appl. Phys. Lett.* **2006**. https://doi.org/10.1063/1.2337996.

(50) Gao, J.; Shen, L.; Wang, Y.; Gray, D.; Li, J.; Viehland, D. Enhanced Sensitivity to Direct Current Magnetic Field Changes in Metglas/$Pb(Mg_{1/3}Nb_{2/3})O_3$-$PbTiO_3$ Laminates. In *Journal of Applied Physics*; 2011. https://doi.org/10.1063/1.3569629.

(51) Chashin, D. V.; Fetisov, Y. K.; Kamentsev, K. E.; Srinivasan, G. Resonance Magnetoelectric Interactions Due to Bending Modes in a Nickel-Lead Zirconate Titanate Bilayer. *Appl. Phys. Lett.* **2008**. https://doi.org/10.1063/1.2896607.

(52) Ryu, J.; Kang, J. E.; Zhou, Y.; Choi, S. Y.; Yoon, W. H.; Park, D. S.; Choi, J. J.; Hahn, B. D.; Ahn, C. W.; Kim, J. W.; Kim, Y. Do; Priya, S.; Lee, S. Y.; Jeong, S.; Jeong, D. Y. Ubiquitous Magneto-Mechano-Electric Generator. *Energy Environ. Sci.* **2015**. https://doi.org/10.1039/c5ee00414d.

(53) Annapureddy, V.; Na, S. M.; Hwang, G. T.; Kang, M. G.; Sriramdas, R.; Palneedi, H.; Yoon, W. H.; Hahn, B. D.; Kim, J. W.; Ahn, C. W.; Park, D. S.; Choi, J. J.; Jeong, D. Y.; Flatau, A. B.; Peddigari, M.; Priya, S.; Kim, K. H.; Ryu, J. Exceeding Milli-Watt Powering Magneto-Mechano-Electric Generator for Standalone-Powered Electronics. *Energy Environ. Sci.* **2018**. https://doi.org/10.1039/c7ee03429f.

(54) Park, C. S.; Ryu, J.; Choi, J. J.; Park, D. S.; Ahn, C. W.; Priya, S. Giant Magnetoelectric Coefficient in 3-2 Nanocomposite Thick Films. *Jpn. J. Appl. Phys.* **2009**. https://doi.org/10.1143/JJAP.48.080204.

(55) Xu, Y. D.; Wu, G.; Su, H. L.; Shi, M.; Yu, G. Y.; Wang, L. Magnetoelectric $CoFe_2O_4$/$Pb(Zr_{0.53}Ti_{0.47})O_3$ Composite Thin Films of 2-2 Type Structure Derived by a Sol-Gel Process. *Journal of Alloys and Compounds*. 2011.

https://doi.org/10.1016/j.jallcom.2010.12.112.

(56) Lage, E.; Lage, E.; Kirchhof, C.; Kirchhof, C.; Hrkac, V.; Hrkac, V.; Kienle, L.; Kienle, L.; Jahns, R.; Jahns, R.; Knöchel, R.; Knöchel, R.; Quandt, E.; Quandt, E.; Meyners, D.; Meyners, D. Exchange Biasing of Magnetoelectric Composites. *Nat. Mater.* **2012**.

(57) Gupta, R.; Tomar, M.; Kumar, A.; Gupta, V. Performance of Magnetoelectric PZT/Ni Multiferroic System for Energy Harvesting Application. *Smart Mater. Struct.* **2017**. https://doi.org/10.1088/1361-665X/26/3/035002.

(58) Van Suchtelen, J. Product Properties: A New Application of Composites Materials. *Philips Res. Reports, 27* **1972**.

(59) Palneedi, H.; Annapureddy, V.; Priya, S.; Ryu, J. Status and Perspectives of Multiferroic Magnetoelectric Composite Materials and Applications. *Actuators*. 2016. https://doi.org/10.3390/act5010009.

(60) Nan, C. W. Magnetoelectric Effect in Composites of Piezoelectric and Piezomagnetic Phases. *Phys. Rev. B* **1994**. https://doi.org/10.1103/PhysRevB.50.6082.

(61) Bichurin, I.; Petrov, M.; Srinivasan, G. Theory of Low-Frequency Magnetoelectric Coupling in Magnetostrictive-Piezoelectric Bilayers. *Phys. Rev. B - Condens. Matter Mater. Phys.* **2003**. https://doi.org/10.1103/PhysRevB.68.054402.

(62) Muchenik, T. I.; Barbero, E. J. Prediction of Extrinsic Charge, Voltage, and Work-Conversion Factors for Laminated Magnetoelectric Composites. *Smart Mater. Struct.* **2015**. https://doi.org/10.1088/0964-1726/25/1/015006.

(63) Hayes, P.; Jovičević Klug, M.; Toxværd, S.; Durdaut, P.; Schell, V.; Teplyuk, A.; Burdin, D.; Winkler, A.; Weser, R.; Fetisov, Y.; Höft, M.; Knöchel, R.; McCord, J.; Quandt, E. Converse Magnetoelectric Composite Resonator for Sensing Small Magnetic Fields. *Sci. Rep.* **2019**. https://doi.org/10.1038/s41598-019-52657-w.

(64) Hayes, P.; Schell, V.; Salzer, S.; Burdin, D.; Yarar, E.; Piorra, A.; Knöchel, R.; Fetisov, Y. K.; Quandt, E. Electrically Modulated Magnetoelectric AlN/FeCoSiB Film Composites for DC Magnetic Field Sensing. *J. Phys. D. Appl. Phys.* **2018**. https://doi.org/10.1088/1361-6463/aad456.

(65) Turutin, A. V.; Vidal, J. V.; Kubasov, I. V.; Kislyuk, A. M.; Malinkovich, M. D.; Parkhomenko, Y. N.; Kobeleva, S. P.; Kholkin, A. L.; Sobolev, N. A. Low-Frequency Magnetic Sensing by Magnetoelectric Metglas/Bidomain $LiNbO_3$ Long Bars. *J. Phys. D. Appl. Phys.* **2018**. https://doi.org/10.1088/1361-6463/aabda4.

(66) Chen, L.; Li, P.; Wen, Y.; Zhu, Y. Near-Flat Self-Biased Magnetoelectric Response in Three-Phase METGLAS/TERFENOL-D/ PZT Laminated Composites. In *2015 IEEE International Magnetics Conference, INTERMAG 2015*; 2015. https://doi.org/10.1109/INTMAG.2015.7157313.

(67) Marauska, S.; Jahns, R.; Greve, H.; Quandt, E.; Knöchel, R.; Wagner, B. MEMS Magnetic Field Sensor Based on Magnetoelectric Composites. *J. Micromechanics Microengineering* **2012**. https://doi.org/10.1088/0960-1317/22/6/065024.

(68) Viehland, D.; Wuttig, M.; McCord, J.; Quandt, E. Magnetoelectric Magnetic Field Sensors. *MRS Bull.* **2018**. https://doi.org/10.1557/mrs.2018.261.

(69) Quandt, E.; Stein, S.; Wuttig, M. Magnetic Vector Field Sensor Using Magnetoelectric Thin-Film Composites. In *IEEE Transactions on Magnetics*; 2005. https://doi.org/10.1109/TMAG.2005.854793.

(70) Li, P.; Wen, Y.; Bian, L.; Yang, J.; Yu, M. A Magnetoelectric Transducer Consisting of and Piezoelectric Composite Array. In *Proceedings - IEEE Ultrasonics Symposium*; 2008. https://doi.org/10.1109/ULTSYM.2008.0251.

(71) Chen, L.; Li, P.; Wen, Y.; Wang, D. Magnetoelectric Transducer Employing Piezoelectric Ceramic/Ferromagnetic Alloy/High-Permeability FeCuNbSiB Composite. In *IEEE Transactions on Magnetics*; 2011. https://doi.org/10.1109/TMAG.2011.2149508.

(72) Yang, G.; Sun, N. X. Magnetoelectric Composites for Miniature Antennas. In *Composite Magnetoelectrics: Materials, Structures, and Applications*; 2015. https://doi.org/10.1016/B978-1-78242-254-9.00010-X.

(73) Annapureddy, V.; Palneedi, H.; Hwang, G. T.; Peddigari, M.; Jeong, D. Y.; Yoon, W. H.; Kim, K. H.; Ryu, J. Magnetic Energy Harvesting with Magnetoelectrics: An Emerging Technology for Self-Powered Autonomous Systems. *Sustain. Energy Fuels* **2017**. https://doi.org/10.1039/c7se00403f.

2

Motivation and scope of the thesis

In terms of the deployment of 5G since 2020 with the IoT (Internet of Things) and increasing WSN (wireless sensors networks) opportunities, and 6G for 2030, the energy demand of these new digital communication protocols is revealed to be one of the big challenges to face. Self-powered microsystems emerge as a relevant opportunity for developing innovative energy harvesting devices to continuously supply low-power autonomous devices without maintenance needs and equipped with sensors and wireless communication abilities. Autonomous devices, such as self-powered WSNs, are in high demand for IoT applications, for example, in smart buildings, smart cities, and smart vehicles, where thousands of electronic devices can communicate with each other.

Energy harvesters are being developed in order to power autonomous devices and for other low-power consumption electronics, and to overcome the limitations of conventional electric suppliers, e.g. electric cables, batteries. Compared to sunlight, heat, mechanical vibrations, wind, and other sources of renewable energies, electromagnetic waves have been identified as a potential suitable candidate due to their ubiquity, since we are surrounded with the electric power transmission infrastructure of buildings, transmission power lines, industrial machinery, and electronic devices, which are strays of electromagnetic fields. These 50/60 Hz background electromagnetic fields are weak and generally considered as noise. For instance, the electric transmission cables produce a low magnetic field in the order of the milliTesla at a distance of 10 mm in a 50 A current flow at a fixed frequency of 50/60 Hz [1–4]. In general, harvesters using the principle of Faraday's induction law can converse electromagnetic energy to electric energy. However, the integration and fabrication of coils (requiring 3D designs) at the scale of microsystems are more complicated in comparison to the fabrication of thin film transducers (which only need planar 2D designs). Therefore, an alternative harvesting principle capable of producing high power density and miniaturizing device dimensions is widely requested. Energy harvesters using magnetoelectric (ME) effect have emerged as potential candidates for harvesting weak magnetic fields at a low frequency of 50/60 Hz [1,5,6]. This is due to the intrinsic coupling inside ME materials.

As pointed out in Chapter 1, there are three common ways of designing ME composites; 0-3 composites made of magnetic nanoparticles embedded in a matrix of the piezoelectric phase, 1-3 composites composed of magnetic nanopillars inside piezoelectric materials, and 2-2 composites consisting of magnetic and piezoelectric layers. However, these 0-3 and 1-3 composites present severe issues[7]: (i) the misfit strain at the interface induced by the thermal expansion mismatch between the two phases reducing the densification; (ii) the interdiffusion and/or chemical reactions between the two constituents due to high temperature processes, which degrade the piezoelectric

and magnetostrictive properties of the two phases; and (iii) a high leakage current arising in the composites due to the randomly distributed magnetic phase. Compared to the 0-3 and 1-3 composites, the 2-2 composite does not present the above-mentioned issues due to its connectivity architect, thus ensuring a high ME response. A giant ME coefficient of 120 $V.cm^{-1}.Oe^{-1}$ was reported in a laminate composite composed of PMN-PZT single crystal fiber composites bonded by epoxy glue with an Ni plate [6]. The output power density of this generator can supply 35 LEDs. More recently, Gupta *et al.* [8] reported a giant ME coefficient of 130.5 $V.cm^{-1}.Oe^{-1}$ in PZT/Ni thin-film composite grown by PLD at 800 °C.

However, there are two rocky issues in 2-2 composites that reduce the performance of the ME harvester and hinder the miniaturization of device applications. Firstly, although bulk laminate composites provide a strong coupling between the two layers and generate high power density, their device dimensions impede the miniaturization because of the dimension of their constituents. Secondly, the anisotropic, high temperature coating and high voltage poling of piezoelectric phases could deteriorate the interface between the piezoelectric and magnetostrictive layers, which is vulnerable with high temperature treatment and low conformal coating techniques. Moreover, the high temperature process can induce a thermal expansion mismatch, delamination and atomic interdiffusion degrading the performance of the magnetostrictive layer.

To overcome the above-mentioned issues, we propose alternative approaches using zinc oxide (ZnO) and aluminum nitride (AlN) thin films grown by (plasma-enhanced, PE-) atomic layer deposition (ALD) at low temperatures (below or equal to 250 °C). ALD is well-known for conformal coating due to its self-limited surface reactions. Therefore, the conformal coating at low temperatures by ALD will diminish the effect of delamination due to the difference in thermal expansion between the two layers, thus ensuring good interface quality. As a result, a high ME response can be achieved. Nonetheless, the growth of ZnO and AlN thin films with a piezoelectric response faces three main challenges:

(i) Low temperature growth of ZnO and AlN thin films with highly (002) preferred orientation and high resistivity. At temperatures below 250 °C, it is extremely challenging to grow highly (002)-oriented films. Especially for AlN thin films, the use of chemical vapor deposition techniques always requires a very high temperature deposition (1000 °C) [9,10].

(ii) Demonstration of piezoelectric properties of ZnO and AlN thin films grown by ALD and PE-ALD. Particularly for AlN thin films grown by PE-ALD, ours is the first work to report piezoelectric characterization.

(iii) Characterization of ME response of composites combining ZnO or AlN thin films and magnetostrictive foils, such as nickel, iron, and cobalt. These foils are used due to their moderate piezomagnetic coefficient and high conductivity, simplifying electrode configurations.

These three challenges are addressed in the frame of this thesis. The general structure of the thesis is given below. Each chapter provides readers with a brief overview, particularly discussing the remaining issue/challenge and its solution approach.

The structure of the thesis is as follows:

Chapter 3 discusses the methodology by which the ZnO and AlN thin films, as well as the ferromagnetic shape memory alloy Ni-Mn-Ga film, are fabricated as an alternative to the foils with giant magnetic-induced strain (in the order of 0.1% to 1%) compared to magnetrostrictive thin films (strain coefficient in the order of tens of ppm). On one hand, thermal and plasma-enhanced atomic layer deposition configurations are both introduced for the deposition of the dielectric films. On the other hand, magnetron sputtering, and deposition synthesis parameters of Ni-Mn-Ga film are also presented. Some characterization techniques used to study the film properties are introduced.

Chapter 4 presents the development of the ZnO growth sequence by thermal ALD. Deionized water and diethylzinc (DEZ) are considered the standard precursors for ALD. The use of gaseous oxygen during ALD growth is unusual and profoundly impacts the structural, optical, electrical, and electronic properties of ZnO thin films. By replacing conventional water with oxygen-isotope-labelled water and combining it with several complex characterization techniques, new reaction mechanisms are introduced to explain the influence of the additional oxygen on the properties of ZnO thin films. The objective of this work is to increase the electrical resistivity of piezoelectric ZnO, avoiding current leakage for obtaining higher piezoelectric response. Two publications were published based on these works.

Chapter 5 discusses the growth of AlN thin films by plasma-enhanced atomic layer deposition (PE-ALD). Due to the high leakage current of ZnO thin film, its piezoelectricity is not achievable. In contrast, AlN is an insulating material, thus high resistivity is expected. The main challenge addressed in this work is the growth of textured AlN thin films at low temperatures with a privileged (002) crystalline orientation for piezoelectric response. To date, no work has demonstrated the piezoelectric properties of AlN thin films grown by PE-ALD. In this chapter, we will show how a piezoelectric AlN thin film grown at low temperatures is achieved. This work has been featured in one publication.

Chapter 6 discusses our final goal, that is, the fabrication and characterization of magnetoelectric (ME) composites. These composites are made by growing a 500nm-thick AlN film on magnetostrictive foils of nickel, iron, and cobalt. Meticulous characterizations are carried out on these composites to unravel the interplay between the interface and composite properties. Two conference papers have been published and one paper has been submitted based on this work.

Chapter 7 discusses perspectives of the thesis that present possible ways in which the magnetoelectric effect in the thin film composites can be enhanced. Preliminary results of Ni-Mn-Ga Heusler alloy films, which replace the magnetostrictive layer with the expected giant magnetoelastic response, have been reported. The uses of ScAlN alloy and resonance structures are mentioned as potential approaches to improve magnetoelectric transducing efficiency.

Chapter 8 concludes by summarizing the results achieved at different stages to realize a magnetoelectric composite. In addition, this chapter also discusses outlooks of the thesis, presenting a general strategy by which to improve the performance of magnetoelectric composites.

References

(1) Annapureddy, V.; Palneedi, H.; Hwang, G. T.; Peddigari, M.; Jeong, D. Y.; Yoon, W. H.; Kim, K. H.; Ryu, J. Magnetic Energy Harvesting with Magnetoelectrics: An Emerging Technology for Self-Powered Autonomous Systems. *Sustain. Energy Fuels* **2017**. https://doi.org/10.1039/c7se00403f.

(2) Tashiro, K.; Wakiwaka, H.; Inoue, S. I.; Uchiyama, Y. Energy Harvesting of Magnetic Power-Line Noise. In *IEEE Transactions on Magnetics*; 2011. https://doi.org/10.1109/TMAG.2011.2158190.

(3) Halgamuge, M. N.; Abeyrathne, C. D.; Mendis, P. Measurement and Analysis of Electromagnetic Fields from Trams, Trains and Hybrid Cars. *Radiat. Prot. Dosimetry* **2010**. https://doi.org/10.1093/rpd/ncq168.

(4) Ptitsyna, N.; Ponzetto, A. Magnetic Fields Encountered in Electric Transport: Rail Systems, Trolleybus and Cars. In *IEEE International Symposium on Electromagnetic Compatibility*; 2012. https://doi.org/10.1109/EMCEurope.2012.6396901.

(5) Annapureddy, V.; Na, S. M.; Hwang, G. T.; Kang, M. G.; Sriramdas, R.; Palneedi, H.; Yoon, W. H.; Hahn, B. D.; Kim, J. W.; Ahn, C. W.; Park, D. S.; Choi, J. J.; Jeong, D. Y.; Flatau, A. B.; Peddigari, M.; Priya, S.; Kim, K. H.; Ryu, J. Exceeding Milli-Watt Powering Magneto-Mechano-Electric Generator for Standalone-Powered Electronics. *Energy Environ. Sci.* **2018**. https://doi.org/10.1039/c7ee03429f.

(6) Ryu, J.; Kang, J. E.; Zhou, Y.; Choi, S. Y.; Yoon, W. H.; Park, D. S.; Choi, J. J.; Hahn, B. D.; Ahn, C. W.; Kim, J. W.; Kim, Y. Do; Priya, S.; Lee, S. Y.; Jeong, S.; Jeong, D. Y. Ubiquitous Magneto-Mechano-Electric Generator. *Energy Environ. Sci.* **2015**. https://doi.org/10.1039/c5ee00414d.

(7) Palneedi, H.; Annapureddy, V.; Priya, S.; Ryu, J. Status and Perspectives of Multiferroic Magnetoelectric Composite Materials and Applications. *Actuators*. 2016. https://doi.org/10.3390/act5010009.

(8) Gupta, R.; Tomar, M.; Kumar, A.; Gupta, V. Performance of Magnetoelectric PZT/Ni Multiferroic System for Energy Harvesting Application. *Smart Mater. Struct.* **2017**. https://doi.org/10.1088/1361-665X/26/3/035002.

(9) Huang, C. P.; Wang, C. H.; Liu, C. P.; Lai, K. Y. High-Quality AlN Grown with a Single Substrate Temperature below 1200 °C. *Sci. Rep.* **2017**. https://doi.org/10.1038/s41598-017-07616-8.

(10) Shih, H. Y.; Lee, W. H.; Kao, W. C.; Chuang, Y. C.; Lin, R. M.; Lin, H. C.; Shiojiri, M.; Chen, M. J. Low-Temperature Atomic Layer Epitaxy of AlN Ultrathin Films by Layer-by-Layer, in-Situ Atomic Layer Annealing. *Sci. Rep.* **2017**. https://doi.org/10.1038/srep39717.

3

Thin-film depositions and characterizations

This chapter reviews key deposition methods used to grow thin films, such as atomic layer deposition (both thermal and plasma configurations) for ZnO and AlN growths, and magnetron sputtering for the growth of Ni-Mn-Ga, Ni, Fe, Co, and Al films. Several main characterization techniques are also introduced, for instance x-ray diffraction, scanning electron microscopy, transmission electron microscopy, x-ray photoelectron spectrometry, secondary-ion mass spectrometry, a four-point bending measurement for piezoelectric characterization, a vibrating-sample measurement, and a magnetoelectric bench.

3.1
Thin-film deposition

This section introduces two main deposition methods used in the thesis: atomic layer deposition in both thermal and plasma configurations for growing ZnO and AlN thin films, and the sputtering method for depositing Heusler alloy films, and Ni and Al thin films as electrode layers. The theoretical background of the deposition techniques and experimental conditions for the growth of thin films will be discussed.

3.1.1. Atomic layer deposition

Atomic layer deposition (ALD) has emerged as one of the most important techniques for the deposition of thin films implemented in a broad range of applications, especially in the semiconductor industry [1–3]. Miniaturization in semiconductor devices has led to requirements for the control of thin film deposition at the atomic scale. ALD has the advantage of a conformal coating profile providing continuous and pinhole-free films that outweigh other thin-film deposition techniques, making it the most suitable method for the abovementioned requirements. The atomic layer control capability of ALD is due to the fact that ALD growth is based on sequential and self-limiting surface reactions [1–3]. Most ALD processes are based on binary reaction sequences where the substrate is exposed sequentially to reactants to produce a binary thin film. The precursors will adsorb and react to a finite number of surface sites until no surface sites are left, and will then subsequently desorb as the reaction reaches completion. Due to this self-limiting nature of ALD, excellent step coverage and conformal coating profile are achievable.

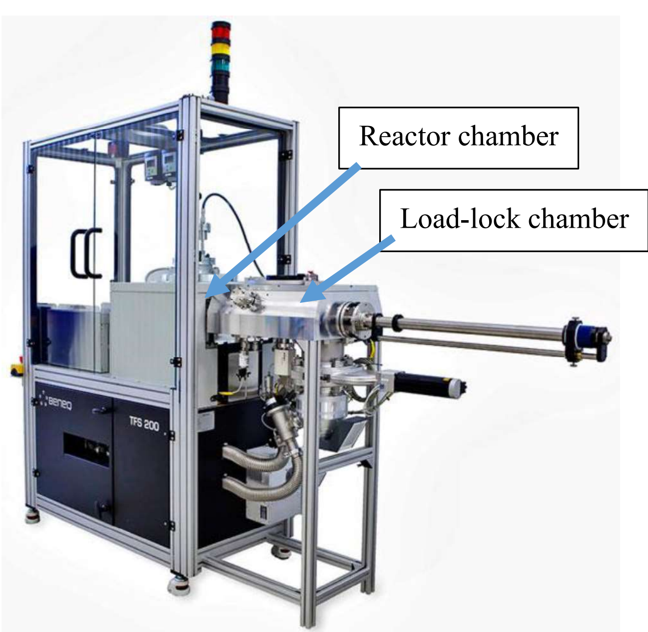

Figure 3.1: *ALD reactor Beneq TFS 200.*

This factor is extremely important for designing magnetoelectric (ME) thin-film composites where the interface between magnetostrictive (MS) and piezoelectric (PE) layers, which is vulnerable due to anisotropic coating techniques, plays a pivotal role in achieving high magnetoelectric-response composites and an efficient mechanical strain transfer between the layers. Our studies rely on the advantage of ALD to design ME composites by depositing ZnO and AlN thin films directly on magnetostrictive foils such as Ni, Fe, and Co and also on a thin film coated in silicon wafer with the three same materials. Here, ZnO thin films are grown using thermal ALD, and AlN thin films are fabricated by plasma-enhanced ALD (PE-ALD). The details will be discussed in the coming sections and in Chapters 4 and 5.

3.1.1.1. Zinc oxide thin-film deposition

Zinc oxide (ZnO) thin films are synthesized by thermal atomic layer deposition. Diethylzinc (DEZ) and deionized (DI) water are the two precursors. The sequence of growing ZnO is followed by a repeating sequence: DEZ pulse → Ar purging → DI water pulse → Ar purging, as shown in Figure 3.2(a). This is widely used as a standard sequence of ZnO thin-film growth [4]. We notice that the argon flow is always continuous along the ALD process, but it is convenient that the purging is mentioned explicitly in relation to the pulsing steps of the precursors during the loops.

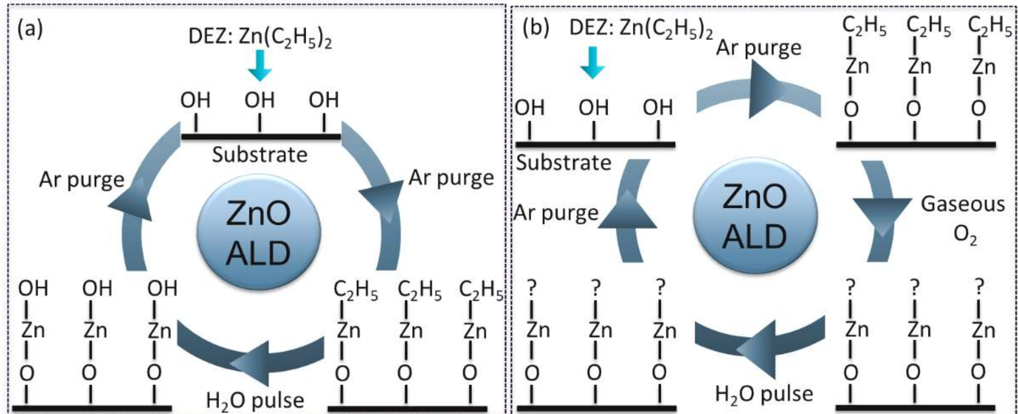

***Figure 3.2**: The schematic growth of ZnO thin films by (a) a standard sequence and (b) in the additional presence of gaseous oxygen. The "?" denotes unknown ligands that will be further discussed in chapter 4.*

The deposition of ZnO using diethylzinc (DEZ) and water precursors follows the net reaction:

$$Zn(C_2H_5)_2 + H_2O \rightarrow ZnO + 2\ C_2H_6 \quad (1)$$

The following elementary reaction sequences are expected [5,6]:

$$\text{DEZ pulse: } Zn(C_2H_5)_2 + |\text{-}OH \rightarrow |\text{-}O\text{-}Zn\text{-}C_2H_5 + C_2H_6 \quad (2a)$$

Where the symbol "ǀ-" denotes the surface.

$$\text{Water pulse: } H_2O + \text{ǀ-O-Zn-}C_2H_5 \rightarrow \text{ǀ-O-Zn-OH} + C_2H_6 \quad (3)$$

The monoethyl zinc (MEZ) may also react further with the hydroxyl groups on the surface to produce a bare zinc:

$$\text{ǀ-O-Zn-}C_2H_5 + \text{ǀ-OH} \rightarrow (\text{ǀ-O})_2\text{-Zn} + C_2H_6 \quad (2b)$$

The dominant end-product after the DEZ pulse is generally MEZ, therefore the reaction (2b) is usually omitted.

An example of the temperature dependence of the growth rate of ZnO thin film is given in Figure 3.3 [7]. The ALD growth window of ZnO is usually from 100 to 180°C. In this temperature range, the crystallinity of ZnO thin film, however, shows different crystallographic structures, as presented in Figure 3.4 [7]**.** At a low-temperature range of 130-150 °C, a mixture of (100) and (002) orientations was observed. The (100) orientation was predominant at 155-220 °C and the (002)-oriented film was dominated with the deposition temperature above 220 °C.

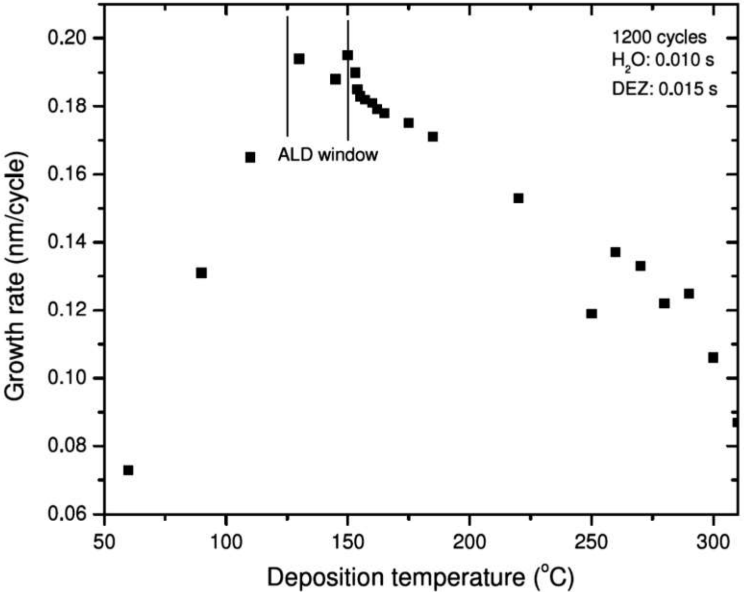

Figure 3.3: *The ALD growth window of ZnO thin films using the standard growth sequence* [7].

For piezoelectric-based applications, the (002)-oriented ZnO film is a prerequisite to ensure the maximum piezoelectric effect because of the symmetry reason, as explained in Chapter 1. The leakage current, due to the semiconducting nature of ZnO, is also an important issue to consider and to reduce in order to obtain an efficient piezoelectric response. Hence, we introduced another sequence to grow ZnO thin film by adding gaseous oxygen pulsing during ALD growth.

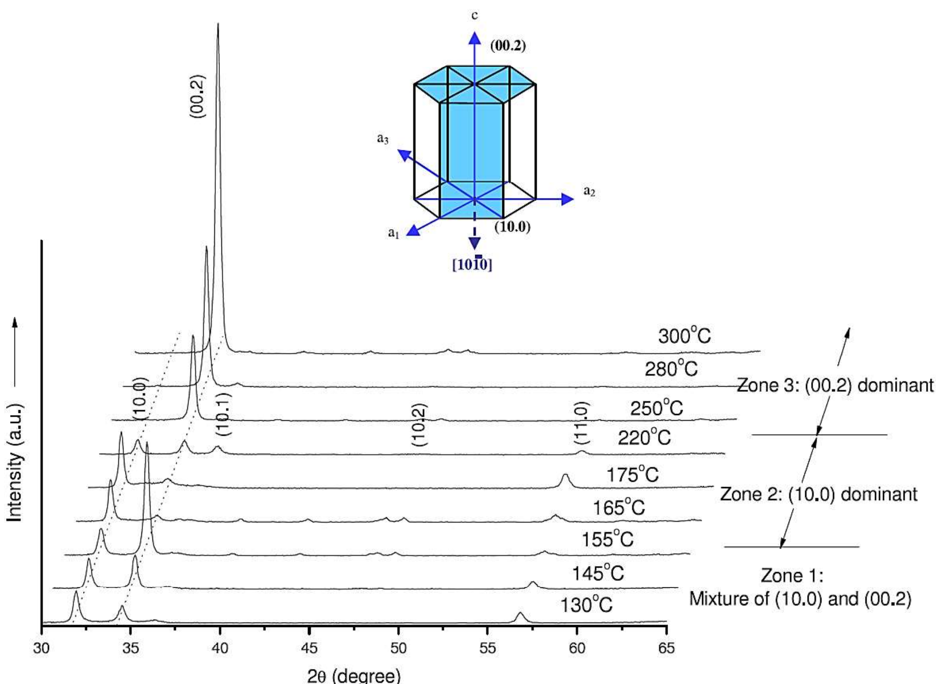

Figure 3.4: *The x-ray diffraction (XRD) patterns of ZnO thin films grown by the standard sequence at different growth temperatures* [7].

The growth sequence can refer to Figure 3.2(b). The pulse time of oxygen is varied to be 1, 3, and 5 s. In addition, the growth temperature is also investigated by altering it from 100 to 200 °C. Details of experimental conditions and the effect of gaseous oxygen on ZnO thin-film growth and its physical and electrical properties will be described in Chapter 4. The question marks "?" in the schematic figure 3.2(b) will also be replaced by answers.

3.1.1.2. Aluminum nitride thin-film growth

Aluminum nitride (AlN) thin films are grown using plasma-enhanced atomic layer deposition (PE-ALD). Trimethylaluminum (TMA) and a mix of $N_2/H_2/Ar$ gases in the plasma head of the reactor are used as precursors. The schematic growth is shown in Figure 3.5. First TMA is introduced into the ALD reactor, following by a purging step (τ_{purge}) with nitrogen. It is noted that the nitrogen flow into the chamber is always continuous along the ALD process, but it is convenient that the purging is mentioned explicitly in relation to the pulsing steps of the precursors in the reactor and in the plasma head during the loops.

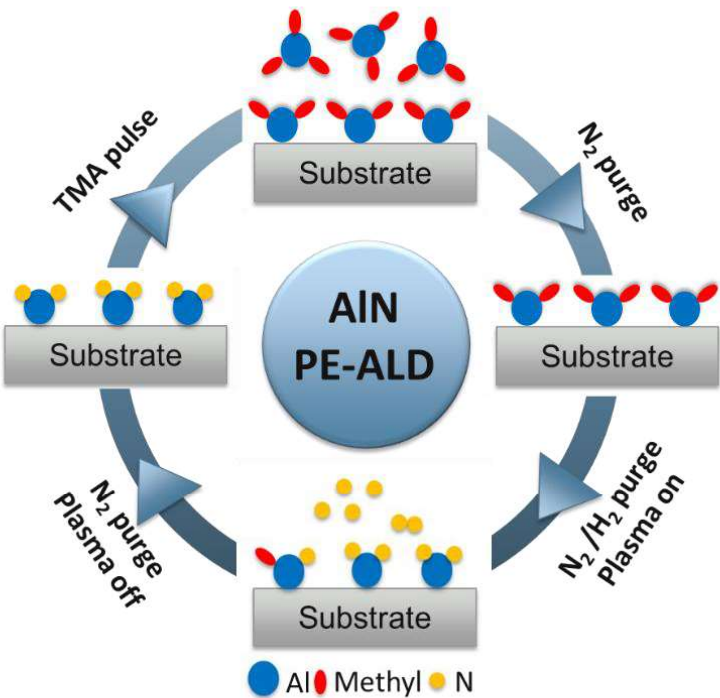

Figure 3.5: *The schematic growth of AlN thin films using PE-ALD.*

The gases are inserted accompanied by a plasma pulse (τ_{PE}), and are purged for 10 s. We found two important parameters which strongly affect the crystallinity of AlN thin films: the deposition temperatures, and the purging time after the TMA precursor pulse. Furthermore, the effect of plasma pulsing, as well as the effect of post-annealing processes were also studied. We will describe this study in Chapter 5.

3.1.2. Magnetron sputtering

Sputtering is a physical vapor deposition (PVD) technique using bombardments of ions accelerated under a high voltage and the target surface to eject atoms. The ejected (sputtered) atoms travel and are deposited on the small distance (few centimeters) substrate surface by an electric bias, gradually forming a film on the substrate. While DC sputtering is usually used for depositing metal films, radiofrequency (RF) sputtering is used for insulating and semiconducting materials. Magnetron sputtering increase the plasma density by introducing a magnetic field on the target surface, thus increasing the deposition rate. In this study, we use the magnetron sputtering techniques to grow Ni-Mn-Ga films, as well as pure Ni, Co, and Fe coatings on silicon wafers. Figure 3.6 shows magnetron sputtering on a semi-industrial scale at LIST.

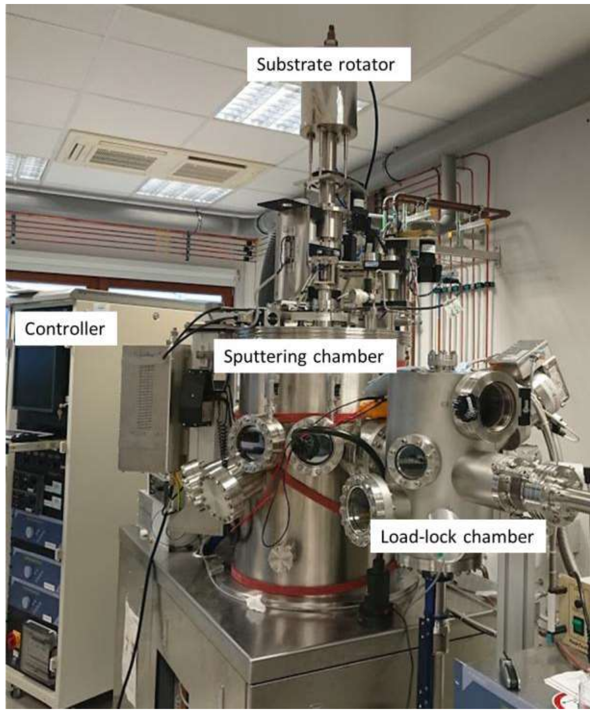

Figure 3.6: *Semi-industrial scale magnetron sputtering chamber at LIST, Belvaux.*

A DC magnetron sputtering is used to fabricate Ni-Mn-Ga films from a starting ternary target of $Ni_{45}Mn_{27.5}Ga_{27.5}$ (ACI Alloys, Inc.). The sputtering parameters are given in Table 1.

Table 1: *The sputtering parameters of Ni-Mn-Ga films.*

Deposition parameters	
Substrate	Si (100)
Target	$Ni_{45}Mn_{27.5}Ga_{27.5}$
Substrate temperature	50 °C
Sputtering power (W)	100 W
Base pressure	~10^{-6} mbar
Gas	The high purity argon gas (>99.9995 %Ar)
Sputtering pressure	1×10^{-2} mbar
Target-substrate distance (cm)	6.5
Substrate rotation	10 rpm

In order to tailor the composition of Ni-Mn-Ga film to the desired composition of $Ni_{50}Mn_{28}Ga_{22}$ to achieve a ferromagnetic shape memory alloy effect at room temperature, co-sputtering is done using an additional Mn target. The Mn target is sputtered by using an RF magnetron source with power varied to be 10-30 W.

The as-deposited films will be crystallized at high temperatures from 400-700 °C in a high vacuum furnace (10^{-6} mbar), minimizing oxidation effects. Figure 3.7 presents the post-annealing processes of Ni-Mn-Ga films. Two annealing strategies will be investigated: the one-step process, where the temperature increases gradually to the desired temperatures, maintained for 2h and finally cooled down to room temperature; and the two-step process, where the temperature is increased to 400 °C and maintained for 1h, then further increased to 700 °C and annealed for 1h. Finally, the furnace is naturally cooled down to room temperature.

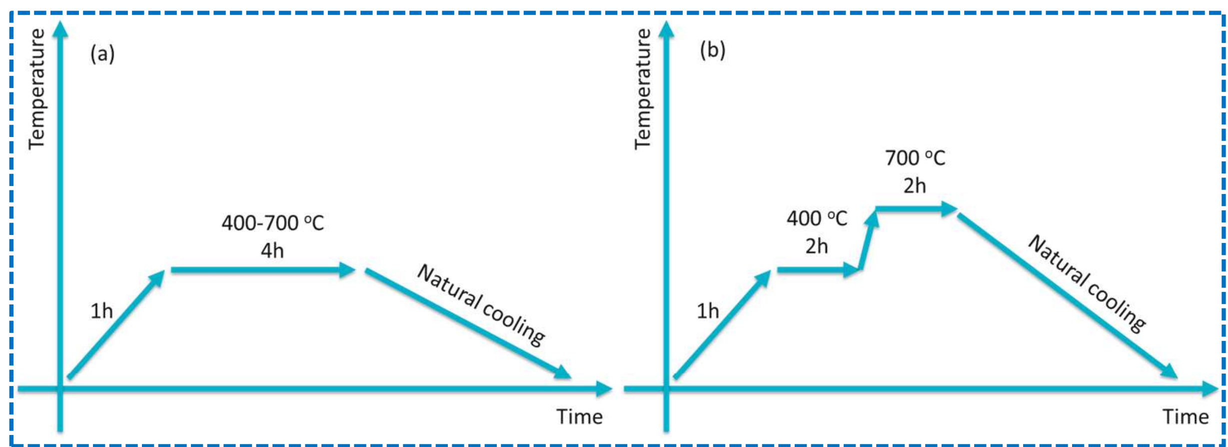

Figure 3.7: *The post-annealing processes for Ni-Mn-Ga films; (a) one-step annealing at varying temperatures of 400-700 °C for 4h, and (b) two-step annealing at 400 °C for 2h then 700 °C for 2h in vacuum conditions.*

3.2 Thin film characterizations

In this section, a brief introduction to several characterization techniques used in the thesis work is given. X-ray diffraction is used to study the crystal structure of ZnO, AlN films and their composites. Atomic force microscopy (AFM) and scanning electron microscopy (SEM) are performed to investigate the film morphology and microstructure in cross-sectional configuration. Transmission electron microscopy (TEM) is conducted to study the crystal structure of ZnO films and AlN layers in detail, as well as the interface between AlN films and the ferromagnetic Ni, Fe, and Co foils. X-ray photoelectron spectrometry (XPS) is carried out to study the binding energy, elemental composition and stoichiometry of ZnO and AlN films. Secondary-ion mass spectrometry (SIMS) is used to study chemical composition and to trace the oxygen isotope. Piezoresponse atomic microscopy (PFM) and four-point bending (4-PB) measurements are performed to evaluate the piezoelectric coefficient of ZnO and AlN thin films. Magnetization by VSM (Vibrating Sample Magnetometer) is used to study the ferromagnetic response of Ni-Mn-Ga, Ni, Co, and Fe substrates. Magnetoelectric characterization is carried out to study the magnetoelectric response of AlN films coated on magnetostrictive foils.

3.2.1. X-ray diffraction

The film crystal structure was examined by X-ray diffraction (Diffractometer Bruker D8 Discover with Cu Kα radiation and a 5-axis Eulerian cradle) in θ/2θ (Bragg-Brentano) configuration. In order to prevent the signal from fluorescence due to the underlying Ni layer, a solid-state point detector (tradename SoIX) was used for all measurements.

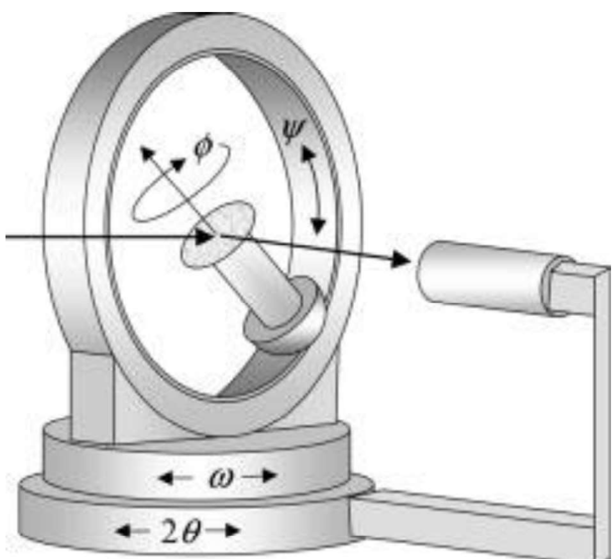

Figure 3.8: *Four-circle Euler cradle with variable azimuth ϕ (phi) and tilt angle ψ (psi)*[8].

By a conventional θ/2θ measurement, the plane orientations contributing to a Bragg reflection are all parallel or nearly parallel to the film surface. The structural information obtained with this

configuration is not enough to deduce the texture or the orientation distribution of the grains. In the pole figure measurement, information is collected on two additional degrees of freedom, which are the sample tilting angle, and the rotation angle or the rotation of the sample around the normal substrate (Figure 3.8). The tilting angle is usually denoted by χ (chi) instead of ψ, here $\chi = 90° - \psi$. A pole figure of a Bragg diffraction (hkl) is constructed by measuring the integral intensity of the Bragg peak for all (ϕ, χ) values. In our studies, pole figure measurements were conducted in $\theta/2\theta$ mode with an increment of 5° in ϕ (phi) and 3° in χ. The measurement was performed at up to 72° in χ using a collimated irradiation of 1 mm beam diameter. For both ZnO and AlN films, pole figures were performed on the (100), (002) and (101) peak positions. For each peak position, the background was measured to the right and the left of the peak position for one angle of phi only. The defocusing correction was carried out based on the number of counts measured on the (104) and (113) peak positions of the NIST standard SRM1976. The pole figure data treatment was performed using the MTEX toolbox (version 5.1.1) [9] in conjunction with Matlab®.

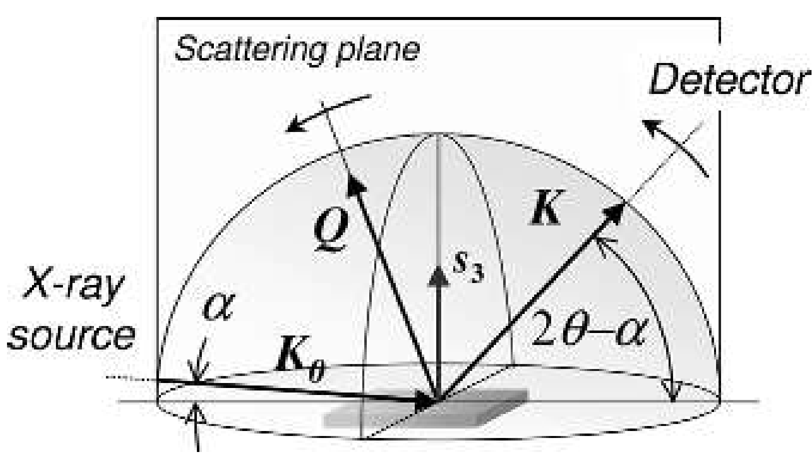

Figure 3.9: *Four-circle Euler cradle with variable azimuth ϕ (phi) and tilt angle ψ (psi)*[8].

In addition, grazing incidence XRD (GI-XRD) was also performed. In GI-XRD configuration, the X-ray beam enters the sample at a very small angle of incidence, as presented in Figure 3.9. An advantage of GI-XRD is that the signal is significantly enhanced for a thin-film sample due to the use of small incidence angles limiting the wave penetration and thus increasing top surface sensitivity.

3.2.2. Atomic force microscopy

Topography acquisitions were carried out with a commercial atomic force microscopy (AFM Innova, Bruker Inc., Santa Barbara) in tapping mode by maintaining the amplitude of the cantilever first resonance constant. Images were taken over 2µm × 2µm at a scan rate of 1 Hz. The tips used were HQ:NSC (MikroMasch, Bulgaria), Diamond Like carbon-coated, with a cantilever stiffness of 40 N/m and a tip apex diameter of below 20 nm. The surface roughness was extracted via the NanoScope software. Prior to calculation, the plane subtraction was applied. The grain size analysis was carried out with SPIP software in watershed mode detection for stacked features. An example of AFM analysis on AlN thin film is shown in Figure 3.10.

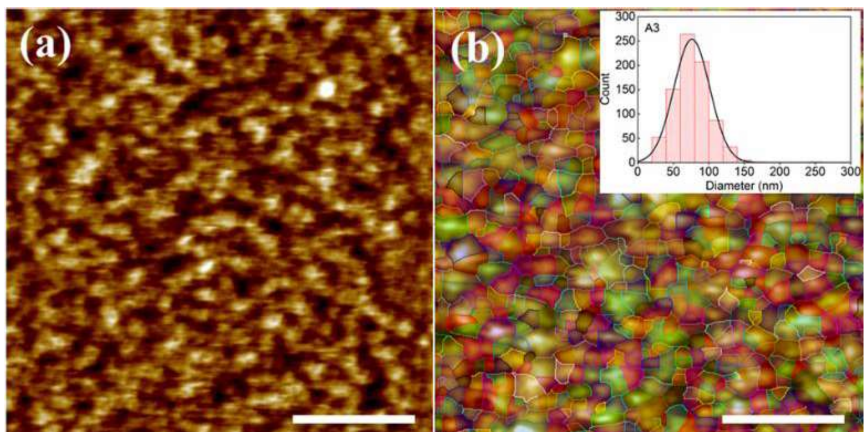

Figure 3.10: *AFM image of AlN thin film; (a) topography, (b) the watershed mode, and the insert is the diameter-grain distribution.*

3.2.3. Piezoresponse force microscopy

The Piezoresponse force microscope (PFM) is an important technique for a local study of ferroelectric and piezoelectric response in materials. The principle of the PFM technique, as presented in Figure 3.11, relies on the detection of local vibrations of a sample induced when an AC electric field is applied between the PFM conductive tip and the bottom electrode of the sample. The local displacements of the sample surface are transmitted to the tip and detected by a lock-in amplifier [10]. The out-of-plane piezoresponse signal is extracted from the z-deflection signal obtained by the PSD (position sensitive detector) and represents the local displacements, which are perpendicular to the plane of the film surface.

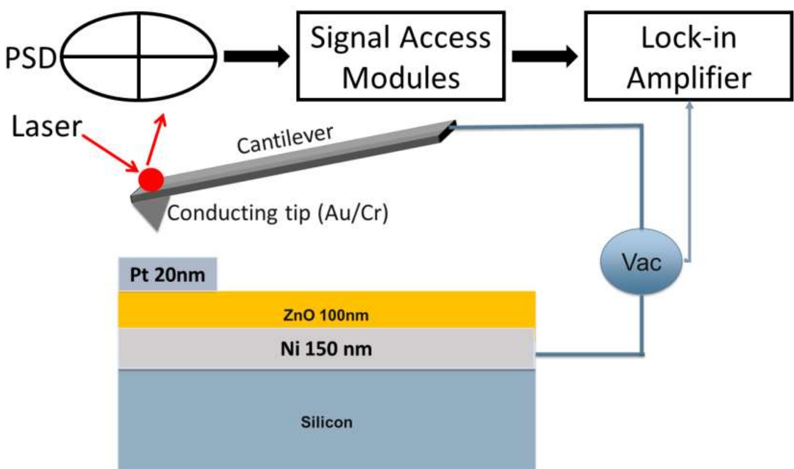

Figure 3.11: *The schematic configuration of the PFM measurement used to characterize ZnO thin films deposited on a nickel layer.*

The effective piezoelectric coefficient $d_{33,f}$ is defined as the slope of the displacement amplitude A_f (nm) versus the input signal U_f (V)

$$A_f = d_{33,f} \, U_f$$

Our measurements were performed on an MFP-3D (Alysum Research); a 20nm-thick Pt layer was coated on ZnO thin films to produce a uniform electric field, to avoid electrostatic effects and tip force artifacts [10].

3.2.4. Scanning electron microscopy

Scanning electron microscopy (Helios 650 FIB-SEM, FEI company, USA) was used to analyze the microstructure of the films. Both top-view and cross-sectional configurations were performed to investigate surface morphology and confirm the thickness of the films, respectively. Figure 3.12 shows an example of SEM images performed on ZnO thin film.

Another capability of the SEM is energy dispersive x-ray spectroscopy (EDX). EDX is an analytical technique for the analysis and characterization of the chemical elements of a sample. This technique was used intensively for identifying the elemental composition of Ni-Mn-Ga thin films in Chapter 7. An example of EDX analysis on Ni-Mn-Ga thin films is shown in Figure 3.13.

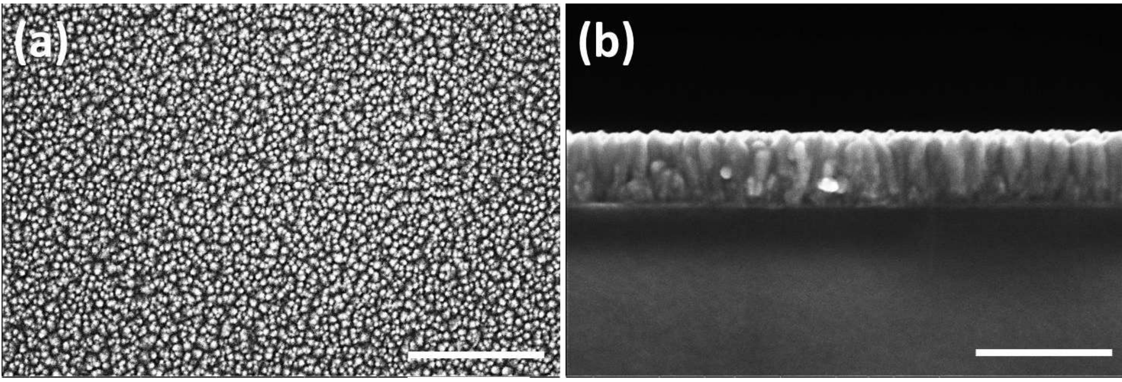

Figure 3.12: *SEM micrographs of ZnO thin film grown at 180°C in presence of oxygen (a) top-view and (b) cross-sectional configurations. The scale bar is 300 nm.*

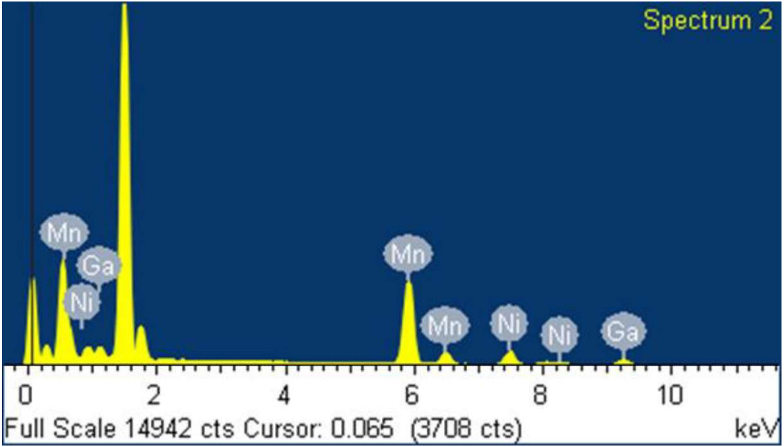

Figure 3.13: *EDX analysis of Ni-Mn-Ga thin film on Si.*

3.2.5. Transmission electron microscopy

Transmission electron microscopy (TEM) investigations were carried out using a JEM - ARM 200F Cold FEG TEM/STEM operating at 200 kV and equipped with a spherical aberration (Cs) probe and image correctors (point resolution 0.12 nm in TEM mode and 0.078 nm in STEM mode).

The TEM preparations and characterizations were done in a CC3M lab in Nancy, France. Figure 3.14 shows an example of TEM observation of an AlN film coated on Ni foil.

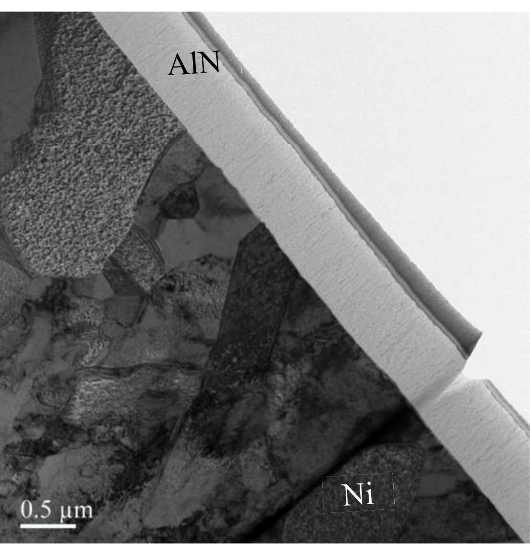

Figure 3.14: *A TEM bright field (BF) micrograph in a cross-section of an AlN film grown on Ni foil.*

3.2.6. X-ray photoelectron spectroscopy

The elemental composition and the chemical states of the elements were studied by x-ray photoelectron spectrometry (XPS) (Axis Ultra DLD, Kratos Analytical Ltd.) using a monochromated Al Kα (E = 1486.6 eV) working at 150 W. The energy resolution, determined by the Ag 3d contribution of a silver sample, was 1.5 eV for survey scans and 0.55 eV for narrow scans. The analyzed area was 110 µm in diameter. The depth profiles were carried out in the etched area of 3mm × 3mm by an Ar^+ ion beam operating at 2 kV and 2 µA. The spectra were calibrated in energy with the Zn 2p peak in ZnO at 1022.0 eV for ZnO thin films, and with the Al 2p (Al-N) component at 73.6 eV for AlN thin films [11].

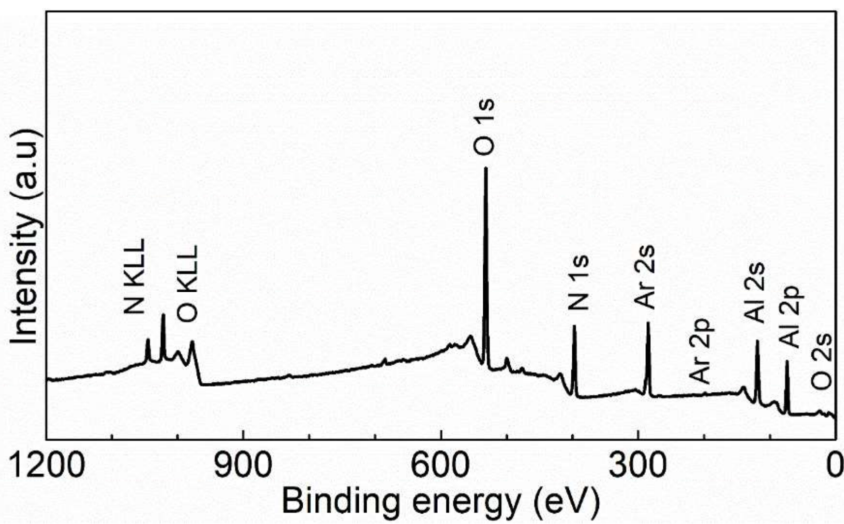

Figure 3.15*: An example of the survey spectrum of AlN thin film.*

3.2.7. Secondary ion mass spectrometry

Dynamic-secondary ion mass spectrometry (D-SIMS) (CAMECA SC-Ultra) was used to analyze the elemental and isotopic composition of the films grown. First, depth profiles were acquired with a Cs^+ bombardment operating at 1 keV and a 6 nA primary ion beam scanned over an area of 500×500 μm^2. Secondary positive ions were detected as MCs^+ clusters (M is the element of interest) from a 60 µm area centered on the scanned area. Secondly, the oxygen isotopic signatures were determined with the M^- mode analysis over an area with a diameter of 8 µm. This method will be discussed in Chapter 4.

Figure 3.16: *Dynamic-secondary ion mass spectrometer (CAMECA SC-Ultra).*

3.2.8. Piezoelectric characterization

For the piezoelectric characterization, AlN films were deposited on a silicon wafer with a 150 nm-thick nickel layer as a bottom electrode and a 100 nm layer of aluminum as the top electrode. The specific bend bars for the four-point bending (4-PB) characterization were fabricated using laser lithography and wet etching processes. An S1813 photoresist (MicroResist technology GmbH) was used as a wet etching mask for defining selective areas of metal electrodes. It was spin-coated, exposed to UV (MLA150, Heidelberg Instruments), baked at 120°C and developed with an MF319 developer. The AlN layer was etched by aluminum etchant (Sigma-Aldrich, 901539). The photoresist layers were removed by PG remover (MicroChem, G050200). Details of photolithography processes are shown in Figure 3.17.

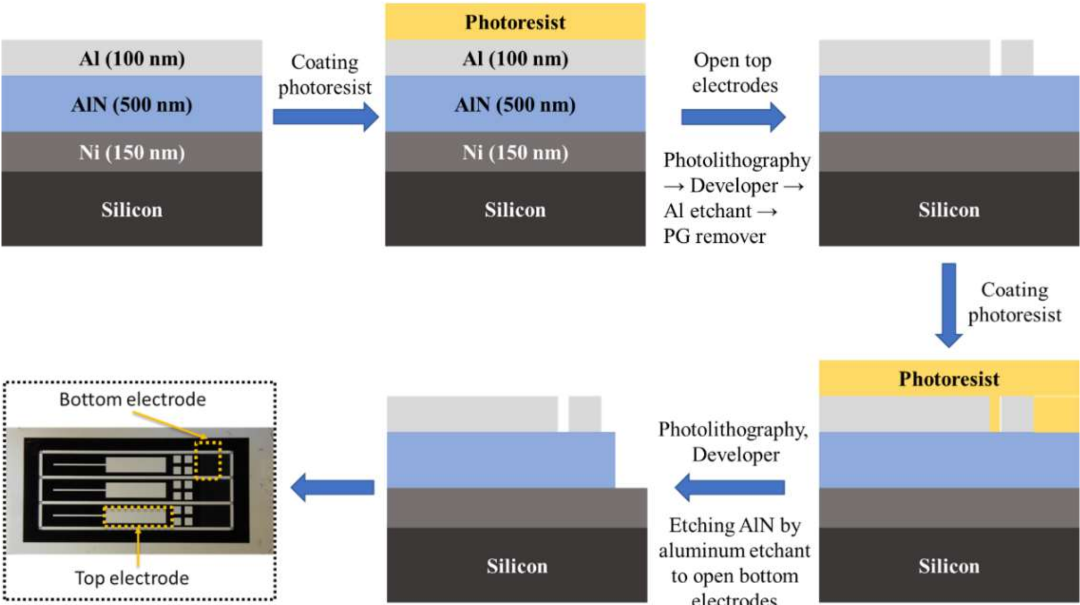

Figure 3.17: *Photolithograph processes for preparing the cantilever structure for the 4-PB measurement.*

The 4-PB electromechanical method shown in Figure 3.18 (aixACCT TF Analyzer 2000) was used to measure the effective transverse piezoelectric coefficient $e_{31,f}$ of the AlN films, which is extracted using the following equation [12]:

$$e_{31,f} \cong \frac{Q.l^2}{4.A.h.u.(1-\nu_{Si})} \quad (1)$$

where Q is the induced charge and l is the load span of the 4-PB configuration (10 mm). A is the top electrode area of 16 mm^2, h is the sample thickness, u is the induced displacement, and ν_{Si} is the Poisson's ratio for silicon (0.064)[12]. The slope of the charge versus strain is directly proportional to the $e_{31,f}$ coefficient.

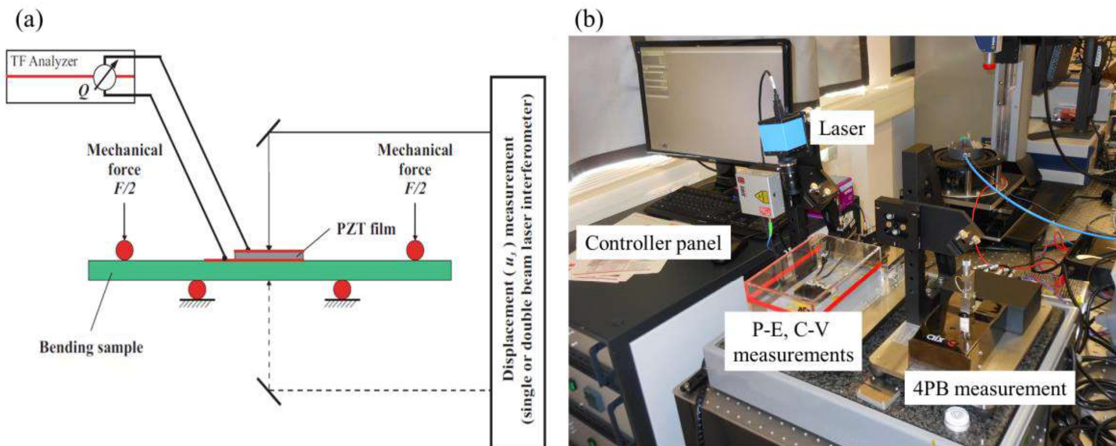

Figure 3.18: *(a) The schematic principle of 4-PB measurement*[12]*, (b) piezoelectric and ferroelectric characterization systems (aixACCT TF 2000).*

3.2.9. Magnetization measurement

Magnetization measurements were performed by a vibrating-sample magnetometer (VSM, cryogenic, UK) in collaboration with the Nanomagnetism group of Prof. Andreas Michels and Dr. Philipp Bender at the University of Luxembourg. A sample was mounted on a long non-magnetic rod and then driven by a mechanical vibrator. The rod was placed in a constant magnetic field generated by two electromagnets, as shown in Figure 3.19.

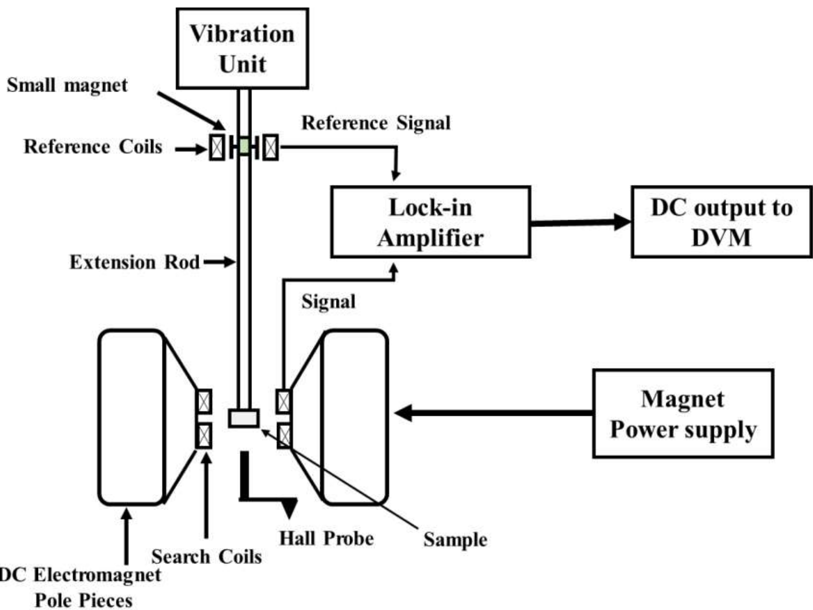

Figure 3.19: *Schema of VSM measurement* [13,14].

The oscillatory motion of the magnetized sample will induce an induction current in the searching coils (or pick-up coils). The induced current followed Faraday's law of induction which is proportional to the sample's magnetization [13,14]. Magnetic hysteresis measurements were carried out at different temperatures, e.g. 300, 60, and 5 K. The temperature dependence of magnetization measurements was also conducted by sweeping the temperature from 300-5 K. Field cooling (FC) and zero-field cooling (ZFC) measurements were performed. In the ZFC process, no magnetic field is applied while cooling the sample to low temperatures. In this process, the spins are locked in random orientation for a polycrystalline sample. In the FC process, a magnetic field is applied while the sample is cooled down to a low temperature. Therefore, spins are locked in the direction of the applied field. The field warming (FW) measurement was also carried out at a constant field with increasing temperature.

Figure 3.20 shows a magnetization measurement of a Ni-Mn-Ga film grown on Si(100). More details can be found in Chapter 7.

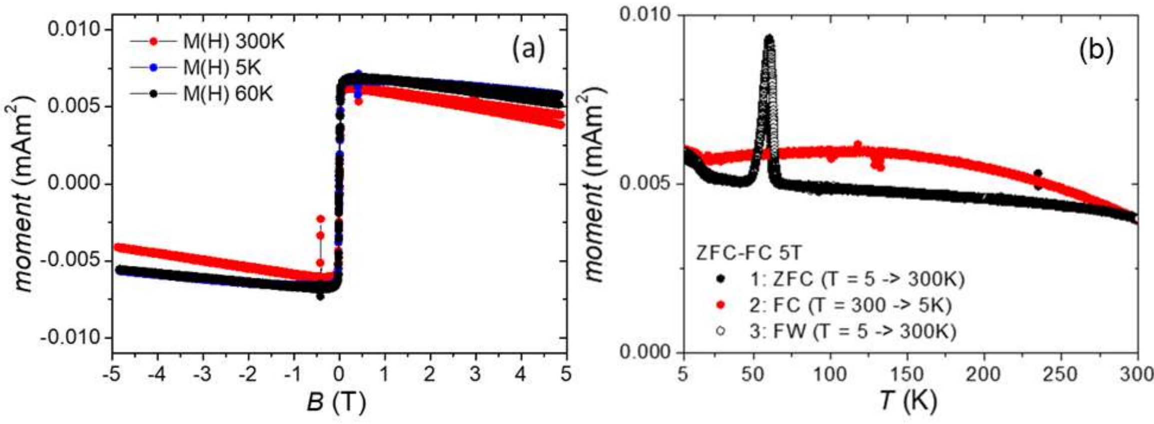

Figure 3.20: *Magnetization measurements of Ni-Mn-Ga 2.5µm-thick film.*

3.2.10. Magnetoelectric measurement

The ME coefficient was measured by the in-house ME bench illustrated in Figure 3.21. A small AC and a bias DC magnetic field are generated by Helmholtz coils (Leybold Shop, ref. 555 604) and an electromagnet (Leybold Shop, Ref. 562 131, Ref. 562 11), respectively. The Hall probe (Hirst Magnetics, GM08) is placed as close as possible to the sample fixed in a sample holder located between the Helmholtz coils. The excitation signal to drive the AC and DC bias magnetic field is made by a two channels frequency generator (Tektronix, AFG1062). The output signal from the ME sample is then analyzed by a lock-in amplifier (SRS865A, 4 MHz Lock-In Amplifier, Stanford), and with data collected by an oscilloscope (Teledyne/Lecroy, WaveAce2024).

Capabilities for the characterization of the ME bench:

DC field max. with electromagnet ~ +/- 0.25 T = +/- 2500 Oe = +/- 200 kA/m

AC field max. with Helmholtz coils ~ +/- 20 mT = T = +/- 200 Oe = +/- 16 kA/m

AC field frequency range = 1Hz to 5 kHz

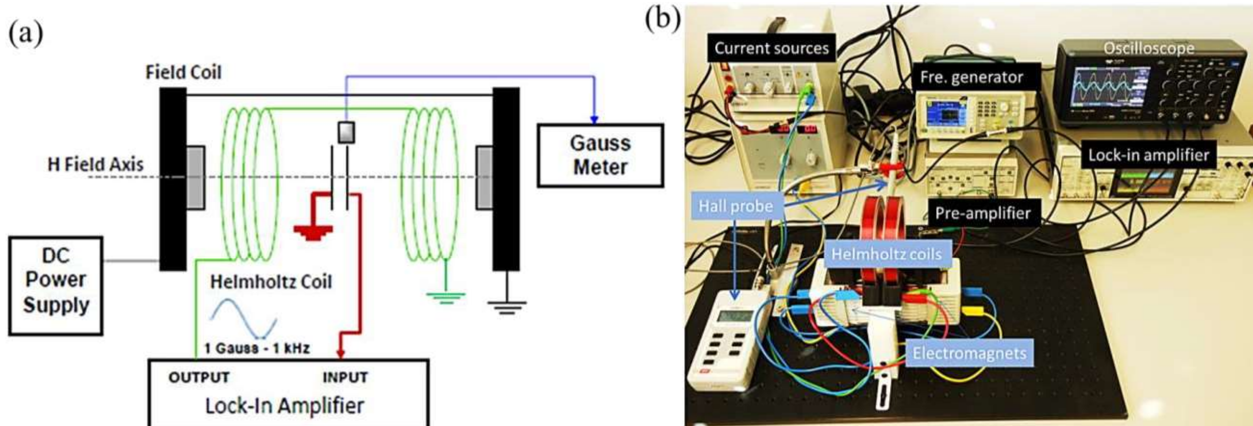

Figure 3.21: *(a) The schematic principle of the ME measurement, (b) an inhouse ME bench.*

The sample of the ME composite is mounted on a PCB for output contacting. Silver glue was used to connect the wire to top and bottom electrodes on the ME chip. Prior to the measurement, a 50 nm-thick Al was deposited over 0.3cm×0.3cm on Al/Ni composites as a top electrode. The ME voltage was extracted using the locking amplifier when the ME sample was exposed to a DC magnetic field (Hdc) varying from -200 to 200 Oe superimposed with a small AC magnetic field of 8.5 Oe at a constant frequency of 46 Hz. Then, the ME coefficient was calculated with a following equation [15,16]: $\alpha_{ME} = \frac{Voutput}{t.Hac}$, where t is a thickness of the piezoelectric layer (in the thin-film composites) and Voutput is the ME voltage extracted in the piezoelectric layer. Both forward ($-H_{dc} \rightarrow 0 \rightarrow +H_{dc}$), and backward ($+H_{dc} \rightarrow 0 \rightarrow -H_{dc}$) measurements were acquired.

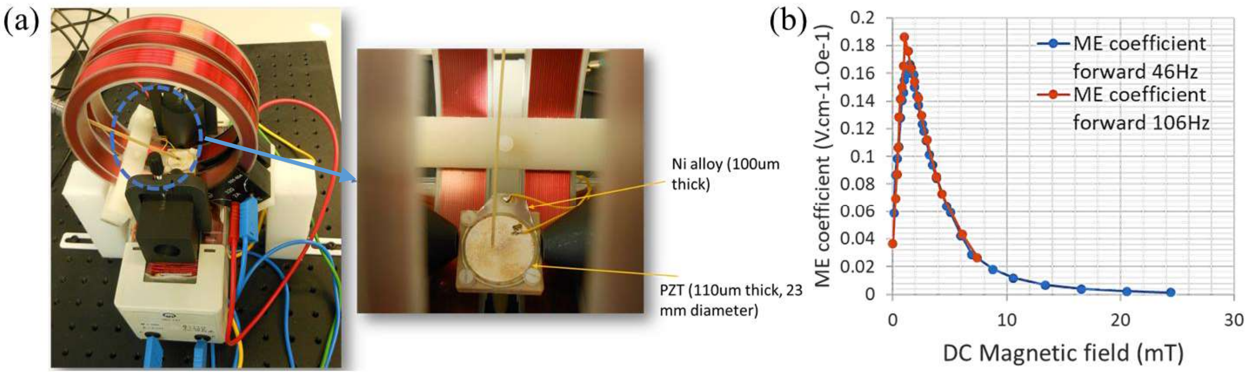

Figure 3.22: *ME measurement of PZT/Ni, (a) sample position and (b) ME coefficient as a function of the DC magnetic field.*

The calibration was performed on a commercial laminated Ni/PZT sample. The sample is placed in the sample holder located at the middle of two Helmholtz coils, as shown in Figure 3.22 (a). The ME coefficient of the laminated Ni/PZT is about 0.18 $V.cm^{-1}.Oe^{-1}$.

3.3. References

(1) Ponraj, J. S.; Attolini, G.; Bosi, M. Review on Atomic Layer Deposition and Applications of Oxide Thin Films. *Critical Reviews in Solid State and Materials Sciences*. 2013. https://doi.org/10.1080/10408436.2012.736886.

(2) Johnson, R. W.; Hultqvist, A.; Bent, S. F. A Brief Review of Atomic Layer Deposition: From Fundamentals to Applications. *Materials Today*. 2014. https://doi.org/10.1016/j.mattod.2014.04.026.

(3) George, S. M. Atomic Layer Deposition: An Overview. *Chem. Rev.* **2010**. https://doi.org/10.1021/cr900056b.

(4) Miikkulainen, V.; Leskelä, M.; Ritala, M.; Puurunen, R. L. Crystallinity of Inorganic Films Grown by Atomic Layer Deposition: Overview and General Trends. *Journal of Applied Physics*. 2013. https://doi.org/10.1063/1.4757907.

(5) The Water Pulse Reactions from First Principles Atomic Layer Deposition of Zinc Oxide : Study on the Water Pulse Reactions from First Principles. **2018**. https://doi.org/10.1021/acs.jpcc.7b11469.

(6) Weckman, T.; Laasonen, K. Atomic Layer Deposition of Zinc Oxide: Diethyl Zinc Reactions and Surface Saturation from First-Principles. *J. Phys. Chem. C* **2016**. https://doi.org/10.1021/acs.jpcc.6b06141.

(7) Pung, S. Y.; Choy, K. L.; Hou, X.; Shan, C. Preferential Growth of ZnO Thin Films by the Atomic Layer Deposition Technique. *Nanotechnology* **2008**, *19* (43). https://doi.org/10.1088/0957-4484/19/43/435609.

(8) Birkholz, M. *Thin Film Analysis by X-Ray Scattering*; 2006. https://doi.org/10.1002/3527607595.

(9) Bachmann, F.; Hielscher, R.; Schaeben, H. Texture Analysis with MTEX – Free and Open Source Software Toolbox. *Solid State Phenom.* **2010**. https://doi.org/10.4028/www.scientific.net/ssp.160.63.

(10) Zhao, M. H.; Wang, Z. L.; Mao, S. X. Piezoelectric Characterization Individual Zinc Oxide Nanobelt Probed by Piezoresponse Force Microscope. *Nano Lett.* **2004**. https://doi.org/10.1021/nl035198a.

(11) Alevli, M.; Ozgit, C.; Donmez, I.; Biyikli, N. Structural Properties of AlN Films Deposited by Plasma-Enhanced Atomic Layer Deposition at Different Growth Temperatures. *Phys. Status Solidi Appl. Mater. Sci.* **2012**. https://doi.org/10.1002/pssa.201127430.

(12) Prume, K.; Muralt, P.; Calame, F.; Schmitz-Kempen, T.; Tiedke, S. Piezoelectric Thin Films: Evaluation of Electrical and Electromechanical Characteristics for MEMS Devices. *IEEE Trans. Ultrason. Ferroelectr. Freq. Control* **2007**. https://doi.org/10.1109/TUFFC.2007.206.

(13) Burgei, W.; Pechan, M. J.; Jaeger, H. A Simple Vibrating Sample Magnetometer for Use in a Materials Physics Course. *Am. J. Phys.* **2003**. https://doi.org/10.1119/1.1572149.

(14) Foner, S. Versatile and Sensitive Vibrating-Sample Magnetometer. *Rev. Sci. Instrum.* **1959**. https://doi.org/10.1063/1.1716679.

(15) Ma, J.; Hu, J.; Li, Z.; Nan, C. W. Recent Progress in Multiferroic Magnetoelectric Composites: From Bulk to Thin Films. *Adv. Mater.* **2011**. https://doi.org/10.1002/adma.201003636.

(16) Wang, Y.; Hu, J.; Lin, Y.; Nan, C. W. Multiferroic Magnetoelectric Composite Nanostructures. *NPG Asia Materials*. 2010. https://doi.org/10.1038/asiamat.2010.32.

4

Highly resistive zinc oxide thin films grown by thermal atomic layer deposition

ZnO is a well-known semiconducting piezoelectric material, which have been used in vast applications such as solar cells, optoelectronics, UV light emitting diodes (LED), gas sensors, surface acoustic wave devices (SAW), and nanogenerators. For piezoelectric-based applications, ZnO thin films are required to give preferred (002) orientation and high resistivity (or low leakage current) to ensure the highest output voltages. Although the ZnO thin films do not present the highest piezoelectric coefficients as highlighted in table 1.1 of chapter 1, they present several advantages such as the presence of no toxic elements and no poling process is required to obtain a piezoelectric response as compared to ferroelectric perovskite materials, such as lead zirconate titanate ($Pb(ZrTi)O_3$), barium titanate ($BaTiO_3$). Several strategies have been reported by using different deposition techniques, for example CVD, sputtering, PLD, ALD. Among these techniques, ALD has emerged as a most suitable method for synthesis of high quality, (002)-oriented and highly conformal thin films with low structural-defect density. The conformal coating obtained by ALD is the pivotal point for optimizing the interface between the piezoelectric coating and the magnetostrictive layer to insure the best elastic coupling between the two layers. Additionally, the relative low temperatures of the ALD processes are compatible with both inorganic and fragile organic substrates. This chapter aims to summarize optimization and development of (002)-oriented ZnO thin film grown by thermal atomic layer deposition.

4.1 Controlling electrical and optical properties of zinc oxide thin films grown by thermal atomic layer deposition with oxygen gas

This chapter is based on the publication: **Tai Nguyen**, et al., "*Controlling electrical and optical properties of zinc oxide thin films grown by thermal atomic layer deposition with oxygen gas*", in Results in Materials 6, 100088 (2020) (DOI: 10.1016/j.rinma.2020.100088)

Results in Materials 6 (2020) 100088

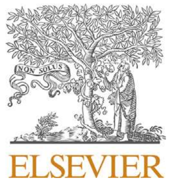

Contents lists available at ScienceDirect

Results in Materials

journal homepage: www.journals.elsevier.com/results-in-materials

Controlling electrical and optical properties of zinc oxide thin films grown by thermal atomic layer deposition with oxygen gas

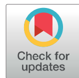

Tai Nguyen [a,b], Noureddine Adjeroud [a], Mael Guennou [b], Jérôme Guillot [a], Yves Fleming [a], Anne-Marie Papon [c], Didier Arl [a], Kevin Menguelti [a], Raoul Joly [a,b], Narciso Gambacorti [c], Jérôme Polesel-Maris [a,*]

[a] Materials Research and Technology Department, Luxembourg Institute of Science and Technology, 41, Rue Du Brill, L-4422, Belvaux, Luxembourg
[b] Physics and Materials Science Research Unit, University of Luxembourg, Campus Limpertsberg, 162 Avenue de La Faïencerie, L-1511, Luxembourg
[c] Univ. Grenoble Alpes, CEA, LETI, F-38000, Grenoble, France

A R T I C L E I N F O

Keywords:
Zinc oxide thin film
Atomic layer deposition
Oxygen chemisorption
Polar surface stabilization
Electrical properties
Optical properties

A B S T R A C T

The preparation of ZnO thin films with controlled electrical resistivity and optical properties is often challenged by the presence of defects, such as oxygen vacancies or interstitial zinc. Here, we investigate the material properties of ZnO polycrystalline thin films prepared by thermal Atomic Layer Deposition (ALD) with the presence of molecular oxygen pulsing during the growth. By means of structural, electrical and optical characterizations, we identify key growth parameters of this unusual ALD process. Unexpectedly, the influence of oxygen molecules on the crystallography, microstructure and morphology of ZnO films is significant from hundred-nanometers to micrometer thick film. The electrical resistivity of the films grown with oxygen gas shows a dramatic increase from 3 to 4 orders of magnitude. Additionally, photoluminescence measurements reveal that deep-level emissions caused by defects located deep in the band gap can be reduced by applying an adequate pulsing of oxygen gas during the process. Finally, we conclude with a discussion about the degree of consistency between the chemical composition, the inner strain and the optical and electrical properties of the films obtained with the different thermodynamic parameters of growth. Several hypotheses are discussed in order to understand the dominance of (002) orientation in the presence of oxygen during the ALD growth process.

1. Introduction

The control of surface morphology and preferred crystallographic orientation has played an essential role in ensuring and upgrading the performance of electronic devices based on zinc oxide thin films [1]. Wurtzite hexagonal zinc oxide has attracted considerable attention due to its excellent properties for transparent electronics, such as a wide direct band gap of 3.37 eV [1,2], large exciton binding energy of 60 meV [3], but also for MEMS actuators with its piezoelectric properties [4]. Therefore, they have been found in vast applications from UV light emitting diodes (LED) [5], flat panel displays [6], and solar cells [7] to gas sensors [8,9], surface acoustic wave devices (SAW) [10], and nanogenerators [11–14]. The properties of zinc oxide thin films strongly depend on their surface morphology and crystallographic structures, and therefore, processing efforts are required for them to fit specific applications. For instance, the non-polar *m*-plane (100) and *a*-plane (110) of ZnO crystals are beneficial for high-efficiency LED and transparent conductive oxide applications [15,16], whereas polar *c*-plane (002) ZnO thin films are employed for potential applications containing sensors [17], nanogenerators [13], piezotronics [18–22], and energy harvesters [23], due to the spontaneous and piezoelectric polarization effects along the *c*-axis [1].

For piezoelectric-based applications, ZnO thin films are required to give preferred (002) orientation and high resistivity (or low leakage current) to ensure the highest output voltages. Several fabrication methods have been reported to achieve polar-plane (002) ZnO thin films, including low gas pressure [24] or control of the Ar:O_2 ratio in sputtering [25], high substrate temperatures and an oxygen-rich environment in pulsed laser deposition (PLD) [26], plasma-enhanced chemical vapor deposition (PECVD) [27], and atomic layer deposition (ALD) [28]. Among these techniques, ALD has emerged as a suitable method for the synthesis of high quality, (002)-oriented and highly conformal thin films

* Corresponding author.
E-mail address: jerome.polesel@list.lu (J. Polesel-Maris).

https://doi.org/10.1016/j.rinma.2020.100088
Received in revised form 14 January 2020; Accepted 20 February 2020
Available online 2 April 2020
2590-048X/© 2020 Luxembourg Institute of Science and Technology. Published by Elsevier B.V. This is an open access article under the CC BY license (http://creativecommons.org/licenses/by/4.0/).

with low structural-defect density. Additionally, the relatively low temperatures of the ALD processes are compatible with both inorganic and fragile organic substrates. In an ALD process using diethylzinc (DEZ) and water as precursors, the non-polar (100) orientation dominates at low temperatures between 100 °C and 250 °C. Conversely, the polar (002) preferred orientation can only be observed at relatively elevated temperatures for ALD, above 250 °C [28,29].

Recently, M. A. Thomas et al. [30] have reported that using oxygen radicals produced during ALD processes can strongly affect the surface morphology, crystallite structure and electrical properties of the ZnO thin films at temperatures as low as 200 °C. In their work, the ZnO thin films were grown with DEZ and water as precursors, and the films were treated *in situ* by oxygen plasma after each cycle–a method called plasma enhanced thermal ALD (PET-ALD). They have observed a giant enhancement of resistivity (about seven orders of magnitude) of the PET-ALD ZnO films compared to simple ALD films without oxygen plasma treatment, and have attributed it to a lower concentration of oxygen vacancies as a result of their neutralization by oxygen radicals after the plasma treatment. They suggested that the ethyl ligands from DEZ can be further cleaved/combusted by energetic oxygen radicals, thus modifying the morphological and crystalline structures. However, the growth mechanism of the preferred (002) orientation has not been clarified in detail. R. Huang et al. [31] have applied *in situ* plasma O_2 treatment after each DEZ – water ALD cycle to highlight the possibility of modulating the ZnO film resistivity and the Fermi level. However, the supercycled ALD processes they proposed were found to barely influence the crystalline orientation. Only S. Park and Y. Lee [32] reported the use of oxygen gas after each cycle of DEZ and water to grow ZnO thin films by thermal ALD without any plasma enhancement. The presence of a molecular oxygen pulse during the ALD process of ZnO profoundly influenced the film morphologies, the crystalline structures, and the electrical properties. The film crystallite modified robustly from nonpolar (100) preferred orientation to polar (002) preferred orientation, and the resistivity of the films increased by two orders of magnitude. Nevertheless, open questions remain about the growth mechanisms, the reason for the significant increase of the electrical resistivity, and the influence of this process on other physical properties like strain or optical absorption.

In the present study, we have systematically investigated the effects of oxygen gas introduced during thermal ALD processes on the ZnO thin film properties by varying the thermodynamic growth parameters. We varied the pulsing time of the molecular oxygen introduced during the process and the substrate temperature separately. The results obtained suggest that by applying the relevant oxygen pulse time and substrate temperature, the crystallographic structure of ZnO films can be highly controlled from random orientations to the preferentially polar orientation. Moreover, due to uncommon treatment by oxygen molecules during the ALD growths, not only electrical and optical properties but also the electronic properties are significantly impacted, as proven by novel characterizations such as four-point probe, UV–visible optical spectroscopy, photoluminescence measurements, and x-ray photoelectron spectrometry. The dramatic increase of the electrical resistivity from 3 to 4 orders of magnitude is expected for improving current leakage issues in the piezoelectric applications of ZnO thin films as actuators or strain sensors. Additionally, the photoluminescence measurements reveal that deep-level emissions caused by defects located deep in the band gap can be reduced. This would have a positive impact on the UV light emission efficiency of ZnO devices like LED. Subsequently, based on those results, the possible growth mechanisms and rational interpretations for the significant increases of resistivity, as well as correlations of the structural, optical and electronic properties of ZnO films are discussed.

2. Experimental details

The ZnO thin films were synthesized using standard precursors, such as diethylzinc [DEZ, $Zn(C_2H_5)_2$] (Strem Chemicals, Inc., France), deionized (DI) MilliQ water (resistivity of 18.2 MΩ cm at 25 °C), and O_2 gas (stand-alone bottle, Air Liquide, alpha 2 O_2 global purity ≥ 99.9995% mol with less than 0.5H_2O ppm. mol impurity) in a commercial atomic layer deposition reactor (TFS-200, Beneq, Finland). The Argon gas used for purging during the ALD process was ALPHAGAZ™ 2 with a global purity of ≥99.9999% mol with less than 0.5H_2O ppm. mol impurity. The supporting surfaces for the ZnO thin film deposition were 2 × 2 cm^2 pieces of single crystal Si(100) wafer (Siegert GmbH, Germany, grade Monitor), pristine and coated by sputtering (Bal-Tec Med 020 high vacuum coating system) with a 150-nm layer of nickel (target purity level of 99.999%, reference NI000565, Goodfellow GmbH, Germany) and glass slides (Thermo Scientific, Germany). Prior to the synthesis of ZnO thin films, the substrates were cleaned in acetone, isopropanol, DI water and dehydrated for 20 min at 200 °C. Just before introduction into the ALD reactor, an additional plasma cleaning (Plasma Therm 790 RIE, 120 W, 10 min, in Ar:O_2 gases environment at 30 mTorr) was performed on the substrates. The ZnO thin films were elaborated without using molecular oxygen gas at a substrate temperature of 180 °C by the following four-step sequence: DEZ pulse (0.1 s), Ar purge (5 s), DI water pulse (0.1 s), and Ar purge (5 s). In contrast, when using oxygen gas pulsing, the ZnO thin films were deposited at 180 °C by a sequence of six pulses; DEZ pulse (0.1 s), Ar purge (5 s), O_2 pulse, Ar purge (20 s), DI water pulse (0.1 s), and Ar purge (10 s), where the pulsing time of oxygen gas varied between 1, 3, and 5 s. The temperature-dependent studies were performed using the sequence of six pulses at substrate temperatures of 100, 150, 180, and 200 °C with a constant oxygen pulsing time of 1 s. The ZnO thin films were deposited by 500 cycles for all studies, except for the films studied by cross-section transmission electron microscopy (TEM) with 5000 cycles, which were set to achieve a thicker layer of about 1 μm. Before processes implying either DEZ/H_2O or DEZ/O_2/H_2O precursors, we performed zinc oxide deposition tests by using DEZ and O_2 as precursors for Zn and O, respectively. No film was formed [32] (not detectable by ellipsometry) at a temperature of 180 °C, confirming the global purity of the O_2 gas source from moisture contamination. We also did the same quality control of the Argon gas by pulsing only the DEZ precursor in the same conditions, and no film was formed, thus also confirming the global purity of the Ar gas source in the ALD reactor.

X-ray diffractometry (Diffractometer Bruker D8 Discover with Cu Kα radiation and a 5-axis Eulerian cradle) was conducted in θ–2θ (Bragg-Brentano) and in grazing incidence ($\omega = 0.5°$) (GIXRD) configurations to estimate the crystalline quality of the ZnO thin films on all samples. The measurement uncertainty in angle 2θ was estimated to 0.02°, based on repetitive measurements following the sample alignment. For pole figures, the measurements were performed in θ–2θ mode with a measurement in increments of 5° in ϕ (phi) and 3° in χ (chi). The measurement was performed up to 72° in χ. The pole figures were performed using collimated irradiation of 1 mm beam diameter. For both samples, pole figures were performed on the (100), (002) and (101) peak positions. For each peak position, the background was measured to the right and the left of the peak position for one angle of phi only. The defocussing correction was performed based on the number of counts measured on the (104) and (113) peak positions of the NIST standard SRM1976. The pole figure data treatment measured was performed using the MTEX toolbox (version 5.1.1) [33] in conjunction with Matlab ®. The microstructure of samples was analyzed by scanning electron microscopy (SEM) on a Helios Nanolab 650 FIB-SEM instrument (FEI Company, USA). Cross-sectional configurations were carried out to further confirm the thickness of the ZnO thin films measured by ellipsometry using a J.A. Woollam M2000 instrument (analysis wavelength 300–1000 nm) with three different angles 65, 70, and 75°. The growth rate was calculated as the ratio of the thickness of the ZnO layer over the number of ALD loops. TEM analysis in cross section and diffraction were performed on a JEOL 3010F microscope operating at 300 kV. The instrument has a 0.17 nm atomic resolution. A four-point probe and Hall measurements (Ecopia HMS-3000) were performed to measure the resistivity and carrier concentration of the thin film samples on glass substrates, respectively. Elemental composition and chemical states were studied by x-ray

photoelectron spectrometry (XPS) (Axis Ultra DLD, Kratos Analytical Ltd.) using an x-ray source (Al K_α monochromated, E = 1486.6 eV) at a power of 150 W, and an energy resolution of 1.5 eV for survey scans and 0.55 eV for narrow scans determined on a silver sample. The surface area analyzed was 110 μm × 110 μm. The spectra have been calibrated in energy from the Zn 2p peak in ZnO at 1022.0 eV. The depth profiles were carried out in the 3 mm × 3 mm etched area by an Ar^+ ion beam operating at 2 kV and 2 μA. The UV–visible measurements (LAMBDA 1050 UV/Vis Spectrophotometer, PerkinElmer) were conducted in a 250-2000 nm-range wavelength to measure the transmittance and reflection spectra of ZnO thin films on glass slides. Photoluminescence (PL) measurements were carried out at room temperature in a Renishaw inVia confocal micro-Raman spectrometer, with an excitation wavelength of 325 nm provided by an 8 mW He–Cd laser focused through a Thorlabs UV objective with 40× magnification and a numerical aperture of 0.5. A 300 gr/mm grating enabled analysis in the 350–900 nm range. The PL spectrum was normalized in intensity for the sake of clarity of comparison between each sample analysis. A hexagonal <0001>-oriented ZnO single crystal purchased from MTI Corporation was characterized and taken as a reference spectrum.

3. Results

3.1. Effect of the pulsing time of oxygen

3.1.1. Structural and morphological properties

Fig. 1(a) illustrates the growth rate of ZnO thin films for varying pulsing times of oxygen for a constant substrate temperature of 180 °C. The growth rate of the ZnO films decreased significantly and stabilized with increasing pulsing times: it was about 2.48, 1.82, 1.67, and 1.69 Å/cycle for films grown with oxygen gas pulsing times of 0, 1, 3, and 5 s, respectively.

Fig. 1(b) presents the grazing incident x-ray diffraction (GIXRD) for four nickel-coated samples. For all ZnO samples, the diffraction patterns match well with the standard diffraction patterns of the wurtzite ZnO crystal structure (JCPDS-36-1451). ZnO thin films grown without oxygen gas displayed a contribution from three different diffraction peaks, i.e. the (100), (002) and (101) orientations. On the other hand, for ZnO thin films grown in the presence of oxygen gas, the (002) diffraction peak, which is characteristic of the polar plane, becomes dominant, and the (100) and (101) diffraction peaks are reduced to tiny peaks located around 31.77° and 36.22°, respectively (Fig. 1(b)). This indicates that these films grow preferentially along the c-axis.

In order to quantify the preferred (002) orientation of the ZnO films, we defined a Grazing Incidence Texture Coefficient (GI-TC) for the *hkl* plane, as shown by the following equations:

$$\mathrm{GI-TC}(hkl) = \frac{I_r(hkl)}{N^{-1}\sum_N I_r(hkl)} \quad (1)$$

and

$$I_r(hkl) = I_{(hkl)}/I^0_{(hkl)} \quad (2)$$

where $I_{(hkl)}$ are the relative intensities of (hkl) peaks measured on the thin film samples, $I^0_{(hkl)}$ corresponds to the relative intensity for the same reflection on an isotropic randomly oriented ZnO powder (NIST Standard SRM674B) measured in exactly the same configuration, and N is the number of Bragg reflections considered. Here, N = 3 because we investigated the orientations (100), (002), and (101). This expression of the GI-TC, although close to the TC definition found in Ref. [34,35], cannot be assimilated to it since we performed the measurement at grazing incidence, with the same incident angle for all samples, and not in θ-2θ mode. By construction, as for TC, the GI-TC is 1 for a non-textured sample and has a value of N for single oriented crystals.

To verify that the ZnO powder really is isotropic and randomly oriented, a measurement was performed in θ-2θ mode and compared to the reference pattern in the JCPDS database. As shown in Fig. S2 in the Supporting Information, the Texture Coefficient (TC) of the three Bragg peaks (100), (002), and (101), as defined in Refs. [34,35] were almost exactly 1, confirming that the powder really was isotropic and randomly oriented and consequently could be used as a reference pattern.

The GI-TC values of the ZnO thin films on nickel-coated silicon substrates, which are shown in Table 1, clearly confirmed that the strong domination of (002) crystal orientation outweighs the (100) and (101) orientations in the ZnO thin films grown with oxygen gas (see Fig. S3, Supporting Information). In addition, the GI-TC (002) of the ZnO film grown with 1-s oxygen gas pulsing shows the highest value in comparison to the other samples. This implies a highly preferred orientation along the c-axis for this sample.

The pole figures shown in Fig. 3 give complementary information about the preferred orientation of the ZnO grains in the polycrystalline film grown without [Fig. 3(a)] and with [Fig. 3(b)] the presence of molecular oxygen pulsing (1 s) at a sample temperature of 180 °C. The calculated Orientation Distribution Functions (ODF) deduced from the measured pole figures show that indeed some degree of texture is present on both samples. Thus, the pole figures of the ZnO film grown with the presence of molecular oxygen pulsing [Fig. 3(b)] present a preferred orientation along the c-axis without any significant misalignment. It can be seen that the (002) orientation (along the c-axis) is significantly more pronounced in the ZnO thin film grown with the presence of the oxygen gas. This change in texture is confirmed by the calculated texture index/entropy [36] changing from 2.42/-0.43 for the ZnO film grown without the O_2 gas (Fig. 3(a)) to 6.89/-1.34 for the ZnO grown with the O_2 gas

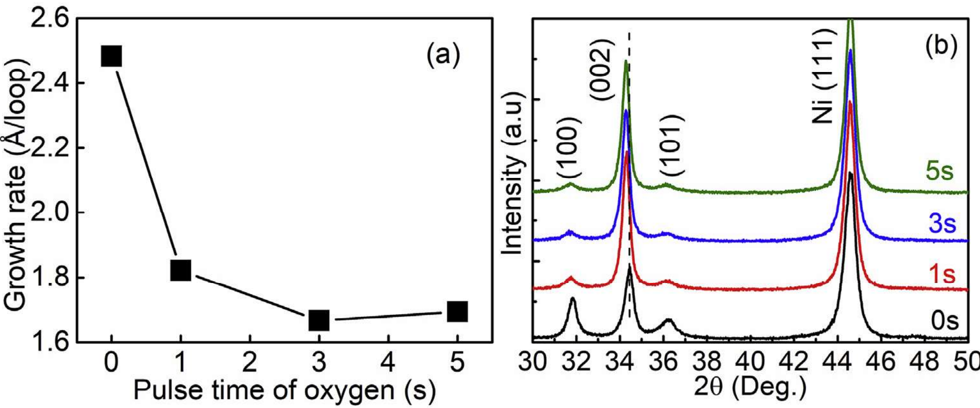

Fig. 1. (a) Growth rate, and (b) grazing incidence x-ray diffraction pattern (ω = 0.5°) of ZnO thin films grown at 180 °C with different oxygen pulsing times. The nickel (111) peak was used as a reference to track the shift of the diffraction peaks of ZnO films. The black dashed vertical line highlights the shift of the (002) peak.

Table 1
Sample references, thicknesses, lattice constants, induced intrinsic strain, grazing incidence texture coefficient, oxygen over zinc ratio (O/Zn), and photoluminescence intensity ratio (I_{NBE}/I_{DLE}) of ZnO thin films processed with different pulsing times of oxygen and substrate temperatures.

Sample	Thickness (nm)	*a*(Å)	*c* (Å)	Strain (%) [a]	|ΔStrain| (%) [b]	$\|\Delta Strain\|_{thickness}$ (%) [c]	GI-TC [d]			O/Zn ratio	I_{NBE}/I_{DLE}
							(100)	(002)	(101)		
0 s	124.2	3.237	5.193	−0.345			0.86	1.87	0.27	0.92 ± 0.02	1.81
1 s	91.1	3.241	5.216	0.096	0.441	0.105	0.25	2.63	0.12	0.96 ± 0.03	17.24
3 s	83.4	3.249	5.218	0.134	0.038	0.024	0.22	2.67	0.11	0.93 ± 0.03	4.70
5 s	84.7	3.245	5.220	0.173	0.039	0.004	0.20	2.68	0.12	0.95 ± 0.04	3.98
100 °C	72.6	3.251	5.225	0.269			1.06	1.59	0.34	0.98 ± 0.04	1.94
150 °C	84.2	3.251	5.221	0.192	0.077	0.037	0.47	2.33	0.20	0.95 ± 0.04	5.25
180 °C	91.1	3.241	5.216	0.096	0.096	0.022	0.25	2.63	0.12	0.96 ± 0.03	17.24
200 °C	103.6	3.237	5.201	−0.192	0.288	0.040	0.26	2.61	0.13	0.95 ± 0.04	2.85
Ref.[e]	–	3.253	5.211	–			–	–	–	–	18.06

[a] Strain is calculated by $\varepsilon = \frac{c - c_0}{c_0}$ with $c_0 = 5.211$ Å.
[b] Absolute strain change calculated as $|\varepsilon_{n-1} - \varepsilon_n|$ from the previous strain column. *n* is the row index in the table.
[c] Absolute strain change induced by thickness change calculated as $|\varepsilon_{n-1} - \varepsilon_n|$ from the thickness column, according to T. Singh et al. [64].
[d] Grazing incidence Texture Coefficient GI-TC (see Figs. S3 and S4 in the Supporting Information).
[e] References: 1) The ZnO reference (JCPDS-36-1451) is used for the lattice parameters a and c; 2) hexagonal <0001>-oriented ZnO single crystal purchased from MTI Corporation was used for the photoluminescence intensity ratio (I_{NBE}/I_{DLE}).

[Fig. 3(b)]. The change in texture is also reflected in the measured TC and GI-TC shown in Figs S2, S3 and S4 (Supporting Information), where the value of the (002) reflection is close to 3 for the sample grown with the presence of molecular oxygen pulsing (1 s) at a sample temperature of 180 °C.

Furthermore, a remarkable shift of the (002) diffraction peak of ZnO thin films fabricated under different pulsing times of oxygen gas was observed. Here, zinc oxide thin films were deposited on nickel-coated silicon substrates, but we observed the same tendency when they were deposited on a glass sample as shown in Fig. S1 in the Supporting Information. For all the samples, the diffraction peak of nickel (111) was located at the same position (around 2Θ = 44.59°) before and after ALD processes ramping up from 100 °C to 200 °C, and was used as a reference to track the shift of the ZnO (002) peak considered. Therefore, a shift in the (002) diffraction peak for the ZnO layer was an intrinsic effect due to the presence of oxygen gas during ALD processes. The positions of the (002) diffraction peak is noted in Table 1. It was around 34.5° for a ZnO thin film fabricated without using oxygen gas. By introducing oxygen gas during the process, it shifted markedly to lower angles. The (002) peak positions were 33.34, 33.33 and 33.32° for ZnO films with oxygen gas pulsing times of 1, 3, and 5 s, respectively. The ZnO reference (JCPDS-36-1451) gives a value of about 34.38° for the (002) peak position. In comparison to the peak position referenced for wurtzite ZnO in the database, the (002) diffraction peak on the ZnO thin film without oxygen gas was located at a higher angle, whereas that of the ZnO thin film using oxygen gas is located at lower angles. The lattice parameters *a* and *c* of the wurtzite hexagonal structure ZnO were calculated by using Bragg's law (cf. detailed expression in the supporting information) and their values for all films are listed in Table 1. It showed that the strain state of ZnO films changed from compressive to tensile for ZnO films with an increasing O_2 pulsing time. In the case of tensile strain, the unit cells of ZnO were elongated along the c-axis, while they slightly shrunk along the a-axis.

Top-view SEM micrographs of ZnO thin films are shown in Fig. 2. It can be seen in Fig. 2(a) that the ZnO thin film grown without using oxygen gas clearly shows a distribution of different grain orientations with

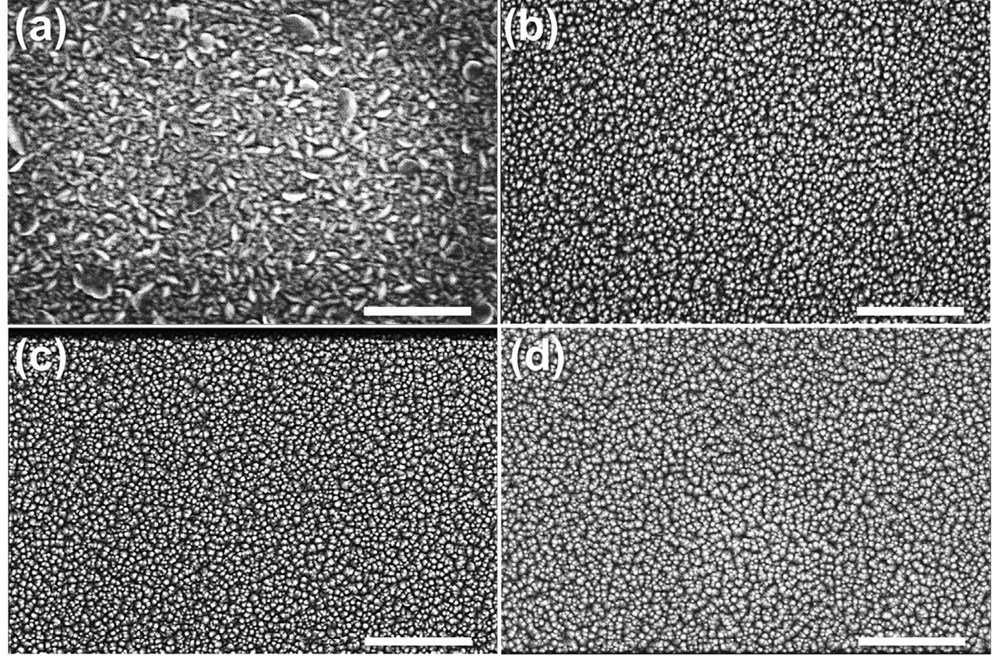

Fig. 2. SEM top view micrographs of ZnO thin films grown at 180 °C with an oxygen pulsing time of (a) 0 s, (b) 1 s, (c) 3 s, and (d) 5 s. The scale bar is 300 nm.

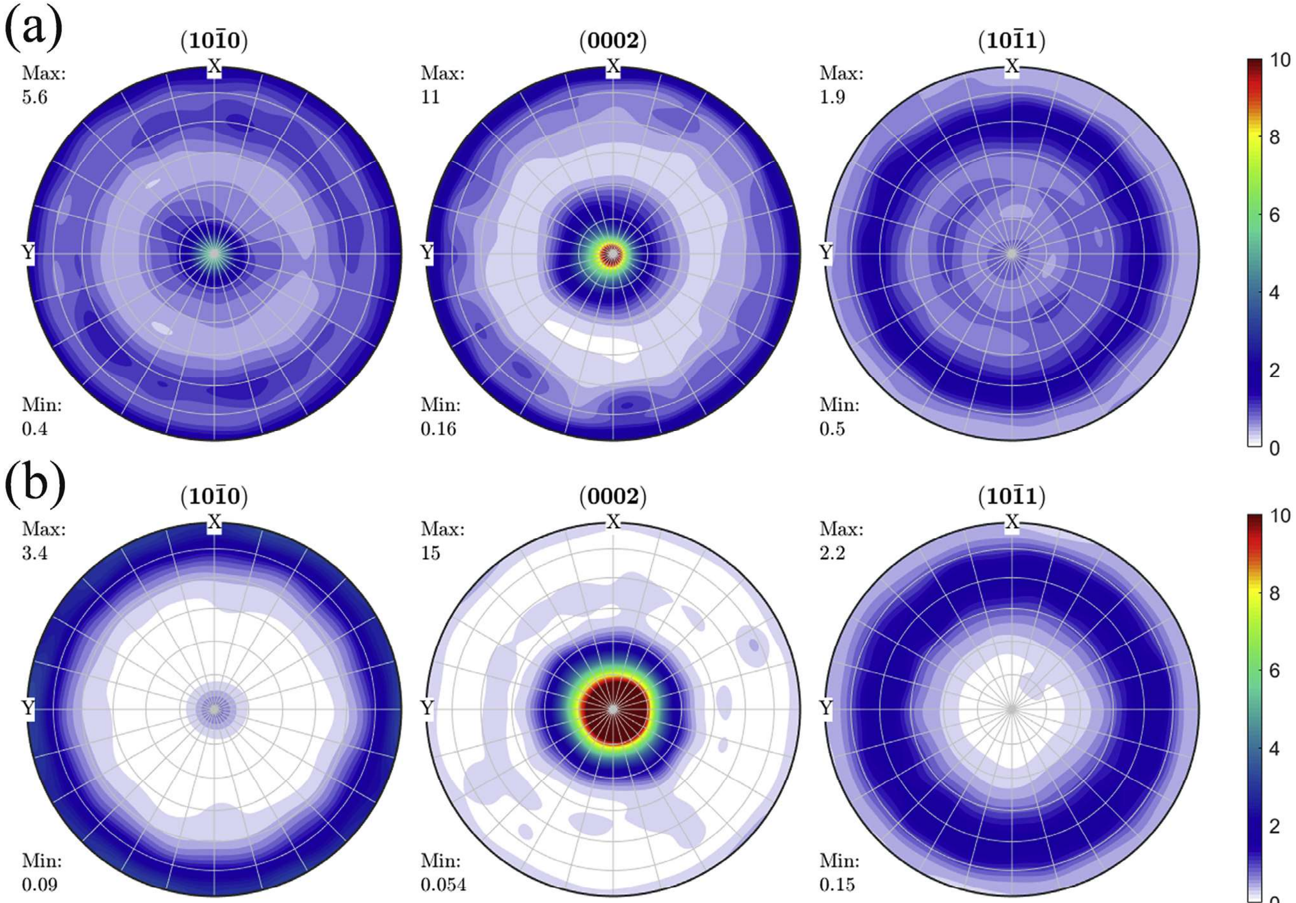

Fig. 3. Calculated Orientation Distribution Functions (ODF) from XRD pole figures of ZnO thin film deposited at 180 °C a) without and b) with the presence of O_2 gas pulses during the ALD growth. In this figure, the depicted poles are denoted using the Bravais-Miller notation (h k i l) with h + k + i = 0. The corresponding measured pole figures are shown in Figs. S5 and S6 in the Supporting Information document.

wedge-like shaped crystallites parallel to the substrate and fine-columnar crystallites perpendicular to the substrate. It is consistent with the x-ray diffraction data that shows a mixture of (100), (002), and (100) orientations. Fig. 2(b)-2(d) present the top-view SEM micrographs of ZnO thin films processed with oxygen. Interestingly, a significant change in the morphologies of those films can be observed, in that they are composed of grains which are mostly vertically oriented along the (002) direction (see Fig. S7 in the Supporting Information). Finally, we did not observe any significant difference between ZnO films grown with different pulsing times of oxygen gas; all exhibit the same morphology and have comparable grain diameters (from 12 to 18 nm).

We investigated the evolution of the grain structure and size distribution by cross section and diffraction TEM on a thicker ZnO layer of 1 μm for the growth process without (Fig. 4) and with (Fig. 5) the presence of molecular oxygen pulsing (1 s) at a sample temperature of 180 °C. Similarly to the previous results, both were performed on a nickel bottom layer. At the end of the process, a top capping layer of aluminum nitride (AlN) was also applied by ALD in the same reactor. The cross section micrographs in Fig. 4(a) highlight a rough polycrystalline ZnO layer of 1.14 μm thickness with a widening of grain sizes from 20 nm at the bottom to 100 nm on top. For 5000 ALD cycles, the growth rate is of 2.28 Å/cycle and the film roughness was estimated to about 120 nm. The detailed view [Fig. 4(b)] of the bottom part of the cross section confirmed small diameter grains from 20 to 30 nm. The TEM diffraction pattern [Fig. 4(c)] shows the <011> pole orientation of the monocrystalline silicon substrate with (111), (200), (022) intense spots and the main ring peak of the (111) orientation of the nickel bottom layer, and for the ZnO layer, weak ring peaks without preferential orientation. The cross-section micrographs in Fig. 5(a) highlight a regular (002) textured ZnO layer of 0.97 μm thickness with a regular preferential orientation of columnar grains with a constant diameter of 40 nm from bottom to top. For the same number of 5000 ALD cycles, the growth rate is reduced to 1.94 Å/cycle in agreement with the previous tendency observed in Fig. 1(a). In addition, the ZnO film roughness was about 30 nm. The TEM diffraction pattern [Fig. 5(b)] clearly revealed an intense peak for ZnO relative to a highly preferential (002) orientation, that is a (002) ZnO spot in a small arc shaped parallel to (200) Si, the normal direction to the substrate. Thus, columnar ZnO grains are similar to monocrystalline grains with their normal direction close to (002) parallel to (200) Si. The same previous diffraction peaks occur for the silicon substrate and the nickel bottom layer with the (111) ring peak. We performed the same ALD recipes for ZnO growth on an AlN bottom seed surface with a similar TEM cross section and diffraction analysis as depicted in the "Supporting Information" document (Figs. S8 and S9). We observed the same qualitative and quantitative tendency of the ZnO film growth as for the nickel bottom layer. For the process without the presence of oxygen gas pulsing (Fig. S8), a ZnO film thickness of 1.26 μm was obtained for a growth rate of 2.52 Å/cycle and a film roughness of 190 nm, with sharp grains. We still observed a widening of grain sizes from 70 nm at the bottom to 200 nm on top. The TEM diffraction pattern in Fig. S8(c) showed relatively strong peaks for the ZnO layer coming from grains without privileged orientation. (002) and (100) ZnO are no longer in a preferential position. For the process in the presence of O_2 gas pulsing (Fig. S9), we observed a regular (002) textured ZnO layer with a regular preferential (002) orientation of columnar grains with a constant diameter of 50 nm from bottom to top. The TEM diffraction pattern in Fig. S9(b) clearly revealed

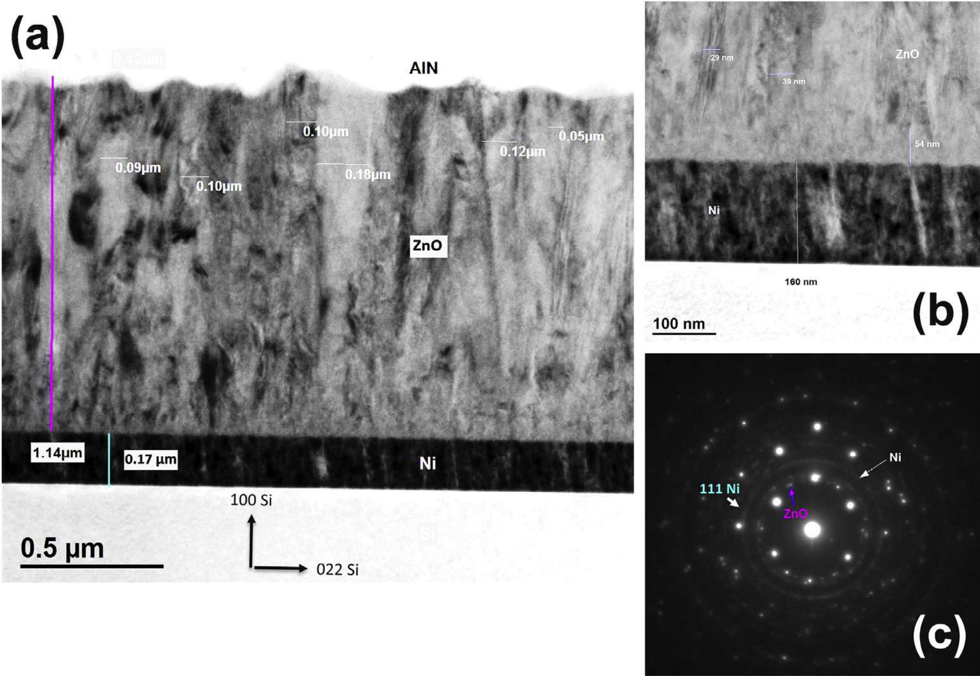

Fig. 4. Transmission Electron Microscopy (TEM) images of ZnO ALD growth during 5000 cycles at a substrate temperature of 180 °C without the presence of O_2 gas pulsing. a) Cross-section view detailing the stacks with nickel as the bottom layer and AlN as the top capping layer. b) Detailed view of the bottom part of the ZnO film at the interface with the nickel layer. c) Diffraction pattern obtained with a 700 nm selected area diaphragm.

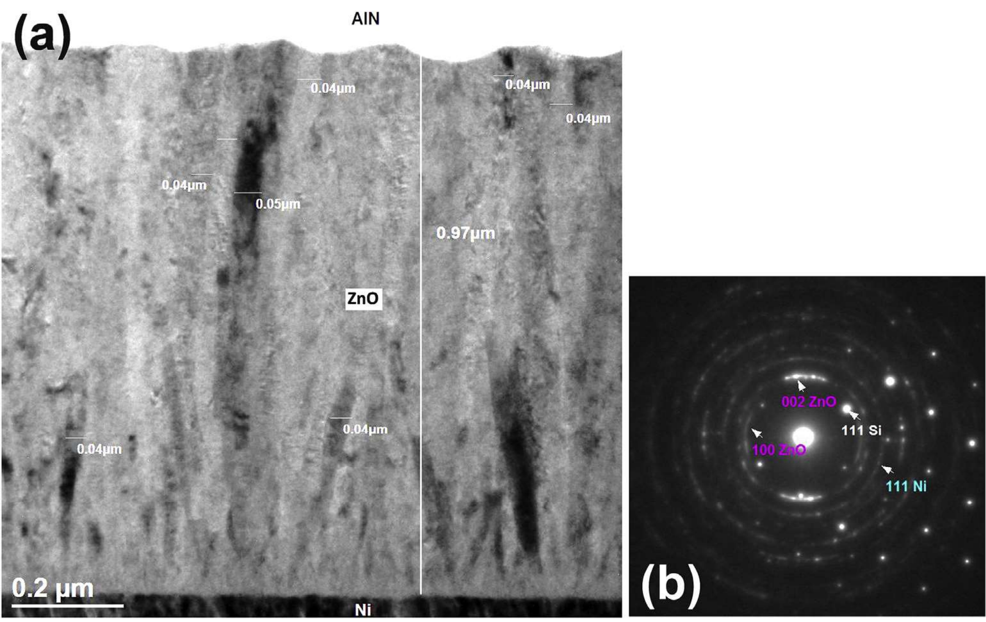

Fig. 5. Transmission Electron Microscopy (TEM) images of ZnO ALD growth during 5000 cycles at a substrate temperature of 180 °C with the presence of O_2 gas pulsing in each cycle. a) Cross-section view detailing the stacks with nickel as the bottom layer and AlN as the top capping layer. b) Diffraction pattern obtained with a 700 nm selected area diaphragm.

an intense peak for ZnO relative to a highly oriented (002).

3.1.2. Electrical and optical properties

In order to evaluate the effect of using oxygen gas during ALD growth on the electrical properties of ZnO thin films, we performed four-point probe measurements. Fig. 6 shows the resistivity of ZnO thin films as a function of oxygen pulsing time. There was a huge increase in the resistivity of ZnO thin films when using oxygen gas during ALD synthesis. While the ZnO thin film had a resistivity of about 0.09 Ω cm without using oxygen gas, the ZnO thin films processed with oxygen were around three orders of magnitude more resistive with values of 56.66, 16.77, and 13.72 Ω cm corresponding to ZnO thin films elaborated with 1, 3, and 5 s of O_2 pulses, respectively.

The effects of using oxygen gas during ALD growth on the band gap energy and optical properties of the films can be concluded by measuring the optical transmittance spectrum. Fig. 7 depicts the optical transmittance spectrum of ZnO thin films grown with and without using oxygen gas. The average transmittance of the ZnO films in either the visible

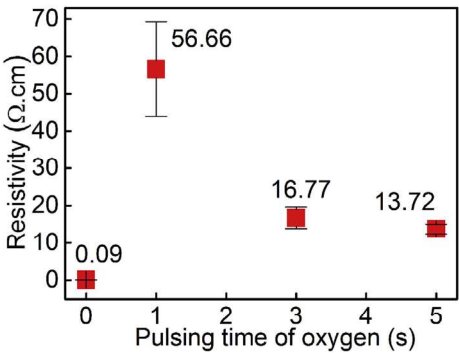

Fig. 6. Resistivity of ZnO thin films as a function of the pulsing time of oxygen gas.

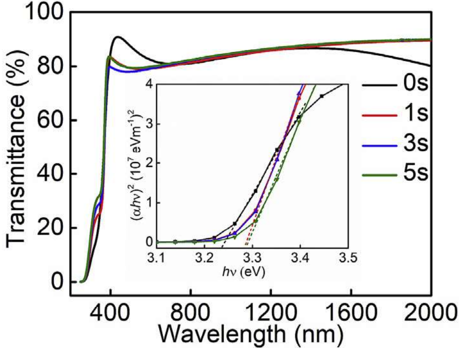

Fig. 7. Optical transmittance spectra of ZnO thin films deposited with different pulsing times of oxygen gas. The inserted figure refers to Tauc plots.

or infrared region was greater than 80% (glass substrate included). The use of oxygen gas during ALD growth induced a higher transmittance of the ZnO films in the infrared domains, whereas a lower transmittance in the visible regions was observed. Namely, the transmittance in infrared and visible regions of ZnO samples with and without oxygen gas is around 85–90% and 80%, 75–80% and 80–92%, respectively. Notably, shallow necks are observed in the UV range (below 400 nm) and their transmittance is higher for the processes with oxygen gas. In fact, these shallow necks were reported before in numerous studies, yet the plausible explanation for it was not mentioned [37–40]. For ZnO nanorods, A. F. Abdulrahman et al. [41] proposed thin films where the transmittance increases when the crystallite size is smaller due to decreased optical scattering. Additionally, the authors mentioned that the transmittance increases with the preferred c-axis orientation, which is consistent with a reduction in light dispersion at grain boundaries as the film structure becomes more oriented along the c-axis. On the other hand, thicker films increase the optical scattering, which reduces the transmittance of the thin layer. Considering the regular (002) textured ZnO was obtained in the presence of oxygen gas during ALD growth, the resulting columnar structure for equivalent film thicknesses and a small grain diameter along the c-axis could fit a similar explanation for the higher transmittance edge in the UV range.

The band-gap energy values of the ZnO thin films can be derived from the Tauc plots, as shown in the detail inserted in Fig. 7. The reflectance and transmittance spectrum of the ZnO films and a reference glass slide was determined to calculate the absorption spectrum of the films (not shown here). For a direct band-gap semiconductor, the relationship between the absorption coefficient α and photon energy $h\nu$ is given by Ref. [42]: $(\alpha h\nu)^2 = A(h\nu - E_g)$. Here, h is Planck's constant; A is a constant and E_g is the optical band gap. By extrapolating the linear part of the Tauc plots to $\alpha = 0$, the band gap can be determined to be about 3.25 eV for the ZnO thin films processed without oxygen gas, and goes up to 3.30 eV for films grown with oxygen pulses, as depicted in Fig. 7. A detailed calculation is given in the Supporting Information.

The room temperature photoluminescence (PL) spectra (Fig. 8) are dominated by strong near band edge (NBE) emission with a peak energy of 3.28–3.31 eV, indicative of the typical excitonic characteristic. The full width at half maximum (FWHM) comprises between 209 and 304 meV for the grown polycrystalline samples, compared with the reference ZnO monocrystalline with a FWHM of 100 meV. The relatively broad linewidth and asymmetric line shape of the NBE emission as compared to the PL signal of the reference single crystal can be attributed to the crystalline quality. For all samples, a broad emission band centered in the green spectral region (2.15–2.35 eV) can also be observed. Although the scientific community has not yet reached a consensus about this visible luminescence, it is accepted that it results from defect-related deep-level emission (DLE), that is, electron transition from the bottom of the conduction band to an antisite defect. The PL intensity ratios of the NBE to DLE emission peaks (I_{NBE}/I_{DLE}) are given in Table 1.

3.1.3. Compositional and chemical state analyses

The composition and chemical state of oxygen and zinc have been investigated by x-ray photoelectron spectroscopy (XPS) through analyses of the O 1s and Zn 2p core levels, as illustrated in Fig. 9. The different O/Zn ratios of ZnO thin films are listed in Table 1. It clearly shows that the O/Zn ratios of ZnO thin films deposited using oxygen gas were higher and closer to 1 than that of a ZnO thin film grown without using oxygen gas, corresponding to a lower concentration of oxygen vacancies in the films. It confirms that the higher resistivity achieved in those ZnO thin films is due to fewer oxygen vacancies.

Detailed XPS information of the chemical state of zinc and oxygen was extracted from the Zn 2p and O 1s narrow scans of the ZnO samples. Before any energy calibration, it is worth remarking that the Zn 2p and O 1s peak position of the ZnO film, grown without the presence of oxygen gas, is located at 0.3 eV, a lower binding energy that the ZnO thin films produced with oxygen gas (spectra not shown here). This sample clearly exhibits a lower intrinsic resistivity allowing a better evacuation of the charges. Fig. 7(a) and (b) illustrate the oxidation state of Zn 2p and O 1s core levels and of ZnO thin films, respectively after energy calibration, as well as illustrating intensity normalization for comparison reasons.Whereas the Zn 2p peaks present no evolution according to synthesis conditions, an increase of the shoulder located above 532 eV is observed in the O 1s spectrum when oxygen gas is added in the synthesis process. Generally, the O 1s peak can be adjusted by two components as we did on Fig. S12 (Supplementary Information): a main oxygen peak located at ~ 530.60 eV [43–45] attributed to the O–Zn bonds in a hexagonal wurtzite structure, and a secondary oxygen peak at 532.25 eV, usually related to Zn–OH bonds, chemisorbed oxygen [44,45], or both. For longer pulse times of oxygen gas during the growth, the main and secondary oxygen peaks remain unchanged both positions and relative intensities. The relative intensities of the secondary oxygen peak were about 0% and 10%

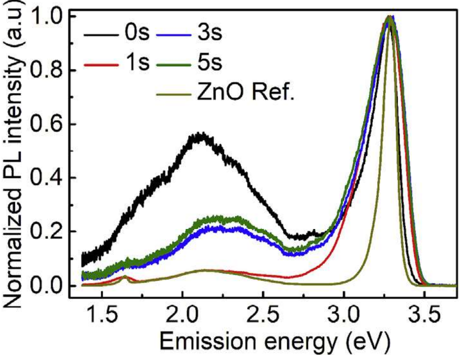

Fig. 8. Photoluminescence spectra of ZnO thin films deposited with different pulsing times of oxygen gas at a constant ALD growth temperature of 180 °C.

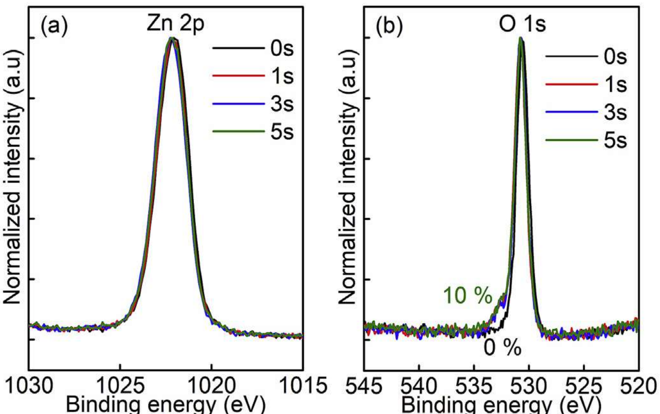

Fig. 9. XPS spectra for ZnO thin films synthesized with different oxygen pulsing times: (a) Zn $2p_{3/2}$ band, (b) O 1s band. The XPS spectra were acquired after Ar + sputter cleaning.

for ZnO films grown without and with oxygen gas, respectively. The binding energy of the secondary oxygen peak can be attributed to Zn–OH bonds originating from water, and/or chemisorbed oxygen. In the case of growing ZnO thin films with oxygen gas, oxygen molecules or ions are adsorbed at grain boundaries [44]. As a result, one possible scenario is a contribution of chemisorbed oxygen on the secondary oxygen peak for the ZnO films using oxygen gas during growth. This scenario will be elaborated further in the Discussion section. It is worth mentioning that an increase in the full-width-half-maximum of the O 1s peak in association with the shift of Zn 2p peak could confirm the presence of oxygen vacancies, leading to a low resistivity of the ZnO films fabricated without oxygen gas.

3.2. Effect of substrate temperature

3.2.1. Crystallographic structure and morphologic properties

Fig. 10(a) shows the growth rate of ZnO thin films grown with 1-s oxygen gas pulsing at different substrate temperatures. It can be seen that the growth rate increased monotonously with substrate temperatures from 100 °C to 200 °C. This result differs from previous reports on the dependence of the growth rate on substrate temperatures for ZnO thin film grown with DEZ and DI water as precursors [46,47]. In those studies, it was shown that the growth rate of ZnO thin films was almost unchanged for temperatures ranging from 100 °C to 180 °C, which is the so-called ALD growth window. The growth window describes a temperature range where the growth rate is both constant and self-limited due to the balance between chemical reactivity and physical desorption. Interestingly, the growth rate of ZnO thin films in our experiment did not follow these studies, but increased constantly in the investigated temperature range of 100–200 °C. This implies that, by inserting the oxygen gas during ALD processes, the equilibrium between chemical reactivity and physical desorption in our experiment could be broken and the growth window in this case could be shifted to a higher temperature range.

The evolution of the crystallographic structure of ZnO thin films was evaluated by GIXRD, as shown in Fig. 10(b). It clearly shows the dominance of the (002) diffraction peak of the ZnO thin films at above 150 °C. Particularly, the ZnO thin films possess highly oriented (002) crystal orientation at 180 °C and 200 °C, indicating film growth with the c-axis perpendicular to the substrate surface. At the low temperature of 100 °C, however, the preferred (002) orientation is lost, and the diffraction pattern displays a contribution of non-polar (100) and (101) planes, as well as polar planes (002). This is consistent with previous reports [27, 28], which showed that (100) and (002) diffraction peaks were found for ZnO thin films deposited at low substrate temperatures (135–150 °C). The degradation of the (002) preferred orientation can be caused by the suppression of crystal growth in this temperature range. As shown in Table 1, the GI-TC was calculated to quantify the preferred orientations of the films. According to the GI-TC calculation, a highly preferred (002) orientation was observed on the films grown at 180 °C and 200 °C, i.e. GI-TC (002) $>$ 2.5 for the three Bragg reflections considered. The films grown at 150 °C and especially at 100 °C show a more isotropic randomly oriented distribution of (100), (002) and (101) crystallographic orientations, i.e. GI-TC (002) $<$ 2.5 for the three Bragg reflections considered (see Fig. S4, Supporting Information).

It is also worth mentioning that the shift of the (002) peak can be observed on ZnO thin films grown under oxygen gas with different substrate temperatures, as listed in Table 1. The (002) peak shifted to higher angles with increasing substrate temperatures, as illustrated in Fig. 10(b). For example, it was 34.28° and 34.50° for the ZnO thin films processed at 100 °C and 200 °C. Notably, the (002) peak of the ZnO films at 200 °C is likely to return to the (002) peak position of the ZnO films grown at 180 °C without using oxygen gas. This could imply that the oxygen gas desorption on the film surface or a change in the chemisorption processes (from molecular to ionic form) could occur at 200 °C [48].

SEM micrographs (Fig. 11) strongly confirmed the evolution of a crystallographic structure displayed on XRD data. While at high temperatures, the ZnO thin films contains fine-columnar grains perpendicular to the substrate surface, the ZnO thin films grown at lower temperatures display a distribution of grains with their polar c-axis perpendicular and parallel to the substrate surface (Fig. S7, Supporting Information). It was also found that the crystalline distribution of ZnO thin film elaborated at 100 °C with an oxygen gas pulsing (Fig. S10,

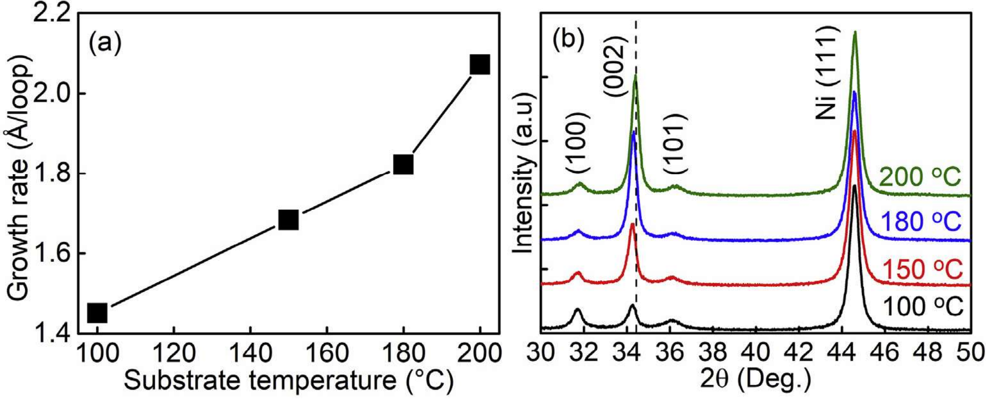

Fig. 10. (a) Growth rate, and (b) grazing incidence x-ray diffraction pattern (ω = 0.5°) of ZnO thin films with different growing temperatures. The nickel (111) peak was used as a reference to track the shift of the diffraction peaks of ZnO films. The black dashed vertical line highlights the shift of the (002) peak.

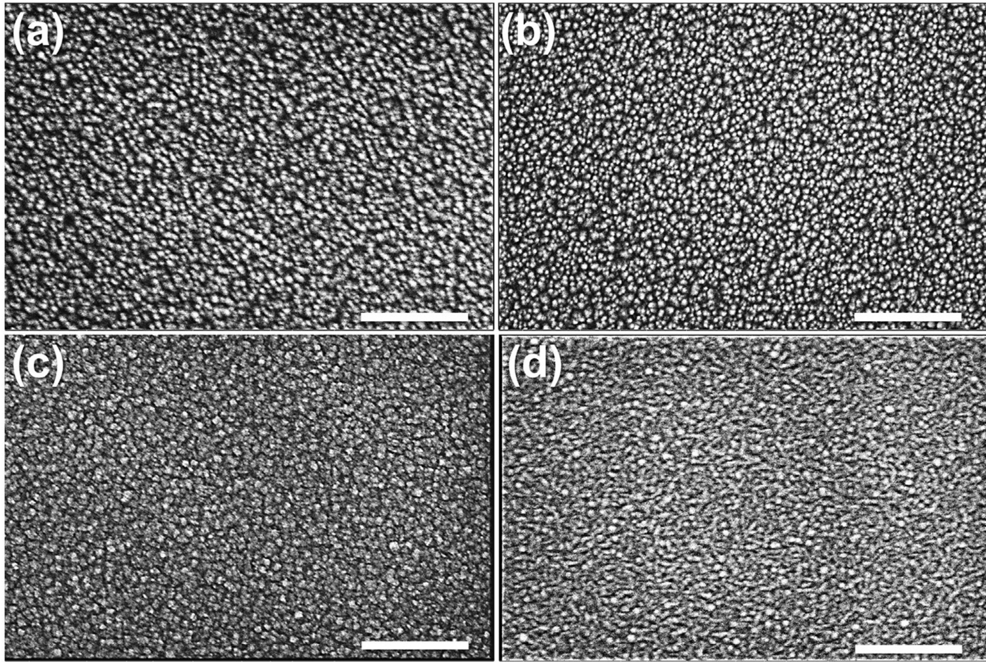

Fig. 11. SEM top-view micrographs of ZnO thin films with different substrate temperatures (a) 200 °C, (b) 180 °C, (c) 150 °C, and (d) 100 °C. The scale bar is 300 nm.

Supporting Information) is very similar to that of a ZnO thin film synthesized without oxygen gas at 180 °C (Fig. 2(a)), but the grain size is slightly finer from 6 to 16 nm average diameters.

3.2.2. Electrical and optical properties

Fig. 12 illustrates a substrate temperature resistivity dependence of ZnO thin films grown in the presence of oxygen gas. In general, the resistivity decreases as the substrate temperature increases. With the exception of the film grown at 180 °C, the resistivity was a bit higher than that of the film at 150 °C. There were about 1196.08, 45.02, 56.66, and 14.39 Ω cm for the ZnO thin films grown at 100, 150, 180 and 200 °C. It should be noted that the resistivity of the ZnO thin film grown at 100 °C was significantly higher than that of others and four orders of magnitude higher than that of the ZnO thin film grown at 180 °C without oxygen. This increase of resistivity at low processing temperatures has been reported previously [48,49]. The plausible reason for this is a lower carrier concentration at lower substrate temperatures in which the resistivity is mainly determined by inter-grain (grain boundary) transport [50,51]. The inter-grain scattering is due to the build-up of potential barriers from the trapping of electrons at the grain boundaries. To confirm the correlation, Hall measurements were performed in the van der Pauw configuration to determine the carrier concentration of the ZnO thin films without and with using oxygen gas. The carrier concentration was 7.11 $\times$ 10^{19} cm^{-3} and 4.08 $\times$ 10^{16} cm^{-3} for the ZnO thin films grown at 180 °C without and with oxygen with a pulsing time of 1 s, respectively. The carrier concentration of the ZnO thin film grown at 100 °C with oxygen gas pulsing was estimated at 10^{14} cm^{-3} due to the limit of the Hall measurement with our equipment for highly insulating materials, as reported by F. Werner for low mobility polycrystalline thin films [52]. In addition, in our processes, chemisorbed oxygen molecules can be trapped at the grain boundaries, which will increase the potential barrier, preventing inter-grain electrical transport. Therefore, in this study, a simultaneous contribution of two phenomena will further decrease the electrical conductivity of ZnO thin films.

Optical transmittance spectroscopy was carried out to study the impact of substrate temperatures on the optical properties of ZnO thin films (Fig. 13). The average transmittance values of all thin films were above 80% in the visible and infrared regions except for the film grown at 100 °C. It should be pointed out that the transmittance values in the visible region slightly increased as substrate temperatures went up. The Tauc plots were also performed to determine the optical band gap of those films, as displayed in the insert in Fig. 13. The band gap values of the ZnO films grown at 150 °C and above are all equal to 3.29 eV while that of the film grown at 100 °C was slightly larger with 3.33 eV, as depicted in Fig. S13 (Supporting Information).

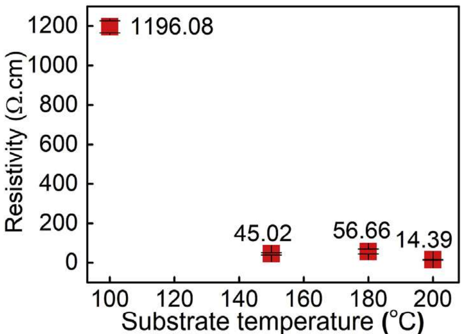

Fig. 12. Resistivity of ZnO thin films deposited at different substrate temperatures.

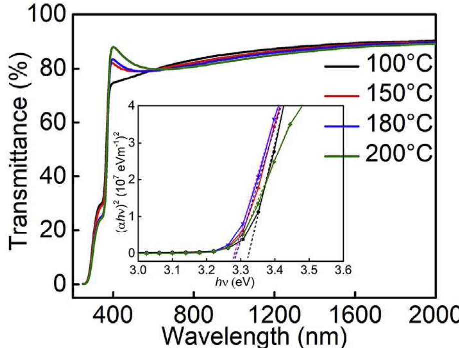

Fig. 13. Optical transmittance spectroscopy of ZnO thin films deposited at different substrate temperatures. The inserted figure refers to Tauc plots.

Here also, the room temperature PL spectra (Fig. 14) are dominated by strong excitonic NBE emissions with peak energy between 3.26 and 3.31 eV. The FWHM of the NBE emission peaks comprises between 278 and 368 meV for the grown polycrystalline samples, compared with the reference ZnO monocrystalline with a FWHM of 100 meV. The broadband emission band centered in the green spectral region (2.15–2.35 eV) can also be observed for every sample. The PL intensity ratios of the NBE to DLE emission peaks (I_{NBE}/I_{DLE}) are indicated in Table 1.

3.2.3. Compositional and chemical state analysis

X-ray photoelectron spectroscopy was carried out to study the influence of substrate temperatures on the chemical stoichiometry and surface bonding of the ZnO films. The in-depth O/Zn ratio was used to understand the effect of substrate temperature on the stoichiometry of the ZnO films. It is clearly shown in Table 1 that the highest value of O/Zn ratio belonged to the film grown at a low temperature of 100 °C, whereas the values of the films grown above 150 °C remain almost unchanged. This is consistent with the discussion by E. Guziewicz et al., and T. S. Bjørheim et al. [47,53] that the formation of defects, such as zinc or oxygen vacancies, can be suppressed in the low temperature regime because of insufficient activation energy.

Binding energies of Zn 2p and O 1s bands are presented in Fig. 15(a)-(b), respectively. The shape of both peaks is very similar. No deviation of the binding energies can be observed on Zn 2p and O 1s bands of the ZnO thin films grown at different substrate temperatures. As noted in Fig. 15(b), the O 1s peak can also be fitted with two sub-peaks, i.e. a main peak at around 530.60 eV indicates the Zn–O bonding in the wurtzite structure, and a secondary peak (532.25 eV) attributed to Zn–OH bonding and/or chemisorbed oxygen.

4. Discussion

4.1. Correlations of chemical composition, optical properties, and electrical properties

It has been pointed out that the electronic trapping at grain boundaries plays an important role in the electrical properties of polycrystalline semiconductors [53–56]. The local charge of these traps induces a potential build-up barrier for the electrons, which impedes the current flow through the grain boundary [54]. In the presence of oxygen gas, oxygen will be chemisorbed in form of molecular O_2^- and/or atomic (O^-, O^{2-}) ions [48] and will be trapped at the grain boundary [46]. Here, absorbed oxygen species can capture electrons from the surface and inner of grains, and then create depletion regions, which further increase the potential barriers at the grain boundaries. Consequently, the potential barriers prevent the electron flow, leading to an increase in resistivity of the ZnO films. This was the situation for the ZnO thin films grown with oxygen gas.

In general, the free charge carriers of intrinsic ZnO are mainly related to some native defects, such as oxygen vacancies, which acts as donors, increasing the surface conductivity. In an oxygen-rich environment, the relatively large amount of chemisorbed oxygen species, acting as surface acceptors, will neutralize the oxygen vacancies and donors, thus reduce the surface conductivity [48]. The chemical composition and appearances of the secondary oxygen peaks (532.25 eV) in XPS have confirmed the suitable stoichiometry promoting the presence of oxygen on zinc in ZnO thin films grown in the presence of oxygen gas. A stoichiometric ratio O/Zn that is closer to one makes a film of higher resistivity. In fact, the highest resistivity of our films (1196.08 Ω cm) was achieved on the ZnO films grown at 100 °C with the highest value of O/Zn ratio (0.98). A possible reason for interpreting the increase in resistivity of the ZnO thin films can be based on chemisorption processes of oxygen gas on the semiconducting surface. For the ALD processes with oxygen gas, oxygen molecules are adsorbed on the surface of the ZnO thin films [48,57]. Those oxygen molecules absorbed play as scavengers, which can capture electrons from the surface and the interior of the ZnO film [58,59]. The

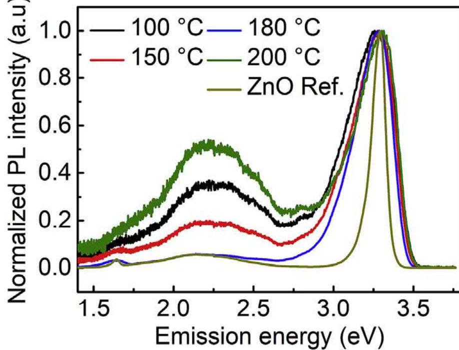

Fig. 14. Photoluminescence spectra of ZnO thin films deposited at different substrate temperatures at a constant O_2 pulse time of 1 s during ALD growth. The spectra have been normalized for the sake of clarity.

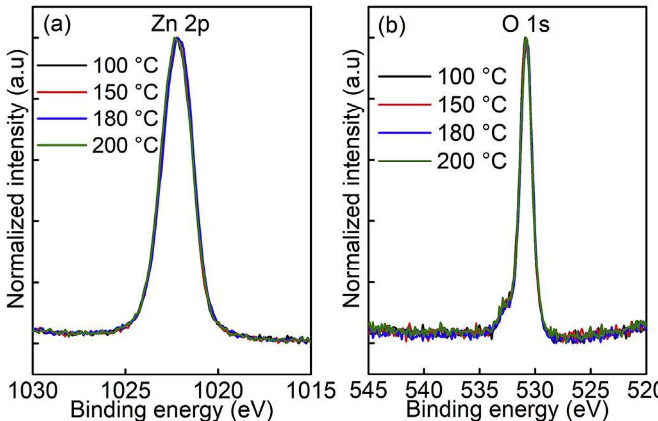

Fig. 15. XPS spectra for ZnO thin films synthesized at different substrate temperatures: (a) Zn $2p_{3/2}$ band, (b) O 1s band. The XPS spectra were acquired after Ar + sputter cleaning. The XPS spectra for ZnO thin films synthesized at different substrate temperatures: (a) Zn $2p_{3/2}$ band, (b) O 1s band.

electron trapped in oxygen species causes a depletion layer, leading to an increase in resistivity [48,57]. Depending on working temperatures, adsorbed oxygen can appear in the form of molecular O_2^- and/or atomic (O^-, O^{2-}) ions. In general, this is controlled by the working temperature: below 150 °C, the molecular form dominates while atomic ions dominate above 150 °C. In our case, with ZnO thin films grown at 180 °C, the presence of atomic ions would dominate.

In addition, the visible region of the photoluminescence spectra illustrated the presence of deep-level emission (DLE) defects against the ALD process parameters: the presence of the O_2 pulses in the sequence and the sample temperature during growth. These DLE defects come from impurities or defects with high ionization energy located deep in the band gap. It is accepted that these deep levels are mainly due to intrinsic defects, impurities and/or a combination of both. Although their nature remains uncertain with often contradictory explanations, there are three main commonly accepted emission regions [60–62]:

(i) The green domain (G1) is located in a wavelength range of ~480–550 nm (~2.58–2.25 eV). This emission has been associated with gaps in oxygen vacancies simply ionized (V_O°), or oxygen antisites, or even zinc vacancies (V_{Zn}°).
(ii) The yellow-orange emission (G2) has wavelengths of ~550–610 nm (~2.25–2.03 eV). This corresponds to the gaps of oxygen vacancies doubly ionized (VO°), and interstitial oxygen (Oi).
(iii) The red emission (G3) of ~610–755 nm (~2.03–1.64 eV) has been attributed to excess oxygen on the ZnO surface.

As a result, it can be observed that the ALD processed at 180 °C with 1 s of oxygen gas pulsing has a larger intensity ratio of NBE to DLE emission peaks (I_{NBE}/I_{DLE}) (Table 1) with a defect presence comparable to the reference ZnO single crystal. It can also be noted that the PL spectra (Fig. 8) in the visible region (2.0–2.5 eV) shows a similar trend in electrical resistivity (Fig. 6) to ZnO thin films grown at 180 °C and with 1–5 s of oxygen pulse time. The 1s pulse sample presents the highest resistivity and the lowest relative visible photoluminescence emissions compared to the other pulse duration samples. The XPS analysis performed on the samples rules out the hypothesis of the presence of a significant amount of impurities (Fig. S11, Supporting Information). As a general tendency, the presence of O_2 during the processes allowed the intensity ratio of the NBE to DLE emission peak to be increased probably by reducing the oxygen vacancy defects. This opens an interesting perspective to improve the UV light emission efficiency of ZnO in LED devices, with the possibility of simultaneously modulating the electrical resistivity of the material.

The dependence of electrical properties on the surface morphology has been discussed previously in several works [27,48,49]. A higher carrier concentration was found in the polar-plane (002)-texture films, whereas a lower carrier concentration was displayed in the non-polar (100), (101)-texture films. Furthermore, the higher carrier concentration was in concomitant with the higher defect density or lower stoichiometry of the ZnO films. It is consistent with our observation, even though the polar-plane (002) films grown with oxygen shown higher resistivity in contrast to the ZnO films grown without oxygen. On the other hand, a too large amount of oxygen during the ALD process with pulsing times of 3 s and 5 s induced a decrease in resistivity (see Fig. 6), but with a similar optical band gap as for 1 s of oxygen pulse grown samples. The corresponding PL spectra (Fig. 8) showed an increase of the yellow-orange emission (G2), which is a possible signature of interstitial oxygen. The picture is different in the most resistive ZnO films grown with oxygen at 100 °C, which show random crystallographic orientations, but the chemical composition was found to be the most stoichiometric in comparison to other films.

Moreover, TEM analysis in cross-section and diffraction patterns illustrates the similar growth profiles of ZnO films (rough polycrystalline with grains widening and regular (002) texture with columnar grains, with and without the presence of the oxygen gas pulsing respectively) on either a metallic (nickel) or an insulating (AlN) bottom seed layers. This implies that the buffer layers have no significant impact on the ZnO thin film structuring during growth. In addition, the detailed cross section by TEM shows that the grains are actually interconnected at their bases.

A remarkable correlation between the chemical composition and the optical band gap is observed. The optical band gap increased when the O/Zn ratio increased in the ZnO films grown with oxygen gas. This can be understood as a filling of oxygen vacancies, annihilating the shadow donor levels [27,59,63]. Interestingly, we noticed an evolution of the strain to band gap energy as observed by T. Singh et al. [64] with an increase of the band gap level against an increase of the tensile strain in the ZnO thin film (Fig. S13, Supporting Information). The authors correlated the ZnO film thickness with the induced inner strain. Table 1 relates the net out-of-plane strain calculated from changes of the c lattice parameter. According to the strain-to-thickness relationship measured by T. Singh et al. [64], in Table 1 we indicated the relative change of the strain in absolute value due to the modulation of the thicknesses being lower than that calculated from the c lattice parameter change measured by GIXRD. This indicates a substantial contribution of the crystalline orientation and/or chemical composition and relative impurities and defects of the film compared to the thickness parameter on the induced strain relative to the different ALD processes.

4.2. Growth mechanisms of (002) preferred orientation

Control of the preferred orientation of ZnO thin films has been investigated here with two varying thermodynamic parameters during the growth. Among deposition parameters such as the pulsing time of precursors [65] and the substrate temperature, the temperature during deposition was the most commonly used, as it enables the crystallographic orientation of the ZnO film to be controlled in a very efficient way [27,28]. Three zones were identified based on the predominance of (100) and (002) orientations: zone 1 (135–155 °C) where the films are dominated by (100) and (002)-oriented crystallites; zone 2 (155–220 °C) with a dominant (100) orientation and finally zone 3 at higher temperatures (220–300 °C) where the (002) orientation dominates. This suppression of the (002) crystallographic orientation in the temperature range of 155–220 °C has been discussed in previous works [27,28]. It could be better understood by considering stacking sequences of the ZnO (002) polar-plane, which can be seen as Zn/O/Zn/O … stacking sequences of the hexagonal type AbBaA … along its polar c-axis [66]. As a result, the (002) polar surface could be negatively or positively charged, corresponding to oxygen ion terminated ZnO (000$\overline{1}$)-O or zinc ion terminated ZnO (0001)-Zn. In the temperature range of 150–300 °C, it has been demonstrated that the premature dissociation of DEZ precursors may occur [67–69]. The dissociated ethyl groups can be cleaved further into ethyl and methyl group fragments, such as CH_3CH_2 and CH_3 in the temperature range of 150–220 °C [28]. These anions can bond to the positively charged ZnO (0001)-Zn polar surface, which prevents growth along the polar c-axis direction. Our ZnO thin films, grown without using oxygen gas during ALD processes, follows this abovementioned argument. In fact, the films show a crystallographic contribution of the nonpolar-plane (100), (101) and polar-plane (002) orientations. However, this was no longer the case for the ZnO thin films processed in an oxygen-rich environment, where the (002) polar-plane orientation became a preferred orientation. It can be interpreted by a picture of cleave/combustion processes during ALD growth. M. A. Thomas et al. [30] pointed out that energetic O radicals from oxygen plasma cleave/combust the ligands CH_3CH_2 and CH_3, which are bonded to Zn and subsequently oxidize Zn. In our situation, when absorbing molecular oxygen on the polar surface, the charges from the ZnO surface transferred to the antibonding π^* orbitals of oxygen, transforming it into a peroxo radical (O_2^{-2}) [58]. This can act as a reactive oxidant and homolytic fission agent. Therefore, the surface in an oxygen-rich environment can be cleaned up by further removing the ligands of ethyl groups. Consequently, the (002)-oriented growth direction will be no longer suppressed, but will keep growing and dominating with its lowest surface energy for the fastest growth rate [25].

The growth mechanism of (002) the polar-plane orientation could also be pinpointed by reviewing a stabilization aspect of the polar surface, which has received significant considerations in the last few decades [70–73]. Generally, the most crucial point of the growing (002) texture is to control the formation of tetrahedral coordination sp^3 in the vapor phase and at the substrate surface in order to change the equilibrium state of the deposition [25]. Fujimura et al. [25] demonstrated that a suitable sputtering gas condition with the ratio $Ar:O_2 = 4:1$ promoted the tetrahedral coordination in the vapor phase. The suitable gas condition could be related to the polar surface stabilization. In fact, on the polar surface of sp^3 hybridized tetrahedral coordination, the fulfilment of electron counting has to satisfy a local charge-neutral surface and the vanishment of the macroscopic dipole, by electrostatically stabilizing the surface [73–75]. Several possible methods for this have been proposed, i.e. the formation of 0.25 ml (monolayer) of zinc vacancies; adsorption of 0.25 ml O_2 or combinations thereof for the case of ZnO (0001)-Zn polar surface. Correspondingly, the ZnO (000$\overline{1}$)-O polar termination can be electrostatically stabilized through oxygen deficiency. P. Gorai et al. revealed that theoretically, the lowest adsorption enthalpies were found on the ZnO (0001)–Zn polar surface reconstruction that were formed under O-rich and H-poor environments and stabilized by adsorbing O species [58]. By contrast, ZnO (000$\overline{1}$)–O surfaces were found to be stabilized by involving adsorbed H under O-rich conditions. In our studies, the preferred (002) oriented films were synthesized in an oxygen-rich environment. Therefore, the ZnO (0001)–Zn polar surface

reconstruction could be the most stable surface by adsorbing oxygen adatoms and/or oxygen molecules; this was confirmed by the appearance of the secondary oxygen peak in XPS spectra. In the same time, the (002) surface possesses the lowest surface energies (0.099 eV/Å^2) in comparison to (100) and (101) surfaces, which are 0.123 and 0.209 eV/Å^2, respectively. As a result, the (002)-oriented ZnO film keeps growing in the preferable way.

5. Conclusion

In summary, the crystallographic, morphological, electrical, optical, and electronic properties have been explored and evaluated for zinc oxide thin films elaborated by thermal atomic layer deposition in the presence of O_2 pulses in the process. It has been demonstrated that using oxygen gas during atomic layer deposition could profoundly affect the properties of zinc oxide thin films. The crystalline structure can be highly tuned from nonpolar plane orientations to a polar plane orientation by inserting oxygen gas. The electrical resistivity of the films grown under O_2 conditions shown a dramatic increase of 3–4 orders of magnitude contrary to that of the film grown without oxygen gas. It could be interesting for improving the issue of current leakage for piezoelectric applications of thin film ZnO as actuators or strain sensors. On the other hand, the electrical properties and optical properties strongly correlated to the electronic properties and chemical composition of zinc oxide thin film. Indeed, the highest resistivity and the largest band gap were found on the zinc oxide deposited with oxygen gas at the substrate temperature of 100 °C, due to it having the lowest oxygen deficiency in comparison with other samples. The intensity ratio of the near band edge emission to the deep-level emission peak, with the deep-level emission caused by defects located deep in the band gap, can be increased by applying an adequate pulsing of oxygen gas during the process. This would have a positive impact on the UV light emission efficiency of ZnO devices such as LED. Also, several hypotheses were discussed in order to understand the dominance of (002) orientation in the presence of oxygen during atomic layer deposition; (i) homolytic fission of residual organic ligands by peroxo radical (O_2^{-2}), (ii) reconstruction and stabilization of the polar surfaces. It could be possible that both mechanisms contribute simultaneously to the growth of a film with a (002) preferred orientation. This theory should be tested by means of a theoretical calculation or molecular dynamic simulation in order to have a complete picture of growth mechanism. However, our study provides reliable methods to tailor the preferred orientations and the optical and electrical properties of the zinc oxide thin films in a simple and inexpensive way that is compatible with the semiconductor industry in order to provide a possible benefit to related applications.

Data availability

The raw/processed data required to reproduce these findings cannot be shared at this time due to technical or time limitations.

Authorship contribution statement

The manuscript was written with contributions from all authors. All authors have given their approval to the final version of the manuscript.

Declaration of competing interest

The authors declare that there are no competing interests.

The authors declare that they have no known competing financial interests or personal relationships that could have appeared to influence the work reported in this paper.

Credit authorship contribution statement

Tai Nguyen: Methodology, experiments (ALD processes, characterizations), manuscript writing - original draft. **Noureddine Adjeroud**: Methodology, experiments (ALD processes). **Mael Guennou**: Photoluminescence analysis and data interpretation, review & editing. **Jérôme Guillot**: XPS analysis and data interpretation, review & editing. **Yves Fleming**: XRD and pole figure analysis and data interpretation, review & editing. **Anne-Marie Papon**: TEM cross section and diffraction analysis and data interpretation, review & editing. **Didier Arl**: SEM analysis and data interpretation, review & editing. **Kevin Menguelti**: experiments (ALD processes, samples preparation). **Raoul Joly**: experiments (ALD processes), review & editing. **Narciso Gambacorti**: TEM data interpretation. **Jérôme Polesel Maris**: Project manager, supervisor, ALD experiments, data analysis, funding acquisition, manuscript writing, review & editing.

Declaration of competing interest

The authors declare that there are no competing interests.

The authors declare that they have no known competing financial interests or personal relationships that could have appeared to influence the work reported in this paper.

Acknowledgements

The authors acknowledge Dr. Petru Lunca Popa for support on optical spectra measurements, Dr. Inmaculada Peral Alonso for facilitating the NFFA collaboration, and Dr. Naoufal Bahlawane for fruitful discussions and advice. The authors gratefully acknowledge the financial assistance provided by the FNR in the framework of the FNR CORE project PSSENS (Project ref.: PSSENS C16/MS/11349047) and the FNR PRIDE MASSENA 15/10935404/MASSENA for funding. The authors acknowledge the contribution of the Nanoscience Foundries and Fine Analysis (NFFA) European Research Infrastructure. In fact, this project has received funding from the EU-H2020 research and innovation program under grant agreement No 654360, and benefitted from the access provided by Laboratoire d'électronique des technologies de l'information (CEA-LETI) in Grenoble.

Appendix A. Supplementary data

Supplementary data to this article can be found online at https://doi.org/10.1016/j.rinma.2020.100088.

References

[1] Ü. Özgür, Y.I. Alivov, C. Liu, A. Teke, M.A. Reshchikov, S. Doğan, V. Avrutin, S.J. Cho, H. Morkọ, A comprehensive review of ZnO materials and devices, J. Appl. Phys. 98 (2005), 041301, https://doi.org/10.1063/1.1992666.

[2] B.J. Jin, S.H. Bae, S.Y. Lee, S. Im, Effects of native defects on optical and electrical properties of ZnO prepared by pulsed laser deposition, Mater. Sci. Eng. B Solid-State Mater. Adv. Technol. 71 (2000) 301–305, https://doi.org/10.1016/S0921-5107(99)00395-5.

[3] R.F. Service, Will UV lasers beat the blues? Science 276 (1997) https://doi.org/10.1126/science.276.5314.895, 895-895.

[4] Y. Yuan, K. Shyong Chow, H. Du, P. Wang, M. Zhang, S. Yu, B. Liu, A ZnO thin-film driven microcantilever for nanoscale actuation and sensing, Int. J. Smart Nano Mater. 4 (2013) 128–141, https://doi.org/10.1080/19475411.2012.749959.

[5] Y.S. Choi, J.W. Kang, D.K. Hwang, S.J. Park, Recent advances in ZnO-based light-emitting diodes, IEEE Trans. Electron. Dev. 57 (2010) 26–41, https://doi.org/10.1109/TED.2009.2033769.

[6] P.K. Nayak, J. Yang, J. Kim, S. Chung, J. Jeong, C. Lee, Y. Hong, Spin-coated Ga-doped ZnO transparent conducting thin films for organic light-emitting diodes, J. Phys. D Appl. Phys. 42 (2009), 035102, https://doi.org/10.1088/0022-3727/42/3/035102.

[7] R.S. Mane, W.J. Lee, H.M. Pathan, S.H. Han, Nanocrystalline TiO_2/ZnO thin films: fabrication and application to dye-sensitized solar cells, J. Phys. Chem. B 109 (2005) 24254–24259, https://doi.org/10.1021/jp0531560.

[8] T. Van Dang, N. Duc Hoa, N. Van Duy, N. Van Hieu, Chlorine gas sensing performance of on-chip grown ZnO, WO_3, and SnO_2 nanowire sensors, ACS Appl. Mater. Interfaces 8 (2016) 4828–4837, https://doi.org/10.1021/acsami.5b08638.

[9] N.D. Khoang, D.D. Trung, N. Van Duy, N.D. Hoa, N. Van Hieu, Design of SnO_2/ZnO hierarchical nanostructures for enhanced ethanol gas-sensing performance, Sensor.

Actuator. B Chem. 174 (2012) 594–601, https://doi.org/10.1016/j.snb.2012.07.118.
[10] L. Le Brizoual, F. Sarry, O. Elmazria, P. Alnot, S. Ballandras, T. Pastureaud, GHz frequency ZnO/Si SAW device, IEEE Trans. Ultrason. Ferroelectrics Freq. Contr. 55 (2008) 442–450, https://doi.org/10.1109/TUFFC.2008.662.
[11] Z.L. Wang, X. Wang, J. Song, J. Liu, Y. Gao, Piezoelectric nanogenerators for self-powered nanodevices, IEEE Pervasive Comput 7 (2008) 49–55, https://doi.org/10.1109/MPRV.2008.14.
[12] Z.L. Wang, J. Song, Piezoelectric nanogenerators based on zinc oxide nanowire arrays, Science 312 (2006) 242–246, https://doi.org/10.1126/science.1124005.
[13] J. Briscoe, S. Dunn, Piezoelectric nanogenerators - a review of nanostructured piezoelectric energy harvesters, Nanomater. Energy 14 (2014) 15–29, https://doi.org/10.1016/j.nanoen.2014.11.059.
[14] R. Hinchet, S. Lee, G. Ardila, L. Montès, M. Mouis, Z.L. Wang, Performance optimization of vertical nanowire-based piezoelectric nanogenerators, Adv. Funct. Mater. 24 (2014) 971–977, https://doi.org/10.1002/adfm.201302157.
[15] Y. Liu, Y. Li, H. Zeng, ZnO-based transparent conductive thin films: doping, performance, and processing, J. Nanomater. 2013 (2013) 196521, https://doi.org/10.1155/2013/196521.
[16] T. Wang, H. Wu, H. Zheng, J.B. Wang, Z. Wang, C. Chen, Y. Xu, C. Liu, Nonpolar light emitting diodes of m-plane ZnO on c-plane GaN with the Al_2O_3 interlayer, Appl. Phys. Lett. 102 (2013) 141912, https://doi.org/10.1063/1.4801761.
[17] K.J. Loh, D. Chang, Zinc oxide nanoparticle-polymeric thin films for dynamic strain sensing, J. Mater. Sci. 46 (2011) 228–237, https://doi.org/10.1007/s10853-010-4940-3.
[18] W. Wu, Z.L. Wang, Piezotronics and piezo-phototronics for adaptive electronics and optoelectronics, Nat. Rev. Mater. 1 (2016) 16031, https://doi.org/10.1038/natrevmats.2016.31.
[19] Z.L. Wang, Piezopotential gated nanowire devices: piezotronics and piezo-phototronics, Nano Today 5 (2010) 540–555, https://doi.org/10.1016/j.nantod.2010.10.008.
[20] Z.L. Wang, W. Wu, Piezotronics and piezo-phototronics: fundamentals and applications, Natl. Sci. Rev. 1 (2014) 62–90, https://doi.org/10.1093/nsr/nwt002.
[21] Z.L. Wang, Progress in piezotronics and piezo-phototronics, Adv. Mater. 24 (2012) 4632–4646, https://doi.org/10.1016/j.scitotenv.2007.05.034.
[22] Z.L. Wang, X. Wang, Nanogenerators and piezotronics, Nanomater. Energy 14 (2015) 1–2, https://doi.org/10.1016/j.nanoen.2015.01.011.
[23] P. Wang, H. Du, ZnO thin film piezoelectric MEMS vibration energy harvesters with two piezoelectric elements for higher output performance, Rev. Sci. Instrum. 86 (2015), 075002, https://doi.org/10.1063/1.4923456.
[24] M. Miura, Crystallographic character of ZnO thin film formed at low sputtering gas pressure, Jpn. J. Appl. Phys. 21 (1982) 264–272, https://doi.org/10.1143/JJAP.21.264.
[25] N. Fujimura, T. Nishihara, S. Goto, J. Xu, T. Ito, Control of preferred orientation for ZnOx films: control of self-texture, J. Cryst. Growth 130 (1993) 269–279, https://doi.org/10.1016/0022-0248(93)90861-P.
[26] F.K. Shan, B.C. Shin, S.W. Jang, Y.S. Yu, Substrate effects of ZnO thin films prepared by PLD technique, J. Eur. Ceram. Soc. 24 (2004) 1015–1018, https://doi.org/10.1016/S0955-2219(03)00397-2.
[27] C.H. Chao, P.W. Chi, D.H. Wei, Investigations on the crystallographic orientation induced surface morphology evolution of ZnO thin films and their wettability and conductivity, J. Phys. Chem. C 120 (2016) 8210–8219, https://doi.org/10.1021/acs.jpcc.6b01573.
[28] S.Y. Pung, K.L. Choy, X. Hou, C. Shan, Preferential growth of ZnO thin films by the atomic layer deposition technique, Nanotechnology 19 (2008) 435609, https://doi.org/10.1088/0957-4484/19/43/435609.
[29] T.A. Krajewski, K. Dybko, G. Luka, E. Guziewicz, P. Nowakowski, B.S. Witkowski, R. Jakiela, L. Wachnicki, A. Kaminska, A. Suchocki, M. Godlewski, Dominant shallow donors in zinc oxide layers obtained by low-temperature atomic layer deposition: electrical and optical investigations, Acta Mater. 65 (2014) 69–75, https://doi.org/10.1016/j.actamat.2013.11.054.
[30] M.A. Thomas, J.B. Cui, Highly tunable electrical properties in undoped ZnO grown by plasma enhanced thermal-atomic layer deposition, ACS Appl. Mater. Interfaces 4 (2012) 3122–3128, https://doi.org/10.1021/am300458q.
[31] R. Huang, S. Ye, K. Sun, K.S. Kiang, C.H.K. de Groot, Fermi level tuning of ZnO films through supercycled atomic layer deposition, Nanoscale Res. Lett. 12 (2017) 541, https://doi.org/10.1186/s11671-017-2308-1.
[32] S.H.K. Park, Y.E. Lee, Controlling preferred orientation of ZnO thin films by atomic layer deposition, J. Mater. Sci. 39 (2004) 2195–2197, https://doi.org/10.1023/B:JMSC.0000017786.81842.ae.
[33] F. Bachmann, R. Hielscher, H. Schaeben, Texture analysis with MTEX – free and open source software toolbox, Solid State Phenom. 160 (2010) 63–68, 10.4028/www.scientific .net/ssp.160.63.
[34] G.B. Harris, X., Quantitative measurement of preferred orientation in rolled uranium bars, London, Edinburgh, Dublin Philos. Mag. J. Sci. 43 (1952) 113–123, https://doi.org/10.1080/14786440108520972.
[35] H.R. Moutinho, F.S. Hasoon, F. Abulfotuh, L.L. Kazmerski, Investigation of polycrystalline CdTe thin films deposited by physical vapor deposition, close-spaced sublimation, and sputtering, J. Vac. Sci. Technol. A Vacuum, Surfaces, Film. 13 (1995) 2877, https://doi.org/10.1116/1.579607.
[36] R. Hielscher, H. Schaeben, D. Chateigner, On the entropy to texture index relationship in quantitative texture analysis, J. Appl. Crystallogr. 40 (2007) 371–375, https://doi.org/10.1107/S0021889806055476.
[37] M. Saleem, L. Fang, A. Wakeel, M. Rashad, C.Y. Kong, Simple preparation and characterization of nano-crystalline zinc oxide thin films by sol-gel method on glass substrate, World J. Condens. Matter Phys. 2 (2012) 10–15, https://doi.org/10.4236/wjcmp.2012.21002.
[38] A. Ismail, M.J. Abdullah, The structural and optical properties of ZnO thin films prepared at different RF sputtering power, J. King Saud Univ. Sci. 25 (2013) 209–215, https://doi.org/10.1016/j.jksus.2012.12.004.
[39] Z.-Y. Ye, H.-L. Lu, Y. Geng, Y.-Z. Gu, Z.-Y. Xie, Y. Zhang, Q.-Q. Sun, S.-J. Ding, D.W. Zhang, Structural, electrical, and optical properties of Ti-doped ZnO films fabricated by atomic layer deposition, Nanoscale Res. Lett. 8 (2013) 108, https://doi.org/10.1186/1556-276X-8-108.
[40] R. Haarindraprasad, U. Hashim, S.C.B. Gopinath, M. Kashif, P. Veeradasan, S.R. Balakrishnan, K.L. Foo, P. Poopalan, Y.K. Mishra, Low temperature annealed zinc oxide nanostructured thin film-based transducers: characterization for sensing applications, PloS One (2015), https://doi.org/10.1371/journal.pone.0132755.
[41] A.F. Abdulrahman, S.M. Ahmed, M.A. Almessiere, Effect of the growth time on the optical properties of ZnO nanorods grown by low temperature method, Dig. J. Nanomater. Biostructures. 12 (2017) 1001–1009.
[42] B.D. Viezbicke, S. Patel, B.E. Davis, D.P. Birnie, Evaluation of the Tauc method for optical absorption edge determination: ZnO thin films as a model system, Phys. Status Solidi Basic Res. 252 (2015) 1700–1710, https://doi.org/10.1002/pssb.201552007.
[43] O. Lupan, T. Pauporté, L. Chow, B. Viana, F. Pellé, L.K. Ono, B. Roldan Cuenya, H. Heinrich, Effects of annealing on properties of ZnO thin films prepared by electrochemical deposition in chloride medium, Appl. Surf. Sci. 256 (2010) 1895–1907, https://doi.org/10.1016/j.apsusc.2009.10.032.
[44] Y. Tak, D. Park, K. Yong, Characterization of ZnO nanorod arrays fabricated on Si wafers using a low-temperature synthesis method, J. Vac. Sci. Technol. B Microelectron. Nanom. Struct. 24 (2006) 2047–2883, https://doi.org/10.1116/1.2216714.
[45] S. Bang, S. Lee, J. Park, S. Park, Y. Ko, C. Choi, H. Chang, H. Park, H. Jeon, The effects of post-annealing on the performance of ZnO thin film transistors, Thin Solid Films 519 (2011) 8109–8113, https://doi.org/10.1016/J.TSF.2011.05.048.
[46] Y.J. Kim, H.J. Kim, Trapped oxygen in the grain boundaries of ZnO polycrystalline thin films prepared by plasma-enhanced chemical vapor deposition, Mater. Lett. 41 (1999) 159–163, https://doi.org/10.1016/S0167-577X(99)00124-X.
[47] E. Guziewicz, M. Godlewski, L. Wachnicki, T.A. Krajewski, G. Luka, S. Gieraltowska, R. Jakiela, A. Stonert, W. Lisowski, M. Krawczyk, J.W. Sobczak, A. Jablonski, ALD grown zinc oxide with controllable electrical properties, Semicond, Sci. Technol. 27 (2012), 074011, https://doi.org/10.1088/0268-1242/27/7/074011.
[48] Y.F. Sun, S.B. Liu, F.L. Meng, J.Y. Liu, Z. Jin, L.T. Kong, J.H. Liu, Metal oxide nanostructures and their gas sensing properties: a review, Sensors 41 (2012) 159–163, https://doi.org/10.3390/s120302610.
[49] K. Ellmer, Resistivity of polycrystalline zinc oxide films: current status and physical limit, J. Phys. D Appl. Phys. 34 (2001) 3097–3108, https://doi.org/10.1088/0022-3727/34/21/301.
[50] L. Fanni, B.A. Aebersold, D.T.L. Alexander, L. Ding, M. Morales Masis, S. Nicolay, C. Ballif, c-texture versus a-texture low pressure metalorganic chemical vapor deposition ZnO films: lower resistivity despite smaller grain size, Thin Solid Films 565 (2014) 1–6, https://doi.org/10.1016/J.TSF.2014.06.033.
[51] J. Steinhauser, S. Faÿ, N. Oliveira, E. Vallat-Sauvain, C. Ballif, Transition between grain boundary and intragrain scattering transport mechanisms in boron-doped zinc oxide thin films, Appl. Phys. Lett. 90 (2007) 142107, https://doi.org/10.1063/1.2719158.
[52] F. Werner, Hall measurements on low-mobility thin films, J. Appl. Phys. 122 (2017) 135306, https://doi.org/10.1063/1.4990470.
[53] T.S. Bjørheim, E. Kotomin, Ab initio thermodynamics of oxygen vacancies and zinc interstitials in ZnO, J. Phys. Chem. Lett. 5 (2014) 4238–4242, https://doi.org/10.1021/jz5018812.
[54] J.W. Orton, M.J. Powell, The hall effect in polycrystalline and powdered semiconductors, Rep. Prog. Phys. 43 (1980) 1263, https://doi.org/10.1088/0034-4885/43/11/001.
[55] F. Greuter, G. Blatter, Electrical properties of grain boundaries in polycrystalline compound semiconductors, Semicond. Sci. Technol. 5 (1990) 111–137, https://doi.org/10.1109/TNS.2004.832574.
[56] N. Barsan, U. Weimar, Conduction model of metal oxide gas sensors, J. Electroceram. 7 (2001) 143–167, https://doi.org/10.1023/A:1014405811371.
[57] A. Varpula, J. Sinkkonen, S. Novikov, Modelling of dc characteristics for granular semiconductors, Phys. Scr., T T141 (2010), 014003, https://doi.org/10.1088/0031-8949/2010/T141/014003.
[58] P. Gorai, E.G. Seebauer, E. Ertekin, Mechanism and energetics of O and O_2 adsorption on polar and non-polar ZnO surfaces, J. Chem. Phys. 144 (2016) 184708, https://doi.org/10.1063/1.4948939.
[59] W. Göpel, Reactions of oxygen with ZnO–10$\bar{1}$0-surfaces, J. Vac. Sci. Technol. 15 (2002) 1298–1310, https://doi.org/10.1116/1.569757.
[60] A.B. Djurišić, Y.H. Leung, K.H. Tam, Y.F. Hsu, L. Ding, W.K. Ge, Y.C. Zhong, K.S. Wong, W.K. Chan, H.L. Tam, K.W. Cheah, W.M. Kwok, D.L. Phillips, Defect emissions in ZnO nanostructures, Nanotechnology 18 (2007), 095702, https://doi.org/10.1088/0957-4484/18/9/095702.
[61] B. Panigrahy, M. Aslam, D.S. Misra, M. Ghosh, D. Bahadur, Defect-related emissions and magnetization properties of ZnO Nanorods, Adv. Funct. Mater. 20 (2010) 1161–1165, https://doi.org/10.1002/adfm.200902018.
[62] H. Morkoç, Ü. Özgür, Zinc Oxide: Fundamentals, Materials and Device Technology, 2009, https://doi.org/10.1002/9783527623945.
[63] B.J. Jin, S. Im, S.Y. Lee, Violet and UV luminescence emitted from ZnO thin films grown on sapphire by pulsed laser deposition, Thin Solid Films 366 (2000) 107–110, https://doi.org/10.1016/S0040-6090(00)00746-X.

[64] T. Singh, T. Lehnen, T. Leuning, D. Sahu, S. Mathur, Thickness dependence of optoelectronic properties in ALD grown ZnO thin films, Appl. Surf. Sci. 289 (2014) 27–32, https://doi.org/10.1016/j.apsusc.2013.10.071.
[65] I. Łukasiewicz, A. Wójcik-Godowska, E. Guziewicz, A. Wolska, T. Klepka, P. Dłuewski, R. Jakieła, E. Łusakowska, K. Kopalko, W. Paszkowicz, Wachnicki, S. Witkowski, W. Lisowski, M. Krawczyk, J.W. Sobczak, A. Jabłoński, M. Godlewski, ZnO, ZnMnO and ZnCoO films grown by atomic layer deposition, Semicond. Sci. Technol. 27 (2012), 074009, https://doi.org/10.1088/0268-1242/27/7/074009.
[66] P.X. Gao, Z.L. Wang, Substrate atomic-termination-induced anisotropic growth of ZnO nanowires/nanorods by the VLS process, J. Phys. Chem. B 108 (2004) 7534–7537, https://doi.org/10.1021/jp049657n.
[67] M.A. Rueter, J.M. Vohs, The surface reactions of ethyl groups on Si(100) formed via dissociation of adsorbed diethylzinc, Surf. Sci. 262 (1992) 42–50, https://doi.org/10.1016/0039-6028(92)90458-I.
[68] H. Dumont, A. Marbeuf, J.E. Bourée, O. Gorochov, Mass-spectrometric study of thermal decomposition of diethylzinc and diethyltellurium, J. Mater. Chem. 2 (1992) 923–930, https://doi.org/10.1039/JM9920200923.
[69] G. Fan, N. Maung, T.L. Ng, J.O. Williams, A.C. Wright, Homogeneous thermal decomposition of dimethylzinc in a metal-organic vapour phase epitaxy reactor, J. Chem. Soc. Faraday. Trans. 91 (1995) 3475–3479, https://doi.org/10.1039/FT9959103475.
[70] G. Kresse, O. Dulub, U. Diebold, Competing stabilization mechanism for the polar ZnO(0001)-Zn surface, Phys. Rev. B Condens. Matter 68 (2003) 1–15, https://doi.org/10.1103/PhysRevB.68.245409.
[71] B. Meyer, First-principles study of the polar O-terminated ZnO surface in thermodynamic equilibrium with oxygen and hydrogen, Phys. Rev. B Condens. Matter 69 (2004) 1–10, https://doi.org/10.1103/PhysRevB.69.045416.
[72] R. Wahl, J.V. Lauritsen, F. Besenbacher, G. Kresse, Stabilization mechanism for the polar ZnO(000$\bar{1}$)-O surface, Phys. Rev. B Condens. Matter 87 (2013) 1–12, https://doi.org/10.1103/PhysRevB.87.085313.
[73] O. Dulub, U. Diebold, G. Kresse, Novel stabilization mechanism on polar surfaces: ZnO(0001)-Zn, Phys. Rev. Lett. 90 (2003), 016102, https://doi.org/10.1103/PhysRevLett.90.016102.
[74] L. Bengtsson, Dipole correction for surface supercell calculations, Phys. Rev. B Condens. Matter 59 (1999) 12301, https://doi.org/10.1103/PhysRevB.59.12301.
[75] R.M. Martin, Comment on calculations of electric polarization in crystals, Phys. Rev. B 9 (1974) 1998, https://doi.org/10.1103/PhysRevB.9.1998.

SUPPORTING INFORMATION TO:

Controlling electrical and optical properties of zinc oxide thin films grown by thermal atomic layer deposition with oxygen gas

Lattice parameter calculation

The lattice parameters a and c of wurtzite hexagonal structure ZnO were calculated by using Bragg's law:

$$\lambda = 2d_{hkl}sin\theta \qquad (1)$$

where λ is the X-ray wavelength; and d_{hkl} is the spacing between planes with Miller indices h, k, and l.

For the hexagonal structure, the relationship between the spacing d_{hkl} and lattice parameters a and c is given below:

$$\frac{1}{d^2_{(hkl)}} = \frac{4}{3}\left(\frac{h^2 + hk + k^2}{a^2}\right) + \frac{l^2}{c^2} \qquad (2)$$

Then the lattice constants a and c were calculated by following equations (3) and (4), according to (100) and (002) diffraction planes:

$$a = \frac{\lambda}{\sqrt{3}\,sin\theta} \qquad (3)$$

and

$$c = \frac{\lambda}{sin\theta} \qquad (4)$$

Absorption coefficient calculation

The absorption coefficient α is calculated by the Beer-Lambert law[1]

$$\alpha = \frac{2.303 * A_f}{t} \qquad (5)$$

here t is the thickness of the film, and A_f is the absorbance of the film calculated by measuring the reflectance and transmittance spectra of the ZnO thin films on glasses and the reference glass and is deduced by following:

On glass:

$$T_g = 1 - A_g - R_g \qquad (6)$$

On glass + film:

$$T_{gf} = 1 - A_g - A_f - R_f \qquad (7)$$

Taking (6) – (7), we have:

$$A_f = (T_g - T_{gf}) - (R_f - R_g)$$

Here T, A, and R are transmittance, absorbance, and reflectance. The subscript g, f, and gf are denoted for glass, film and glass + film.

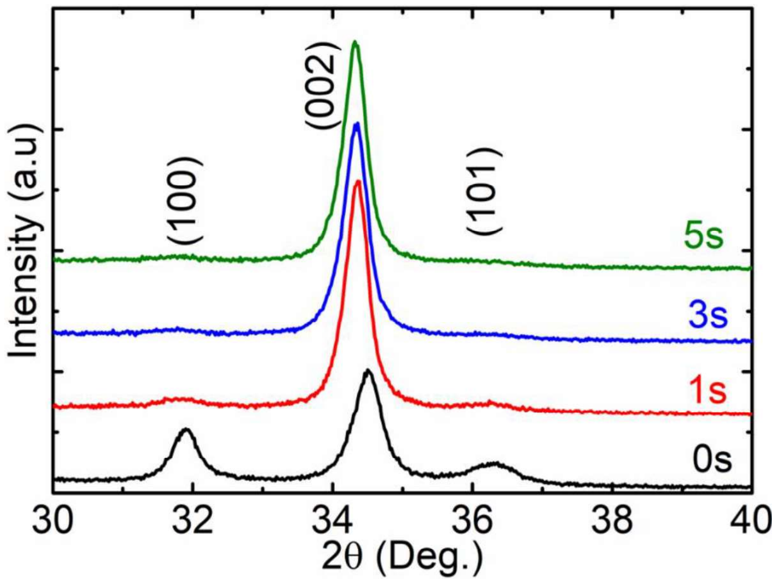

Figure S1: *Grazing incidence X-ray diffraction (ω=0.5°) of ZnO thin films samples with differences of oxygen gas pulsing time on glass samples.*

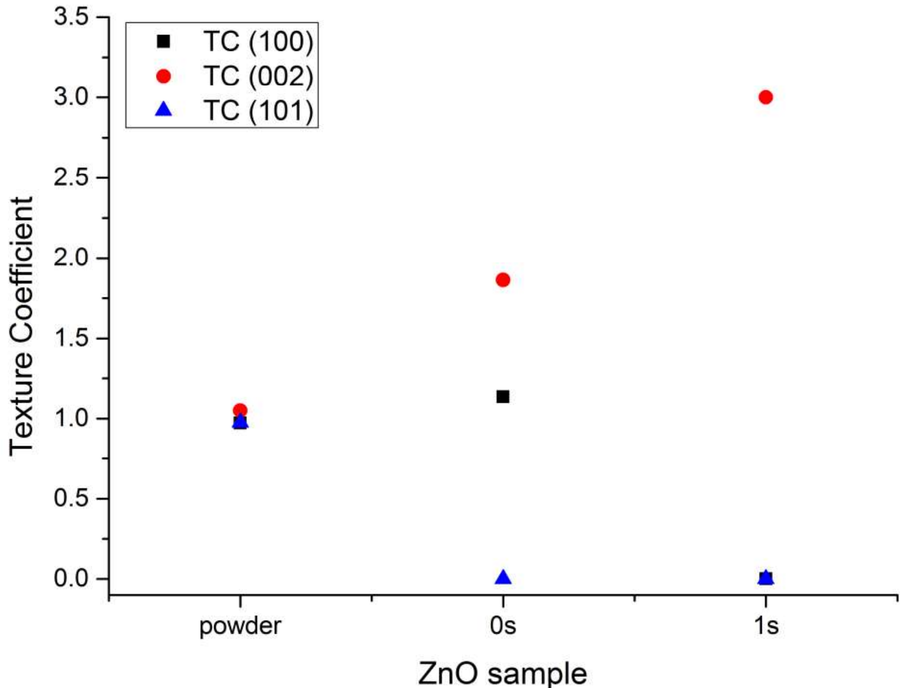

Figure S2: *Texture Coefficients measured in θ-2θ mode in accordance to Harris et al.[2] and Moutinho et al.[3]. For the calculation of TC, the (100), (002) and (101) Bragg reflections for the ZnO powder sample as well as the two ZnO thin film samples grown without oxygen (0 s) and grown in the presence of oxygen gas (1 s). As expected for an isotropic randomly oriented ZnO powder sample, the texture coefficients are very close to 1.*

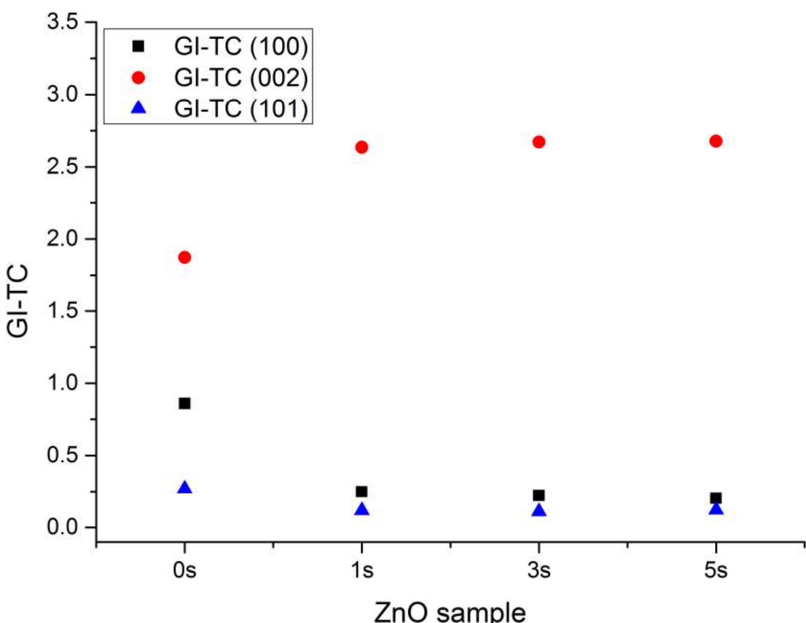

Figure S3: *GI-TC values measured on the ZnO thin film samples 0 s, 1 s, 3 s and 5s . It can be noticed that the GI-TC of (002) Bragg reflection for samples 1 s, 2 s and 3 s is almost 3. This means that these ZnO thin film samples have a strong (002) preferred orientation. Reference sample as well as ZnO thin film samples were measured in grazing incidence. The instrument configuration was the same for all samples.*

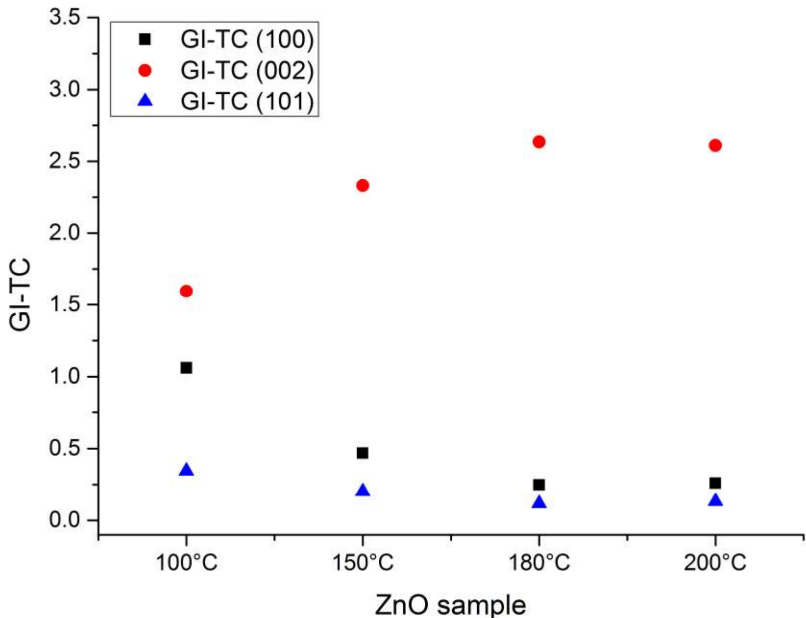

Figure S4: *GI-TC values measured on the ZnO thin film samples 100 °C, 150 °C, 180 °C and 200 °C. It can be noticed that the GI-TC of (002) Bragg reflection for samples 180 °C and 200 °C is almost 3. This means that these ZnO thin film samples have a strong (002) preferred orientation whereas samples 100 °C and 150 °C have some degree of preferred orientation. Reference sample as well as ZnO thin film samples were measured in grazing incidence. The instrument configuration was the same for all samples.*

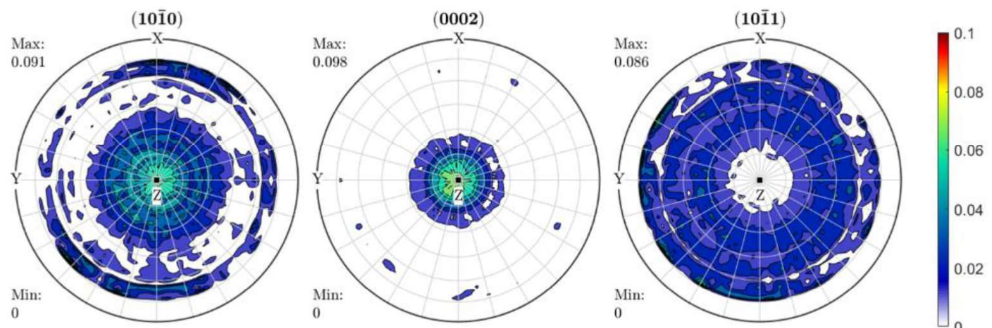

Figure S5: *Pole figures measured on ZnO thin film deposited at 180 °C without the presence of O_2 gas pulses (filled and non-filled contour plot respectively). In this figure, the depicted poles are denoted using the Bravais-Miller notation (h k i l) with h+k+i =0.*

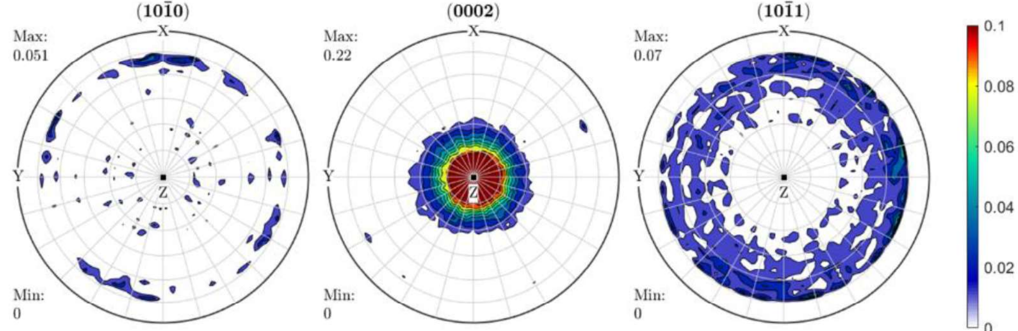

Figure S6: *Pole figures measured on ZnO thin film deposited at 180 °C with the presence of O_2 gas pulses (filled and non-filled contour plot respectively). In this figure, the depicted poles are denoted using the Bravais-Miller notation (h k i l) with h+k+i =0.*

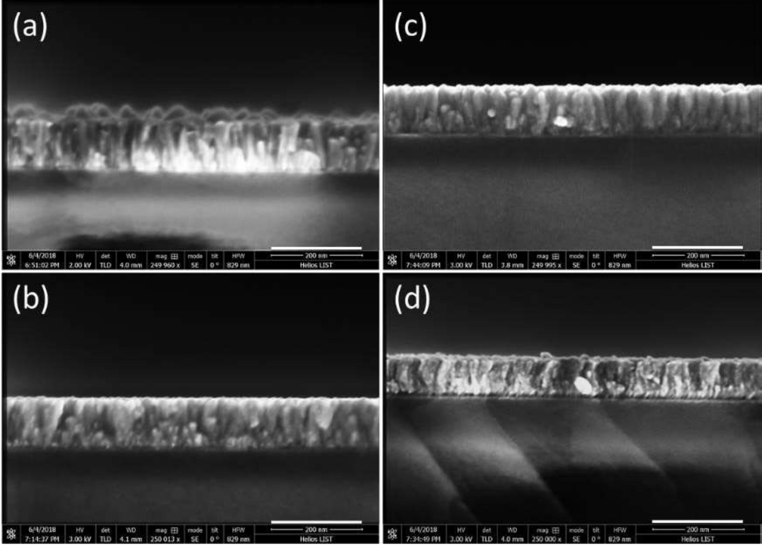

Figure S7: *SEM cross-sections of ZnO thin films with varying the O_2 pulsing time in the ALD sequence and the sample temperature such as: a) 0 s, 180 °C, b) 1 s, 180 °C, c) 1 s, 200 °C, and d) 1 s, 100 °C . The scale bar is 200 nm.*

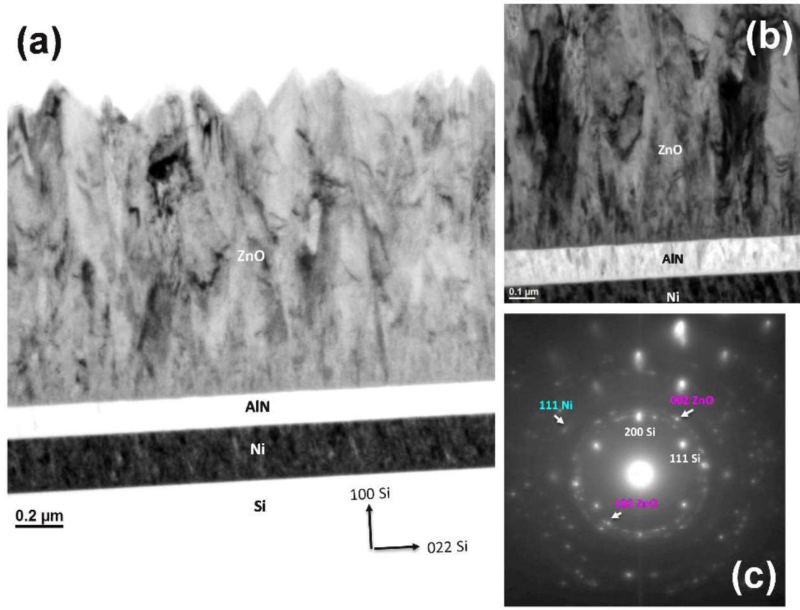

Figure S8: *Transmission Electron Microscopy (TEM) images of ZnO ALD growth during 5000 cycles at substrate temperature of 180 °C without the presence of O_2 gas pulsing. a) Cross section view detailing the stacks with AlN as a bottom layer. b) Detailed view of the bottom part of the ZnO film at the interface with the AlN film. c) Diffraction pattern obtained with 1300 nm selected area diaphragm.*

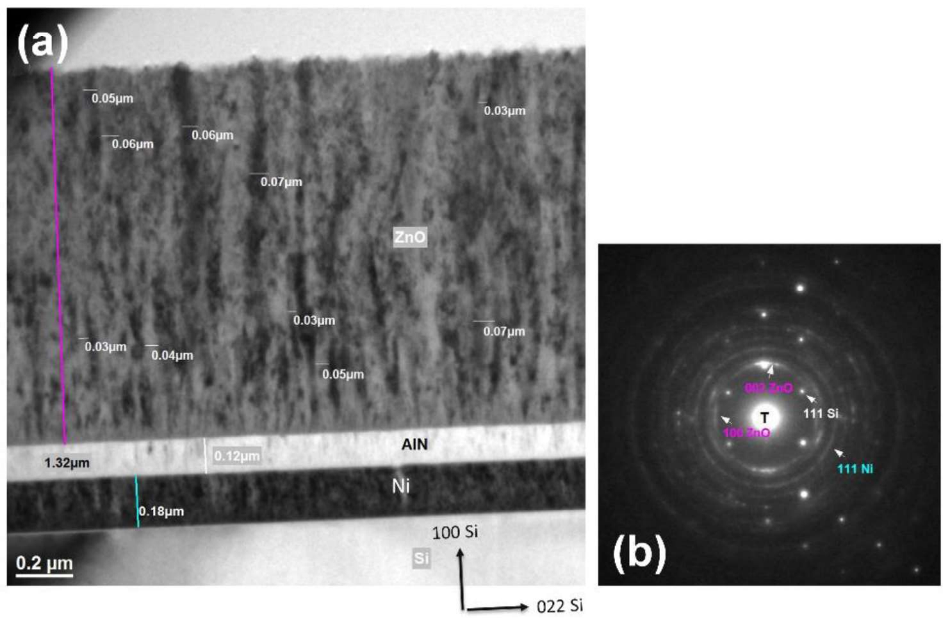

Figure S9: *Transmission Electron Microscopy (TEM) images of ZnO ALD growth during 5000 cycles at substrate temperature of 180 °C with the presence of O_2 gas pulsing in each cycle. a) Cross section view detailing the stacks with AlN as a bottom layer. b) Diffraction pattern obtained with 700 nm selected area diaphragm.*

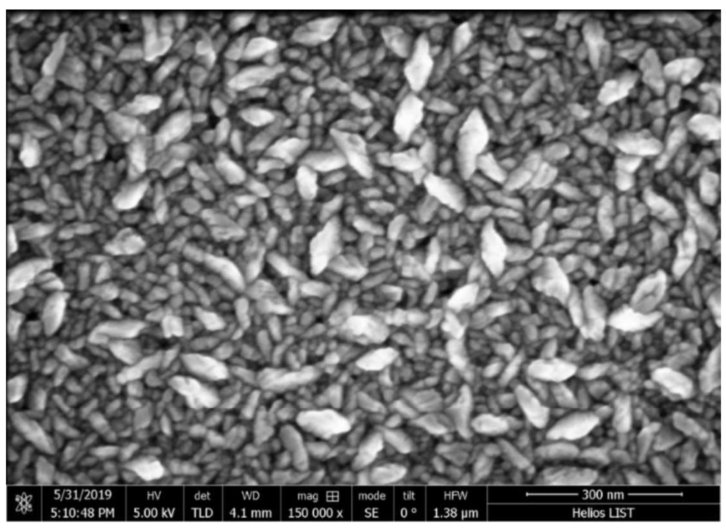

Figure S10: *SEM top view micrograph of ZnO thin film grown at 100 °C without O_2*

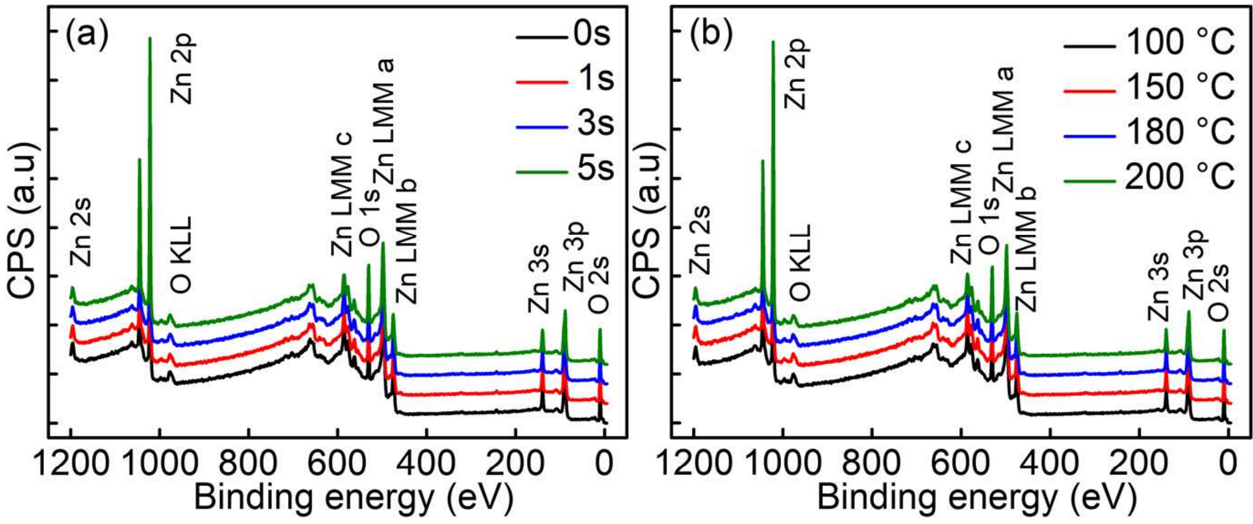

Figure S11: *XPS survey of ZnO thin films with (a) varying oxygen pulsing times, and (b) different substrate temperatures acquired after Ar^+ sputter cleaning. The XPS analysis performed on the samples oust the hypothesis of a significant impurities presence, the detection limit of this technique[4] being in the range of 0.5 at.% for elements such as C, N and Cl in a ZnO film .*

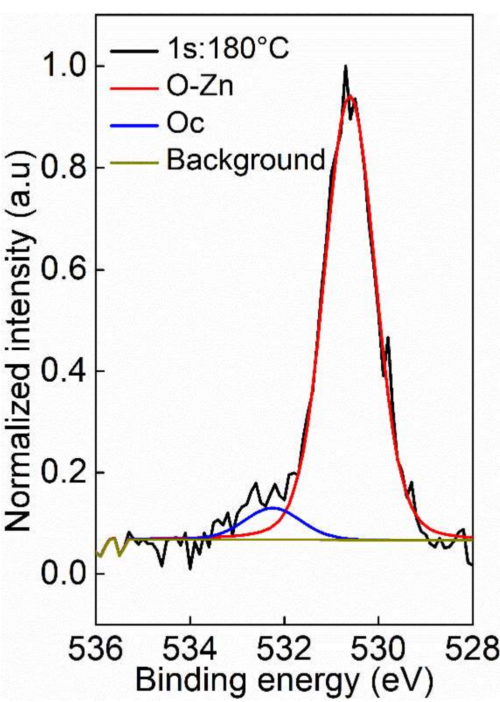

Figure S12: *Peak deconvolution of O 1s edge for the ZnO sample grown with 1s of oxygen gas at 180 °C. A main peak located at 530.60 eV and a secondary peak located at 532.25 eV are referred to O-Zn bond of Zn-OH and chemisorbed oxygen, respectively.*

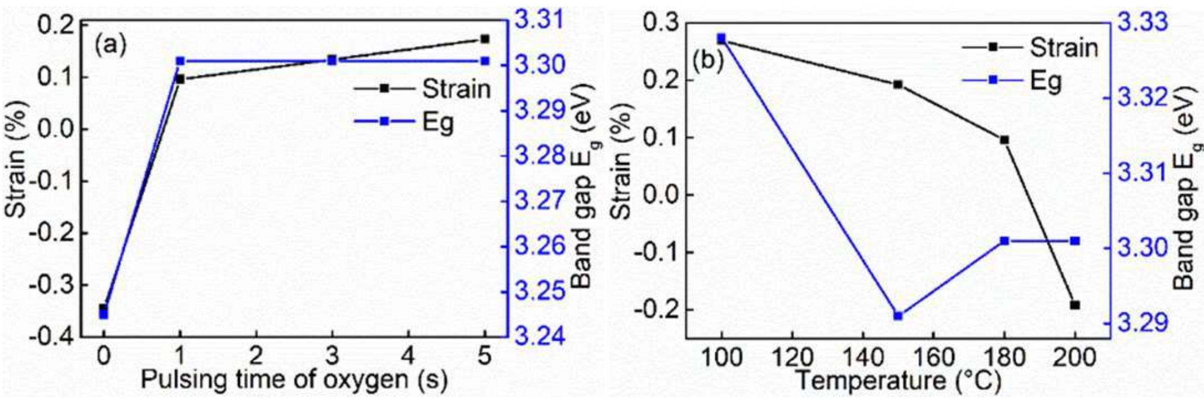

Figure S13: *Dependences of strain and optical band gap of ZnO thin films by varying (a) oxygen pulsing times, and (b) substrate temperatures.*

References

(1) Rakesh, K. S.; Rabhajeet, S. R.; Yadav, B. C.; TiO_2-PANI nanocomposite thin film prepared by spin coating technique working as room temperature CO_2 gas sensing, J Mater Sci: Mater Electron, 27 (2016) 11726-11732. doi:10.1007/s10854-016-5310-y

(2) Harris, G. B. X. Quantitative Measurement of Preferred Orientation in Rolled Uranium Bars. *London, Edinburgh, Dublin Philos. Mag. J. Sci.,* 43 (1952)113-123. doi:10.1080/14786440108520972

(3) Moutinho, H. R.; Hasoon, F. S.; Abulfotuh, F.; Kazmerski, L. L. Investigation of Polycrystalline CdTe Thin Films Deposited by Physical Vapor Deposition, Close-spaced Sublimation, and Sputtering. *J. Vac. Sci. Technol. A Vacuum, Surfaces, Film.,* 13 (1995)2877-2883. doi: 10.1116/1.579607

(4) Shard, A. G., Detection limits in XPS for more than 6000 binary systems using Al and Mg Kα X-rays, *Surf. Inter. Analysis*, 46 (2014) 175-185. doi:10.1002/sia.5406

4.2 Elucidating the growth mechanism of ZnO films by atomic layer deposition with oxygen gas via isotopic tracking

In previous section, we have reported profound effects of presence of gaseous oxygen during ALD process on ZnO film properties, particularly a preferential (002) orientation during growth and more insulating electrical properties as compared to the film grown by a standard process with a giant increasing of the electrical resistivity of 3 to 4 orders of magnitude. This result could pave the way to improve the piezoelectric response of this semiconducting material by decreasing the leakage current in our objective to get an optimized magnetoelectric transducer. Consequently, tentative measurements will be done at the end of this chapter to correlate the parameters of these new processes with O_2 with the piezoelectric coefficients of the thin films. Moreover, defects related to oxygen vacancies became minor as seen in photoluminescence spectroscopy. In this chapter, isotopic water $H_2{}^{18}O$ is used as ALD precursor instead of a standard deionized water with ^{18}O atom as a tracker to elucidate the growth mechanisms. By implementing quartz crystal microbalance (QCM) in situ ALD reactor chamber and using secondary ion mass spectrometry (SIMS), the presence of gaseous oxygen ^{16}O is identified and the reaction mechanism of the two processes are discussed.

This chapter is based on the publication: **Tai Nguyen**, et al., "*Elucidating the growth mechanism of ZnO films by Atomic Layer Deposition with Oxygen Gas via isotopic tracking*", accepted in RSC Journal of Materials Chemistry C.

Abstract:

The growth process of zinc oxide (ZnO) thin films by atomic layer deposition (ALD) accompanied by the presence of oxygen gas pulsing is investigated by means of the isotopic tracking of oxygen ^{18}O from the water precursor and oxygen ^{16}O from the gas. In a previous study [*T. Nguyen et al., DOI:10.1016/j.rinma.2020.100088*], by means of structural, electrical, and optical characterizations, we identified key growth parameters of this unusual ALD process. Unexpectedly, the influence of molecular oxygen on the crystallography, microstructure, and morphology of the hundred-nanometer- to micrometer-thick ZnO films was significant. In this study, we present an unprecedented methodology by combining isotopic tracers with mass spectrometry to elucidate the role of the two different sources of oxygen atoms during the evolution of the growth. Notably, the use of *in situ* quartz crystal microbalance (QCM) and Secondary Ion Mass Spectrometry (SIMS) reveals new insights into the reaction mechanism for ZnO thin film growth. On the one hand, the non-negative mass change during the ZnO growth without O_2 gas is attributed to the presence of bare zinc atoms on the surface due to the reaction between monoethyl zinc and hydroxyl groups of the water precursor after the diethyl zinc pulse. On the other hand, the detection of $Zn_xO_yC_2H_5^-$ ions by Time-of-Flight SIMS (TOF-SIMS) and the mass increase during the O_2 pulse suggest a new reaction mechanism for the ZnO thin film growth in the presence of gaseous O_2 where the ethyl ligand of the zinc precursor can react with O_2 to form ethylperoxy radicals. The formations of the ethylperoxy zinc and/or zinc atoms lead to more adsorption of water to form ethylhydroperoxide during the water pulse, inducing the positive mass change. The use of an isotopic substitution allowed us to unambiguously associate the mass gain with the gradual incorporation of gaseous oxygen throughout the growth process and thereby support the chemical reaction.

Keywords: oxygen isotopic tracing, ZnO thin films, thin film growth, *in situ* QCM, SIMS.

4.2.1. Introduction

A proper control over the crystallographic structure of ZnO thin films and their properties is needed for various applications, such as optoelectronics[1], solar-based devices[2], harvesters, sensors and actuators[3–7]. This control is usually achieved by varying the single crystal substrates[8–11] and the deposition temperature[12–15], however practical applications are limited due to requirements in the crystallographic structure of substrates, as well as elevated deposition temperatures. Park *et al.*[16], and our previous study[17] demonstrated that the crystallographic structure, the optical and the electronic properties of ZnO thin film were highly tuned by the introduction of gas pulsing of molecular oxygen during atomic layer deposition growth at quite low temperatures (100-200 °C) and even on glass substrates. The randomly oriented film structure was transformed into a highly preferred (002) orientation. Concomitantly, the ZnO thin films obtained were electrically more resistive (by 3 to 4 orders of magnitude) with a wider bandgap and a substantially weaker deep-level emission (DLE) in photoluminescence spectra, *i.e.* green, yellow-orange, and red emissions. However, there are still questions about the adsorption of oxygen inside the ZnO film or its desorption after each ALD cycle. In addition, the deposition of ZnO from diethylzinc (DEZ) and water precursors follows the net reaction:

$$Zn(C_2H_5)_2 + H_2O \rightarrow ZnO + 2C_2H_6 \qquad (1)$$

The following elementary reaction sequences are expected[18,19]:

$$\text{DEZ pulse: } Zn(C_2H_5)_2 + |\text{-}OH \rightarrow |\text{-}O\text{-}Zn\text{-}C_2H_5 + C_2H_6 \qquad (2a)$$

$$\text{Water pulse: } H_2O + |\text{-}O\text{-}Zn\text{-}C_2H_5 \rightarrow |\text{-}O\text{-}Zn\text{-}OH + C_2H_6 \qquad (3)$$

The monoethyl zinc (MEZ) may also react further with the hydroxyl groups on the surface to produce a bare zinc:

$$|\text{-}O\text{-}Zn\text{-}C_2H_5 + |\text{-}OH \rightarrow (|\text{-}O)_2\text{-}Zn + C_2H_6 \qquad (2b)$$

Where "|-" denotes the surface. The dominant end-product after the DEZ pulse is generally considered to be MEZ, therefore the reaction (2b) is usually omitted. This leads to the new question of whether, in the presence of gaseous oxygen during the ALD growth, the reaction mechanism will be similar to the reaction mechanism of the ZnO film grown with only DEZ and water.

Here, we address these issues using an innovative approach based on a combination of isotopic substitution during the film growth and secondary ion mass spectrometry (SIMS) to monitor the contribution of each source of oxygen atoms. We used ^{18}O-labelled water as a precursor in order to distinguish between the respective contributions of oxygen atoms from water precursor ($H_2{}^{18}O$) and from gaseous oxygen ($^{16}O_2$). *In situ* quartz crystal microbalance (QCM) was implemented to study the effect of oxygen presence on the ALD growth characteristics of ZnO thin films. In addition, time-of-flight SIMS (ToF-SIMS) was carried out to identify the resulting chemical composition of the ZnO thin films.

4.2.2. Experimental procedure

ZnO thin films were grown with a commercial ALD reactor (Beneq, TFS 200) in thermal configuration. Details of the ALD growth can be found in our previous report[17]. In the present work, ^{18}O-labeled deionized (DI) water (Sigma-Aldrich, Ref. ALDRICH: 329878, isotopic purity of 97 at.% ^{18}O) was used. The oxygen gas was delivered by a stand-alone bottle (Air Liquide,

alpha 2 O_2 global purity ≥ 99.9995% mol with less than 0.5 H_2O ppm.mol impurity) in the ALD reactor. The argon gas used for purging during the ALD process was ALPHAGAZ™ 2 with a global purity of ≥ 99.9999% mol with less than 0.5 H_2O ppm.mol impurity. The supporting surfaces for the ZnO thin film deposition were 2×2 cm^2 pieces of pristine single crystal Si(100) wafer (Siegert GmbH, Germany, grade Monitor) and glass slides (Thermo Scientific, Germany). Prior to the synthesis of ZnO thin films, the substrates were cleaned in acetone, isopropanol, conventional DI water and finally dehydrated on a hotplate for 20 minutes at 200 °C. Just before their introduction into the ALD reactor, an additional plasma cleaning (Plasma Therm 790 RIE, 120 W, 10 minutes, in Ar:O_2 gas environment at 30 mTorr) was performed on the substrates. ZnO thin films without oxygen gas were synthesized at a deposition temperature of 180 °C by the following sequence of four steps: Diethylzinc (DEZ) pulse (0.1 s), Ar purge (5 s), $H_2{}^{18}O$ pulse (0.1 s), and Ar purge (5 s). The ZnO thin films with the presence of oxygen gas were deposited at 180 °C by a sequence of six pulses; DEZ pulse (0.1 s), Ar purge (5 s), O_2 pulse (1 s), Ar purge (20 s), $H_2{}^{18}O$ pulse (0.1 s), and Ar purge (10 s). Both films were grown with 500 cycles corresponding to thicknesses of 96 and 120 nm for ZnO thin films synthesized with and without gaseous oxygen, respectively. *In situ* QCM (Q-Pod Quartz Monitor, IPN 074-547-P1B, INFICON Inc.) was implemented in the ALD reactor to track mass variations during the growth. The mass change is detected by measuring the change of the resonance frequency of the quartz sensor, as given by the equation below[20]:

$$\Delta m/S = -(\mu\rho)^{0.5}\Delta f/(2f_0^2) \quad (1)$$

where S is the quartz electrode area, ρ the density of quartz (2.648 g.cm^{-3}), μ the shear modulus (2.947 × 10^{11} g.s^{-2}.cm^{-1}) at room temperature, and f_0 the resonance frequency (5 MHz).

X-ray diffractometry (Diffractometer Bruker D8 Discover with Cu Kα radiation and a 5-axis Eulerian cradle) was conducted in θ–2θ configuration to examine the crystalline quality of the ZnO thin films on all samples. The microstructure of samples was studied by scanning electron microscopy (SEM) on a Helios Nanolab 650 FIB-SEM instrument (FEI Company, USA). A four-point probe (Ecopia HMS-3000) was performed to measure the resistivity of the thin film on glass substrates. Elemental composition and chemical states were investigated by X-ray photoelectron spectroscopy (XPS) (Axis Ultra DLD, Kratos Analytical Ltd.) over a surface area of 110×110 μm^2 using an x-ray source (Al K_α monochromated, E = 1486.6 eV) at a power of 150 W, and an energy resolution of 1.5 eV for survey scans and 0.55 eV for narrow scans determined on a silver sample. The spectra were calibrated in energy from the Zn 2p peak in ZnO at 1022.0 eV. The surface contamination was removed by etching an area of 3×3 mm^2 with an Ar^+ ion beam operating at 2 kV and 2 μA.

The transmittance and reflection spectra of ZnO thin films on glass slides were collected by UV-visible measurements (LAMBDA 1050 UV/Vis Spectrometer, PerkinElmer) in a 250–2000 nm range. Room-temperature photoluminescence (PL) spectra were acquired by a Renishaw inVia confocal microRaman spectrometer using an excitation wavelength of 325 nm produced by an 8 mW He-Cd laser focused through a Thorlabs UV objective with 40× magnification and a numerical aperture of 0.5. A 300 gr/mm grating enabled analysis in the 350–900 nm range. A single crystal ZnO (MTI Corporation) was used as a reference.

Dynamic-secondary ion mass spectrometry (D-SIMS) (CAMECA SC-Ultra) was used to analyze the elemental and isotopic composition of the films grown. First, depth profiles were acquired with a Cs^+ bombardment operating at 1 keV and a 6 nA primary ion beam scanned over an area of

500×500 µm^2. Secondary positive ions were detected as MCs^+ clusters (M is the element of interest) from a 60 µm area centered on the scanned area. Secondly, the oxygen isotopic signatures were determined with the M^- mode analysis over an area with a diameter of 8 µm. A mass resolution of 1000 allowed isobaric interference on ^{18}O to be eliminated.

A Helium Ion Microscope (HIM, Nanofab, ZEISS, Peabody, USA) coupled with in-house SIMS system (HIM-SIMS)[21,22] was used to analyze and map the ^{16}O and ^{18}O isotopes. SIMS images were acquired by collecting the secondary ions emitted from the film surface scanned by a 20 keV Ne^+ ion beam of 2 pA over a matrix of 512×512 pixels with a counting time of 5 ms per pixel.

The Time-of-flight Secondary Ion Mass Spectrometry experiments were performed using a commercial TOF-SIMS V time-of-flight mass spectrometer (ION-TOF GmbH, Münster, Germany) operating at a pressure of 10^{-9} mbar. Mass spectra were carried out with a 25 keV pulsed Bi^{3+} cluster ion source, delivering a 0.31 pA target current. The analyzed area was 500mmx500mm. The analyses were performed using a primary ion dose density maintained at 10^{11} ions/cm^2, which is below the so-called static SIMS limit. In these conditions, secondary ions are produced, reflecting the molecular and elemental composition of the first nanometer of a sample. The data were obtained in negative mode and the secondary ion mass spectra were calibrated using Cn- carbon clusters.

4.2.3. Results

4.2.3.1. Microstructural, optical, and electronic properties

Figure 1 shows the XRD results and SEM images of the ZnO thin films grown with and without a 1 s pulsing of oxygen gas by ALD loop at a sample temperature of 180 °C. The diffraction patterns match the standard diffraction patterns of the hexagonal wurtzite ZnO crystal structure (JCPDS-36-1451). The film grown without the presence of oxygen gas at the same deposition temperature shows a polycrystalline structure consisting of a random distribution of (100), (002), and (101) orientations (Figure 1(a)). The top-view SEM micrograph further confirms that different grain shapes co-exist, with wedge-shaped crystallites parallel to the substrate surface and fine-columnar crystallites perpendicular to the substrate surface. The ZnO film grown in the presence of oxygen gas, however, shows a preferred (002) orientation (Figure 1(b)), which is further supported by a top-view SEM image of the film where fine-columnar crystallites are mainly identified.

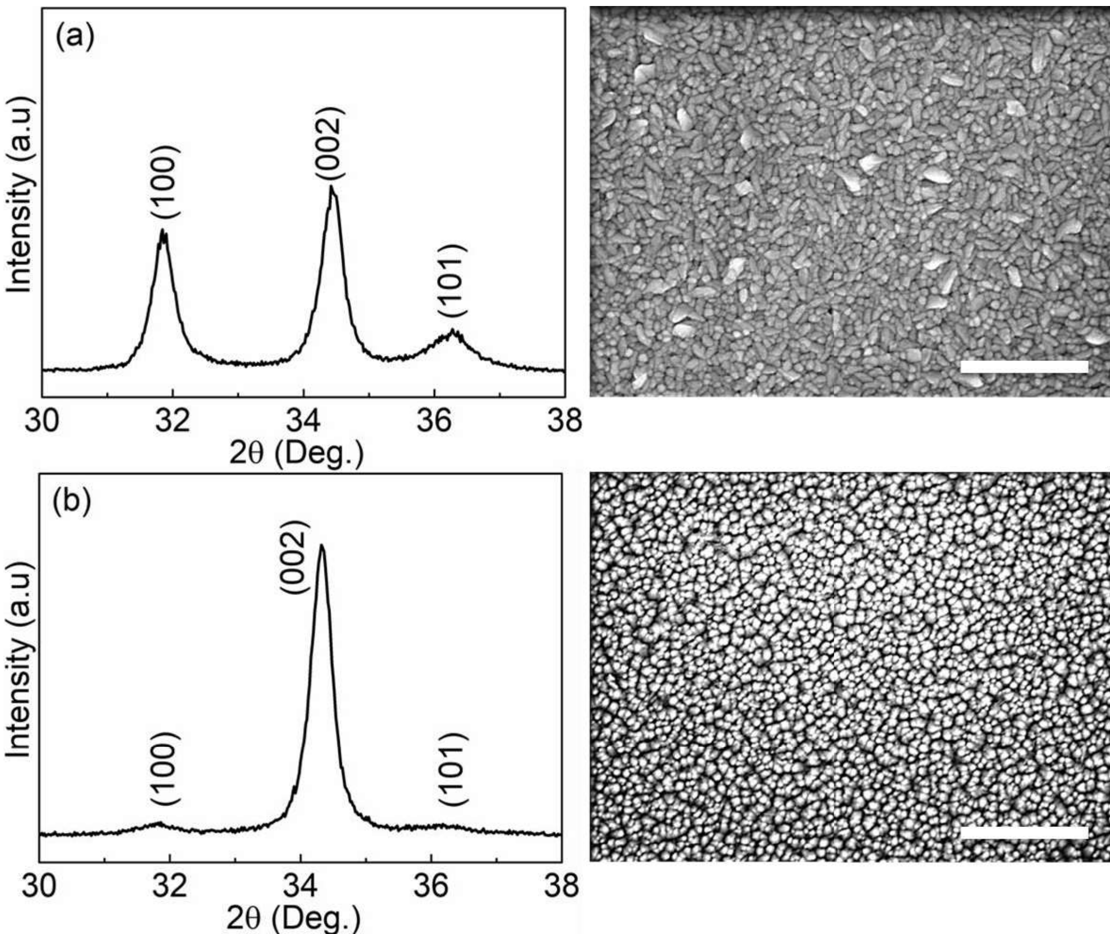

Figure 1: *XRD patterns and top-view SEM images of (a) the ZnO thin film grown without, (b) with gaseous oxygen. The scale bar in the SEM images is 300 nm.*

The optical bandgap of ZnO thin films is derived from the Tauc plot, as shown in Figure 2(a). The reflectance and transmittance spectra of ZnO thin films and a glass slide were carried out to calculate the absorption spectra of ZnO thin films. For a direct bandgap semiconductor[23], the relationship between the absorption coefficient α and photon energy hv is given by: $(\alpha hv)^2 = A(hv - E_g)$, where h is Planck's constant, A is a constant and E_g is the optical bandgap. The bandgap is determined by extrapolating the linear part of the Tauc plots to $\alpha = 0$, which is 3.2 eV for ZnO thin films grown without oxygen gas and increases up to 3.3 eV for the film grown with the 1s pulse of oxygen.

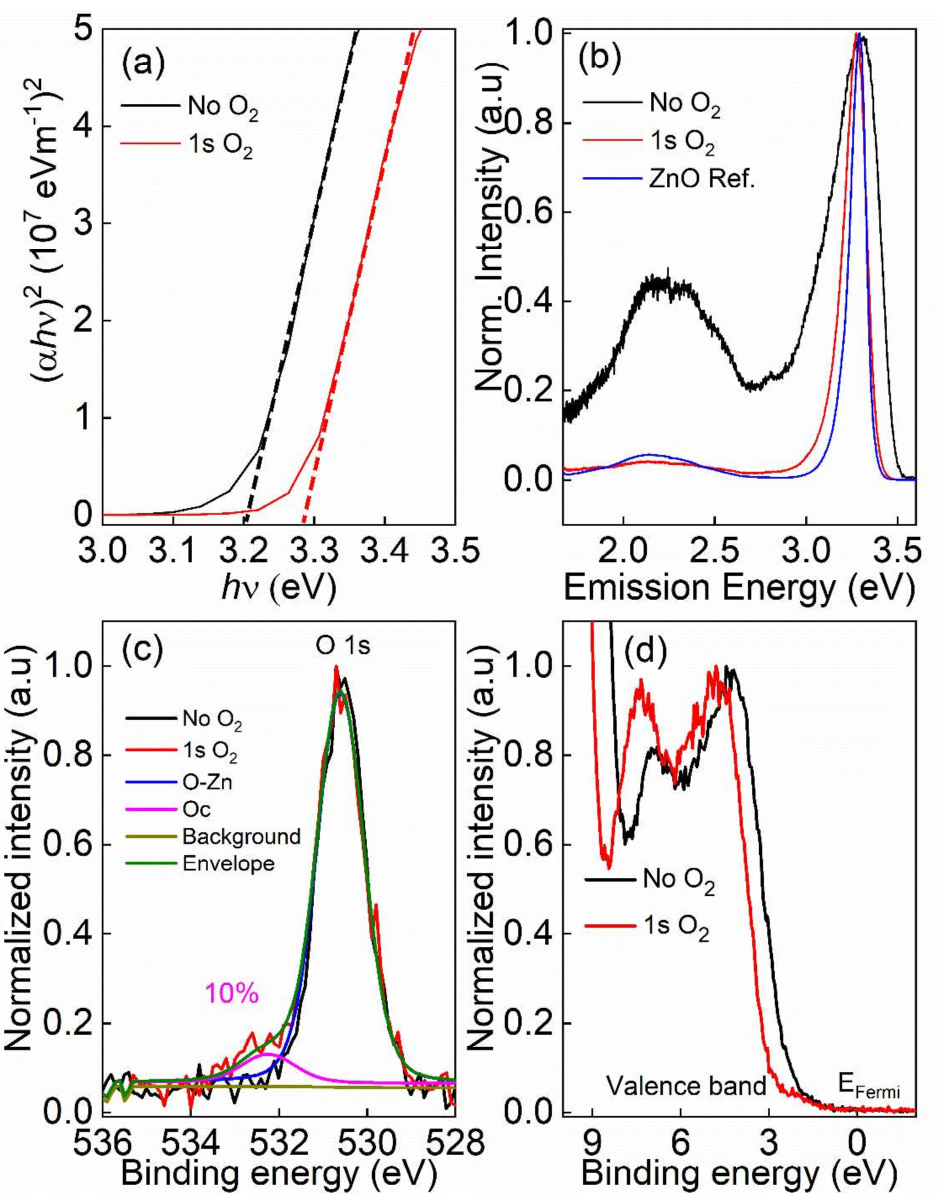

Figure 2: *(a) Tauc plots of ZnO thin films grown with and without gaseous oxygen, (b) Photoluminescence spectra of the ZnO thin films and a reference ZnO single crystal, (c) XPS narrow scans of O 1s spectra, (d) the valence band spectra of the ZnO thin films. The peak fitting on (c) was performed on the O 1s peak of the ZnO thin film grown in the presence of gaseous oxygen. The O 1s peak was deconvoluted into two peaks: a main peak O-Zn (530.6 eV) and a secondary peak Oc (532.2 eV) for hydroxides and/or chemisorbed oxygen.*

Figure 2(b) presents the normalized photoluminescence spectra performed at room temperature. The strong energy peak located from 3.28 to 3.31 eV is assigned to the near band edge (NBE) emission. A broad emission band (1.5 to 2.7 eV) is observed that results from defect-related DLE and can be deconvoluted into green (2.58 to 2.25 eV), yellow-orange (2.25 to 2.03 eV), and red (2.03 to 1.64 eV) emission bands. Although the nature of the deep-level emission is controversial, there are three main arguments that are widely accepted[24,25]:

(i) The green emission is associated either with oxygen vacancies simply ionized (V_O°), oxygen antisites, or even zinc vacancies (V_{Zn}°).

(ii) The yellow-orange emission corresponds to oxygen vacancies doubly ionized (VO°°).

(iii) The red emission is attributed to excess oxygen on the ZnO surface.

Interestingly, by adding oxygen molecules during the ALD process, the DLE region became minor compared to the NBE emission peak, whereas the DLE region can be clearly observed for ZnO thin film processed without oxygen gas at the same deposition temperature.

The chemical state and environment of oxygen and zinc were studied by X-ray photoelectron spectroscopy, as shown in Figures 2(c)-(d). The Zn 2p peak is not affected by the presence of oxygen gas (not shown). In contrast, an additional peak located above 530 eV is observed in the O 1s spectrum when oxygen gas is added during the ALD processes (Figure 2(c)). In general, the O 1s peak in ZnO compounds can be split into two components: a main peak related to the O-Zn bonds in the hexagonal wurtzite ZnO structure (~ 530.60 eV)[26–28], and an additional peak located at ~ 532.2 eV assigned to hydroxides[29,30] or to chemisorbed oxygen[27,28]. The O 1s spectra acquisition was completed in less than 300s after the end of the Ar sputtering to limit the adsorption of hydroxides occurring even under ultra-high vacuum on Zn dangling bonds present at the surface of the film (Figure 2(c)). It can clearly be seen that not only O but also hydroxides are inserted inside the bulk of the film during the ZnO growth only when oxygen gas is added. This is also confirmed by the higher hydrogen level found in the SIMS depth profiles (Figures 5(a)-(b)). They represent around 10% of the oxygen in the ZnO network. The valence band shape, sensitive to the filling of the oxygen vacancies, is also modified when adding oxygen gas into the synthesis process (Figure 2(d)). The two structures around 4 eV and 7.5 eV are mainly due to electrons in the O 2p orbitals and the O 2p - Zn 4sp hybridized state respectively[31–33]. An increase of the O 2p – Zn 4sp states, meaning these orbitals are more populated, is observed when oxygen gas is added during the synthesis process and is linked to a higher number of zinc atoms surrounded by oxygen atoms (O and/or OH) in the final wurtzite structure, thus decreasing the vacancy density in the film. Furthermore, the valence band positions of the two samples (determined without any energy calibration) clearly show a shift of 0.5 eV. Without the O_2 pulse in the synthesis process, the Fermi level is closer to the conduction band, due to the higher oxygen vacancies amount in this n-type material. Based on this result, it is worth noting that the defects density due to oxygen vacancies (sample without O_2 pulse) is much higher than the defects related to the incorporation of carbon resulting of the incomplete decomposition of DEZ (sample with the O_2 pulse). This is confirmed by the fact that a peak shape evolution is observed in the O 1s spectrum versus the synthesis condition whereas carbon has not been detected in any sample by XPS whose sensitivity is lower than dynamic or ToF-SIMS. The O/Zn ratio was found to be 0.96 ± 0.03 and 0.92 ± 0.02 for the ZnO films grown with and without O_2.

4.2.3.2.The in-situ QCM characteristics of the ALD ZnO thin films

Figure 3 presents the *in situ* QCM characteristics of the ZnO thin film grown without using oxygen gas pulsing. The timing sequence can be written as 0.1 s (DEZ pulsing) – 5 s (Ar purging) – 0.1 s (^{18}O-labeled DI water pulsing) – 5 s (Ar purging). The whole growth processes present a linear dependence of the mass gain with deposition time, as shown in Figure 3(a). Noticeable features visible in the QCM curve are the presence of regular steps, which are clearly observed in the enlarged views of the QCM curves for selected periods, as presented in Figures 3(b)-(d). As can

be seen in the first stages of the growth before 500 seconds corresponding to about 50 cycles (Figure 3(b)), DEZ exposures are barely self-limiting. The mass gain for the first DEZ exposures is $\Delta m_{DEZ} \approx 215$ ng/cm^2. The mass loss for the first H_2O exposures is $\Delta m_{H2O} \approx 60$ ng/cm^2. The total mass gain per cycle for the first growth stages of ZnO films is $\Delta m \approx 155$ ng/cm^2. After 500 s, steady-state growth conditions are reached. Interestingly, the mass change during the water pulse is first negative (mass loss) and gradually decreases (in absolute value) during growth, as shown in Figures 3 (c) and (d). It becomes positive after the first 266 growth cycles, corresponding to approximately 2750 s. However, the total mass gain per cycle remains unchanged over the entire growth process at $\Delta m \approx 155$ ng/cm^2.

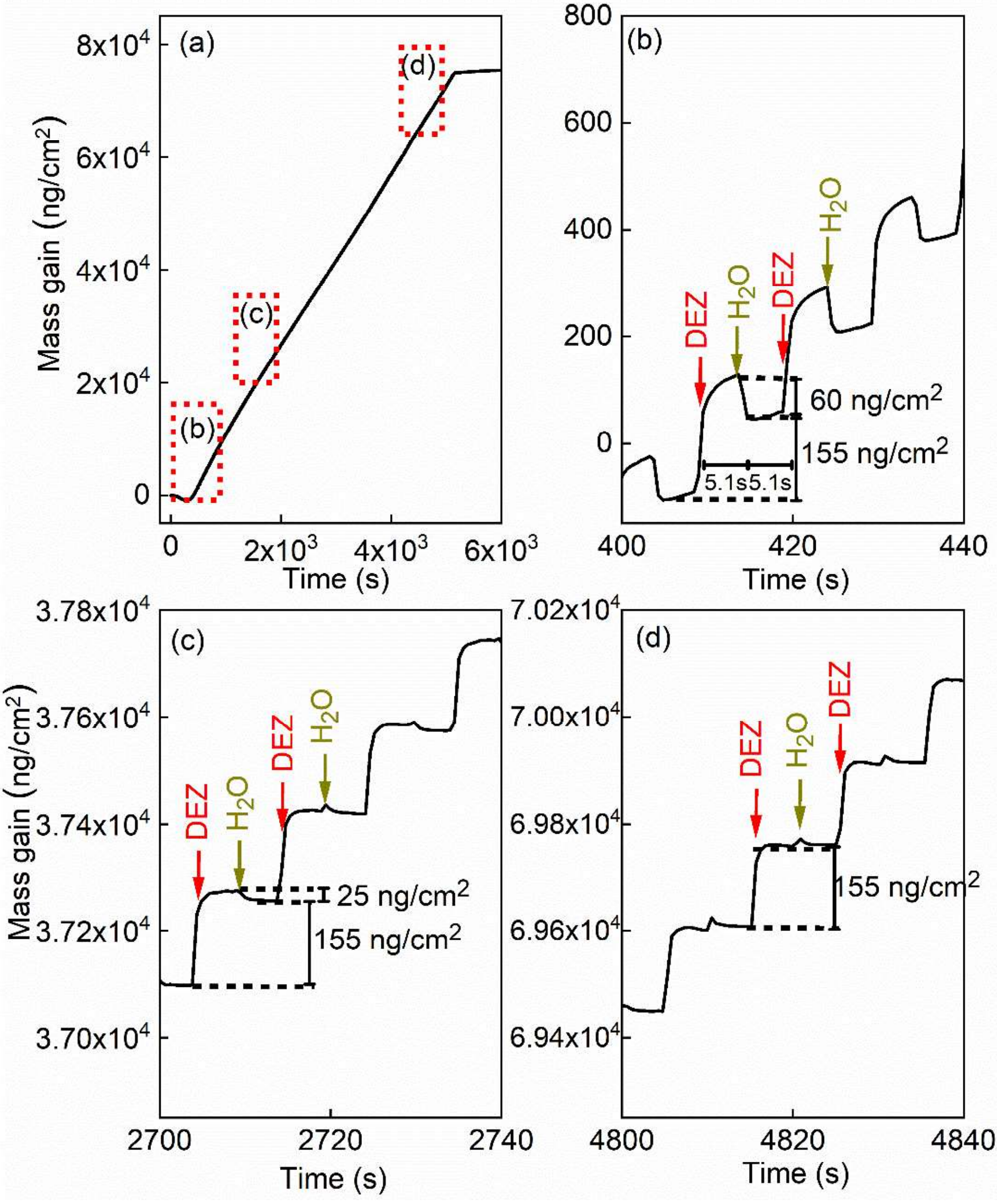

Figure 3: *In situ QCM growth characteristics of the ZnO thin film grown without O₂; (a) a completed growth process, (b)–(d) enlargements of QCM characteristics at different moments of the growth, as indicated in the graph (a).*

The *in situ* QCM characteristics of the ZnO thin film synthesized in the presence of oxygen gas are shown in Figure 4. The timing sequence is written as 0.1 s (DEZ pulsing) – 5 s (Ar purging) – 1 s (O_2 pulsing) – 20 s (Ar purging) – 0.1 s (^{18}O-labeled DI water pulsing) – 10 s (Ar purging).

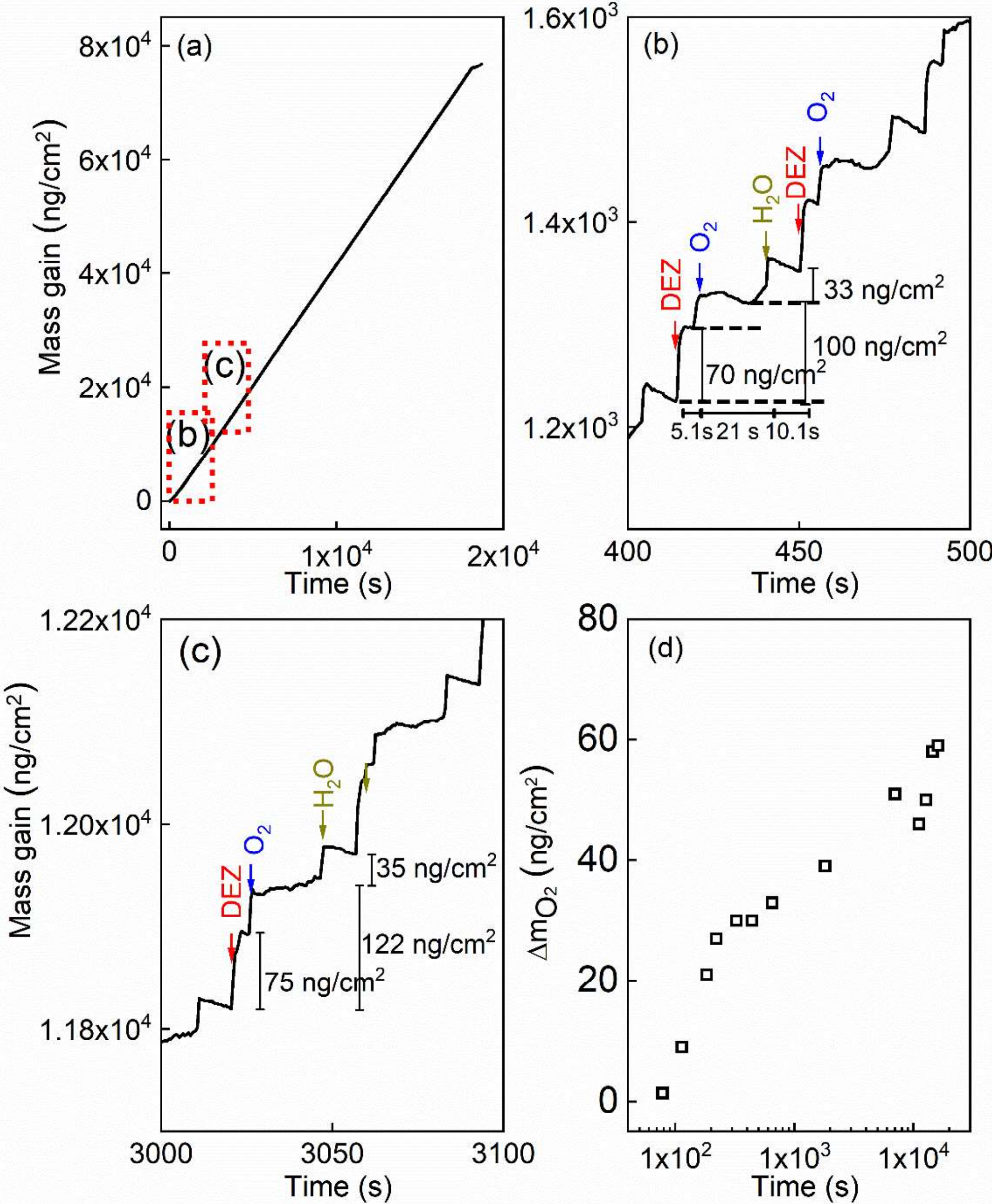

Figure 4: *In situ QCM growth characteristics of the ZnO thin film grown with O_2; (a) a completed growth process, (b)–(c) enlarged views of QCM characteristics at different moments of the growth, as indicated in (a), and (d) mass gain after the oxygen pulse as a function of deposition time.*

Here also, the whole growth processes present a linear dependence of the mass gain on deposition time, as shown in Figure 4(a). Enlarged views of the QCM results that highlight the growth characteristics of the ZnO film at indicated periods are shown in Figures 4(b)-(c). After the first 3000 s, corresponding to 80 cycles, the steady-state in mass gain is achieved during the ALD loop

stages for DEZ pulsing, inserted oxygen exposures, and water pulsing. The mass gain for the DEZ, oxygen gas, and H_2O exposures is $\Delta m_{DEZ} \approx$ 70–75 ng/cm^2, $\Delta m_{O2} \approx$ 30–47 ng/cm^2, $\Delta m_{H2O} \approx$ 33–35 ng/cm^2, respectively. The total mass gain per cycle is $\Delta m \approx$ 133-157 ng/cm^2. It is worth mentioning that the mass gain after the oxygen pulse rises as the deposition time increases, as presented in Figure 4(d). Moreover, a positive mass change during the water pulse was observed instead of a negative one for the ALD process without oxygen gas.

4.2.3.3. D-SIMS and ToF-SIMS analysis of the ALD ZnO thin films

D-SIMS analysis was used to trace the contribution of each source of oxygen atoms: ^{18}O from the DI water precursor, and ^{16}O from the O_2 gas pulsing during the ALD cycles. Figures 5 (a)-(b) present the SIMS depth profiles of both ZnO films. A higher amount of oxygen is observed in the film grown with gaseous O_2, which is in line with the XPS results that showed a secondary peak in the O 1s spectrum and the increase of the O1s-Zn 4sp hybridized states in the valence band spectra.

Figures 5 (c)-(d) show that the depth-resolved SIMS analysis of ^{18}O originated predominantly from the ^{18}O-enriched water ($H_2{}^{18}O$), ^{16}O stemmed mainly from oxygen gas, and the $^{18}O/^{16}O$ ratio for ZnO thin films grown with and without an additional presence of oxygen gas, respectively. On one hand, the $^{18}O/^{16}O$ ratio remains unchanged at around 4.7 versus the sputtering time for the film grown with DEZ and water only. The $^{18}O/^{16}O$ obtained value of 4.7 is significantly small compared to the $^{18}O/^{16}O$ ratio of ^{18}O-labeled deionized water of 32. This is due to a dilution effect as the introduction of $H_2{}^{18}O$ is done in the reaction chamber with certain levels of residual gases and moisture (the chamber pressure of approximately 1.2 mbar) where ^{16}O predominates (^{16}O: 99.757% and ^{18}O: 0.205%, i.e. $^{18}O/^{16}O \sim 2.05 \times 10^{-3}$). Consequently, the $^{18}O/^{16}O$ ratio of the ZnO film drastically decreases. On the other hand, it decreases from a value of 1.8 to 1.5 as the film grows (i.e. towards the low value of sputtering time) with the additional O_2.

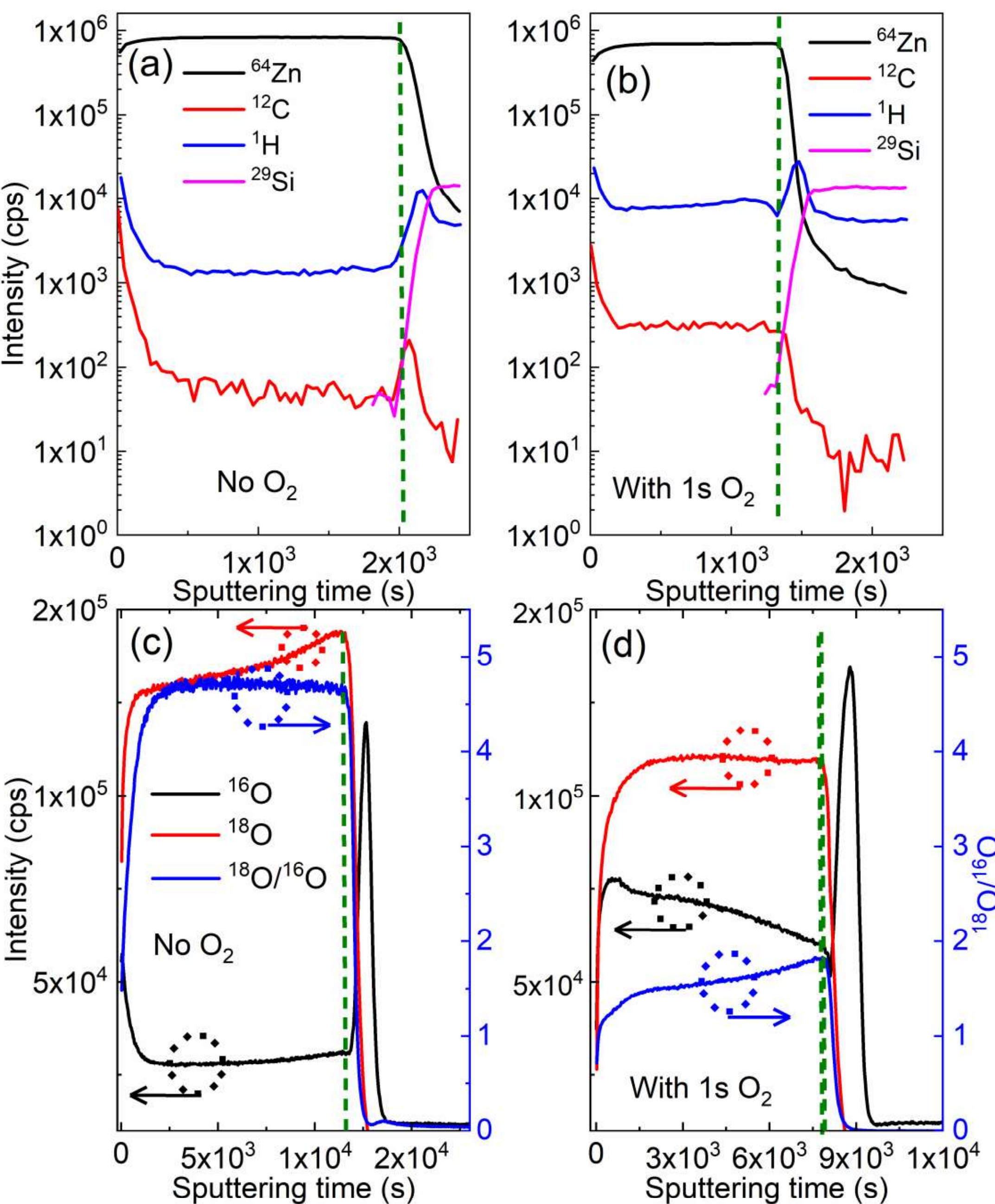

Figure 5: SIMS depth-profile acquired with a Cs^+ bombardment of ZnO thin films grown (a) without and (b) with O_2 gas, oxygen isotopic signatures determined with the M^- mode analysis of ZnO thin films synthesized (c) without and (d) with gaseous O_2. The olive short dash lines indicate the transition between films (the left sides) and silicon substrates (the right sides).

This decrease in the $^{18}O/^{16}O$ ratio upon the sputtering time implies that the oxygen atoms mainly stem from water at the early stage of the growth, meaning that the contribution of the water precursor is predominant. However, the contribution of additional O_2 gas in the growth process gradually becomes significant as the film gets thicker. This is in line with the observation from the QCM data (Figure 4 (d)), which shows the increase in the mass gain after the O_2 pulse. It is also worth noticing that amounts of carbon and hydrogen present in bulk in the ZnO film grown with

O_2 are about 50% higher than those of the ZnO film grown without O_2 (Figures 5(a)-(b)). This will be commented on later in the discussion.

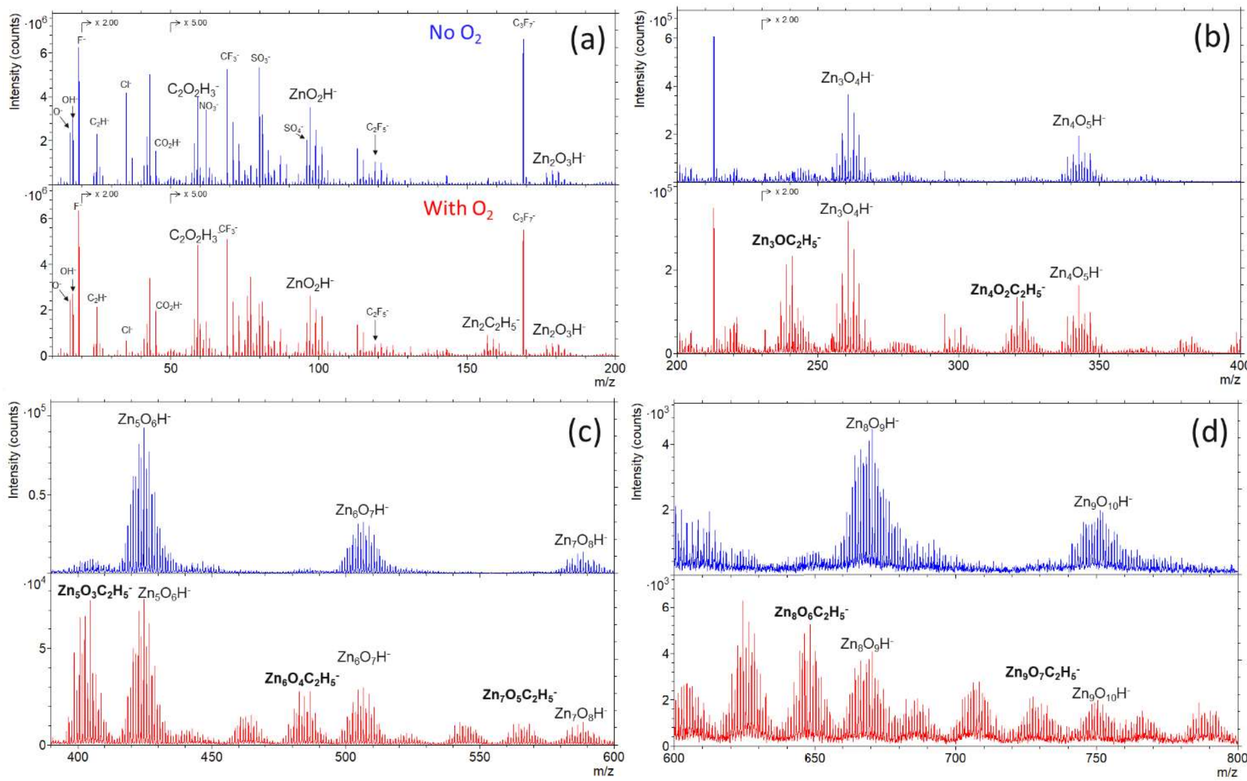

Figure 6: *TOF-SIMS spectra with the m/z ranges of (a) 0-200, (b) 200-400, (c) 400-600, and (d) 600-800 acquired by negative mode of ZnO thin films grown with (red) and without (blue) O_2 gas.*

Figure 6 presents the ToF-SIMS analysis of the ZnO thin films. $Zn_xO_yH^-$ ions are detected for both ZnO thin films due to the fact that the films were grown by using DEZ and DI water as precursors. Interestingly, $Zn_xO_yC_2H_5^-$ ions are only detected in the ZnO films grown in the presence of gaseous O_2. This signature suggests a direct chemical reaction of the O_2 gas molecules with the growing ZnO-based thin film during the ALD process. This is also supported by the lower $^{18}O/^{16}O$ ratios measured (Figures 5c and d) through the whole thickness of the film with the additional presence of O_2 during the ALD process. It is also noticing that the presences of Cl^-, NO_3^-, SO_4^{2-}, and fluor were observed. The presences of these ions can be due to contaminants on the surface, which were not detected by XPS because its sensitivity is lower than dynamic or ToF-SIMS.

A high resolution lateral mapping by HIM-SIMS of the ^{18}O and ^{16}O atoms, and respective overlaps of (^{18}O + ^{16}O), on Figure S1 (in the Supporting Information) show a uniform distribution of both atoms among the structure of the grains, depicted in Figure 1, of the polycrystalline ZnO thin films synthesized with and without 1 s of oxygen gas pulsing for each ALD loop.

4.2.4. DISCUSSION

The present study confirms and complements our previous work[17], by showing how the presence of oxygen gas pulsing during the ALD process profoundly affects the crystallographic, morphological, optical, electrical, and electronic properties of ZnO thin films (Figures 1-2 and Figures S2-S3 in the Supporting Information). In particular, the crystal structure of ZnO thin film

changed to a polycrystalline structure with a highly preferred (002) orientation as oxygen gas pulsing was applied at 180 and 200 °C. Compared to ZnO films grown using only DEZ and water, the electrical resistivity of ZnO thin film increased by 3 to 4 orders of magnitude for the films grown at 180 and 100 °C in the presence of oxygen gas pulsing, respectively (Figure S3 in the Supporting Information). Complementary to our first work[17] highlighting the impact of the oxygen gas presence in the growth process on the properties of ZnO films, in this study, we point out that these profound features are in intimate correlation with the oxygen chemisorption incorporated in the ZnO surface during growth, which is identified by the XPS analysis showing an additional peak at 532.2 eV, allocated to hydroxides, and an increase of the O 2p – Zn 4sp hybridized states in the valence bands, due to the incorporation of O and/or OH in the ZnO films. By chemisorbing oxygen, the ZnO(001)-Zn polar surface can be electrostatically stabilized as highlighted by P. Gorai et al.[34]. Thus, the (002) orientation films grew preferentially. In addition, it was found that the native defects, mainly oxygen vacancies, decreased by absorbing oxygen molecules[17], resulting in an increase in resistivity.
For ZnO film growth using DEZ and water precursors, the reaction mechanism usually follows the reactions (2a) and (3). If all hydroxyl groups are linked to MEZ groups after the DEZ saturation, the mass change during the water pulse should be negative as the ethyl ligands are replaced by much lighter hydroxyl groups via the ligand-exchange reaction. For the first 266 cycles of growth (about 2700 s of growth duration), the reaction mechanism follows reactions (2a) and (3), as shown in Figures 3(b) and(c). After that, the non-negative mass change during the water pulse was observed (Figures 3(c),(d)). This behavior was also reported by Yousfi and co-workers[20]. It suggests that the reaction mechanism postulated in equations (2a) and (3) does not completely reflect the nature of the growth process. It is possible that after reaction (2a), reaction (2b) can also occur, thus leading to the presence of bare zinc atoms in addition to the monoethyl zinc on the surface [18,35]. These bare zinc atoms can adsorb more water onto the surface and counterbalance the mass change due to the ligand-exchange reaction. T. Weckman and K. Laasonen proposed this explanation based on density functional theory study on the atomic layer deposition of zinc oxide and supported by experimental results from other publications [18,35]. The surface ethyl-ligand elimination during the water pulse is incomplete, resulting in persisting ethyl ligands on the surface after the water pulse has ended. The fraction of these persisting ligands is strongly dependent on temperature, suggesting that there is a kinetic barrier to ligand elimination by water. At elevated temperatures the kinetic barrier for the ligand removal is overcome, and the number of persisting ligands can be expected to be reduced as a function of temperature. As the surface becomes rapidly saturated with monoethyl zinc, the adsorption of diethyl zinc slows and the monoethyl zinc slowly reacts with the remaining hydroxyl groups into bare zinc atoms. In addition, the effect of surface morphology on the ligand-exchange reactions have been theoretically studied [35]. Their calculation suggested that the initial ligand-exchange reactions are preferred on the planar surface over the step surface. Yousfi et al. [20] also discussed that a film crystal structure may be invoked in the change of growth mechanisms due to polar (002) and non-polar (100) planes. Therefore, as the film grew the film structure and morphology can be changed. These may contribute to the change of the reaction mechanisms.

In the presence of oxygen gas during the ALD growth, the growth characteristic is completely different from the one grown by DEZ and water precursors only, as shown in Figure 4. Ignatyev et al.[36] and Rienstra-Kiracofe et al.[37] demonstrated that the monoethyl radical could react to O_2 in the event of the additional presence of gaseous O_2 during ALD processes to form the ethylperoxy radical:

$$C_2H_5\bullet + O_2 \rightarrow CH_3CH_2OO\bullet \qquad (4)$$

Our hypothesis is that the gaseous oxygen can react with the remaining ethyl ligand of DEZ after the DEZ pulse (2a).

$$|\text{-O-Zn-}C_2H_5 + O_2 \rightarrow |\text{-O-Zn-}C_2H_5O_2 \qquad (2c)$$

A higher intensity of carbon and hydrogen by D-SIMS in the film grown with O_2 compared to the film grown without O_2 and particularly the significant detection of $Zn_xO_yC_2H_5^-$ ion by TOF-SIMS supports our hypothesis. As a result, the formation of ethylperoxy groups induces the positive mass change during the gaseous O_2 pulse. Possibly, reactions (2b) and (2c) occur simultaneously, leading to the presence of zinc atoms and the formation of $|\text{-O-Zn-}C_2H_5O_2$. As pointed out by D.H. Ehhalt et al.[38], the ethylperoxy radical is polar, relatively long-lived and water-reactive. This form of Criegee intermediate is known to have a very high reactivity with water vapor to form mainly alkylhydroperoxides[39]. L. Sheps et al. also determined the additional minor formation of aldehydes and carboxylic acids[40]. Hence, these ethylperoxy radical formations would cause more adsorption of water during the water pulse in the ALD cycle to form mainly ethylhydroperoxide chains, resulting in the positive mass change during the water pulse, which is consistent to the *in-situ* QCM data (Figure 4). A quantitative estimation of the incorporation of oxygen atoms from H_2O and O_2 by the D-SIMS measurements of the $^{18}O/^{16}O$ ratio in Figure 5 would deserve a more complete analysis of the final end products reaction rates of the Criegee intermediates with water during growth of the film with steric interactions to consider and not treated in this work.

4.2.5. Conclusions

The use of ^{18}O-labelled isotopic water as precursor to track the origin of oxygen atoms in ZnO film from two different sources is an original and powerful approach to conclusively demonstrate that the presence of additional gaseous O_2 in the atomic layer deposition (ALD) process causes a new chemical reaction mechanism in the growth of ZnO thin film, modifying its properties. The detection of $Zn_xO_yC_2H_5^-$ ions accompanied by the *in situ* quartz crystal microbalance characteristics suggests a new reaction mechanism in the ZnO thin films grown with O_2 gas presence, i.e. monoethyl zinc reacts further with O_2, leading to the positive mass changes during the O_2 and water pulses by the respective formation of ethylperoxy radicals and ethylhydroperoxide chains in the bulk of the film. The monitoring of the $^{18}O/^{16}O$ ratio along the depth of the film highlighted the evolution of the chemical contribution of the water precursor and gaseous O_2 during the ALD growth. It is shown, when coupling the water precursor with gaseous O_2 in the ALD process, that the gaseous O_2 contribution of the oxygen atoms in the chemistry of the thin film continuously increases during the growth process. D-SIMS and XPS results have also proven that additional oxygen species are present in the ZnO films when gaseous O_2 is added in the ALD process. The increase of the O 2p – Zn 4sp hybridized states in the valence band, observed when oxygen gas was added during the synthesis process, corresponds to a decrease of the oxygen vacancies density in the film, leading to the drop of the electrical conductivity. As another consequence, the green emission band is suppressed due to the presence of added oxygen inside the ZnO film that counter-balances the formation of oxygen vacancies.

4.2.6. References

(1) Choi, Y. S.; Kang, J. W.; Hwang, D. K.; Park, S. J. Recent Advances in ZnO-Based Light-Emitting Diodes. *IEEE Trans. Electron Devices* **2010,** 57, 26-41.

(2) Mane, R. S.; Lee, W. J.; Pathan, H. M.; Han, S. H. Nanocrystalline TiO_2/ZnO Thin Films: Fabrication and Application to Dye-Sensitized Solar Cells. *J. Phys. Chem. B* **2005**, 51, 24254-24259.

(3) Van Dang, T.; Duc Hoa, N.; Van Duy, N.; Van Hieu, N. Chlorine Gas Sensing Performance of On-Chip Grown ZnO, WO_3, and SnO_2 Nanowire Sensors. *ACS Appl. Mater. Interfaces* **2016**, 8,7, 4828-4837.

(4) Le Brizoual, L.; Sarry, F.; Elmazria, O.; Alnot, P.; Ballandras, S.; Pastureaud, T. GHz Frequency ZnO/Si SAW Device. *IEEE Trans. Ultrason. Ferroelectr. Freq. Control* **2008**, 55, 442-450.

(5) Wang, Z. L.; Song, J. Piezoelectric Nanogenerators Based on Zinc Oxide Nanowire Arrays. *Science.* **2006**, 312, 242-246.

(6) Hinchet, R.; Lee, S.; Ardila, G.; Montès, L.; Mouis, M.; Wang, Z. L. Performance Optimization of Vertical Nanowire-Based Piezoelectric Nanogenerators. *Adv. Funct. Mater.* **2014**, 24, 971-977.

(7) Joly, R.; Girod, S.; Adjeroud, N.; Nguyen, T.; Grysan, P.; Klein, S.; Menguelti, K.; Vergne, C.; Polesel-Maris, J. Polymeric Cantilevered Piezotronic Strain Microsensors Processed by Atomic Layer Deposition. *Sensors Actuators A Phys.* **2020**, *315*, 112280.

(8) Bellingeri, E.; Marré, D.; Pallecchi, I.; Pellegrino, L.; Canu, G.; Siri, A. S. Deposition of ZnO Thin Films on $SrTiO_3$ Single-Crystal Substrates and Field Effect Experiments. In *Thin Solid Films*; **2005**, 486, 186-190.

(9) Matsubara, K.; Fons, P.; Yamada, A.; Watanabe, M.; Niki, S. Epitaxial Growth of ZnO Thin Films on $LiNbO_3$ Substrates. *Thin Solid Films* **1999**, 347, 238-240.

(10) Liu, H. F.; Chua, S. J.; Hu, G. X.; Gong, H.; Xiang, N. Effects of Substrate on the Structure and Orientation of ZnO Thin Film Grown by Rf-Magnetron Sputtering. *J. Appl. Phys.* **2007**, 102, 083529.

(11) Novotný, M.; Cižek, J.; Kužel, R.; Bulíř, J.; Lančok, J.; Connolly, J.; McCarthy, E.; Krishnamurthy, S.; Mosnier, J. P.; Anwand, W.; et al. Structural Characterization of ZnO Thin Films Grown on Various Substrates by Pulsed Laser Deposition. *J. Phys. D. Appl. Phys.* **2012**, 45, 225101.

(12) Kang, S. J.; Joung, Y. H. Influence of Substrate Temperature on the Optical and Piezoelectric Properties of ZnO Thin Films Deposited by Rf Magnetron Sputtering. *Appl. Surf. Sci.* **2007**, 253, 7330-7335.

(13) Rosa, A. M.; Da Silva, E. P.; Amorim, E.; Chaves, M.; Catto, A. C.; Lisboa-Filho, P. N.; Bortoleto, J. R. R. Growth Evolution of ZnO Thin Films Deposited by RF Magnetron Sputtering. In *Journal of Physics: Conference Series*; **2012**, 370, 012020.

(14) Husna, J.; Mannir Aliyu, M.; Aminul Islam, M.; Chelvanathan, P.; Radhwa Hamzah, N.; Sharafat Hossain, M.; Karim, M. R.; Amin, N. Influence of Annealing Temperature on the Properties of ZnO Thin Films Grown by Sputtering. In *Energy Procedia*; **2012**, 25, 55-61.

(15) Wang, F. H.; Chang, C. L. Effect of Substrate Temperature on Transparent Conducting Al and F Co-Doped ZnO Thin Films Prepared by Rf Magnetron Sputtering. *Appl. Surf. Sci.* **2016**, 370, 83-91.

(16) Park, S. H. K.; Lee, Y. E. Controlling Preferred Orientation of ZnO Thin Films by Atomic Layer Deposition. *J. Mater. Sci.* **2004**, 39, 2195-2197.

(17) Nguyen, T.; Adjeroud, N.; Guennou, M.; Guillot, J.; Fleming, Y.; Papon, A.-M.; Arl, D.; Menguelti, K.; Joly, R.; Gambacorti, N.; et al. Controlling Electrical and Optical Properties of Zinc Oxide Thin Films Grown by Thermal Atomic Layer Deposition with Oxygen Gas. *Results Mater.* **2020**, 6, 100088.

(18) Weckman, T.; Laasonen, K. Atomic Layer Deposition of Zinc Oxide: Study on the Water Pulse Reactions from First-Principles. *J. Phys. Chem. C* **2018**, 122, 7685-7694.

(19) Weckman, T.; Laasonen, K. Reactions and Surface Saturation from First Principles Atomic Layer Deposition of Zinc Oxide : Diethyl Zinc Reactions and Surface Saturation from First Principles. **2016**, 120, 38, 21460-21471.

(20) Yousfi, E. B.; Fouache, J.; Lincot, D. Study of Atomic Layer Epitaxy of Zinc Oxide by In-Situ Quartz Crystal Microgravimetry. *Appl. Surf. Sci.* **2000**, 153, 223-234.

(21) Wirtz, T.; De Castro, O.; Audinot, J.-N.; Philipp, P. Imaging and Analytics on the Helium Ion Microscope. *Annu. Rev. Anal. Chem.* **2019**, 12, 523-543.

(22) Dowsett, D.; Wirtz, T. Co-Registered in Situ Secondary Electron and Mass Spectral Imaging on the Helium Ion Microscope Demonstrated Using Lithium Titanate and Magnesium Oxide Nanoparticles. *Anal. Chem.* **2017**, 89, 17, 8957-8965.

(23) Viezbicke, B. D.; Patel, S.; Davis, B. E.; Birnie, D. P. Evaluation of the Tauc Method for Optical Absorption Edge Determination: ZnO Thin Films as a Model System. *Phys. Status Solidi Basic Res.* **2015**, 252, 1700-1710.

(24) Djurišić, A. B.; Leung, Y. H.; Tam, K. H.; Hsu, Y. F.; Ding, L.; Ge, W. K.; Zhong, Y. C.; Wong, K. S.; Chan, W. K.; Tam, H. L.; et al. Defect Emissions in ZnO Nanostructures. *Nanotechnology* **2007**, 18, 095702.

(25) Panigrahy, B.; Aslam, M.; Misra, D. S.; Ghosh, M.; Bahadur, D. Defect-Related Emissions and Magnetization Properties of ZnO Nanorods. *Adv. Funct. Mater.* **2010**, 20, 1161-1165.

(26) Lupan, O.; Pauporté, T.; Chow, L.; Viana, B.; Pellé, F.; Ono, L. K.; Roldan Cuenya, B.; Heinrich, H. Effects of Annealing on Properties of ZnO Thin Films Prepared by Electrochemical Deposition in Chloride Medium. *Appl. Surf. Sci.* **2010**, 256, 1895-1907.

(27) Thomas, M. A.; Cui, J. B. Highly Tunable Electrical Properties in Undoped ZnO Grown by Plasma Enhanced Thermal-Atomic Layer Deposition. **2012**, 4, 3122-3128.

(28) Bang, S.; Lee, S.; Park, J.; Park, S.; Ko, Y.; Choi, C.; Chang, H.; Park, H.; Jeon, H. The

Effects of Post-Annealing on the Performance of ZnO Thin Film Transistors. *Thin Solid Films* **2011**, *519* (22), 8109–8113.

(29) Kamarulzaman, N.; Kasim, M. F.; Chayed, N. F. Elucidation of the Highest Valence Band and Lowest Conduction Band Shifts Using XPS for ZnO and $Zn_{0.99}Cu_{0.01}O$ Band Gap Changes. *Results Phys.* **2016**, 6, 217-230.

(30) Coppa, B. J.; Davis, R. F.; Nemanich, R. J. Gold Schottky Contacts on Oxygen Plasma-Treated, n-Type ZnO(000Γ). *Appl. Phys. Lett.* **2003**, 82, 400.

(31) Sawada, K.; Shirotori, Y.; Ozawa, K.; Edamoto, K.; Nakatake, M. Valence Band Structure of the ZnO(1 0 Γ0) Surface Studied by Angle-Resolved Photoemission Spectroscopy. In *Applied Surface Science*; **2004**, 237, 343-347.

(32) Al-Saadi, M. J.; Al-Harthi, S. H.; Kyaw, H. H.; Myint, M. T. Z.; Bora, T.; Laxman, K.; Al-Hinai, A.; Dutta, J. Influence of Atomic Hydrogen, Band Bending, and Defects in the Top Few Nanometers of Hydrothermally Prepared Zinc Oxide Nanorods. *Nanoscale Res. Lett.* **2017**, 12, 22.

(33) Chiou, J. W.; Ray, S. C.; Tsai, H. M.; Pao, C. W.; Chien, F. Z.; Pong, W. F.; Tsai, M. H.; Wu, J. J.; Tseng, C. H.; Chen, C. H.; et al. Charge Transfer in Nanocrystalline- AuZnO Nanorods Investigated by x-Ray Spectroscopy and Scanning Photoelectron Microscopy. *Appl. Phys. Lett.* **2007**, 92, 192112.

(34) Gorai, P.; Seebauer, E. G.; Ertekin, E. Mechanism and Energetics of O and O_2 Adsorption on Polar and Non-Polar ZnO Surfaces. *J. Chem. Phys.* **2016**, 144, 184708.

(35) Weckman, T.; Laasonen, K. Atomic Layer Deposition of Zinc Oxide: Diethyl Zinc Reactions and Surface Saturation from First-Principles. *J. Phys. Chem. C* **2016**, 120, 21460-21471.

(36) Ignatyev, I. S.; Xie, Y.; Allen, W. D.; Schaefer, H. F. Mechanism of the C_2H_5+O_2 Reaction. *J. Chem. Phys.* **1997**, 107, 141.

(37) Rienstra-Kiracofe, J. C.; Allen, W. D.; Schaefer, H. F. C_2H_5+O_2 Reaction Mechanism: High-Level Ab Initio Characterizations. *J. Phys. Chem. A* **2000**, 144, 9823.

(38) Jaeschke, W. Multiphase Atmospheric Chemistry. In *Chemistry of Multiphase Atmospheric Systems*; **1986**, vol 6. Springer, Berlin, Heidelberg.

(39) Chao, W.; Hsieh, J. T.; Chang, C. H.; Lin, J. J. M. Direct Kinetic Measurement of the Reaction of the Simplest Criegee Intermediate with Water Vapor. *Science.* **2015**, 347, 751-754.

4.2.7. Supporting information

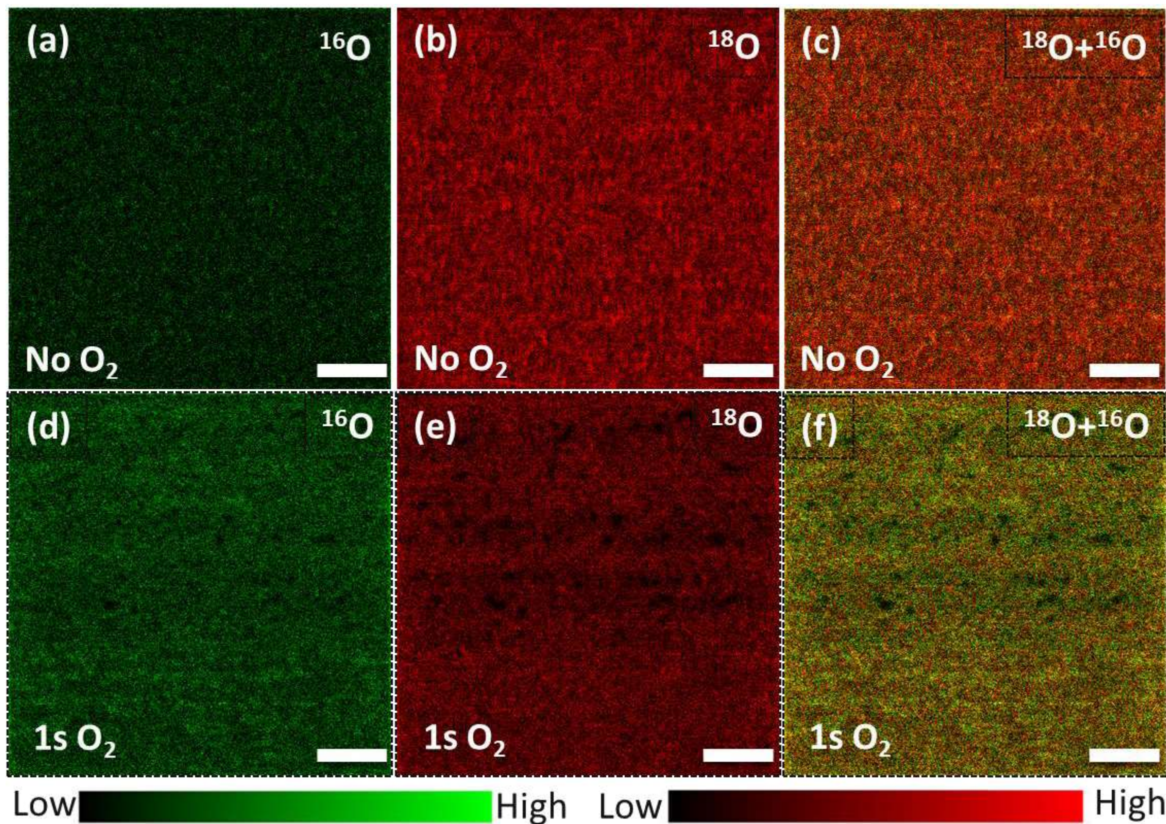

Figure S1: *HIM–SIMS mapping. Distribution of ^{18}O (the red scale bar) and ^{16}O (the green scale bar), and respective overlaps of (^{18}O + ^{16}O) of ZnO samples synthesized with and without 1 s of oxygen gas pulsing for each ALD loop at a deposition temperature of 180 °C. The scale bar is 500 nm.*

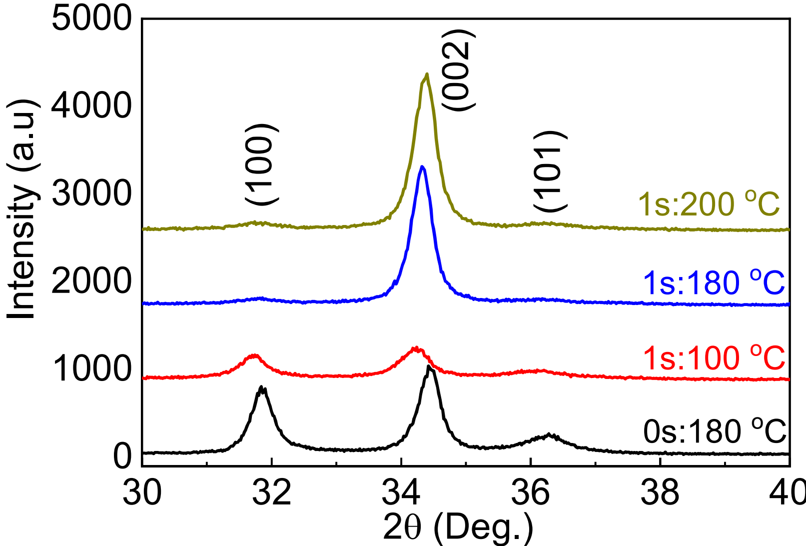

Figure S2: *XRD spectra of the ZnO thin film grown with and without oxygen gas pulsing at different deposition temperatures.*

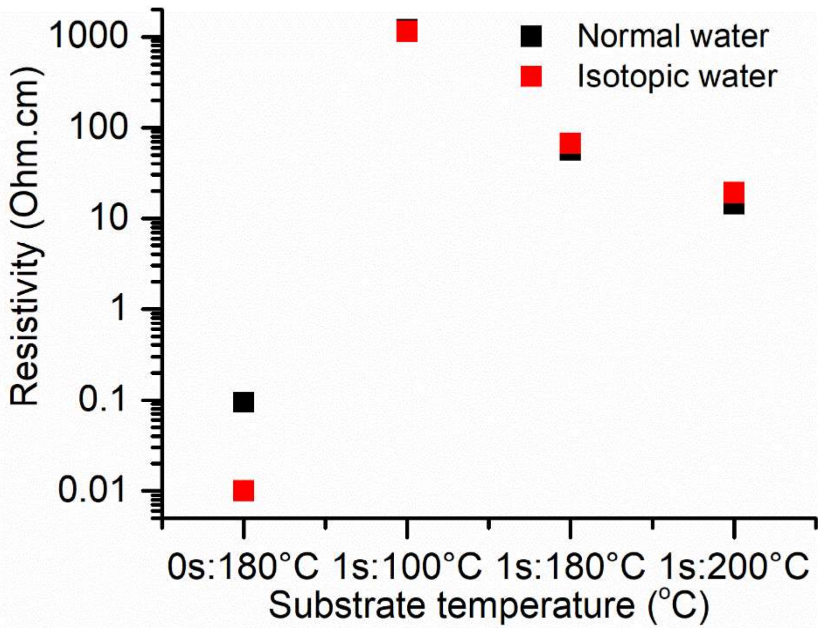

Figure S3: *Electrical resistivity of ZnO thin films grown at different temperatures with conventional DI water and ^{18}O-labelled water.*

In situ QCM characteristics of ZnO thin films grown with 1s of O_2 at 100 and 200 °C

For ZnO thin film grown at 100 °C, a negative mass gain was observed after the O_2 pulse which could be related to the reaction of adsorbed O_2 and ethyl group from DEZ leading to the removal of products from the surface. While a positive mass gain after the water pulse is presumable due to the presence of non-saturated surfaces after DEZ pulse and/or the presence of bare zinc atoms, causing more the adsorption of water on the surface.

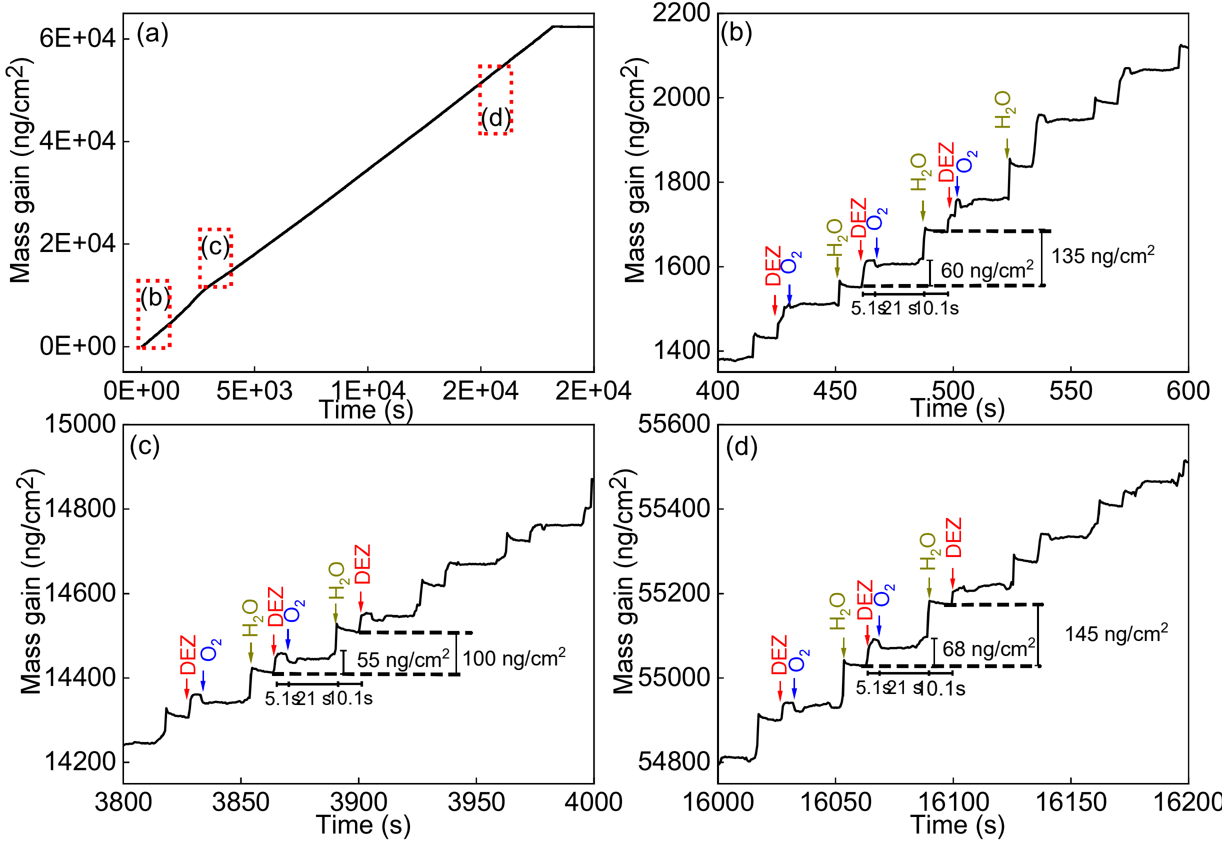

Figure S4: *In situ QCM growth characteristics of the ZnO thin film grown with 1s of oxygen gas at 100 °C; (a) a completed growth process, (b)–(d) enlargements of QCM characteristics at different moments of the growth, as indicated in the graph (a).*

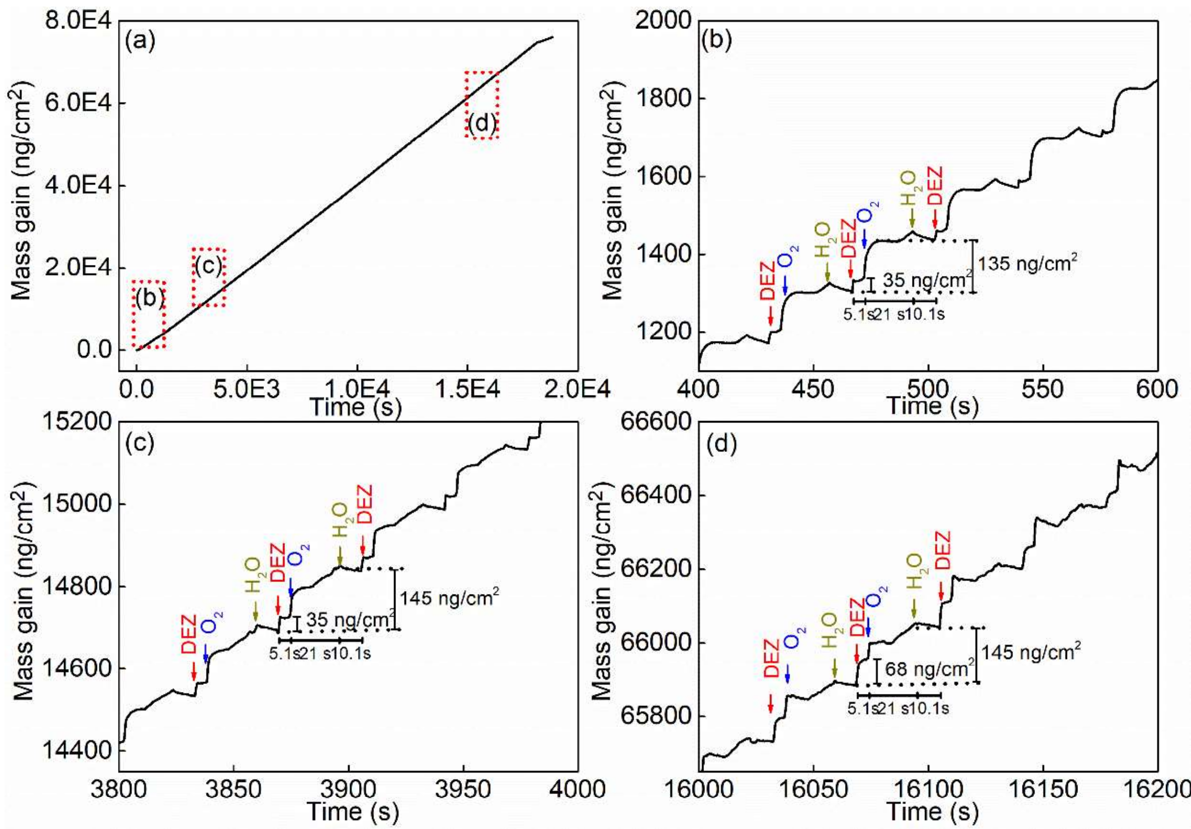

Figure S5: *In situ QCM growth characteristics of the ZnO thin film grown with 1s of oxygen gas at 200 °C; (a) a completed growth process, (b)–(d) enlargements of QCM characteristics at different moments of the growth, as indicated in the graph (a).*

At 200 °C, QCM characteristics show different features. Before 600 seconds of the growth time (about 17 ALD cycles), the adsorption of O2 shows a steady state, however it keeps increasing after 3800 seconds of the growth time (about 105 ALD cycles). It could be due to a higher reactivity of O_2 at higher temperatures, as well as the role of polar ZnO surfaces as the film grown at 200 °C shown highly preferred (002) orientation. The total mass gain after an ALD cycle is 135-145 ng/cm^2.

4.3 Piezoelectric characterization of ZnO thin films

4.3.1. Piezoresponse force microscope characterizations

The piezoresponse force microscope (PFM) characterizations were performed following the set-up in the chapter 3. A Pt top electrode with an area of 5mm×5mm was deposited on top of the ZnO thin films by sputtering. The use of the top electrode is to produce a uniform electrical field on the top surface. The PFM amplitude acquisition was collected by varying the applied voltage from 1 to 5 V at frequency of 300 kHz, as shown in figures 4.1 and 4.2. The d_{33} values are about 3.6, 3.7, 3.3 and 3.3 for the ZnO thin films grown without and with 1, 3, and 5 s of O_2, respectively. While these values of ZnO thin films grown with 1 s of O_2 at deposition temperatures of 100, 150, 180, and 200 °C are approximately 3.2, 2.9, 3.7, and 3.1 ppm, respectively. It is noting that even though PFM measurements were able to extract d_{33} value, the values are highly unreliable due to the noisy background of environment.

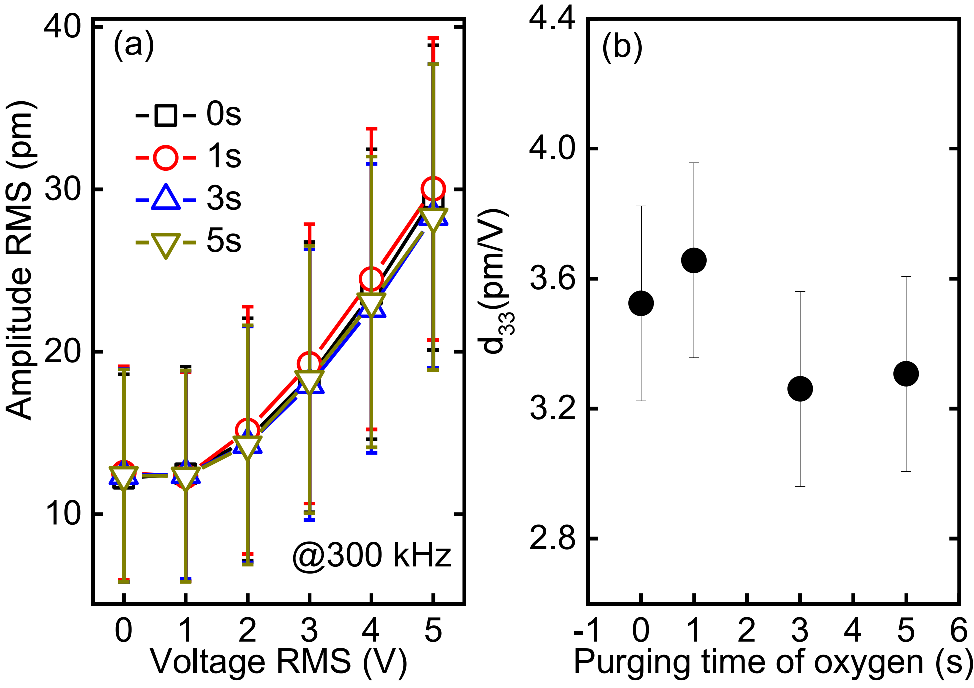

Figure 4.1: *The PFM measurements for ZnO thin films grown at 180°C without and with 1, 3, and 5 s of gaseous oxygen. Graphs in a) represent the evolution of the average value of the oscillation amplitude of the cantilever for different applied voltage on the Pt/ZnO/Ni pad. In b), the relative d33 piezoelectric coefficient is determined for the different conditions of O2 gas pulse duration in the ALD loop.*

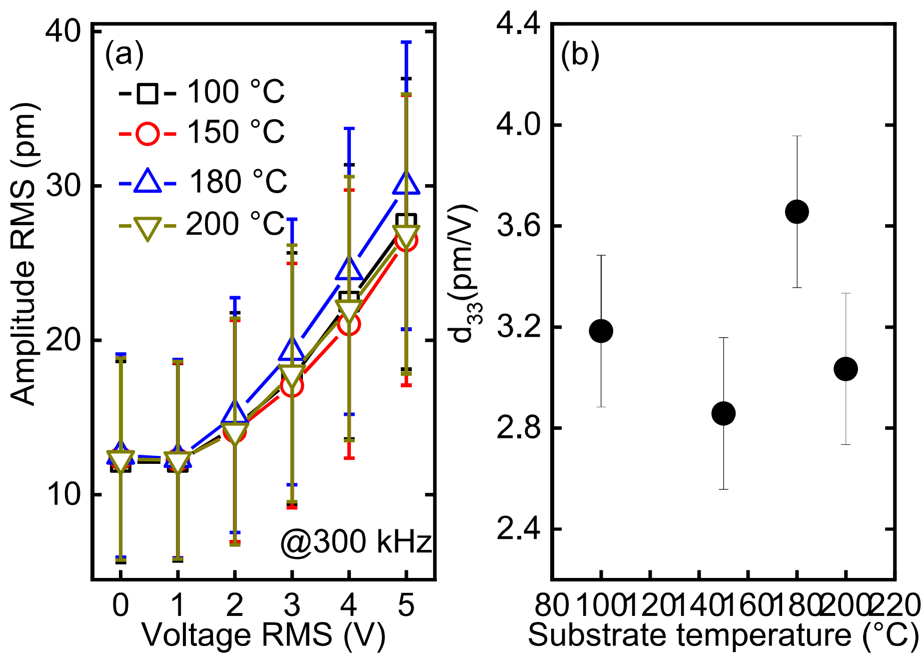

Figure 4.2: The PFM measurement for ZnO thin films grown at 100, 150, 180, and 200 °C with 1s of gaseous oxygen. Graphs in a) represent the evolution of the average value of the oscillation amplitude of the cantilever for different applied voltage on the Pt/ZnO/Ni pad. In b), the relative d33 piezoelectric coefficient is determined for the different conditions of deposition temperature

4.3.2. C-V characteristic

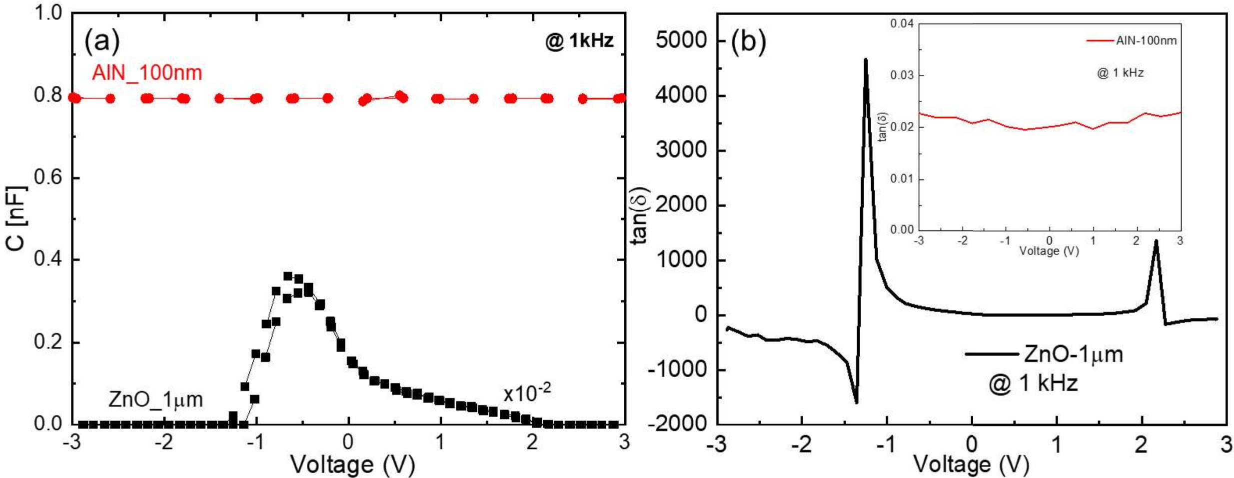

Figure 4.3: (a) C-V and (b) tan(δ) measurements at 1 kHz of the 1μm-thick ZnO film grown at 180 °C with 1 s of oxygen and 100nm-thick AlN film.

As can be seen in figure 4.3(a), the 1μm-thick ZnO film presents a diode behaviour which is non-constant capacitance versus an applied voltage. While an example of insulating AlN thin film shows a constant capacitance against an applied voltage. High loss tan(δ) is presented in the ZnO film, while that is as low as about 0.02 for the 100nm-thick AlN film.

4.3.3. Discussion

Despite the progresses that we have obtained in understanding the growth mechanisms of ZnO thin films and controlling the important decreasing in the leakage currents, the C (V) measurements have shown that these improvements were not sufficient to expect a stable piezoelectric response over time for applications concerning energy harvesting devices. These advances have nevertheless made it possible to master the realization of a highly strain sensor based on ZnO thin film and piezotronics effect by diode junction in another project of the group I participated actively, and as we have demonstrated in the article: R. Joly *et al.* DOI: 10.1016/j.sna.2020.112280. Regarding the application of magnetoelectric composites for energy harvesting we must turn now to another piezoelectric material we will described in the next chapter.

5

Growth of AlN thin film by plasma-enhanced atomic layer deposition

Due to the remaining issues of leakage current in ZnO thin films, even though (002)-oriented films are achieved with an important increase of the resistivity by 3 to 4 orders of magnitude, the piezoelectric response is not accessible for the long-term storage of strain-induced charges in the film and is thus not suited to our energy-harvesting objective. As an alternative, Aluminum Nitride (AlN) is an insulating piezoelectric material, which also has a wurtzite structure and piezoelectric properties similar to ZnO. In addition, AlN thin films can be synthesized by plasma-enhanced atomic layer deposition (PE-ALD), which ensures the necessary interface quality between AlN and a magnetostrictive material in fabricating magnetoelectric composites to get optimum elastic energy transfer. Similarly, AlN thin film requires a (002) preferential orientation so that the piezoelectric coefficient is maximized. In this chapter, we present optimal processes to synthesize AlN films at temperatures as low as 250 °C with a quantified piezoelectric response, which have not previously been reported for PE-ALD AlN thin films. Although this was the first time a nitride film process was developed by PE-ALD in our group at LIST, we considered this alternative a good candidate to synthesize magnetoelectric composites.

5.1
Optimization growth of AlN thin films

This section is dedicated to the optimization of the AlN growth process by plasma-enhanced atomic layer deposition at low temperatures. Indeed, the (002) orientation on the surface of wurtzite aluminum nitride is a necessary condition for obtaining a piezoelectric response. Also, the stoichiometry of the Al:N ratio to 1 with the lowest level of impurities, mainly oxygen and carbon, are mandatory conditions to maximize the piezoelectric behavior of the film. It is not an obvious solution to fulfill these conditions with low temperature processing (below 500°C) of AlN. Indeed, the synthesis of AlN thin films via chemical vapor deposition techniques always requires very high temperatures [1,2]. Based on the PE-ALD process we developed and described in Chapter 3, we modulated the different experimental parameters described in the next sections to converge with the most suitable formula to realize a highly conformal piezoelectric thin film at a low temperature.

5.1.1. Effect of plasma power

The effect of plasma time on the crystallinity of AlN thin films was investigated, as shown in Figure 5.1. AlN thin films were grown at 180 °C with the plasma time τ_{PE} that varied from 10-30 s. As can be seen, at the deposition temperature of 180 °C, the plasma time does not impact the film crystal structure, it remains (100) preferred orientation.

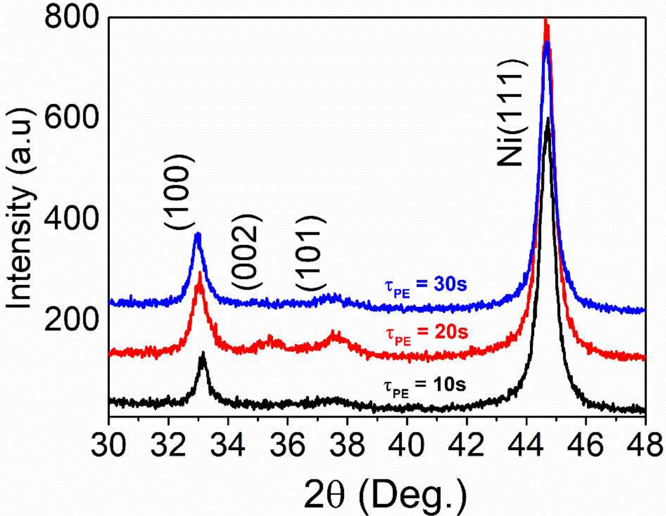

Figure 5.1: *XRD patterns of AlN thin films grown by PE-ALD at 180 °C with the plasma time of 10, 20, and 30 s.*

5.1.2. Effect of post-annealing processes

The high temperature post annealing is often suggested in the literature as a way to improve or change the crystallinity of a thin film [3–5]. We tried to apply the post-annealing process on the AlN

thin film grown at 180 °C with a plasma time of 20 s. The film was annealed *ex situ* at different temperatures from 400-800 °C for 1h. By the end of the post-annealing process, the (100) orientation was enhanced and dominant. (002) and (101) orientations was developed, however they remain minor compared to (100) orientation.

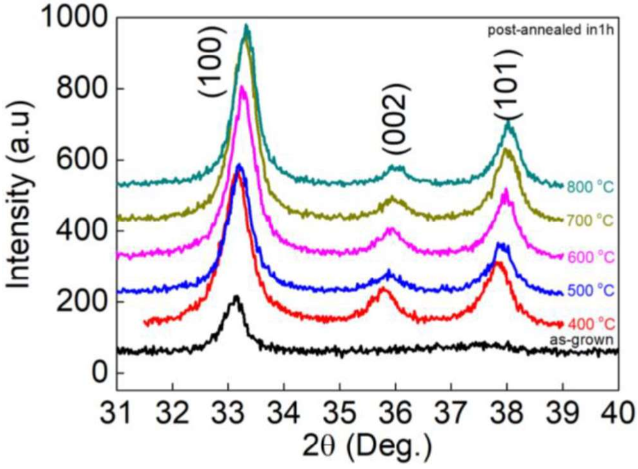

Figure 5.2: *XRD patterns of AlN thin films with post-annealing processed at 400-800 °C for 1h.*

5.1.3. Effect of ZnO buffer layers

P. Dutheil et al. and Eunju Lee et al. proposed stacking an AlN layer on top of a ZnO layer and *vice versa* with the role of the bottom layer being for the close epitaxial parameters of wurtzite AlN and wurtzite ZnO to induce a privileged (002) orientation of growth by PLD and radiofrequency (RF) magnetron sputtering, respectively [6,7]. In our case, AlN thin films was grown on ZnO buffer layers at 180 °C with a plasma time of 20 s. The ZnO buffer layers with a thickness of about 1 µm were (100) and (002) strongly preferred orientations. As can be seen from Figures 5.3 and 5.4, (002)-oriented AlN film is not achieved, even grown on a (002) strongly oriented ZnO film.

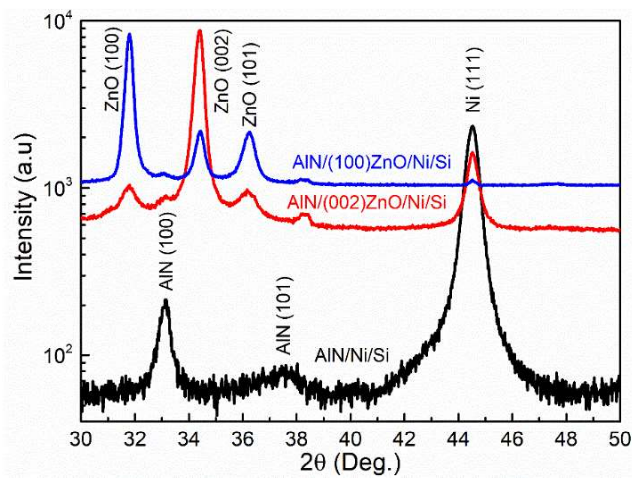

Figure 5.3: *XRD patterns of AlN thin films grown on (100)-oriented and (002)-oriented ZnO/Ni/Si(100).*

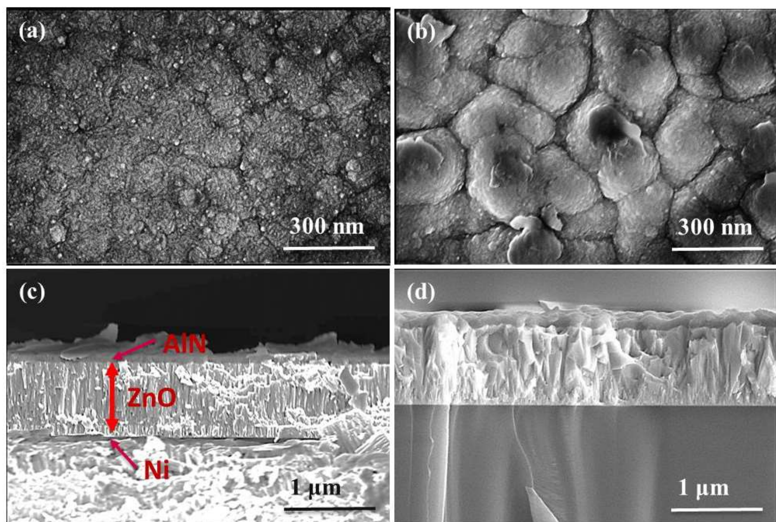

Figure 5.4: *Top-view and cross-sectional SEM micrographs of AlN thin films grown on (a,c) (002)-oriented- and (b,d) (100)-oriented and ZnO/Ni/Si(100).*

5.1.4. Discussion

As can be seen, at the growth temperature of 180 °C (002)-oriented AlN thin films cannot be obtained, despite several approaches such as the high-temperature post annealing and the use of (002)-oriented ZnO buffer layers being applied. Table 5.1 presents a survey on deposition techniques used to synthesize AlN thin films. For chemical methods such as PE-ALD, MOCVD, High Temperature Hydride Vapor Phase Epitaxy (HT-HVPE), a higher deposition temperature (above 250°C) is required. The next section will present how (002)-oriented AlN thin films and their piezoresponse can be achieved.

Table 5.1: *A summary of deposition techniques for the synthesis of AlN thin films.*

References	Techniques	Substrates	Temperature (°C)	Crystallite	e_{31} (C/m^2)
M. Gillinger et al. [8]	DC sputtering	(0001) Sapphire	110	(002)	Not reported
M. Schneider. [9]	DC sputtering	(100) Si	25-300	(002)	Not reported
Pelegrini et al.[10]	DC sputtering	(0001) Sapphire	550	(002)	-0.3 to -0.8
Akiyama et al.[11]	RF sputtering	Si_3N_4/Si	300	(002)	
Assouar et al.[12]	DC sputtering	(100) Si	350	(002)	
Shih et al.[2]	PE-ALD	c-sapphire	300	(002)	Not reported

Tarala et al.[13]	PE-ALD	Si/sapphire	250	Mostly (002)	Not reported
Dai et al.[14]	MOCVD	Si(111)	1150	(002)	Not reported
Sánchez et al.[15]	PE-CVD	(100) Si	>500	(002)	Not reported
M. Pons et al.[16]	CVD	(0001) Sapphire	1500	(002)	Not reported
R. Boichot et al.[17]	HT-HVPE	(0001) Sapphire	1500	(002)	Not reported
L. Tian[18]	PE-ALD	(100) Si	200-400	(002)	Not reported

5.1.5. References

(1) Huang, C. P.; Wang, C. H.; Liu, C. P.; Lai, K. Y. High-Quality AlN Grown with a Single Substrate Temperature below 1200 °c. *Sci. Rep.* **2017**. https://doi.org/10.1038/s41598-017-07616-8.

(2) Shih, H. Y.; Lee, W. H.; Kao, W. C.; Chuang, Y. C.; Lin, R. M.; Lin, H. C.; Shiojiri, M.; Chen, M. J. Low-Temperature Atomic Layer Epitaxy of AlN Ultrathin Films by Layer-by-Layer, in-Situ Atomic Layer Annealing. *Sci. Rep.* **2017**. https://doi.org/10.1038/srep39717.

(3) Jang, K.; Lee, K.; Kim, J.; Hwang, S.; Lee, J.; Kumar Dhungel, S.; Jung, S.; Yi, J. Effect of Rapid Thermal Annealing of Sputtered Aluminium Nitride Film in an Oxygen Ambient. *Mater. Sci. Semicond. Process.* **2006**. https://doi.org/10.1016/j.mssp.2006.10.052.

(4) Liu, B.; Gao, J.; Wu, K. M.; Liu, C. Preparation and Rapid Thermal Annealing of AlN Thin Films Grown by Molecular Beam Epitaxy. *Solid State Commun.* **2009**. https://doi.org/10.1016/j.ssc.2009.02.008.

(5) Phan, D. T.; Chung, G. S. The Effect of Geometry and Post-Annealing on Surface Acoustic Wave Characteristics of AlN Thin Films Prepared by Magnetron Sputtering. *Appl. Surf. Sci.* **2011**. https://doi.org/10.1016/j.apsusc.2011.05.050.

(6) Lee, E.; Park, J.; Yim, M.; Kim, Y.; Yoon, G. Characteristics of Piezoelectric ZnO/AlN-Stacked Flexible Nanogenerators for Energy Harvesting Applications. *Appl. Phys. Lett.* **2015**. https://doi.org/10.1063/1.4904270.

(7) Dutheil, P.; Orlianges, J. C.; Crunteanu, A.; Catherinot, A.; Champeaux, C. AlN, ZnO Thin Films and AlN/ZnO or ZnO/AlN Multilayer Structures Deposited by PLD for Surface Acoustic Wave Applications. *Phys. Status Solidi Appl. Mater. Sci.* **2015**. https://doi.org/10.1002/pssa.201431747.

(8) Gillinger, M.; Shaposhnikov, K.; Knobloch, T.; Stöger-Pollach, M.; Artner, W.; Hradil, K.; Schneider, M.; Kaltenbacher, M.; Schmid, U. Enhanced C-Axis Orientation of Aluminum Nitride Thin Films by Plasma-Based Pre-Conditioning of Sapphire Substrates for SAW Applications. *Appl. Surf. Sci.* **2018**. https://doi.org/10.1016/j.apsusc.2017.11.113.

(9) Schneider, M.; Bittner, A.; Schmid, U. Impact of Film Thickness on the Temperature-Activated Leakage Current Behavior of Sputtered Aluminum Nitride Thin Films. *Sensors Actuators, A Phys.* **2015**. https://doi.org/10.1016/j.sna.2015.01.032.

(10) Pelegrini, M. V.; Pereyra, I. Characterization of AlN Films Deposited by r.f. Reactive Sputtering Aiming MEMS Applications. In *Physica Status Solidi (C) Current Topics in Solid State Physics*; 2010. https://doi.org/10.1002/pssc.200982861.

(11) Akiyama, M.; Ueno, N.; Tateyama, H.; Nagao, K.; Yamada, T. Preparation of Highly Oriented Aluminum Nitride Thin Films on Molybdenum Bottom Electrodes Using Metal Interlayers. *J. Mater. Sci.* **2005**. https://doi.org/10.1007/s10853-005-6932-2.

(12) Assouar, M. B.; Elmazria, O.; Le Brizoual, L.; Alnot, P. Reactive DC Magnetron Sputtering of Aluminum Nitride Films for Surface Acoustic Wave Devices. *Diam. Relat. Mater.* **2002**. https://doi.org/10.1016/S0925-9635(01)00708-7.

(13) Tarala, V.; Ambartsumov, M.; Altakhov, A.; Martens, V.; Shevchenko, M. Growing C-Axis Oriented Aluminum Nitride Films by Plasma-Enhanced Atomic Layer Deposition at Low Temperatures. *J. Cryst. Growth* **2016**. https://doi.org/10.1016/j.jcrysgro.2016.10.015.

(14) Dai, Y.; Li, S.; Sun, Q.; Peng, Q.; Gui, C.; Zhou, Y.; Liu, S. Properties of AlN Film Grown on Si (111). *J. Cryst. Growth* **2016**. https://doi.org/10.1016/j.jcrysgro.2015.11.016.

(15) Sánchez, G.; Abdallah, B.; Tristant, P.; Dublanche-Tixier, C.; Djouadi, M. A.; Besland, M. P.; Jouan, P. Y.; Bologna Alles, A. Microstructure and Mechanical Properties of AIN Films Obtained by Plasma Enhanced Chemical Vapor Deposition. *J. Mater. Sci.* **2009**. https://doi.org/10.1007/s10853-009-3847-3.

(16) Pons, M.; Boichot, R.; Coudurier, N.; Claudel, A.; Blanquet, E.; Lay, S.; Mercier, F.; Pique, D. High Temperature Chemical Vapor Deposition of Aluminum Nitride, Growth and Evaluation. *Surf. Coatings Technol.* **2013**. https://doi.org/10.1016/j.surfcoat.2013.06.011.

(17) Boichot, R.; Coudurier, N.; Mercier, F.; Lay, S.; Crisci, A.; Coindeau, S.; Claudel, A.; Blanquet, E.; Pons, M. Epitaxial Growth of AlN on C-Plane Sapphire by High Temperature Hydride Vapor Phase Epitaxy: Influence of the Gas Phase N/Al Ratio and Low Temperature Protective Layer. *Surf. Coatings Technol.* **2013**. https://doi.org/10.1016/j.surfcoat.2013.08.016.

(18) Tian, L.; Ponton, S.; Benz, M.; Crisci, A.; Reboud, R.; Giusti, G.; Volpi, F.; Rapenne, L.; Vallée, C.; Pons, M.; Mantoux, A.; Jiménez, C.; Blanquet, E. Aluminum Nitride Thin Films Deposited by Hydrogen Plasma Enhanced and Thermal Atomic Layer Deposition. *Surf. Coatings Technol.* **2018**. https://doi.org/10.1016/j.surfcoat.2018.04.031.

5.2

A film-texture driven piezoelectricity of AlN thin films grown at low temperatures by plasma-enhanced atomic layer deposition

This chapter is based on the publication: **Tai Nguyen**, et al., "*A film-texture driven piezoelectricity of AlN thin films grown at low temperatures by plasma-enhanced atomic layer deposition*", in APL Materials 8(7), 71101 (2020). (DOI: 10.1063/5.0011331).

A film-texture driven piezoelectricity of AlN thin films grown at low temperatures by plasma-enhanced atomic layer deposition

Cite as: APL Mater. 8, 071101 (2020); doi: 10.1063/5.0011331
Submitted: 20 April 2020 • Accepted: 15 June 2020 •
Published Online: 1 July 2020

View Online

Export Citation

CrossMark

Tai Nguyen,[1,2] Noureddine Adjeroud,[1] Sebastjan Glinsek,[1] Yves Fleming,[1] Jérôme Guillot,[1] Patrick Grysan,[1] and Jérôme Polesel-Maris[1,a)]

AFFILIATIONS

[1] Materials Research and Technology Department, Luxembourg Institute of Science and Technology, 41, Rue du Brill, L-4422 Belvaux, Luxembourg
[2] Department of Physics and Materials Science, University of Luxembourg, Campus Limpertsberg, 162 Avenue de la Faïencerie, L-1511 Luxembourg, Luxembourg

[a)] Author to whom correspondence should be addressed: jerome.polesel@list.lu

ABSTRACT

Simultaneously inducing preferred crystalline orientation with a strong piezoelectric response in polycrystalline aluminum nitride (AlN) thin films by atomic layer deposition is a technical challenge due to the upscaling of the integration of piezoelectric functionalities, such as sensing and actuation, in micro-devices without any poling process. Utilizing low-temperature plasma-enhanced atomic layer deposition (PE-ALD), highly c-axis-oriented AlN films have been prepared with precise control over the relative composition, purity levels, and chemical states of constituent elements. Tailoring thermodynamic parameters, such as the growth temperature and purging time after the trimethylaluminum precursor pulsing before the N_2:H_2:Ar plasma reaction, provide the possibility of modulating the texture coefficient and the relative piezoelectric response. The effective transverse piezoelectric $e_{31,f}$ coefficient of 0.37 C/m^2 was achieved on the AlN film grown at 250 °C and 30 s with the highest texture coefficient TC(002) of 2.75 along the c-axis orientation. The process proposed, at a low temperature with the highly conformal growth of aluminum nitride thin films by PE-ALD, opens up pathways to design novel piezoelectric functional materials for micro-electro-mechanic system devices with complementary metal oxide semiconductor process temperature compatibility.

© 2020 Author(s). All article content, except where otherwise noted, is licensed under a Creative Commons Attribution (CC BY) license (http://creativecommons.org/licenses/by/4.0/). https://doi.org/10.1063/5.0011331

I. INTRODUCTION

Aluminum nitride (AlN) thin films have attracted significant attention in optoelectronics[1] and micro-electro-mechanic system (MEMS) applications, for example, energy harvesting,[2–4] and surface-acoustic-wave transducers and resonators,[2,4] due to their excellent properties such as a wide direct bandgap of 6.2 eV, piezoelectricity along the c-axis, high phase velocities, and high thermal stability.[2] In addition, the AlN film does not require any poling processes due to its oriented structure that facilitates its integration into micro-systems. However, these applications require a (002) crystalline structure of the AlN film to achieve the piezoelectric effect and highest surface acoustic velocity[2] because it is well known that the hexagonal wurtzite AlN has a spontaneous polarization along the c-axis.[5] There are many techniques, including physical and chemical deposition methods, which can be used to grow (002)-oriented AlN films. For instance, (002)-oriented AlN films can be synthesized by radio frequency (RF) sputtering,[6–8] pulsed laser deposition (PLD),[9–11] chemical vapor deposition (CVD),[12–14] and molecular beam epitaxy.[15,16] Nevertheless, the abovementioned techniques present severe drawbacks: either the anisotropy of the deposited film prevents the conformal coating of sophisticated micro-systems or they often require high temperatures of over 350 °C to deposit AlN films that may lead to incompatibility with complementary metal oxide semiconductor (CMOS) and MEMS processing. Moreover, the recent emergence of electronics based on organic flexible substrates demand low-temperature processes to enable integration and functionalization.[3,17,18]

To overcome the abovementioned issues, plasma-enhanced atomic layer deposition (PE-ALD) has emerged as a promising technique to grow high-quality AlN films with superior conformity.[19–25] Sadeghpour *et al.*[19] presented PE-ALD processes to fabricate AlN films by tuning several deposition parameters, such as deposition temperature at 280 °C and 300 °C, and surface pre-treatment by Piranha. However, the obtained AlN films were of (100) preferred orientation and not conducive for obtaining a high piezoelectric coefficient. However, the (002)-oriented film was barely achieved even though the high temperature of 900 °C was applied for post-annealing. Shih and co-workers[22] reported high-quality AlN thin films grown using the PE-ALD technique accompanied by *in situ* atomic layer annealing (ALA). Thanks to a long *in situ* ALA process of 40 s, the AlN thin film was converted from the amorphous to a single-crystalline epitaxial film at a low deposition temperature of 300 °C. Tarala *et al.*[21] studied a low-temperature PE-ALD process of 250 °C to grow AlN thin films. They demonstrated that by carefully adjusting PE-ALD parameters, the preferentially (002)-oriented AlN thin films can be obtained. So far, although high-quality AlN films are achieved by the PE-ALD technique, the piezoelectric properties of the AlN films and the correlation between the film texture and the piezoelectric property have not yet been reported. This situation is summarized in Table S1 of the supplementary material.

In this scope, the aim of the current study is to propose a procedure to grow AlN films at low temperatures of 180 °C and 250 °C with a controlled preferential (002) orientation and to evaluate the piezoelectric properties of the obtained AlN films. We have systematically investigated several PE-ALD parameters, such as the deposition temperatures and the purging time after the precursor short pulsing, to unravel the interplay of the thermodynamic parameters in the growth of the (002)-oriented AlN films and the correlation between the crystal structures and the piezoelectricity of AlN films. We demonstrate that the deposition temperature associated with the purging time is a control knob to tune the AlN film texture. Indeed, the film texture is converted from the preferred (100) orientation to the strongly preferred (002) orientation by increasing the deposition temperature from 180 °C to 250 °C and the purging time from 5 s to 30 s. In addition, piezoelectric characterization reveals that a higher texture coefficient TC(002) induces a higher piezoelectric coefficient $e_{31,f}$. Comparing to other deposition techniques, e.g., PLD, CVD, and sputtering, an advantage of PE-ALD is that it is able to produce a conformal coating on complex and non-planar structures, which are often present in MEMS structures. By this means, one can get improved material interfaces at low temperatures for composite film stacking, allowing manipulation of material properties as it is the case, for example, for thin-film magnetoelectric composites.[26–28]

II. EXPERIMENTAL

The AlN thin films were grown by using a commercial PE-ALD reactor (TFS-200, Beneq, Finland) using standard precursors such as trimethylaluminum $Al_2(CH_3)_6$ (TMA, Strem Chemicals, Inc., France) and a mixture of N_2:H_2:Ar gases with a flow ratio of 100 ppm/80 ppm/30 ppm. The gases used during PE-ALD were ALPHAGAZ 2 grade with a global purity of ≥99.9999% mol with less than 0.5 H_2O ppm mol impurity. The AlN films were deposited on pristine single crystal Si(100) substrates (Siegert GmbH, Germany, grade Monitor) and on 150 nm-thick nickel-coated silicon substrates. The nickel layer was deposited by sputtering (Bal-Tec Med 020 high vacuum coating system, nickel target ≥99.9999% purity level from Goodfellow GmbH, Germany) in order to use the Ni(111) diffraction peak as a reference for the diffraction peak overlay of the AlN films against the different PE-ALD growth parameters. The substrates were cleaned in acetone, isopropanol, and DI water, followed by dehydration for 20 min at 200 °C prior to the PE-ALD growth of AlN films. Before being introduced into the reactor, an additional plasma cleaning (Plasma-Therm 790 RIE, 120 W, 10 min, in Ar:O_2 gas environment at 25 mTorr) was performed on the substrates. The AlN films were grown by the following sequence of four steps: TMA (0.1 s), N_2 purge (t_{purge} seconds), N_2:H_2:Ar plasma (20 s), and N_2 purge (5 s). The purging time t_{purge} after the TMA pulse was varied to be 5 s, 10 s, 20 s, and 30 s, and the deposition temperature was 180 °C and 250 °C. The plasma power was set at 100 W. All AlN films presented in this study were grown with 1500 cycles of the abovementioned sequence, except for sample A1 and sample A5, which were grown with 5000 cycles. Detailed processing information is summarized in Table I.

The thickness of AlN films was measured by ellipsometry (J. A. Woolam ellipsometer). The film crystal structure was examined by x-ray diffraction (Bruker D8 Discover diffractometer with Cu Kα radiation and a 5-axis Eulerian cradle) in the θ/2θ (Bragg–Brentano) configuration. In order to prevent the signal from fluorescence due to the underlying Ni layer, a solid-state point detector (tradename SoIX) was used for all measurements. Pole figure measurements were conducted on samples A1 and A5 in the θ/2θ mode with an increment of 5° in φ (phi) and 3° in χ (chi). The measurement

TABLE I. List of the PE-ALD AlN thin films with the process parameters. A1 and A5 were processed with 5000 cycles; A2, A3, and A4 were processed with 1500 cycles.

Samples	Deposition temperature (°C)	Purging time t_{purge} (s)	Thickness (nm)	Growth rate (Å/cycle)
A1	180	5	600	1.20
A2	250	10	120	0.80
A3	250	20	157	1.05
A4	250	30	160	1.07
A5	250	30	590	1.18

© Author(s) 2020

was performed at up to 72° in chi using a collimated irradiation of 1 mm beam diameter. For both samples, pole figures were performed on the (100), (002), and (101) peak positions. For each peak position, the background was measured to the right and the left of the peak position for one angle of phi only. The defocusing correction was carried out based on the number of counts measured on the (104) and (113) peak positions of the NIST standard SRM1976. The pole figure data treatment was performed using the MTEX toolbox (version 5.1.1)[29] in conjunction with Matlab®. Scanning electron microscopy (Helios 650 FIB-SEM, FEI company, USA) was used to analyze the microstructure of the films. Both top-view and cross-sectional configurations were performed to investigate surface morphology and confirm the thickness of the films, respectively. Topography acquisitions were carried out with a commercial atomic force microscopy (AFM Innova, Bruker Inc., Santa Barbara) in tapping mode by maintaining the amplitude of the cantilever first resonance constant. Images were taken over $2 \times 2\ \mu m^2$ at a scan rate of 1 Hz. The tips used were HQ:NSC (MikroMasch, Bulgaria), diamond-like carbon coated, with a cantilever stiffness of 40 N/m. The surface roughness was extracted via the NanoScope software. Prior to calculation, the plane subtraction was applied. The grain size analysis was carried out with the SPIP software in watershed mode detection for stacked features. The elemental composition and the chemical states of the elements were studied using x-ray photoelectron spectrometry (XPS) (Axis Ultra DLD, Kratos Analytical Ltd.) using a monochromated Al K_α (E = 1486.6 eV) working at 150 W. The energy resolution, determined from the Ag 3d contribution of a silver sample, was 1.5 eV for survey scans and 0.55 eV for narrow scans. The analyzed area was 110 μm in diameter. The depth profiles were carried out in the etched area of 3×3 mm^2 by an Ar^+ ion beam operating at 2 kV and 2 μA. The spectra have been calibrated with the Al 2p (Al–N) component at 73.6 eV.[30] For the piezoelectric characterization, AlN films were deposited on silicon wafers with a 150 nm-thick nickel layer as the bottom electrode and a 100 nm layer of aluminum as the top electrode. The specific cantilevers for the four-point bending (4-PB) characterization[31] were fabricated using laser lithography and wet etching processes. An S1813 photoresist (micro resist technology GmbH) was used as a wet etching mask for defining selective areas of metal electrodes. It was spin-coated, exposed to UV (MLA150, Heidelberg Instruments), baked at 120 °C, and developed with a MF319 developer. The 4-PB electromechanical method (aixACCT TF Analyzer 2000) was used to measure the effective transverse piezoelectric coefficient $e_{31,f}$ of the AlN films, which is extracted using the following equation:[31]

$$e_{31,f} \cong \frac{Ql^2}{4Ahu(1 - \nu_{Si})}, \quad (1)$$

where Q is the induced charge and l is the load span of the 4-PB configuration (10 mm). A is the top electrode area of 16 mm^2, h is the sample thickness, u is the induced displacement, and ν_{Si} is Poisson's ratio for silicon (0.064).[31] The slope of the charge vs strain is directly proportional to the $e_{31,f}$ coefficient.

III. RESULTS AND DISCUSSION

Figure 1(a) shows the x-ray diffraction patterns of five AlN films A1–A5 deposited on nickel-coated silicon wafers. The patterns of AlN films match with the standard diffraction pattern of

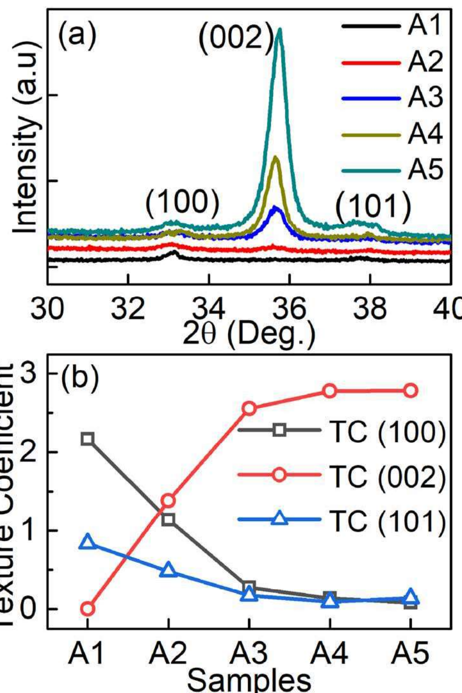

FIG. 1. (a) XRD data of AlN films grown on (100) silicon with a 150 nm-thick nickel bottom layer and (b) calculated texture coefficient (TC) of (100), (002), and (101) planes of samples A1 (180 °C, 5 s), A2 (250 °C, 10 s), A3 (250 °C, 20 s), A4 (250 °C, 30 s), and A5 (250 °C, 30 s).

the hexagonal AlN crystal structure (JCPDS-65-3409). It can be seen that AlN thin film A1 deposited at the substrate temperature of 180 °C and with the purging time of 5 s displayed a (100) preferred orientation, whereas the crystal structure of AlN films grown at 250 °C (A2 to A5) was modulated by the purging time. A preferential (002) orientation of the polycrystalline film started developing as the deposition temperature increased to 250 °C and the purging time of 10 s (sample A2). Further increasing the purging time to 20 s and 30 s, the films grew mainly in the (002) direction.

In Fig. 1(b), the texture coefficient (TC) for the (002) plane is calculated to quantify the (002)-preferred orientation of the AlN film, as defined by the following equation:[32,33]

$$\mathrm{TC}(hkl) = \frac{I(hkl)/I_0(hkl)}{N^{-1}\sum_N I(hkl)/I_0(hkl)}, \quad (2)$$

where $I(hkl)$ is the measured relative intensity of the (hkl) peak, $I_0(hkl)$ is the standard intensity from the JCPDS-65-3409 PDF data, and N is the number of diffraction peaks considered in the calculation.

It can be derived from Eq. (2) that for a polycrystalline film with no preferred orientation, the TC values for all reflections equal one. For a film with a preferential orientation, the TC of the preferred orientation increases and reaches a maximum value of N in the extreme case where no other reflections are present in the XRD data. In these calculations, we used N = 3 for the peaks (100), (002), and (101)

© Author(s) 2020

investigated. From the results in Fig. 1(b), the texture coefficient of the (002) plane, TC(002), became prominent as the purging time increased from 10 s to 30 s. While the TC(002) of AlN films A4 and A5 grown at 250 °C and 30 s are about 2.78, the TC(002) of an AlN film A1 deposited at 180 °C and 5 s is almost 0. On the other hand, the texture coefficient of the (100) plane is approximately 2.17, 0.14, and 0.08 for samples A1, A4, and A5, respectively. It strongly implies that the preferred orientation of samples A4 and A5 is the (002) plane, whereas sample A1 is the preferentially (100)-oriented film. Thus, the modulation of the crystalline structure of AlN thin films reveals the strong impact of the substrate temperature and purging time on the nucleation and preferential growth of the film.

The pole figures were constructed to provide complementary information about the preferred orientations of the AlN grains in the polycrystalline film synthesized at 180 °C and 5 s (A1) and the film grown at 250 °C and 30 s (A5), as presented in Fig. 2. The calculated Orientation Distribution Functions (ODFs) derived from the pole figures confirm that some degrees of texture are observed in both samples. Namely, the pole figures of the AlN film grown at 250 °C and with a purging time of 30 s display a preferred orientation along the c-axis without any significant misalignment [Fig. 2(a)], whereas the (100) orientation is prominent in the AlN film synthesized at 180 °C and 5 s [Fig. 2(b)]. This evolution in texture is verified from the calculated texture index/entropy[29] changing from 3.07/−0.67 for the AlN film synthesized at 180 °C and 5 s to 5.25/−0.89 for the AlN film deposited at 250 °C and 30 s.

To elucidate the growth mechanisms of the preferentially (002)-oriented AlN films, our hypothesis is based on a thermodynamic aspect that the kinetic energy and the surface mobility of adatoms determine the crystalline orientations of the films. In our case, the growth mechanism of the film is impacted by the deposition temperature on the kinetic energy of the adatoms and the diffusion time of the adatoms related to the purging time between the TMA pulsing and the N_2:H_2:Ar plasma step. Table I reports the different growth rate depending on the deposition temperature and the purging time. While samples A1 and A2 have a quite different growth rate but show a similar XRD pattern with a main (100) orientation, sample A5 with a strong (002) orientation has the same growth rate as sample A1. The growth rates estimated in Table I show a trend of higher growth values for longer purging time for the samples synthesized at 250 °C and with 1500 cycles. A higher substrate temperature and longer purging time increase the kinetic energy and mobility of adatoms. It is worth mentioning that among the (100), (101), and (001) planes, the surface energy of (002) is highest.[34] Namely, the surface energies of (100), (110), Al-polar (002), and N-polar (002) surfaces are 145 meV/Å^2, 234 meV/Å^2, 355 meV/Å^2, and 374 meV/Å^2, respectively. Increasing the movement of adatoms by a higher substrate temperature and a longer purging time, therefore,

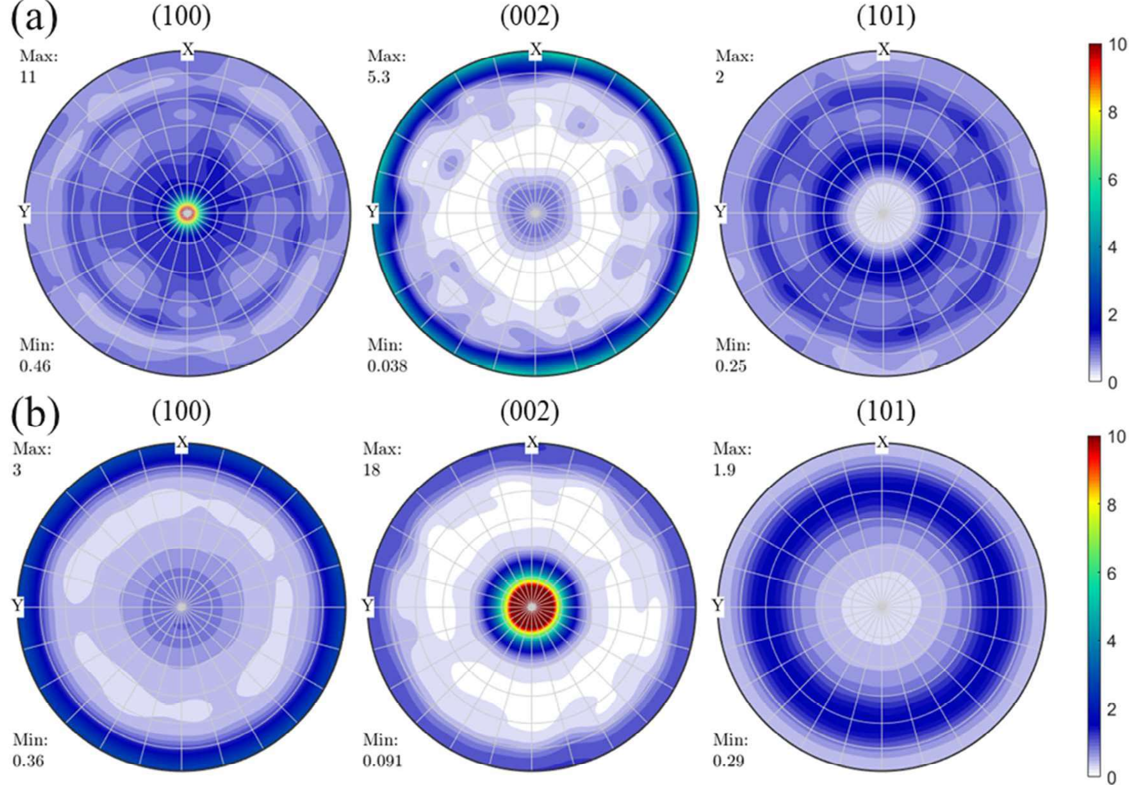

FIG. 2. Pole figure measurement of (a) AlN sample A1 (180 °C, 5 s) and (b) AlN sample A5 (250 °C, 30 s) grown on 150 nm-thick nickel-coated (100) silicon substrates.

© Author(s) 2020

facilitates the movement and arrangement of adatoms, thus promoting growth along the (002) orientation. Additionally, the effect of a number of ALD cycles on the growth rate was observed by Sadeghpour *et al.*[19] In this study, a plausible explanation for the deviation is due to the incomplete reaction of N_2 and H_2 to methyl groups of the TMA precursor and/or nonuniform nucleation on the surface substrate in the early cycles.

The top-view SEM images shown in Fig. S1 of the supplementary material confirm a homogeneous surface of the films without pinholes or cracks. The growth temperatures and pulsing times considered did not significantly influence the surface morphologies of the AlN layers. The AFM images were taken to further confirm the films' topography quality, as presented in Fig. 3. The film roughnesses (Rq) were estimated to be 1.69 nm, 2.83 nm, 2.69 nm, and 2.05 nm for samples A1, A2, A3, and A4, respectively. In addition, the grain-diameter distribution histogram was extracted from the topography. The mean diameters in nanometers were 61.63 ± 22.83, 95.98 ± 36.28, 76.22 ± 25.22, and 53.24 ± 18.64 for samples A1, A2, A3, and A4, respectively.

Figures 4(a) and 4(b) show the XPS survey scans for samples A1–A4 before and after Ar^+ etching, respectively. The elemental composition of the samples (main elements and impurities) is detailed in Table S2 of the supplementary material. As indicated in Fig. 4(a), among the aluminum and nitrogen peaks, a considerable amount of carbon was observed, which is attributed to the contaminants on the surface. Notably, a prominence of oxygen level indicates that the top surface of the film is strongly oxidized. The carbon and oxygen levels were significantly lowered after etching. While the carbon level was found to be about 1.3%–2%, there was a noticeable presence of an oxygen level of 6%–9% inside the films. The low amount of carbon in the films implies that no considerable incorporation of carbon containing ligands from the TMA and a complete decomposition of the precursors occurred.[23] However, the oxygen is likely a result of oxidization during the synthesis, which can occur in the presence of moisture in the reactor chamber and/or the remaining moisture in the gas flow. There are two small peaks corresponding to Ar, implanted in the film by the sputter cleaning process. The level of the impurity concentrations observed is similar to the results in the literature.[23,30] In addition, the Al/N ratios are calculated to be 1.10, 1.09, 1.08, and 1.10 for samples A1 to A4, respectively.

The Al 2p and N 1 s narrow scans were also acquired for the further investigation of the chemical states of aluminum and nitrogen, as depicted in Figs. 5(a) and 5(b), respectively. Subsequently, the peak fitting was carried out for the Al 2p and N 1s spectra of sample A4 [Figs. 5(c) and 5(d)]. Due to the complicated contribution of

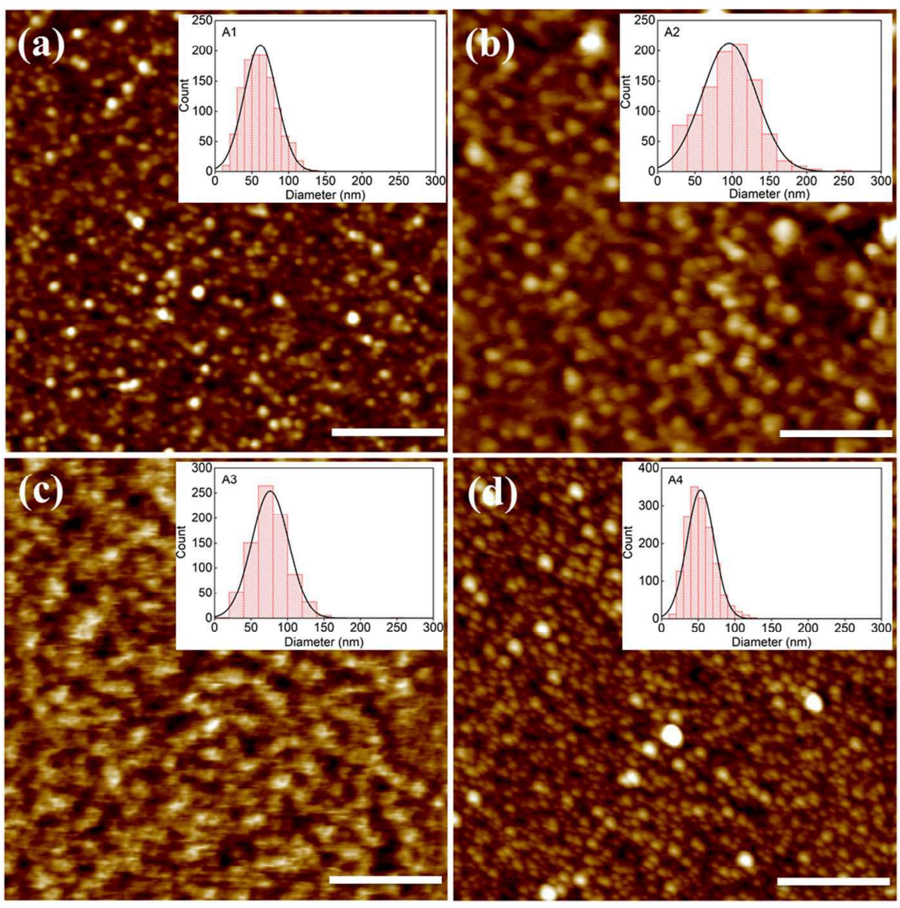

FIG. 3. AFM images of [(a)–(d)] AlN film samples A1–A4 on nickel-coated (100) silicon substrates, respectively. The respective insets present the grain-diameter distribution histogram extracted from the AFM images. The scale bar is 500 nm.

© Author(s) 2020

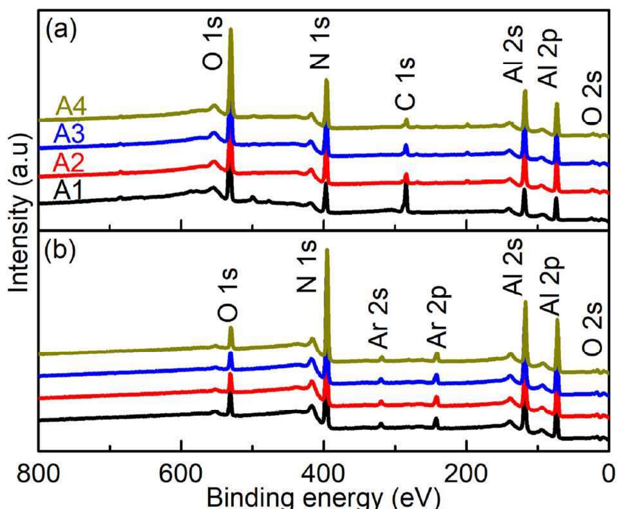

FIG. 4. XPS survey scans of AlN films grown on (100) silicon substrates (a) before and (b) after surface cleaning by Ar^+ sputtering.

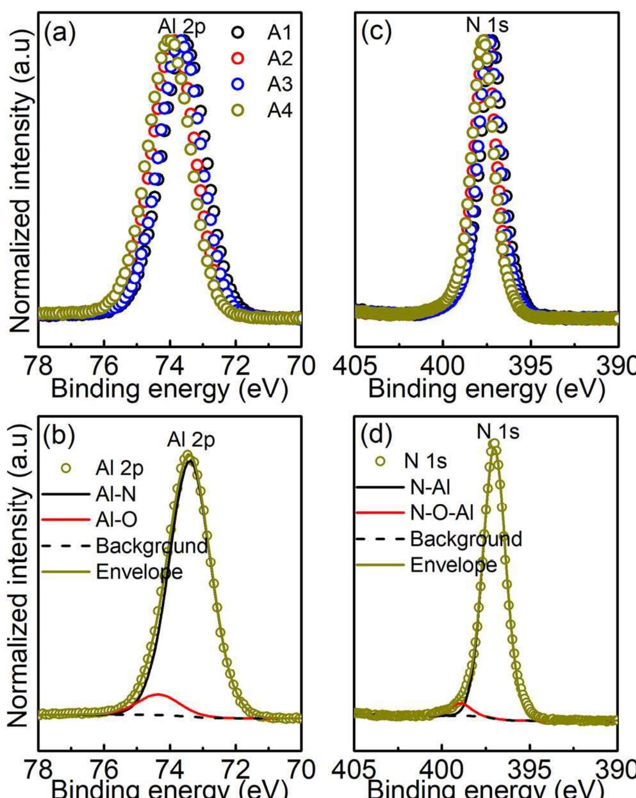

FIG. 5. The narrow scans of AlN films grown on (100) silicon substrates: (a) Al 2p and (b) N 1s spectra of samples A1–A4; and the peak fitting of (c) Al 2p and (d) N 1s spectra of sample A4. The spectra were acquired after surface cleaning by Ar^+ sputtering.

oxygen presented in the films, we propose a robust method in order to obtain the precise fitting of the Al 2p peak. The method is followed by a sequence of three steps: (i) the C 1s peak is fitted to estimate the CO_x components, (ii) the O–Al contribution is estimated from the O 1s peak using the CO_x results, and (iii) the Al 2p is fitted by taking into account the previously determined O–Al contribution and combining it with the elemental composition.

As a result, the Al 2p peak located at 73.6 eV is split into two subcomponents [Fig. 5(c)]: a predominant peak (92.6%) at 73.6 eV ascribed to Al–N bonds and a secondary peak (7.4%) at 74.6 eV allocated to Al–O bonds.[23,35,36] The percentages of the main peak and the secondary peak are 90.9% and 9.1%, 93.5% and 6.6%, and 94.3% and 5.7% for samples A1, A2, and A3, respectively. The origin of oxygen defects has been discussed so far.[36] Harris *et al.* and Slack *et al.*[37] have demonstrated that depending on the oxygen concentrations, the oxygen defect can be located in different positions and can form an additional phase: (i) at low oxygen concentrations, the oxygen substitutes a nitrogen site O_N, (ii) at the oxygen concentration of about 0.75 at. %, a transition in the oxygen accommodating defect occurs, and (iii) upon this transition, a new type of oxygen defect based on octahedrally coordinated aluminum forms. Since the oxygen concentration of the present AlN films is 6–9.3 at. %, above the transition, one can reasonably suppose that oxygen is chemically bound to aluminum. The N 1s narrow scan [Fig. 5(d)] can be deconvoluted into two subpeaks, i.e., a main peak (96%) located at 397.01 eV is assigned to the N–Al bond and a small peak (4%) located at 398.9 eV is assigned to the N–O–Al bond. It is noted that all narrow scans were acquired after cleaning the surface by Ar^+ sputtering; thus, the elemental levels and binding energies were values in the bulk of the film.

Figure 6(a) shows the results of the 4-PB measurement. It can be seen that the $e_{31,f}$ coefficient of the AlN film A1 grown at 180 °C and with 5 s of purging time was almost zero, whereas this coefficient was measured to be 0.05 C/m^2, 0.25 C/m^2, 0.33 C/m^2, and 0.37 C/m^2 for samples A2, A3, A4, and A5, respectively. Interestingly, the $e_{31,f}$ coefficient rose up as the deposition temperature and the purging time increased. The increase in the deposition temperature and the purging time subsequently modulates the crystalline structure of AlN films, which influences the piezoelectricity of AlN. Figure 6(b) presents an intimate correlation between the TC(002) and the $e_{31,f}$ coefficient. The $e_{31,f}$ coefficient is increased by increasing the TC(002) of AlN films by a higher deposition temperature (250 °C) and a longer purging time. The maximum value of the $e_{31,f}$ coefficient was about 0.37 C/m^2 for the 590 nm-thick AlN film synthesized at 250 °C and with a purging time of 30 s, which possessed the highest TC(002) among the other samples. Consequently, a higher (002) crystalline structure of AlN film results in a higher piezoelectric coefficient.

It should be noted that there is a variation in the thickness of the samples. However, this variation does not significantly impact the $e_{31,f}$ coefficient of the AlN film as for samples A4 and A5, but the crystalline structure of AlN films does. Comparing samples A1 and A4, while sample A1 with a thickness of 600 nm and (100)-preferred orientation did not show a piezoelectric effect, the $e_{31,f}$ coefficient was measured as 0.33 C/m^2 for sample A4 with a thickness of 160 nm and (002)-preferred orientation. Increasing the thickness of the (002)-oriented sample, the $e_{31,f}$ coefficient of the 590 nm-thick AlN film (A5) slightly increased to 0.37 C/m^2 compared to sample

© Author(s) 2020

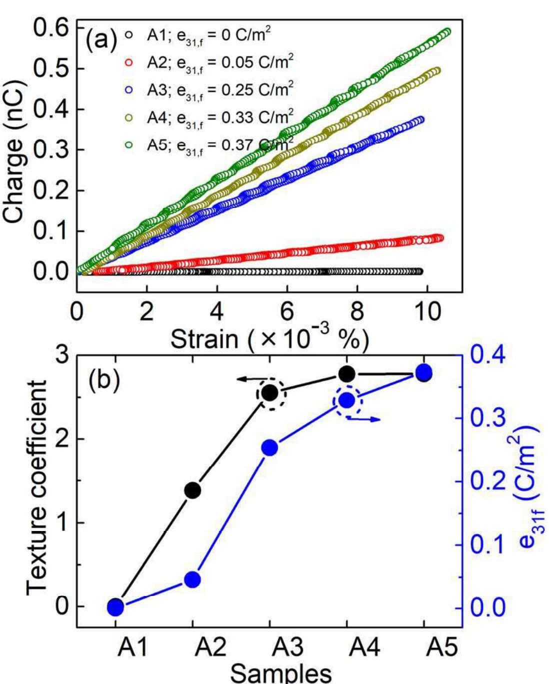

FIG. 6. (a) The four-point bending measurement of AlN films on (100) silicon substrates coated with a 150 nm of nickel layer as a bottom electrode and (b) a correlation of texture coefficient of (002) plane TC(002) (black dots) and $e_{31,f}$ coefficient (blue dots).

A4. Indeed, the thickness dependence of the piezoelectric coefficient was reported by Schneider and co-workers.[38] They pointed out that the piezoelectric coefficient d_{33} of AlN films was almost doubled as the thickness of the AlN film increased from 40 nm to 100 nm. This evolution of the piezoelectric response resulted from the initial inhomogeneous growth regime, which becomes less significant when the film thickness is increased. Beyond 100 nm, further increasing the thickness of the AlN film has no remarkable influence on the piezoelectric coefficient d_{33}. Therefore, the increase in the $e_{31,f}$ coefficient of our films is mainly due to an improvement of the (002) crystal structure of AlN films triggered by the deposition temperature and the purging time.

IV. CONCLUSION

In summary, we have presented a study to control the growth of aluminum nitride thin films with a piezoelectric response by plasma-enhanced atomic layer deposition at low deposition temperatures of 180 °C and 250 °C. By carefully adjusting some thermodynamic parameters of the plasma-enhanced atomic layer deposition, such as the deposition temperature and the purging time, the deposition of preferentially (002)-oriented aluminum nitride films has been achieved. X-ray diffraction and pole figure measurements pointed out that the high quality and preferentially (002)-oriented film was obtained at the deposition temperature of 250 °C and with the purging time of 30 s. X-ray photoelectron spectrometry confirmed the high-quality of AlN films with a carbon level of 1 at. %, an oxygen amount of 6 at. %–9 at. %, and an Al/N stoichiometric ratio close to one even at low deposition temperatures. Moreover, the effective transverse piezoelectric $e_{31,f}$ coefficients were assessed. Their measurements revealed a strong correlation between the film texture and the piezoelectric response of the aluminum nitride layer. Accordingly, the highest value of the effective transverse piezoelectric $e_{31,f}$ coefficient of 0.37 C/m^2 was achieved on the AlN film grown at 250 °C and 30 s with the highest texture coefficient TC(002) of 2.75 along the c-axis orientation. Our procedure for the low-temperature and highly conformal growth of aluminum nitride thin films by plasma-enhanced atomic layer deposition opens up pathways to design novel piezoelectric functional materials for MEMS devices with CMOS process temperature compatibility. An advantage of this is that the effect of morphology (roughness and pinholes) and interfacial issues between materials with different thermal expansion coefficients (microcracks and interdiffusion), easily occurring in high temperature processes, can thus be alleviated.

SUPPLEMENTARY MATERIAL

The supplementary material contains a survey on AlN film growth by various techniques (Table S1), the elemental concentration and the Al/N stoichiometric ratio of the AlN thin films (Table S2), and the SEM top-view images of samples A1–A4 (Fig. S1).

ACKNOWLEDGMENTS

The authors acknowledge Dr. Stéphanie Girod for training and advice on the laser lithography machine to process the AlN cantilevers for the 4-PB measurement. The authors gratefully acknowledge the financial assistance provided by the FNR in the framework of the FNR PRIDE MASSENA 15/10935404/MASSENA programme.

DATA AVAILABILITY

The data that support the findings of this study are available from the corresponding author upon reasonable request.

REFERENCES

[1]H. X. Jiang and J. Y. Lin, *Optoelectronic Devices III Nitrides* (Elsevier, 2005).
[2]C. Fei, X. Liu, B. Zhu, D. Li, X. Yang, Y. Yang, and Q. Zhou, Nano Energy **51**, 146–161 (2018).
[3]L. Algieri, M. T. Todaro, F. Guido, V. Mastronardi, D. Desmaële, A. Qualtieri, C. Giannini, T. Sibillano, and M. De Vittorio, ACS Appl. Energy Mater. **10**, 5203–5210 (2018).
[4]A. Khan, Z. Abas, H. Soo Kim, and I.-K. Oh, Smart Mater. Struct. **25**, 053002 (2016).
[5]F. Bernardini, V. Fiorentini, and D. Vanderbilt, Phys. Rev. B **56**, R10024 (1997).
[6]P. Frach, S. Barth, H. Bartzsch, and D. Gloess, Proc. SPIE **10194**, 101942Z (2017).
[7]A. Taurino, M. A. Signore, M. Catalano, and M. J. Kim, Mater. Lett. **200**, 18–20 (2017).
[8]S. Barth, H. Bartzsch, D. Glöß, P. Frach, T. Modes, O. Zywitzki, G. Suchaneck, and G. Gerlach, Microsyst. Technol. **22**, 1613–1617 (2016).
[9]C. Cibert, M. Chatras, C. Champeaux, D. Cros, and A. Catherinot, Appl. Surf. Sci. **253**, 8151–8154 (2007).
[10]Y. F. Lu, Z. M. Ren, T. C. Chong, B. A. Cheong, S. K. Chow, and J. P. Wang, J. Appl. Phys. **87**, 1540 (2000).

© Author(s) 2020

[11] G. S. Sudhir, H. Fujii, W. S. Wong, C. Kisielowski, N. Newman, C. Dieker, Z. Liliental-Weber, M. D. Rubin, and E. R. Weber, Appl. Surf. Sci. **127-129**, 471–476 (1998).
[12] C. P. Huang, K. Gupta, C. H. Wang, C. P. Liu, and K. Y. Lai, Sci. Rep. **7**, 7135 (2017).
[13] R. M. Guerrero and J. R. V. García, Mater. Manuf. Processes **15**, 259–267 (2000).
[14] Y. Li, C. Zhang, X. Luo, Y. Liang, D.-S. Wuu, C.-C. Tin, X. Lu, K. He, L. Wan, and Z. C. Feng, Appl. Surf. Sci. **458**, 972–977 (2018).
[15] M. Nemoz, R. Dagher, S. Matta, A. Michon, P. Vennéguès, and J. Brault, J. Cryst. Growth **461**, 10–15 (2017).
[16] G. Koblmueller, R. Averbeck, L. Geelhaar, H. Riechert, W. Hösler, and P. Pongratz, J. Appl. Phys. **93**, 9591 (2003).
[17] K. Y. Lee, M. K. Gupta, and S.-W. Kim, Nano Energy **14**, 139–160 (2015).
[18] F. R. Fan, W. Tang, and Z. L. Wang, Adv. Mater. **28**, 4283–4305 (2016).
[19] S. Sadeghpour, F. Ceyssens, and R. Puers, J. Phys.: Conf. Ser. **757**, 012003 (2016).
[20] M. Bosund, T. Sajavaara, M. Laitinen, T. Huhtio, M. Putkonen, V.-M. Airaksinen, and H. Lipsanen, Appl. Surf. Sci. **257**, 7827–7830 (2011).
[21] V. Tarala, M. Ambartsumov, A. Altakhov, V. Martens, and M. Shevchenko, J. Cryst. Growth **455**, 157–160 (2016).
[22] H. Y. Shih, W. H. Lee, W. C. Kao, Y. C. Chuang, R. M. Lin, H. C. Lin, M. Shiojiri, and M. J. Chen, Sci. Rep. **7**, 39717 (2017).
[23] P. Motamedi and K. Cadien, Appl. Surf. Sci. **315**, 104–110 (2014).
[24] S. Liu, M. Peng, C. Hou, Y. He, M. Li, and X. Zheng, Nanoscale Res. Lett. **12**, 279 (2017).
[25] V. Rontu, P. Sippola, M. Broas, G. Ross, T. Sajavaara, H. Lipsanen, M. Paulasto-Kröckel, and S. Franssila, J. Vac. Sci. Technol., A **36**, 021508 (2018).
[26] I. Bichurin, M. Petrov, and G. Srinivasan, Phys. Rev. B **68**, 054402 (2003).
[27] J. Ma, J. Hu, Z. Li, and C.-W. Nan, Adv. Mater. **23**, 1062–1087 (2011).
[28] Y. Wang, J. Hu, Y. Lin, and C.-W. Nan, NPG Asia Mater. **2**, 61–68 (2010).
[29] F. Bachmann, R. Hielscher, and H. Schaeben, Solid State Phenom. **160**, 63–68 (2010).
[30] M. Alevli, C. Ozgit, I. Donmez, and N. Biyikli, Phys. Status Solidi A **209**, 266–271 (2012).
[31] K. Prume, P. Muralt, F. Calame, T. Schmitz-Kempen, and S. Tiedke, IEEE Trans. Ultrason. Ferroelectrics Freq. Contr. **54**, 8–14 (2007).
[32] G. B. Harris, London, Edinburgh Dublin Philos. Mag. J. Sci. **43**, 113–123 (1952).
[33] H. R. Moutinho, F. S. Hasoon, F. Abulfotuh, and L. L. Kazmerski, J. Vac. Sci. Technol., A **13**, 2877 (1995).
[34] D. Holec and P. H. Mayrhofer, Scr. Mater. **67**, 760–762 (2012).
[35] E. Hug, S. Thibault, D. Chateigner, and L. Maunoury, Surf. Coat. Technol. **206**, 5028–5035 (2012).
[36] J. H. Harris, R. A. Youngman, and R. G. Teller, J. Mater. Res. **5**, 1763–1773 (1990).
[37] G. A. Slack, R. A. Tanzilli, R. O. Pohl, and J. W. Vandersande, J. Phys. Chem. Solids **48**, 641–647 (1987).
[38] M. Schneider, A. Bittner, and U. Schmid, J. Phys. D: Appl. Phys. **48**, 405301 (2015).

© Author(s) 2020

6

Magnetoelectric composites made of AlN films and magnetostrictive foils

Utilizing a superior property of PE-ALD technique, a conformal coating profile over rough and complex surfaces, magnetoelectric (ME) composites with high interface quality consist of AlN films and magnetostrictive (MS) foils (Ni, Fe, Co) are achieved. This chapter present a fabrication process and characterization of ME composites. The ME composites were made by synthesizing AlN films on Ni, Fe, and Co foils. Here AlN film plays as a piezoelectric player, and Ni (Fe, Co) foil serves as a magnetostrictive layer. An advantage of using magnetostrictive foils is that no need of an additional metal layer as a bottom electrode, thus excluding the external contribution in evaluation of ME performance. The figure below present ME coefficient of our thin-film composite in comparison with several typical ME materials [1].

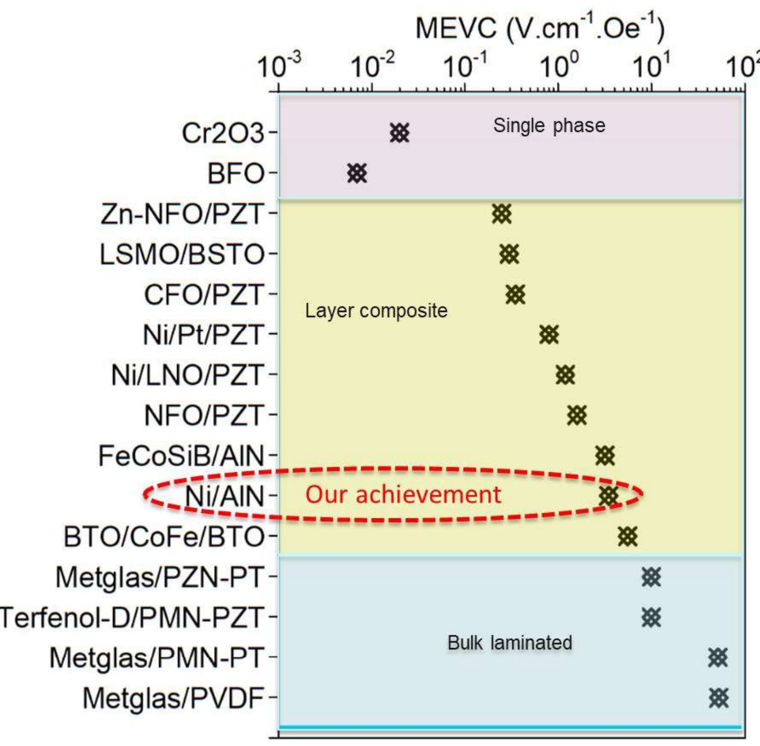

The performance of our magnetoelectric composite compared to the state-of-the art according to the review paper of Z. Chu et al. (2018) [1].

Low-temperature growth of AlN films on magnetostrictive foils for high-magnetoelectric-response thin-film composites

This chapter is based on the paper: "*Low-temperature growth of AlN films on metal foils by plasma-enhanced atomic layer deposition for high-magnetoelectric-response thin-film composites*", to be submitted ACS Applied Materials and Interfaces.

Abstract:

We report on a deposition process of aluminum nitride (AlN) thin film via plasma-enhanced atomic layer deposition (PE-ALD) to enhance magnetoelectric (ME) transduction in magnetostrictive–piezoelectric composite structures. Synthesis of thin-film magnetoelectric composites with a strong ME response has been attempted for practical purposes, but with limited success due to its poor interfacial quality caused by anisotropic coating techniques and high-temperature processes. The current study reports a strong ME effect in thin-film composites consisting of nickel, iron or cobalt foils and 550 nm thick AlN films grown by PE-ALD at a (low) temperature of 250 °C and ensuring isotropic and highly conformal coating profiles. The AlN film quality and the interface between the film and the foils are meticulously investigated by means of high-resolution transmission electron microscopy. An interface (transition) layer of partially amorphous Al_xO_y / AlO_xN_y with thicknesses of 10 and 20 nm, corresponding to the films grown on Ni, Fe and Co foils, is revealed. AlN film is found to be composed of a mixture of amorphous and nano-crystalline grains at the interface. However, its crystallinity is improved as the film grew and shows a highly preferred (002) orientation. High self-biased ME coefficients (α_{ME} at a zero bias magnetic field) of 3.3, 2.7, and 3.1 $V.cm^{-1}Oe^{-1}$ are achieved at an off-resonance frequency of 46 Hz in AlN/Ni thin-film composites with different Ni foil thicknesses of 7.5, 15, and 30 µm, respectively. In addition, the magnetoelectric measurements have also been carried out in composites made of 550nm-thick films grown on 12.5 µm-thick Fe and 15 µm-thick Co foils. The maximum magnetoelectric coefficients of AlN/Fe and Al/Co composites are 0.32 and 0.12 $V.cm^{-1}Oe^{-1}$, measured at 46 Hz at a bias magnetic field (H_{dc}) of 6 and 200 Oe, respectively. The difference of magnetoelectric transducing responses of each composite is discussed according to the interface analysis. We report a maximum delivered power density of 75 nW/cm^3 for the AlN/Ni composite with a load resistance of 200 kΩ to address potential energy harvesting and electromagnetic sensor applications.

Keywords: magnetoelectric effect, thin-film magnetoelectric composites, AlN thin film, low-temperature process, conformal coatings, PE-ALD, interface.

6.1. Introduction

The simultaneous exhibition of ferroelectricity (piezoelectricity) and ferromagnetism (anti-, ferrimagnetism) has received significant attention for both fundamental and practical purposes. This is because ferroelectric properties can be manipulated by an external magnetic field, or magnetic properties can be controlled by an electrical field, or *vice versa* [2–7]. In multiferroic-based applications, the coexistence of ferroelectricity (PE) and ferromagnetism (FM) is not enough. In fact, a strong coupling of the two phenomena, the so-called magnetoelectric (ME) coupling effect, is highly demanded. The first observation of the ME coupling effect was in Cr_2O_3, even though the Cr_2O_3 compound is not multiferroic [8]. Some transition metal compounds, such as bismuth ferrite ($BiFeO_3$), bismuth manganite ($BiMnO_3$), terbium manganite ($TbMnO_3$), or $LuFe_2O_4$ and so on, possess both ferroelectric and ferromagnetic properties. However, the mechanisms driving multiferroicity are unique and specific for each compound. In $BiFeO_3$, it is believed that the mechanism governing multiferroicity comes from two different cations; the off-centring movement of the Bi^{3+} ion with the "lone pair" electrons in the 6s orbital induces ferroelectricity, whereas a robust antiferromagnetism is given by the 3d electrons of the Fe ion (Fe^{3+} and/or Fe^{2+}) [9,10]. Meanwhile charge ordering occurring in a ferrimagnetic $LuFe_2O_4$ is believed to be likely to produce ferroelectricity [11–13]. Some other mechanisms have triggered multiferroicity, such as geometric ferroelectricity in hexagonal-RMnO$_3$ (R = Sc, Y, In, or Dy-Lu) [14,15] or spin-driven mechanisms as present in Cr_2BeO_4 or in orthorhombic-$TbMnO_3$ [16–19]. Unfortunately, the ME coupling effect of these single-phase multiferroic materials is often too weak and/or at very low temperatures, which impedes practical applications.

Alternatively, ME composites open a pathway to outweigh the above-mentioned disadvantages of single-phase multiferroics by connecting ferroelectric (piezoelectric) and ferromagnetic (magnetostrictive) materials into an ME composite [20]. In these composites, the ME coupling is governed by a strain-mediated interaction between the two phases, i.e. the strain induced in the ferromagnetic phase is mechanically transferred through to the ferroelectric phase via the interface. The notation, such as 1-3, 0-3 and 2-2, is used to classify the structure of an ME composite, in which the number describes the dimensional geometry of each phase [21]. Various deposition techniques, such as electrochemical coating, pulsed laser deposition (PLD), molecular beam epitaxy (MBE), and metal-organic chemical vapour deposition (MOCVD), were used to fabricate ME composites.

On one hand, a 1-3 composite consists of a single-phase nanopillar (denoted 1) embedded into a matrix of another phase (denoted 3). Intensive work has been carried out to design composites with a strong ME effect in both ceramic and thin-film composites. Bulk ME ceramic composites, such as $BaTiO_3$-Ni(Co,Mn)Fe_2O_4 [22] and (Sr,La)$PbZrTiO_3$-($Ni_{0.7}Zn_{0.3}$)Fe_2O_4 [23], were synthesized via co-sintering at high-temperatures. Zavaliche and co-workers [24] demonstrated the ME effect in CFO nanopillars embedded in a $BiFeO_3$ matrix. However, the ME effect in these bulk composites was very weak because of interfacial inter-diffusion and/or interface reactions, leading to high leakage current, and a poor coupling. This poor coupling generated is due to the high-temperature treatment for fabrication with a difference in thermal expansion between the two bulk phases inducing delamination/cracks, thus reducing the coupling. The 0-3 ceramic composites face similar issues and a high leakage current in composites, which is due to the electrically conductive constituent of the magnetostrictive phase that is embedded in the ferroelectric matrix with a high particle density. By utilizing a sol-gel technique, Wan *et al.* [25] reported 0-3 composite films by dispersing $CoFe_2O_4$ (CFO) nanoparticles in Pb(Zr,Ti)O_3 (PZT). Exploiting PLD, Ryu *et al.* [26] did

grow PZT/$CoFe_2O_4$ composites on $SrTiO_3$ substrates. Unfortunately, the ME coefficient was limited because of a poor interface between the two phases and a high leakage current, and/or a strong clamping effect induced by the substrates. On the other hand, a high ME coefficient in the 2-2 bulk laminate composites is expected because of the elimination of the leakage current [27–31]. However, in these bulk laminate composites, the use of epoxy to connect the two layers as well as the need of additional electrodes significantly affect the ME response of the composites with poor coupling interfaces between consecutive layers [32–34].

Compared to bulk ME composites, thin-film composites have superior transduction properties from a combination of the layers at the atomic level, precise control of the lattice mismatch between materials, and the possibility of growing epitaxial composite films. In addition, a thin-film composite facilitates its ability to integrate into microelectronics and microelectromechanical systems (MEMS). Recently, Gupta *et al.* [35] reported a giant ME coefficient of 130.5 $V.cm^{-1}Oe^{-1}$ in PZT/Ni composite grown by PLD. However, its ME response is only effective after a nonobvious supplementary stage of poling of the PZT layer. Furthermore, the authors claimed nickel oxide was formed due to the high deposition temperature of PZT at 800°C, which degraded the performance of Ni in the composites.

Although presenting a lower piezoelectric coefficient, the use of intrinsically piezoelectric materials after thin film deposition such as wurtzite crystals (e.g. AlN, ZnO, GaN), represent a substantial advantage with respect to a simplification of the fabrication of ME microdevices with materials compatible with cleanroom facilities. In particular, aluminum nitride (AlN) thin film with its dielectric properties has paved the way for piezoelectric actuators being used in different applications [36] and their coupling with magnetostrictive layers for ME devices [37]. Recently, we proposed the usage of plasma-enhanced ALD (PE-ALD) to obtain conformal and fully active piezoelectric thin films made of AlN [38]. The thin film growth was done at 250°C, a significantly lower deposition temperature compared to most piezoelectric materials deposition. In comparison to ceramic lead zirconate titanate (PZT) processed at high temperature (> 650°C), or even to piezoelectric polymers (PVDF based) difficult to process in thin and conformal layer while exhibiting very poor piezoelectric coefficients, AlN thin layer processing represents the best alternative for piezoelectric MEMS-CMOS fabrication without the need of poling.

In the current study, we aimed at applying highly conformal AlN thin films made by PE-ALD to different magnetostrictive materials to overcome the issues of the thin-film ME composites processing and the interface between the two phases. Commercial Ni, Fe and Co foils with different thicknesses were exploited as a magnetostrictive layer due to their non-zero and moderate piezomagnetic coefficient [39]. Furthermore, these were shown to have a high electrical conductivity, simplifying electrode interfacing. AlN films grown directly on the foils by PE-ALD at a low temperature of 250 °C were contributed as a piezoelectric layer. Our earlier work [38] demonstrated that even at a low deposition temperature, AlN films show good piezoelectric properties with a direct piezoelectric coefficient $e_{31,f}$ of 0.37 C/m^2. Compared to other coating methods, such as spin coating, sputtering, CVD and PLD, utilizing the PE-ALD technique to design ME composites is believed to ensure an excellent interface owing to its low-temperature processes and highly conformal coating profile. Therefore, the effect of differences in lattice mismatch, thermal expansion and morphology quality between the two phases can be mitigated. As a result, a strong ME coupling in these composites is expected.

6.2. Experimental

The AlN thin film was synthesized with a commercial plasma-enhanced atomic layer deposition PE-ALD reactor (TFS-200, Beneq, Finland) using standard precursors, such as trimethyl aluminum $Al_2(CH_3)_6$ (TMA, Strem Chemicals, Inc., France), and a mixture of N_2:H_2:Ar gases with a flow ratio of 100sccm/80sccm/30sccm. The AlN films presented in this study were grown by 5000 cycles to obtain a 550nm-thick film. Details in the optimization of AlN film growth can refer to our previous work [38]. The films were grown at a temperature of 250 °C on three different substrates: (1) 2 × 2 cm^2 Ni (NI000270), Fe (FE000160) and Co (CO000170) foils (Goodfellow GmbH, Germany), (2) 150nm thick nickel-coated silicon substrates by sputtering (Baltec Med-020 high vacuum coating system, Ni target purity level of 99.999%, reference NI000565, Goodfellow GmbH, Germany), and (3) pristine (100) silicon substrates (1 × 1 cm^2 pieces of single crystal Si(100) wafer, grade Monitor, Siegert GmbH, Germany).

The thickness of AlN films was verified by ellipsometry (J. A. Woolam Ellipsometer). The film crystal structure was examined by X-ray diffractometry (Diffractometer Bruker D8) in grazing incidence (GI-XRD) configuration with an incidence angle of $\omega = 0.5°$. Transmission electron microscopy (TEM) and scanning transmission electron microscopy (STEM) investigations were carried out using a JEOL JEM - ARM 200F Cold FEG operating at 200 kV and equipped with a spherical aberration (Cs) probe and image correctors (point resolution 0.12 nm in TEM mode and 0.078 nm in STEM mode). Electron energy-loss (EEL) spectra were collected for O-K, Ni-L2,3, Fe-L2,3, Co-L2,3, N-K and Al-K edges in STEM mode. TEM lamellas were prepared by means of a FIB/SEM FEI Helios NanoLab 600i equipped with a platinum Gas Injection System.

The topographic structure was acquired by a commercial atomic force microscopy (AFM Innova, Bruker Inc., Santa Barbara) in tapping mode by maintaining the amplitude of the cantilever first resonance constant. Images were taken over 2 × 2 μm^2 at a scan rate of 1 Hz. The tips used were denominated HQ:NSC/Hard (MikroMasch, Bulgaria), Diamond-like carbon-coated, with a nominal cantilever stiffness of 40 N/m and an apex diameter of below 20 nm. For the piezoelectric characterization, AlN films were deposited on a silicon wafer with a 150 nm-thick nickel layer as a bottom electrode. Thereafter a 100 nm aluminum layer was sputtered on top of the deposit as a top electrode. The specific cantilevers for the four-point bending (4-PB) characterization, in order to measure the effective transverse piezoelectric coefficient $e_{31,f}$ of the AlN films, were fabricated using laser lithography and wet etching processes according to the protocol of K. Prume et al. [40]. The magnetization measurement was performed at room temperature with a vibrating-sample magnetometer (VSM, Cryogenic, UK) with the magnetic field swept from - 4→4 Tesla. The ME coefficient was measured with an in-house magnetoelectric testing bench, described in Figure S1 (supplementary information). Prior to measurement, a 100nm-thick Al metal as a top electrode was deposited over 0.3 × 0.3 cm^2 on AlN/Ni composites. The ME voltage, measured between the aluminum top electrode and the nickel bottom electrode, was extracted using a locking amplifier (SR865A, 4 MHz DSP) where composites were exposed to a bias DC magnetic field (Hdc) from an electromagnet varying from -200 to 200 Oe superimposed with a small AC magnetic field (Hac) from Helmholtz coils at an amplitude of 8.5 Oe at a constant frequency of 46 Hz. Then, the ME coefficient was calculated using the following equation [20,33]: $\alpha_{ME} = \frac{Voutput}{t.Hac}$, where t is the thickness of the piezoelectric layer (in the thin-film composites) and V_{output} is the ME voltage extracted in the piezoelectric layer. Both forward ($-H_{dc}$ → 0 → $+H_{dc}$), and backward ($+H_{dc}$ → 0 →

-H_{dc}) measurements were acquired. The power density was calculated by dividing the output power by the device volume.

6.3. Results and discussion

Figure 1 shows GI-XRD (ω = 0.5°) patterns of 550 nm-thick AlN films grown on 30µm-, 12.5 µm- and 15 µm-thick Ni, Fe, and Co foils, respectively. The AlN film on Ni and Fe exhibits a highly (002)-preferred orientation, meanwhile (100) and (002) orientations are observed in the film grown on the Co surface. No formation of metal-oxide phases such as Ni_xO_y and Co_xO_y is detected. It is noted that the strong noise intensity background in GI-XRD data for Fe and Co is due to a strong fluorescence of these elements.

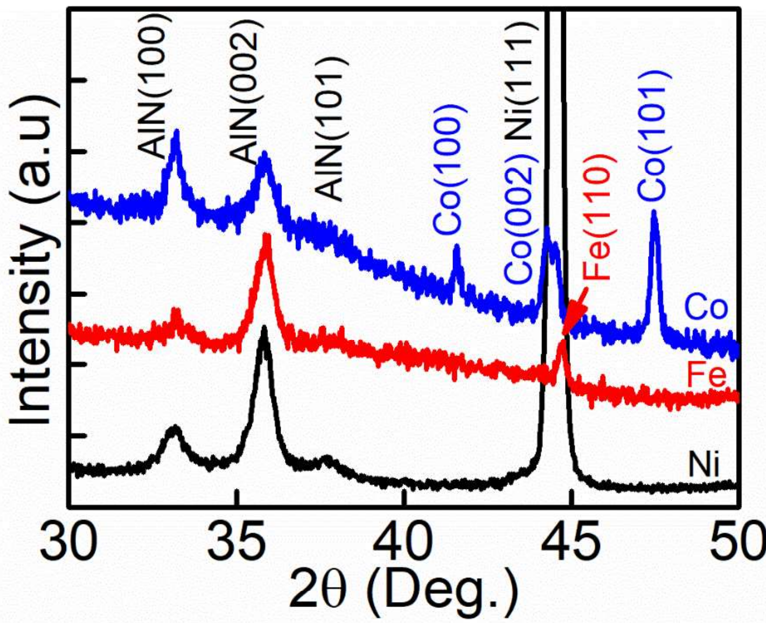

Figure 1: *(a) GI-XRD (ω = 0.5°) patterns of a 550nm-thick AlN film deposited on a 30 µm-thick nickel, 12.5 µm-thick Fe, and 15 µm-thick Co foils.*

The topography of the AlN film surfaces on Ni, Fe, and Co foils was measured by AFM on Figures 2(a), (d), and (g), respectively. The surface roughness was about 38, 8, and 15 nm for the films grown on Ni, Fe and Co, respectively. The grain-diameter distribution is obtained from the particles analysis of topography images by a watershed detection method processed under MountainSPIP software (Digital Surf, France) Particles segmented image and its grain-diameter histogram (the insert) are shown in Figures 2(b), (e), (h) and (c), (f), (k). The mean diameter of the grains extracted was 77 ± 20, 80 ± 23, and 56 ± 20 nm for the AlN films grown on Ni, Fe and Co foils, respectively.

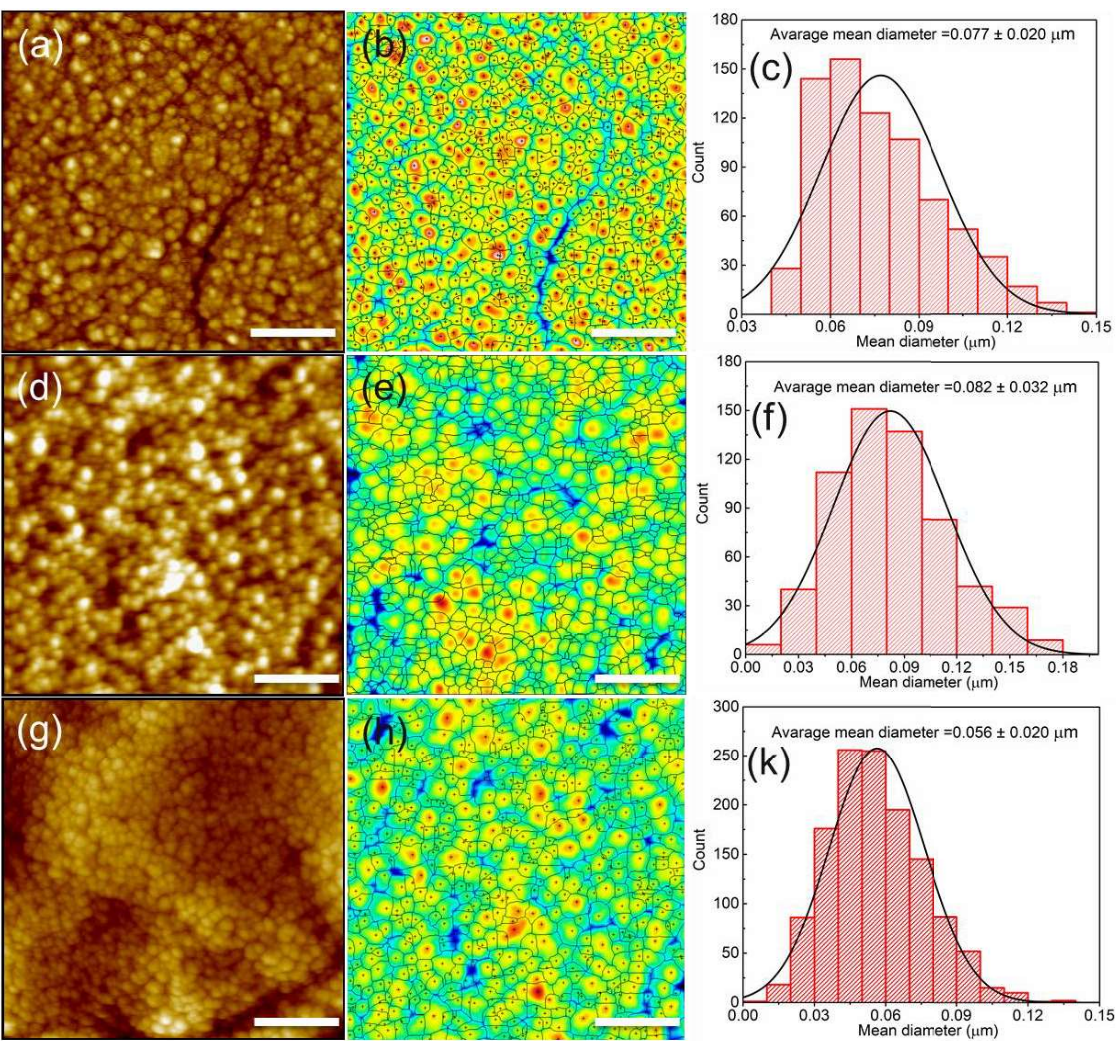

Figure 2: *AFM topography, particles segmentation images and the grain-diameter histogram extracted from watershed detection method of (a) – (c) AlN film on 30 µm - Ni foil, (d) – (f) AlN film on 12.5 µm - Fe foil, and (g) – (k) AlN film on 15 µm - Co foil, respectively. The scale bar is 500 nm.*

Figure 3 presents TEM observations in a cross-section for AlN films grown on 30 µm-Ni foil. The interface between AlN and Ni is clear, and no delamination is observed, as shown in the TEM bright-field (BF) and dark-field (DF) micrographs (Figures 3(a) and (b)). The inserted selected area electron diffraction (SAED) pattern in Figure 3(a) shows a ring at a d_{hkl} distance of 0.248 nm, confirming the (002)-preferred orientation of the AlN film in accordance with the XRD data (Figure 1). The matrices of amorphous grains and nano-crystalline grain (20-30 nm), and the columnar structure are observed in the AlN film.

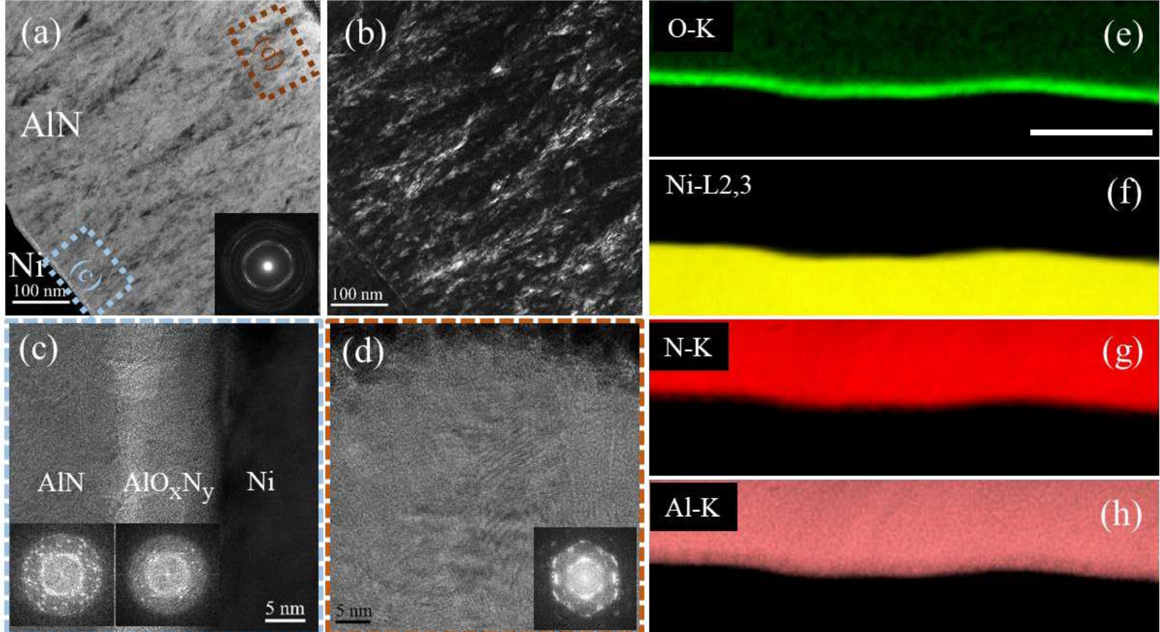

Figure 3: *(a) Bright-field (BF) micrograph and inserted SAED pattern of AlN layer in cross-section, (b) dark-field (DF) TEM micrograph of AlN film on 30 µm-Ni foil. HR-TEM images and inserted Fast-Fourier-Transform: (c) at the interface between AlN and Ni (the blue dash square in Figure a), and (d) the top layer of AlN (the brown dash square in Figure a), and (e)-(h) STEM-EELS mappings for O-K, Ni-L2,3, N-K, and Al-K edges, respectively. The scale bar in STEM-EELS images is 100 nm.*

High-resolution TEM (HR-TEM) was performed to further study the interface between AlN and Ni, as well as the crystallinity of the AlN film. Figure 3(c) shows an HR-TEM image and SAED pattern accompanied by fast-Fourier-transform (FFT) observed at the interface. Notably, a transition layer of approximately 10 nm is observed in the AlN layer. The SAED reveals that the crystallinity of AlN at the interface is poor, highly defective and disordered, however, at the top layer the crystallinity of AlN is highly improved, as illustrated in Figure 3(d) with the SAED pattern. The STEM-EELS (Figures 3(e)-(h)) was carried out to study chemical composition and elemental diffusion at the interface, and the origin of the transition layer. No significant Ni and Al/N diffusion is detected through the interface. Significant amounts of O, Al and N in the transition layer are observed, implying that the transition layer is amorphous with Al_xO_y oxides and potential oxynitride forms AlO_xN_y. It is worth noting that a remarkable amount of oxygen is also observed in AlN film that is coincident with our previous report [38], showing that about 6 at.% of O was presented in AlN film. No formation of Ni_xO_y has been detected

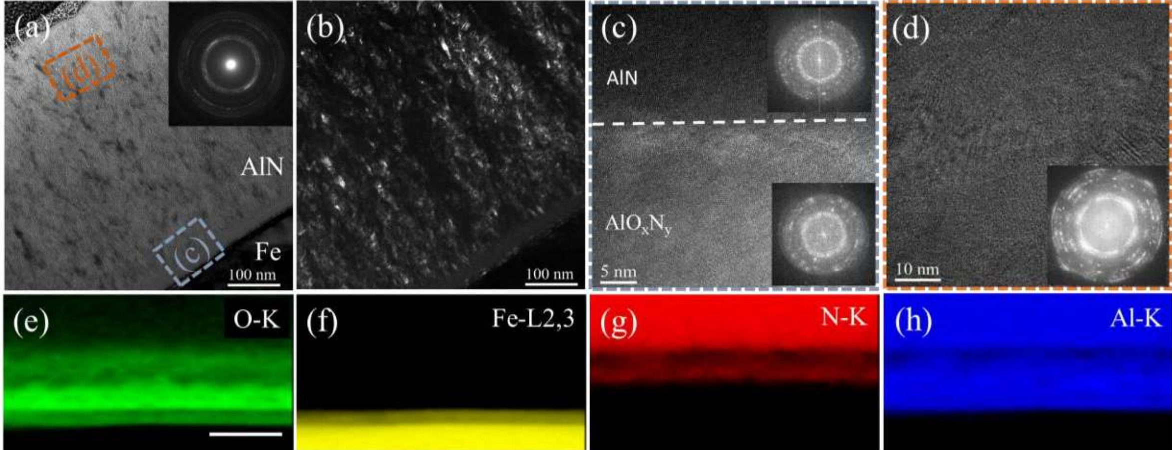

Figure 4: *(a) Bright-field (BF) micrograph and inserted SAED pattern of AlN layer in cross-section, (b) dark-field (DF) TEM micrograph of AlN film on 12.5 µm-Fe foil. HR-TEM images and inserted Fast-Fourier-Transform: (c) at the interface between AlN and Fe (the blue dash square), and (d) at the top layer of AlN (the brown dash square), and (e)-(h) STEM-EELS mappings for O-K, Fe-L2,3, N-K, and Al-K edges, respectively. The scale bar in STEM-EELS images is 100 nm.*

Furthermore, Figures 4 and 5 present TEM observations in a cross-section for AlN films grown on Fe and Co foils, respectively. Similarly to the AlN film grown on Ni foil, AlN films grown on Fe and Co foils show a sharp interface without delamination. It is also observed that the nano-crystalline grains are embedded in an amorphous phase, and a columnar structure is present. SAED patterns inserted in Figures 4(a) and 5(a) reveal that AlN films grown on Fe and Co foils have (002) preferred orientation. Among the three samples, AlN films grown on Ni and Co show better crystallinity compared to the film grown on Fe, as sharp and intense rings are observed.

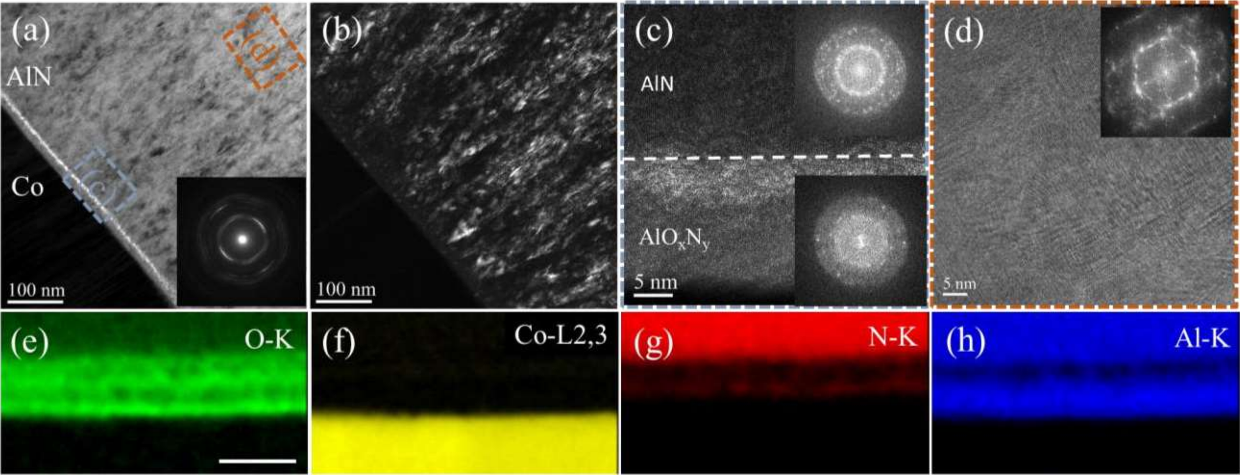

Figure 5: *(a) Bright-field (BF) micrograph and inserted SAED pattern of AlN layer in cross-section, (b) dark-field (DF) TEM micrograph of AlN film on 15 µm-Co foil, HR-TEM images and inserted Fast-Fourier-Transform: (c) at the interface between AlN and Co (the blue dash square) and (d) at the top layer of AlN (the orange dash square), and (e)-(h) STEM-EELS mappings for O-K, Co-L2,3, N-K, and Al-K edges, respectively. The scale bar in STEM-EELS images is 100 nm.*

The transition layers of 30 and 20 nm are observed in Fe and Co samples, as shown in Figures 4(c) and 5(c), respectively. These layers are partially amorphous, consisting of Al_xO_y, AlO_xN_y and AlN layers. These are further confirmed by chemical analyses (EEL spectra shown in Figures 4(e)-(h) and in Figures 5(e)-(h)). Otherwise, the FFT shows strong diffuse amorphous rings (Figure 4c-5c). As the films grows, its crystallinity increases with a (002) preferred orientation (Figures 4(d) and 5(d)). It can be noted that an iron oxide layer of 10 nm is observed in STEM-EELS (Figures 4(e)-(h)), which may due to iron foil processing. Furthermore, no significant diffusion of elements through the interface can be detected. The origin of the formation of amorphous Al_xO_y and AlO_xN_y layers is due to the presence of hydroxyl groups on surface substrates that act as radical groups in the ligand exchange reaction, causing the formation of a transition layer. In addition, the presence of residual water molecules and oxygen gas inside the reaction chamber during the first stages of the PE-ALD process is also a source of oxygen atoms participating in the chemical reaction of the film deposition. During the process, the complete saturation of the reactor chamber with the nitrogen/argon/hydrogen gases lowers the presence of this water and O_2 molecules. Notably, the film microstructure grown on Ni and Fe is quite different from the film grown on Co. The continuous columnar structure is observed in AlN/Ni and AlN/Fe samples, as shown in Figures S1 and S2. It is still obtained in the AlN/Co sample, however "twin boundaries" are also present (Figure S3). The twin boundaries are formed due to the misalignment between AlN grains, which originates from the microstructure of the Co substrate. Whereas Ni and Fe foils are constructed by grains with different sizes and different orientations causing quite a smooth surface. The misalignment of crystalline grains may cause a cancellation among the electrical dipoles in the conformal AlN film, leading to a decrease in the piezoelectric response, as well as magnetoelectric transducing in the AlN/Co composite. This will be discussed further in the section about the magnetoelectric measurements.

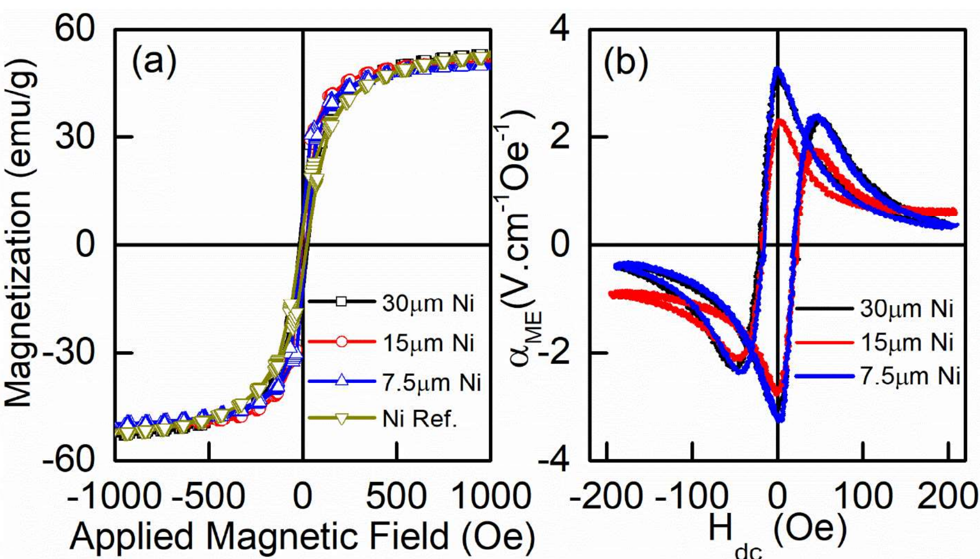

Figure 6: *(a) Magnetization measurements of nickel samples with the thickness of 7.5, 15, 30 µm with a 550 nm-thick AlN film deposited on top and a pristine 100 µm-thick Ni foil, (b) Magnetoelectric coefficient (α_{ME}) measurements, performed at a constant AC magnetic field amplitude of 8.5 Oe and at a frequency of 46 Hz, of AlN/Ni composites. The magnetic DC bias forward ($-H_{dc} \rightarrow 0 \rightarrow +H_{dc}$) and backward ($+H_{dc} \rightarrow 0 \rightarrow -H_{dc}$) ME measurements are both performed.*

Figure 6(a) shows the magnetization measurement data of a pristine Ni foil and Al/Ni composites. All the Al/Ni samples show ferromagnetic behaviours with typical symmetric magnetic hysteresis loops. It should be noted that a pure AlN thin film is diamagnetic in nature. Therefore, the ferromagnetic characteristics of AlN/Ni samples stem from the Ni foils. It can be seen that the magnetic hysteresis loops are the same among Al/Ni composites regardless of the thickness of Ni foils. The saturation magnetization of a pure Ni foil and Al/Ni composite is approximately 56 emu/g, which is quite close to the expected value for a bulk Ni of 58.6 emu/g.

Figure 6(b) illustrates the ME coefficient (α_{ME}) as a function of a DC-biased magnetic field (H_{dc}) for AlN/Ni thin-film composites, measured at an off-resonance frequency of 46 Hz. The asymmetry of the ME coefficient curve is related to the asymmetry of the magnetostriction nature of nickel [41]. When a DC magnetic field superimposed with a weak AC magnetic field is applied parallel to the plane of the AlN/Ni samples, spins present in nickel are aligned to the direction of the applied magnetic field. The alignment of spins causes the magnetic domain movements and surface modulations. This magnetic domain switching results in magnetoelastic deformation, which is then mechanically transferred to the AlN film via the interface, subsequently generates charges and an electrical field in the piezoelectric film. For all measurements, α_{ME} exhibited a typical H_{dc} dependence showing the hysteresis behavior during the H_{dc} sweep and a sign change with respect to the reversal of the H_{dc} direction. The H_{dc} dependence of α_{ME} is correlated to the first derivative of magnetostriction or the piezomagnetic coefficient, $d\lambda/dH$, where λ is the magnetostriction and H is the applied magnetic field [41]. In general, the α_{ME} increases as the H_{dc} increases, reaching its maximum value at a particular H_{dc} value at which the maximum piezomagnetic coefficient is achieved, after which it drastically decreases as the H_{dc} continues to increase. Interestingly, in our AlN/Ni thin-film composites, a maximum α_{ME} was obtained at a zero bias field (H_{dc} = 0 Oe). The nearly maximum α_{ME} at zero DC magnetic field has also been reported in other composites such as Ni/PMT ($0.8[Pb(Zr_{0.52}Ti_{0.48}O_3]+0.2[Pb(Zn_{1/3}Nd_{2/3})O_3]$ + 2 mol.% MnO_2) [42], Ni/MFC (macro-fibre composite) [43], Ni/SFC (single crystal fibre composite) [30,44]. The intrinsic self-biased α_{ME} is attributed to the hysteretic magnetic nature of the Ni foil. Zhou et al. [42] demonstrated that Ni foil possesses macro-sized domains with a long range ordering, which resulted in the larger coercive field. When the magnetic domains are reoriented, a higher magnetic field is required to achieve the random state, causing larger hysteresis in the magnetization curve. In the present study, the maximum α_{ME} value was about 3.3, 2.8, and 3.1 $V.cm^{-1}.Oe^{-1}$ for AlN/Ni thin-film composites with an Ni foil thickness of 7.5, 15, and 30 µm, respectively. Greve et al. [45] reported a giant ME coefficient of 3.1 $V.cm^{-1}.Oe^{-1}$ measured at an off-resonance frequency of 100 Hz in an AlN/Metglas thin-film composite coated in a free-standing cantilever. The AlN layer used is 1.8µm-thick with an $e_{31,f}$ value of 1.2 $C.m^{-2}$, which is approximately three times thicker than our AlN thin film with a piezoelectric coefficient $e_{31,f}$ of 0.37 $C.m^{-2}$ [38]. Moreover, the piezomagnetic coefficient of Metglas of about 1.4 ppm/Oe is also almost three times higher than Ni with a value of 0.3 ppm/Oe [46]. Therefore, the high α_{ME} obtained in our AlN/Ni thin-film composites can be attributed to an excellent interface quality between the AlN thin film and Ni foils produced by a highly conformal coating by PE-ALD and a low-temperature process limiting atomic interdiffusion, microcracks and delamination due to the different coefficients of thermal expansion of the two layers.

Figures 7 (a)-(b) show magnetization and magnetoelectric measurements for AlN/Fe and AlN/Co samples. The saturation magnetization is about 205 and 160 emu/g for AlN/Fe and AlN/Co, as shown in Figure 7(a). The maximum magnetoelectric coefficient, α_{ME} of AlN/Fe and Al/Co

composites (Figure 7(b)) was measured as being approximately 0.32 and 0.12 $V.cm^{-1}.Oe^{-1}$ at 46 Hz with a bias magnetic field (H_{dc}) of 6 and 200 Oe, respectively. Compared to the AlN film grown on Ni foils, the magnetoelectric response in Al/Fe and Al/Co samples is about one order of magnitude weaker. This can be attributed to a stronger magnetostrictive effect in Ni compared to Fe and Co. E. Klokholm et al. reported magnetostrictive hysteresis loop measurements on nickel, iron and cobalt in the shape of thin polycrystalline films [41].

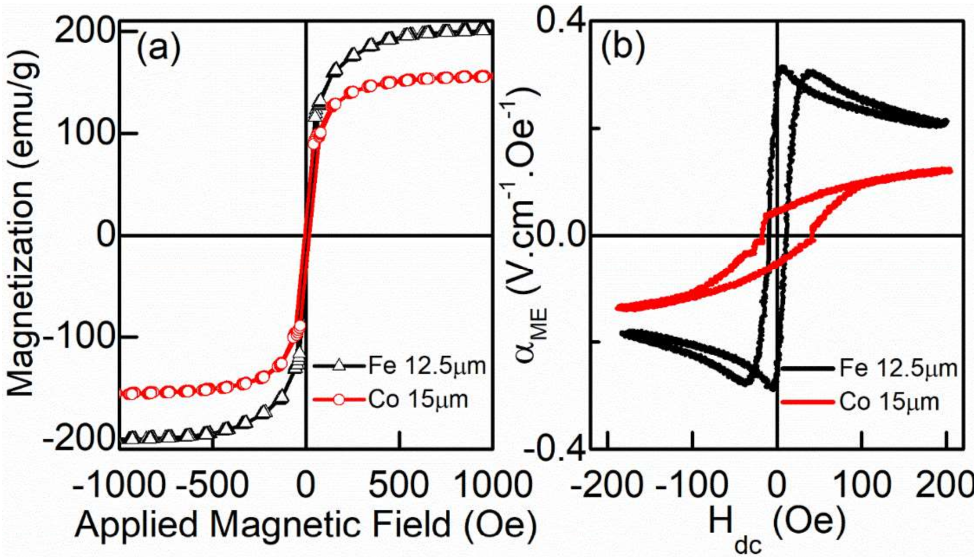

Figure 7: *(a) Magnetization measurements of 12.5 μm-thick Fe, and 15 μm-thick Co samples with a 550 nm-thick AlN film deposited on top; (b) Magnetoelectric coefficient (α_{ME}) measurements, performed at a constant AC magnetic field amplitude of 8.5 Oe and at frequency of 46 Hz, of AlN/Fe and AlN/Co composites. The magnetic DC bias forward ($-H_{dc} \rightarrow 0 \rightarrow +H_{dc}$) and backward ($+H_{dc} \rightarrow 0 \rightarrow -H_{dc}$) ME measurements are both performed.*

The authors highlighted maximum magnetostriction coefficients of λ = -6 ppm, -3.5 ppm and -11.2 ppm for iron, cobalt and nickel, respectively. The same authors experienced a large variation of this saturation magnetostriction coefficient for cobalt, which is quite sensitive to the deposition process (sputtering and thermal evaporation in this study) and post-annealing eliminating fcc phase with an unusual change in the magnetostrictive behavior. This is also confirmed by the trend we observed about the maximum magnetoelectric coefficient values we measured for these three metals. In our case we could explain the lowest α_{ME} coefficient in the AlN/Co composite due to the misalignment of (002)-oriented columnar grains of the piezoelectric AlN film conformally grown on a Co surface, as revealed by the HR-TEM micrographs in Figure S4 (supplementary information).

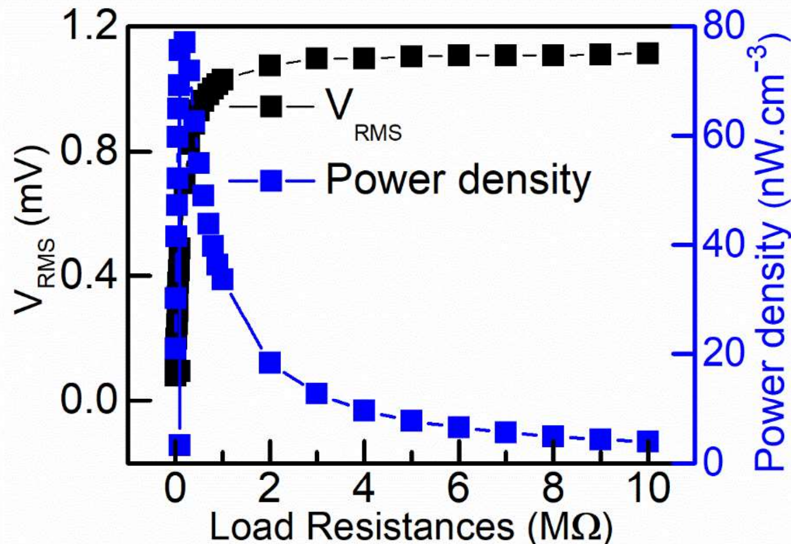

Figure 8: *Output voltage and power density as a function of load resistance measured for AlN/Ni composite sample under an AC magnetic field intensity of 8.5 Oe at out-of-resonance frequency of 46 Hz. No DC magnetic field bias was applied.*

For potential applications of such ME composites for transducing an electromagnetic background into a usable electrical field with energy harvesting or sensor applications, it is interesting to point out that we measured a maximum power density of approximately 75 nW/cm^3 on a load resistance of 200 kΩ, as illustrated in Figure 8, showing output voltage and power density as a function of load resistance measured for the AlN/Ni sample. It has been reported that the power density can be further improved by using the resonance structures [30,44,45]. It, therefore, will be a future approach by which to upgrade the performance of our composites.

6.4. Conclusion

Thin-film magnetoelectric composites made of piezoelectric AlN thin films and magnetostrictive foils were synthesized with a detailed analysis of the interfaces in order to optimize the mechanical energy transfer. The AlN film deposited using plasma-enhanced atomic layer deposition (PE-ALD) at a low temperature of 250 °C exhibited a preferred (002) orientation and a usable piezoelectric response with the direct piezoelectric coefficient $e_{31,f}$ of 0.37 C/m^2. The film crystal properties and the interface between the films and the foils were carefully investigated by high-resolution transmission electron microscopy. It was found that a transition layer of amorphous Al_xO_y/AlO_xN_y was formed between the films and the foils. The thickness of this transition layer was 10, 30 and 20 nm for the films grown on Ni, Fe and Co. The evolution of the crystallinity of AlN film was studied showing that the film was amorphous at the interface and significantly improved during the ALD growth. The interface between AlN films and the foils was clear and continuous. A strong self-biased magnetoelectric coefficient was achieved in AlN/Ni composites. Namely, the maximum magnetoelectric coefficient of AlN/Ni composites with Ni foil thickness of 7.5, 15, and 30 µm correspondingly was 3.3, 2.8, and 3.1 V.cm^{-1}Oe^{-1} measured at an off-resonance frequency of 46 Hz and at a zero-bias DC magnetic field. Moreover, the magnetoelectric effect was studied in composites made of 550nm-thick films grown on 12.5µm-thick Fe and 15µm-thick Co foils. The maximum magnetoelectric coefficient of AlN/Fe and Al/Co composites was approximately 0.32 and 0.12 V.cm^{-1}Oe^{-1} characterized at 46 Hz with a bias field (H_{dc}) of 6 and

200 Oe. A maximum power density of 75 nW/cm^3 was produced on a load resistance of 200 kΩ. A strong magnetoelectric coupling obtained in AlN/Ni composites, compared to Fe and Co samples, can be attributed to a higher magnetostrictive response of nickel and an excellent interface quality between the AlN film and Ni surface, which is due to a highly conformal coating profile and a low-temperature process. With these advantages, plasma-enhanced atomic layer deposition opens up a simple and efficient pathway to design a novel material compatible with cleanroom facilities, for MEMS energy harvesters and electromagnetic sensors in which the interface effects, such as morphologic roughness, microcracks, delamination, and interdiffusion, can be alleviated.

6.5. References

(1) Chu, Z.; Pourhosseiniasl, M.; Dong, S. Review of Multi-Layered Magnetoelectric Composite Materials and Devices Applications. *Journal of Physics D: Applied Physics*. 2018. https://doi.org/10.1088/1361-6463/aac29b.

(2) Schmid, H. Multi-Ferroic Magnetoelectrics. *Ferroelectrics* **1994**. https://doi.org/10.1080/00150199408245120.

(3) Ramesh, R.; Spaldin, N. A. Multiferroics: Progress and Prospects in Thin Films. *Nature Materials*. 2007. https://doi.org/10.1038/nmat1805.

(4) Wang, K. F.; Liu, J. M.; Ren, Z. F. Multiferroicity: The Coupling between Magnetic and Polarization Orders. *Adv. Phys.* **2009**. https://doi.org/10.1080/00018730902920554.

(5) Dong, S.; Liu, J. M.; Cheong, S. W.; Ren, Z. Multiferroic Materials and Magnetoelectric Physics: Symmetry, Entanglement, Excitation, and Topology. *Adv. Phys.* **2015**. https://doi.org/10.1080/00018732.2015.1114338.

(6) Fiebig, M.; Lottermoser, T.; Meier, D.; Trassin, M. The Evolution of Multiferroics. *Nature Reviews Materials*. 2016. https://doi.org/10.1038/natrevmats.2016.46.

(7) Kimura, T.; Goto, T.; Shintani, H.; Ishizaka, K.; Arima, T.; Tokura, Y. Magnetic Control of Ferroelectric Polarization. *Nature* **2003**. https://doi.org/10.1038/nature02018.

(8) Astrov, D. N. Magnetoelectric Effect in Chromium Oxide. *J. Exp. Theor. Phys.* **1961**.

(9) Catalan, G.; Scott, J. F. Physics and Applications of Bismuth Ferrite. *Advanced Materials*. 2009. https://doi.org/10.1002/adma.200802849.

(10) Khomskii, D. Classifying Multiferroics: Mechanisms and Effects. *Physics (College. Park. Md).* **2009**. https://doi.org/10.1103/physics.2.20.

(11) Ikeda, N.; Ohsumi, H.; Ohwada, K.; Ishii, K.; Inami, T.; Kakurai, K.; Murakami, Y.; Yoshii, K.; Mori, S.; Horibe, Y.; Kitô, H. Ferroelectricity from Iron Valence Ordering in the Charge-Frustrated System LuFe2O4. *Nature* **2005**. https://doi.org/10.1038/nature04039.

(12) Van Den Brink, J.; Khomskii, D. I. Multiferroicity Due to Charge Ordering. *J. Phys. Condens. Matter* **2008**. https://doi.org/10.1088/0953-8984/20/43/434217.

(13) De Groot, J.; Mueller, T.; Rosenberg, R. A.; Keavney, D. J.; Islam, Z.; Kim, J. W.; Angst, M. Charge Order in $LuFe_2O_4$: An Unlikely Route to Ferroelectricity. *Phys. Rev. Lett.* **2012**. https://doi.org/10.1103/PhysRevLett.108.187601.

(14) Van Aken, B. B.; Palstra, T. T. M.; Filippetti, A.; Spaldin, N. A. The Origin of Ferroelectricity in Magnetoelectric $YMnO_3$. *Nat. Mater.* **2004**. https://doi.org/10.1038/nmat1080.

(15) Lilienblum, M.; Lottermoser, T.; Manz, S.; Selbach, S. M.; Cano, A.; Fiebig, M. Ferroelectricity in the Multiferroic Hexagonal Manganites. *Nat. Phys.* **2015**. https://doi.org/10.1038/nphys3468.

(16) Kimura, T. Spiral Magnets as Magnetoelectrics. *Annu. Rev. Mater. Res.* **2007**.

https://doi.org/10.1146/annurev.matsci.37.052506.084259.

(17) Tokura, Y.; Seki, S. Multiferroics with Spiral Spin Orders. *Adv. Mater.* **2010**. https://doi.org/10.1002/adma.200901961.

(18) Cheong, S. W.; Mostovoy, M. Multiferroics: A Magnetic Twist for Ferroelectricity. *Nature Materials*. 2007. https://doi.org/10.1038/nmat1804.

(19) Tokura, Y.; Seki, S.; Nagaosa, N. Multiferroics of Spin Origin. *Reports Prog. Phys.* **2014**. https://doi.org/10.1088/0034-4885/77/7/076501.

(20) Ma, J.; Hu, J.; Li, Z.; Nan, C. W. Recent Progress in Multiferroic Magnetoelectric Composites: From Bulk to Thin Films. *Adv. Mater.* **2011**. https://doi.org/10.1002/adma.201003636.

(21) Wang, Y.; Hu, J.; Lin, Y.; Nan, C. W. Multiferroic Magnetoelectric Composite Nanostructures. *NPG Asia Materials*. 2010. https://doi.org/10.1038/asiamat.2010.32.

(22) van den Boomgaard, J.; Born, R. A. J. A Sintered Magnetoelectric Composite Material $BaTiO_3$-Ni(Co,Mn)Fe_2O_4. *J. Mater. Sci.* **1978**. https://doi.org/10.1007/BF00553210.

(23) Premkumar, S.; Varadharajan, E.; Rath, M.; Mathe, V. L.; Ramachandra Rao, M. S. Microstructural Analysis of Co-Sintered PSLZT-NZFO Layered Magnetoelectric Composite. *Ferroelectrics* **2017**. https://doi.org/10.1080/00150193.2017.1362283.

(24) Zavaliche, F.; Zheng, H.; Mohaddes-Ardabili, L.; Yang, S. Y.; Zhan, Q.; Shafer, P.; Reilly, E.; Chopdekar, R.; Jia, Y.; Wright, P.; Schlom, D. G.; Suzuki, Y.; Ramesh, R. Electric Field-Induced Magnetization Switching in Epitaxial Columnar Nanostructures. *Nano Lett.* **2005**. https://doi.org/10.1021/nl051406i.

(25) Wan, J. G.; Wang, X. W.; Wu, Y. J.; Zeng, M.; Wang, Y.; Jiang, H.; Zhou, W. Q.; Wang, G. H.; Liu, J. M. Magnetoelectric $CoFe_2O_4$-Pb(Zr,Ti)O_3 Composite Thin Films Derived by a Sol-Gel Process. *Appl. Phys. Lett.* **2005**. https://doi.org/10.1063/1.1889237.

(26) Ryu, H.; Murugavel, P.; Lee, J. H.; Chae, S. C.; Noh, T. W.; Oh, Y. S.; Kim, H. J.; Kim, K. H.; Jang, J. H.; Kim, M.; Bae, C.; Park, J. G. Magnetoelectric Effects of Nanoparticulate $Pb(Zr_{0.52}Ti_{0.48})O_3$-$NiFe_2O_4$ Composite Films. *Appl. Phys. Lett.* **2006**. https://doi.org/10.1063/1.2338766.

(27) Ryu, J.; Priya, S.; Uchino, K.; Kim, H. E. Magnetoelectric Effect in Composites of Magnetostrictive and Piezoelectric Materials. *Journal of Electroceramics*. 2002. https://doi.org/10.1023/A:1020599728432.

(28) Mori, K.; Wuttig, M. Magnetoelectric Coupling in Terfenol-D/Polyvinylidenedifluoride Composites. *Appl. Phys. Lett.* **2002**. https://doi.org/10.1063/1.1491006.

(29) Ryu, J.; Priya, S.; Carazo, A. V.; Uchino, K.; Kim, H.-E. Effect of the Magnetostrictive Layer on Magnetoelectric Properties in Lead Zirconate Titanate/Terfenol-D Laminate Composites. *J. Am. Ceram. Soc.* **2001**. https://doi.org/10.1111/j.1151-2916.2001.tb01113.x.

(30) Ryu, J.; Kang, J. E.; Zhou, Y.; Choi, S. Y.; Yoon, W. H.; Park, D. S.; Choi, J. J.; Hahn, B.

D.; Ahn, C. W.; Kim, J. W.; Kim, Y. Do; Priya, S.; Lee, S. Y.; Jeong, S.; Jeong, D. Y. Ubiquitous Magneto-Mechano-Electric Generator. *Energy Environ. Sci.* **2015**. https://doi.org/10.1039/c5ee00414d.

(31) Annapureddy, V.; Na, S. M.; Hwang, G. T.; Kang, M. G.; Sriramdas, R.; Palneedi, H.; Yoon, W. H.; Hahn, B. D.; Kim, J. W.; Ahn, C. W.; Park, D. S.; Choi, J. J.; Jeong, D. Y.; Flatau, A. B.; Peddigari, M.; Priya, S.; Kim, K. H.; Ryu, J. Exceeding Milli-Watt Powering Magneto-Mechano-Electric Generator for Standalone-Powered Electronics. *Energy Environ. Sci.* **2018**. https://doi.org/10.1039/c7ee03429f.

(32) Nan, C. W.; Liu, G.; Lin, Y. Influence of Interfacial Bonding on Giant Magnetoelectric Response of Multiferroic Laminated Composites of Tb_1-XDy_xFe_2 and $PbZr_xTi_{1-x}O_3$. *Appl. Phys. Lett.* **2003**. https://doi.org/10.1063/1.1630157.

(33) Bichurin, I.; Petrov, M.; Srinivasan, G. Theory of Low-Frequency Magnetoelectric Coupling in Magnetostrictive-Piezoelectric Bilayers. *Phys. Rev. B - Condens. Matter Mater. Phys.* **2003**. https://doi.org/10.1103/PhysRevB.68.054402.

(34) Wang, X.; Pan, E. Magnetoelectric Effects in Multiferroic Fibrous Composite with Imperfect Interface. *Phys. Rev. B - Condens. Matter Mater. Phys.* **2007**. https://doi.org/10.1103/PhysRevB.76.214107.

(35) Gupta, R.; Tomar, M.; Kumar, A.; Gupta, V. Performance of Magnetoelectric PZT/Ni Multiferroic System for Energy Harvesting Application. *Smart Mater. Struct.* **2017**. https://doi.org/10.1088/1361-665X/26/3/035002.

(36) Sinha, N.; Wabiszewski, G. E.; Mahameed, R.; Felmetsger, V. V.; Tanner, S. M.; Carpick, R. W.; Piazza, G. Piezoelectric Aluminum Nitride Nanoelectromechanical Actuators. *Appl. Phys. Lett.* **2009**. https://doi.org/10.1063/1.3194148.

(37) Hayes, P.; Jovičević Klug, M.; Toxværd, S.; Durdaut, P.; Schell, V.; Teplyuk, A.; Burdin, D.; Winkler, A.; Weser, R.; Fetisov, Y.; Höft, M.; Knöchel, R.; McCord, J.; Quandt, E. Converse Magnetoelectric Composite Resonator for Sensing Small Magnetic Fields. *Sci. Rep.* **2019**. https://doi.org/10.1038/s41598-019-52657-w.

(38) Nguyen, T.; Adjeroud, N.; Glinsek, S.; Fleming, Y.; Guillot, J.; Grysan, P.; Polesel-Maris, J. A Film-Texture Driven Piezoelectricity of AlN Thin Films Grown at Low Temperatures by Plasma-Enhanced Atomic Layer Deposition. *APL Mater.* **2020**. https://doi.org/10.1063/5.0011331.

(39) Liang, X.; Dong, C.; Chen, H.; Wang, J.; Wei, Y.; Zaeimbashi, M.; He, Y.; Matyushov, A.; Sun, C.; Sun, N. A Review of Thin-Film Magnetoelastic Materials for Magnetoelectric Applications. *Sensors (Switzerland)*. 2020. https://doi.org/10.3390/s20051532.

(40) Prume, K.; Muralt, P.; Calame, F.; Schmitz-Kempen, T.; Tiedke, S. Piezoelectric Thin Films: Evaluation of Electrical and Electromechanical Characteristics for MEMS Devices. *IEEE Trans. Ultrason. Ferroelectr. Freq. Control* **2007**. https://doi.org/10.1109/TUFFC.2007.206.

(41) Klokholm, E.; Aboaf, J. The Saturation Magnetostriction of Thin Polycrystalline Films of Iron, Cobalt, and Nickel. *J. Appl. Phys.* **1982**. https://doi.org/10.1063/1.330930.

(42) Zhou, Y.; Chul Yang, S.; Apo, D. J.; Maurya, D.; Priya, S. Tunable Self-Biased Magnetoelectric Response in Homogenous Laminates. *Appl. Phys. Lett.* **2012**. https://doi.org/10.1063/1.4769365.

(43) Zhou, Y.; Apo, D. J.; Priya, S. Dual-Phase Self-Biased Magnetoelectric Energy Harvester. *Appl. Phys. Lett.* **2013**. https://doi.org/10.1063/1.4829151.

(44) Patil, D. R.; Zhou, Y.; Kang, J. E.; Sharpes, N.; Jeong, D. Y.; Kim, Y. Do; Kim, K. H.; Priya, S.; Ryu, J. Anisotropic Self-Biased Dual-Phase Low Frequency Magneto-Mechano-Electric Energy Harvesters with Giant Power Densities. *APL Mater.* **2014**. https://doi.org/10.1063/1.4870116.

(45) Greve, H.; Woltermann, E.; Quenzer, H. J.; Wagner, B.; Quandt, E. Giant Magnetoelectric Coefficients in $(Fe_{90}Co_{10})_{78}Si_{12}B_{10}$-AlN Thin Film Composites. *Appl. Phys. Lett.* **2010**. https://doi.org/10.1063/1.3377908.

(46) Sreenivasulu, G.; Mandal, S. K.; Bandekar, S.; Petrov, V. M.; Srinivasan, G. Low-Frequency and Resonance Magnetoelectric Effects in Piezoelectric and Functionally Stepped Ferromagnetic Layered Composites. *Phys. Rev. B - Condens. Matter Mater. Phys.* **2011**. https://doi.org/10.1103/PhysRevB.84.144426.

Supplementary information:

Low-temperature growth of AlN films on magnetostrictive foils for high-magnetoelectric-response thin-film composites

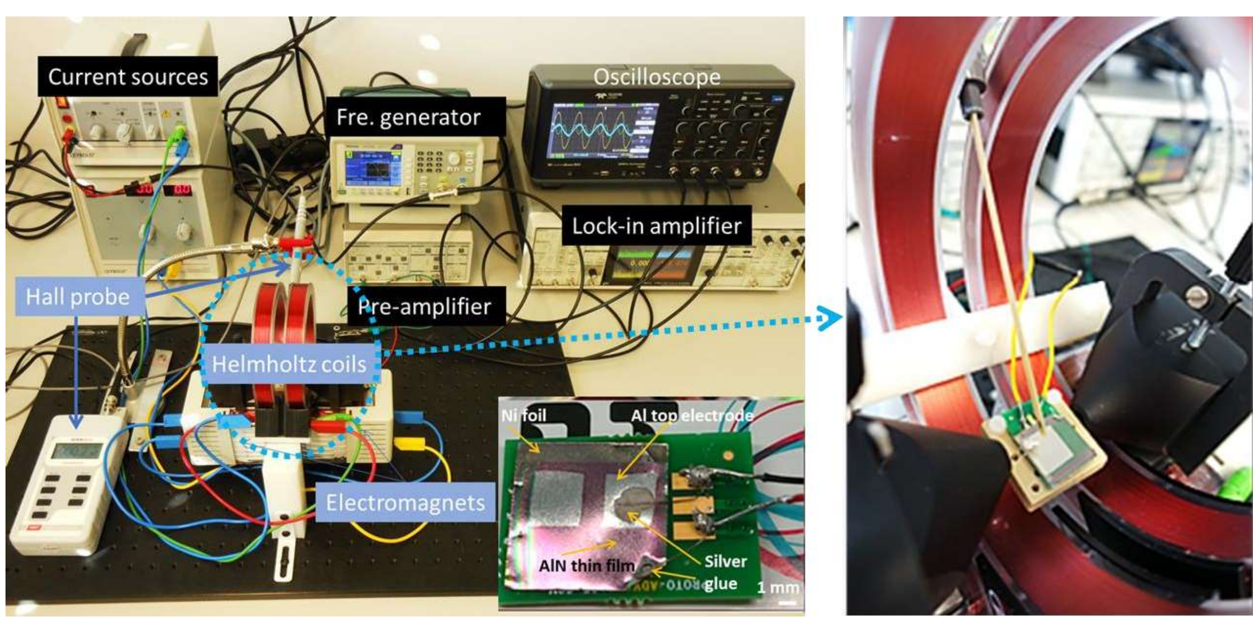

Figure S1: In-housed magnetoelectric characterization bench.

A small AC and a bias DC magnetic field are generated by Helmholtz coils (Leybold Shop, ref. 555 604) and an electromagnet (Leybold Shop, ref. 562 131, ref. 562 11), respectively. The Hall probe (Hirst Magnetics, GM08) is placed as close as to the sample fixed in a sample holder located between Helmholtz coils. An excitation signal to drive the AC and DC bias magnetic field is made by a two-channel frequency generator (Tektronix, AFG1062). The output signal from the ME sample is then analysed by a lock-in amplifier (SRS865A, 4 MHz Lock-In Amplifier, Stanford), and with data collected by an oscilloscope (Teledyne/Lecroy, WaveAce2024). The sample showed in the figure is the AlN/Ni composite mounted on a PCB for output contacting. Silver glue was used to connect the wire on the ME chip top and bottom electrodes.

Capabilities for characterization of the ME bench:

DC field max. with an electromagnet ~ +/- 0.25 T = +/- 2500 Oe = +/- 200 kA/m

AC field max. with Helmholtz coils ~ +/- 20 mT = T = +/- 200 Oe = +/- 16 kA/m

AC field frequency range = 1Hz to 5 kHz

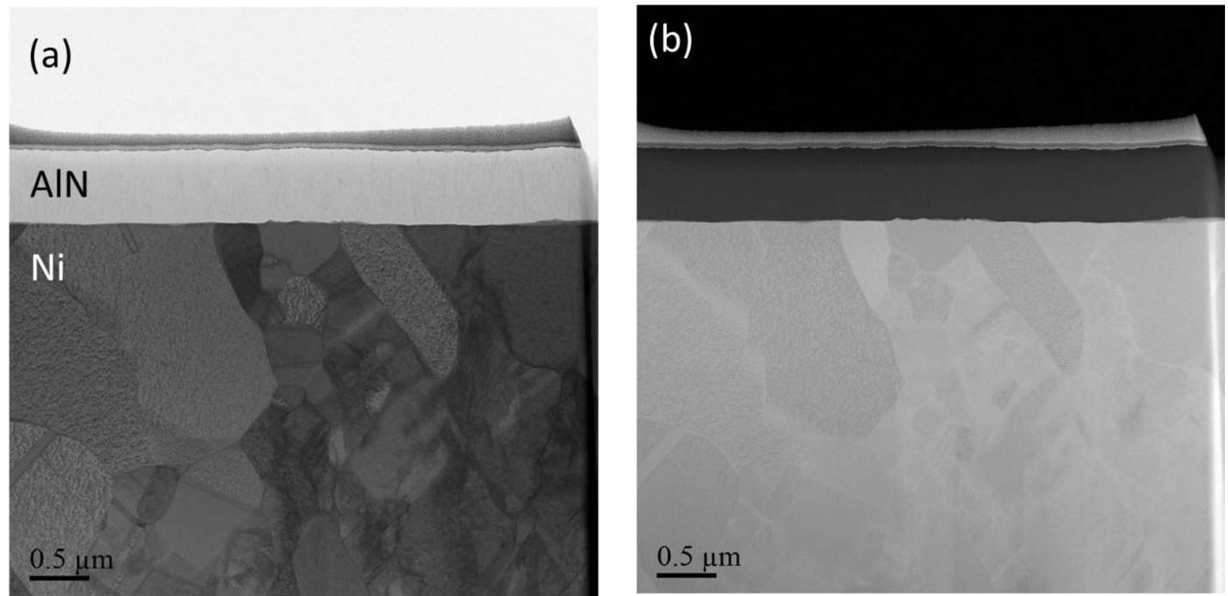

Figure S2: (a) Cross-sectional STEM BF, (b) STEM-HAADF micrographs of AlN/Ni.

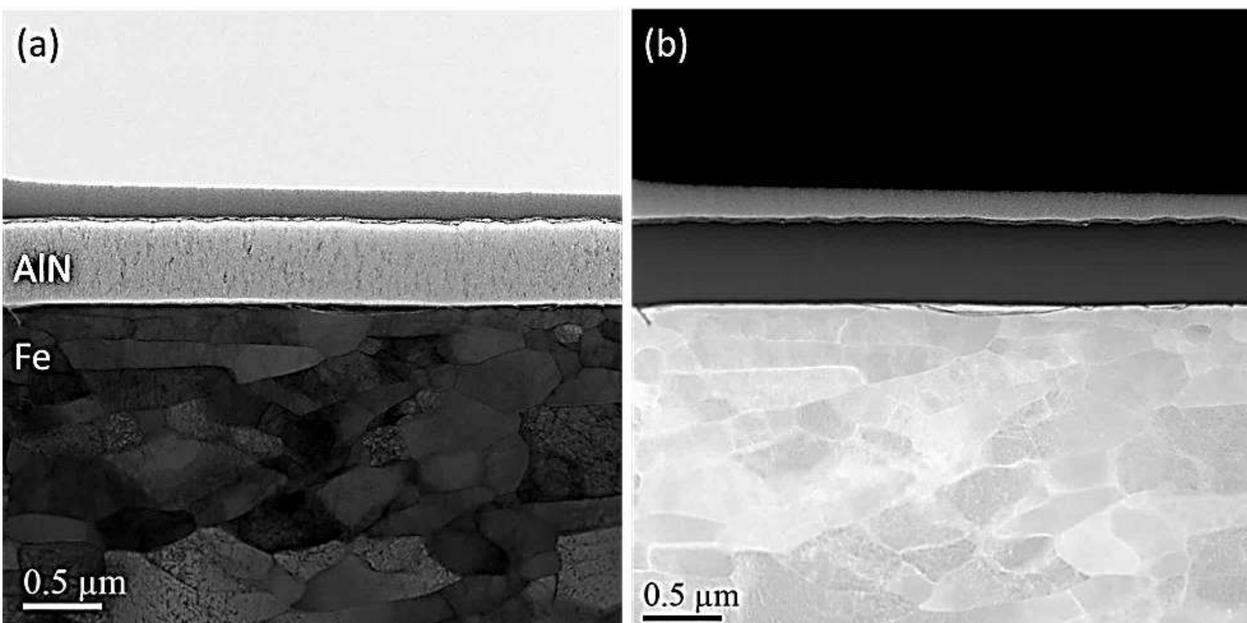

Figure S3: (a) Cross-sectional STEM BF, (b) STEM-HAADF micrographs of AlN/Fe.

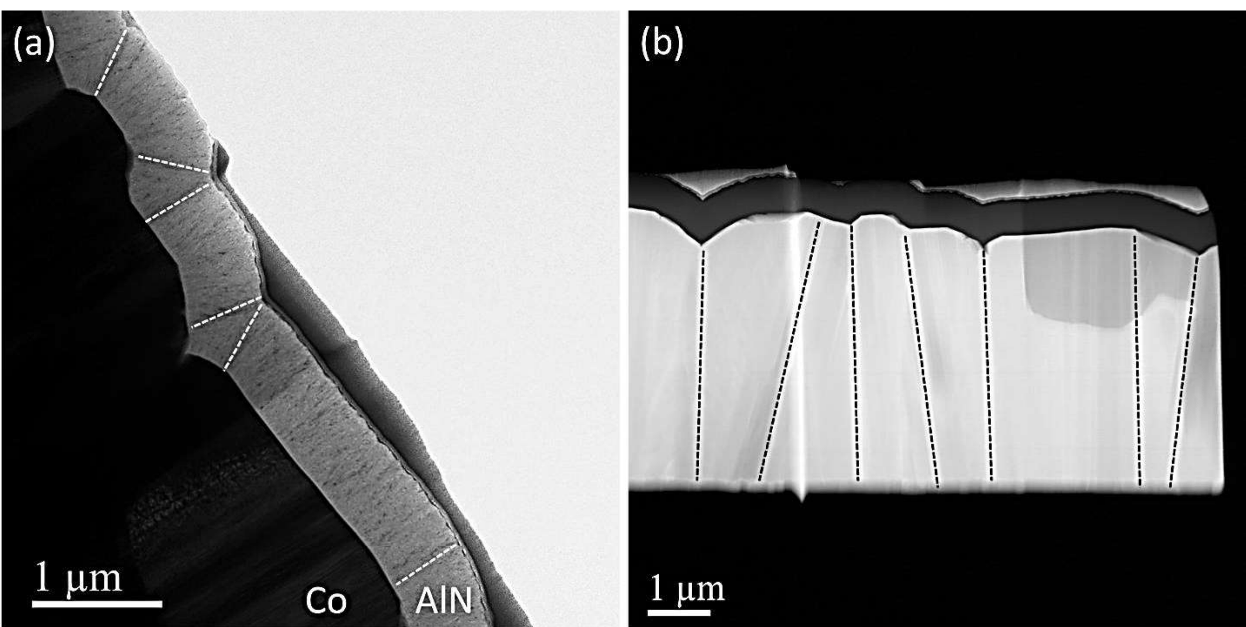

Figure S4: (a) Cross-sectional STEM BF, (b) STEM-HAADF micrographs of AlN/Co. The dash lines guide for directions of the film grains (a) and Co grains (b).

7

Perspectives: ways to improve the magnetoelectric effect in thin-film composites

This chapter introduces possible ways to enhance magnetoelectric coupling in thin-film composites. In general, there are two methods by which the magnetoelectric response can be improved. One is to upgrade constituent layers, i.e. magnetostrictive and/or piezoelectric layers, and another is the use of mechanical resonance structures. In this chapter, we attempt to summarize our efforts on the fabrication of promising candidates, such as ferromagnetic shape memory alloy Ni-Mn-Ga off-stoichiometric film and ScAlN alloy film, used as magnetostrictive and piezoelectric layers, as well as the capability of resonance structures to enhance the magnetoelectric effect.

7.1
Off-stoichiometric Ni-Mn-Ga films: fabrication and characterizations

Explored in 1996, ferromagnetic shape memory alloys have demonstrated great potential for sensing and actuating devices [1]. Among them, Ni-Mn-Ga and its off-stoichiometric analogs in both bulk and thin films show the largest strain induced by thermal and/or magnetic field excitation [1]. Terfenol-D ($Tb_xDy_{1-x}Fe_2$) is well-known as the strongest magnetostrictive material with strains < 0.2% [1]. In comparison to Terfenol-D, the strain generated by the external magnetic field in Ni_2MnGa is about two orders of magnitude greater [1]. To date, strains of up to 9.5% have been reported in an Ni-Mn-Ga single crystal [2]. A giant strain induced in Ni-Mn-Ga is attributed to the movement of twin variants caused by an external magnetic field that is different from Terfenol-D where domain switching by a magnetic field induces strain. In bulk form, this alloy is very brittle, however, its ductility can be greatly improved in thin film. Yet, the fabrication of Ni-Mn-Ga thin films faces several technical challenges, e.g. control of composition stoichiometry, elemental diffusion and film delamination caused by post-annealing processes at high temperatures (above 650°C). This chapter reports our efforts on the fabrication, optimization, and characterization of off-stoichiometric Ni-Mn-Ga thin films prepared by magnetron sputtering. We described the experimental methods in Chapter 3.

7.1.1. Introduction to Heusler alloys

7.1.1.1. Ferromagnetic shape memory effect

Shape memory effect is a phenomenon of the phase-transition-induced deformation occurring in some metal alloys in which austenite and martensite phases coexist. The phase transition is diffusionless and can be triggered by applying either temperatures or an external magnetic field. At the phase transition temperature, the transition between the austenite phase and martensite phase occurs. Above the phase transition temperature, the material has a cubic austenite phase, while below this temperature, the material exhibits a martensite phase with a more disordered structure. The martensite phase exists in more than one variant that has a lower ordered structure, e.g. tetragonal, monoclinic, triclinic etc. [3,4].

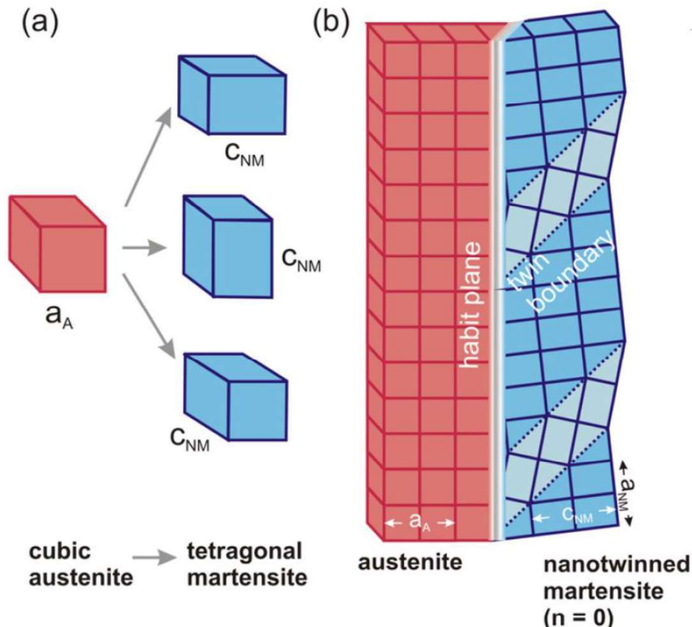

***Figure 7.1**: (a) The unit cell of a cubic austenite can transform into three equivalent orientations of a tetragonal martensite unit cell, (b) the orientation structure of austenite and nanotwinned martensite phases [4].*

Twin variants refer to martensite zones with slight variations in crystal structures or orientations [3,4]. Twin boundaries are formed between these variants, as presented in Figure 7.1. In the Ni-Mn-Ga Heusler alloy, both austenite and martensite phases are ferromagnetic, thus the shape memory effect in this alloy is also called the ferromagnetic shape memory effect. In the Ni-Mn-Ga alloy, the twin variants in the martensite phase have magnetic moments in different directions. On application of an external magnetic field, the twin variants of those magnetic moments, which are not parallel to the applied field, de-twin to align their magnetic moments with the applied field. This movement results in the macro-deformation of material, as presented in Figure 7.2.

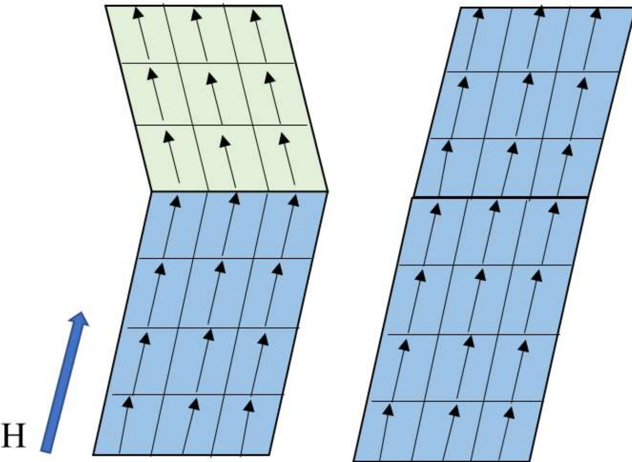

***Figure 7.2**: Sketch of magnetic-field-induced reorientation.*

Many systems have been intensively investigated to search for ferromagnetic shape memory alloys of both full and half Heusler alloys, such as Ni_2MnGa, Ni_2MnAl, Co_2MnAl, Ni_2MnIn, Ni_2MnSn,

NiMnGa, NiMnGaIn, etc. Amongst them, full and half Ni-Mn-Ga alloys present the largest strain induced by a magnetic field at room temperature.

***Table 7.1**: Summarizes several bulk magnetostrictive and magnetoelastic materials.*

Materials	λ_s(ppm) bulk	Origin	Stimuli
Ni-Zn Ferrite	20-40	Magnetostriction	Magnetic field
Nickel	-20 to -50	Magnetostriction	Magnetic field
Metglas	20-50	Magnetostriction	Magnetic field
Galfenol	200-400	Magnetostriction	Magnetic field
Terfenol-D	1000-1500	Magnetostriction	Magnetic field
$Ni_{50}Mn_{28}Ga_{22}$	100000	Shape memory	Magnetic field Temperature

Compared to the highest magnetostrictive Terfenol-D, the Ni-Mn-Ga alloy exhibits a giant magnetic-induced strain which is about 2 orders of magnitude higher than Terfenol-D. It shows great potential for designing ME composites.

7.1.1.2. Structure

In the austenite state, an Ni_2MnGa has an empirical formula X_2YZ exhibiting a $L2_1$ structure, which resembles four interpenetrating f.c.c lattices, as presented in Figure 7.3. In this structure, X atoms possess the corner positions in the unit cell, while Y and Z atoms occupy the body center positions of the sub lattices.

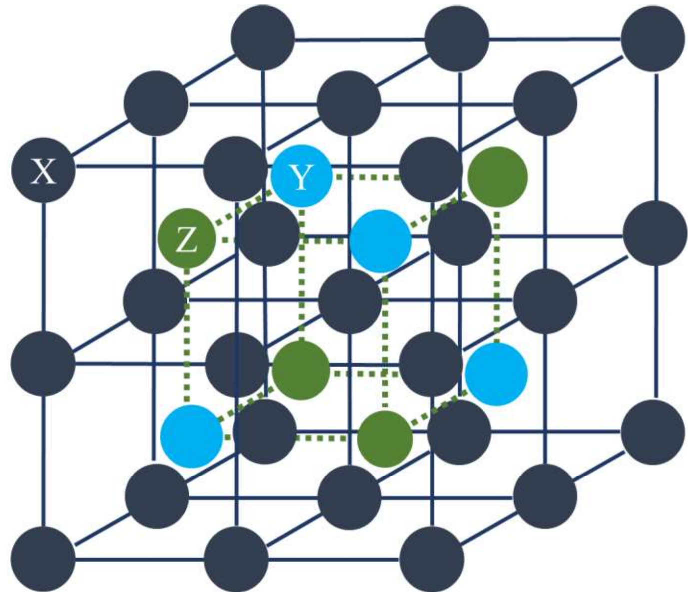

***Figure 7.3:** Crystallographic structure of Ni_2MnGa Heusler alloy.*

As the temperature decreases, this alloy undergoes a martensitic phase transition. In the martensite state, its structure not only has a tetragonal structure, but also modulated structures related to the tetragonal structure. Figure 7.4 shows the relationship between $L2_1$ and the tetragonal structures, and the most common modulated structures [5].

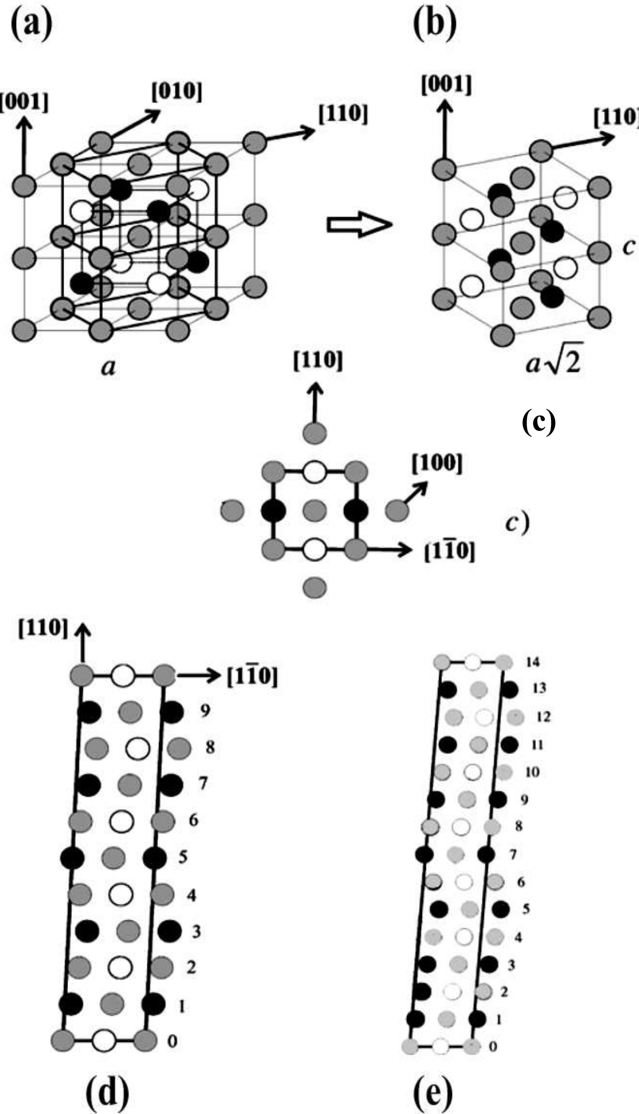

Figure 7.4: *The austenite and martensite structures of Ni_2MnGa. Light gray: Ni, white: Mn, black: Ga. (a) The $L2_1$ structure, (b) the tetragonal unit cell and (c) its top view, (d) and (e) the 5M (or 10M) and 7M (or 14M) modulated structures obtained by shearing the tetragonal cell. "M" refers to the monoclinicity resulting from the distortion associated with the modulation [5].*

7.1.1.3. Magnetic properties

Figure 7.5 shows an example of the temperature dependence of magnetization M(T) for an off-stoichiometric Ni-Mn-Ga alloy [5]. When applied to a small magnetic field, the alloy undergoes a martensitic transformation at a temperature below T_C^A. The measurements are carried out on a zero-field-cooled (ZFC), field-cooled (FC), and (field-heating) sequences.

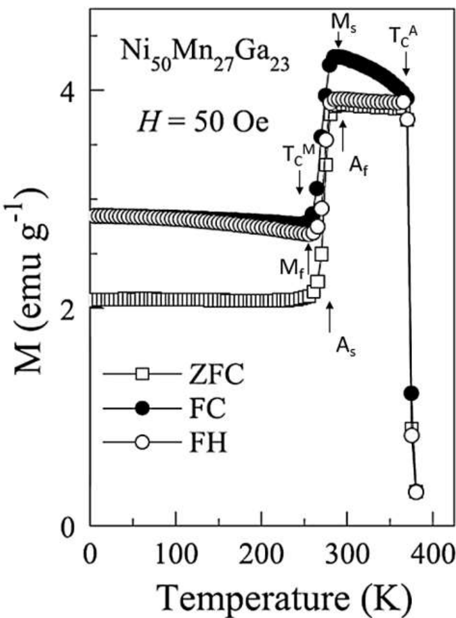

Figure 7.5: *Magnetization as a function of temperature for a Ni-Mn-Ga alloy* [5].

Following the FC curve, the magnetization exhibits a fast increase with decreasing temperature and ferromagnetic (FM) state sets at T_C^A. By further decreasing temperature, the martensitic phase begins to form at a temperature M_S and finishes at M_f. Below M_S, the M(T) are quite plateaued,

which is due to the higher twin boundary mobility and stronger magnetocrystalline anisotropy in the martensitic state. The drop in M(T) below M_S is due to the occurrence of AF (antiferromagnetic) short-range exchange [5].

7.1.1.4. Composition dependence of structural and magnetic properties

In Heusler alloys, the stoichiometry of the three elements is found as one of the key parameters in manipulating the properties in both film and bulk forms. Structural properties, martensitic-austenitic phase transition, Curie temperature (T_C), saturation magnetization, and magnetocrystalline anisotropy strongly depend on the Ni-Mn-Ga composition [6,7]. It shows that replacing Mn or Ga with Ni or adding Mn to replace Ga increase the phase transformation temperature coincidence with a decrease in T_C. The valence electron concentration (e/a) is defined as the number f valence electron per atom, as shown below:

$$\frac{\mathrm{e}}{\mathrm{a}} = \frac{10(\%\mathrm{Ni}) + 7\ (\%\mathrm{Mn}) + 3\ (\%\mathrm{Ga})}{(\%\mathrm{Ni} + \%\ \mathrm{Mn} + \%\mathrm{Ga})}$$

Here, the nominal valence electrons of Ni, Mn and Ga are 10, 7, 3, respectively.

It is found that the crystal structure of the austenite and martensite phases in Ni-Mn-Ga is highly sensitive to the composition or the valence electron concentration e/a, as shown in Figure 7.6. The structure of the Ni-Mn-Ga alloy evolves essentially as cubic $L2_1$ → 10M (or 5 M) → 14M (or 7 M) → $L1_0$ as increasing e/a.

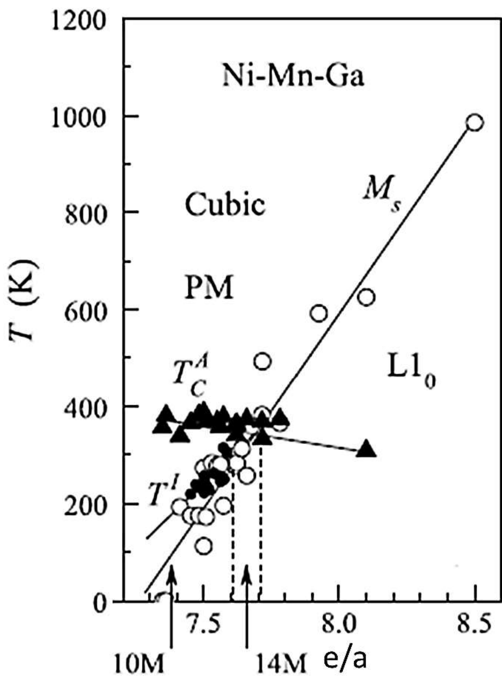

Figure 7.6: *The magnetic and structural phase diagram in Ni-Mn-Ga alloy* [5].

Figure 7.7 presents a dependence of the martensitic transformation temperature (T_{mart}) on the valence electron concentration e/a. The literature data was fitted by taking the linear relationship as T_{mart} = 702.5 (e/a)- 5067. The fitting presents large errors, suggesting that the T_{mart} may also be sensitive to the microstructure of the alloy as in the fabrication process [7].

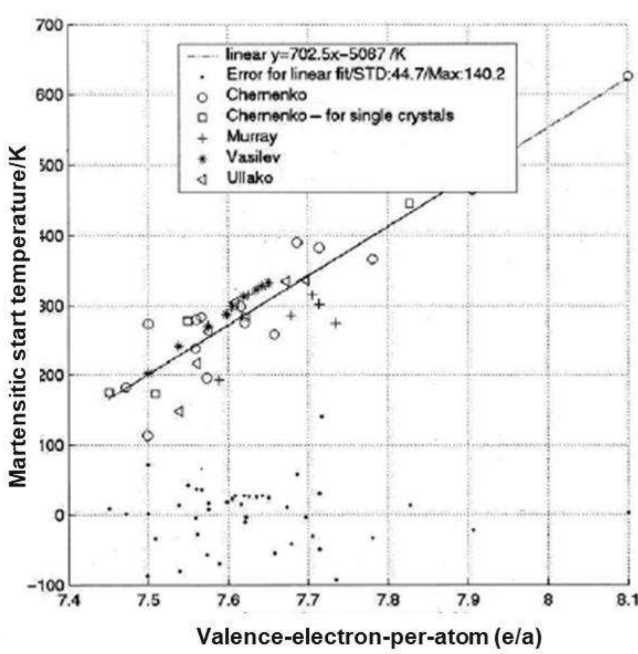

Figure 7.7: *Martensitic transformation temperature as a function of valence electron concentration e/a* [7].

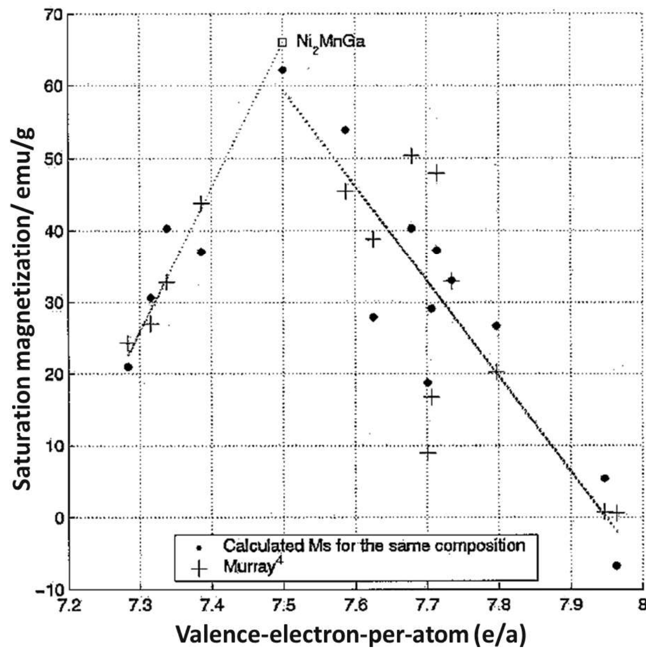

Figure 7.8: *Dependence of saturation magnetization on valence electron concentration e/a* [7].

The dependence of saturation magnetization on valence electron concentration is shown in Figure 7.8. It appears as a peak at a valence electron concentration of 7.5 corresponding to stoichiometric Ni_2MnGa.

7.1.2. Results

7.1.2.1. Effect of the post-annealing process

The deposition process of the Ni-Mn-Ga thin films on silicon wafers is based on the magnetron sputtering described in Chapter 3 Section "3.1.2 Magnetron sputtering". As-deposited films with a thickness of about 100 nm underwent a post-annealing process. The one-step process is performed with a temperature varied between 400, 500, and 600 °C. In addition, the two-step process is carried out at 400 and 700 °C.

The XRD patterns of the as-deposited film and the annealed films is given in Figure 7.9(a). As can be seen, the as-grown film shows a broad peak at around 43°, implying a highly amorphous phase, while the annealed films exhibit typical diffraction peaks at about 42°, 43.5° and 45°. These peaks become sharper, implying the film crystallinity is better, as the annealing temperature increases. However, due to higher annealing temperatures, oxide phases, such as NiO, MnO, Mn_xO_y and Ga_2O_3 are formed. The dominant peak at 43.5° refers to the austenite phase, while the two minor peaks at 42° and 45° refer to the martensite phase. V. A. Chernenko et al. reported similar XRD diffraction patterns for the thin film deposition of Ni-Mn-Ga alloys on SiO2 samples after annealing, as illustrated in Figure 7.9(b) [8].

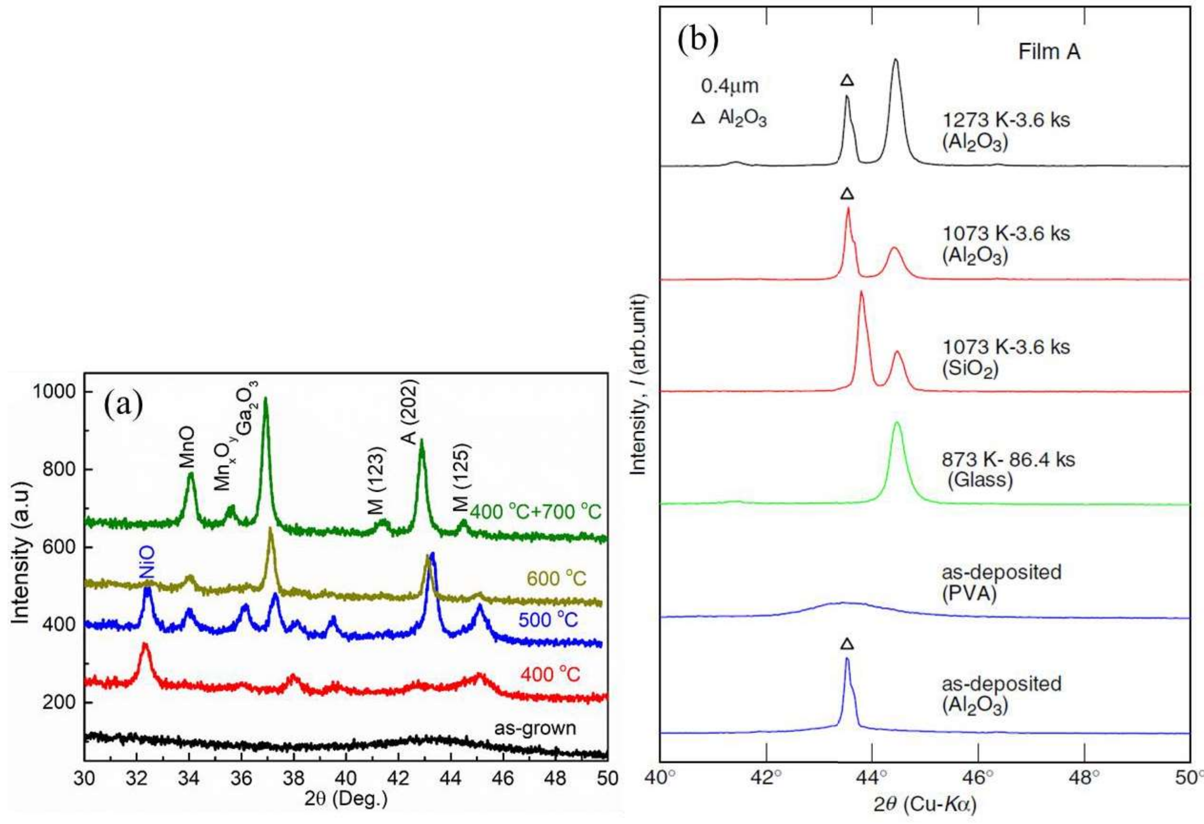

Figure 7.9: *XRD patterns of (a) our Ni-Mn-Ga films annealed at different temperatures, (b) 400nm-thick Ni-Mn-Ga films on different substrates from the reference* [8].

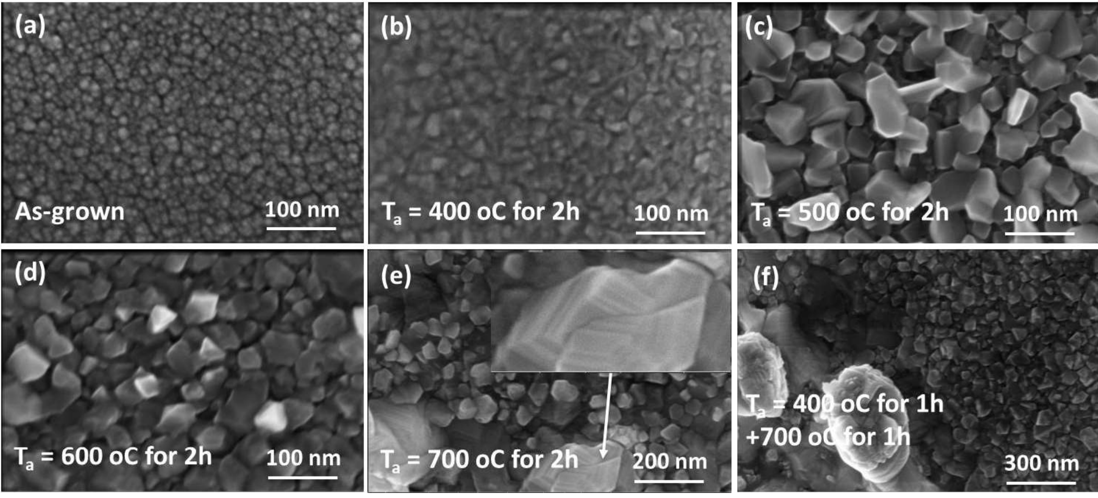

Figure 7.10: *Top-view SEM micrographs of Ni-Mn-Ga film annealed at different temperatures. Stripes appearing on grains as highlighted in (e) are a typical signature of the twin boundaries of Heusler alloys.*

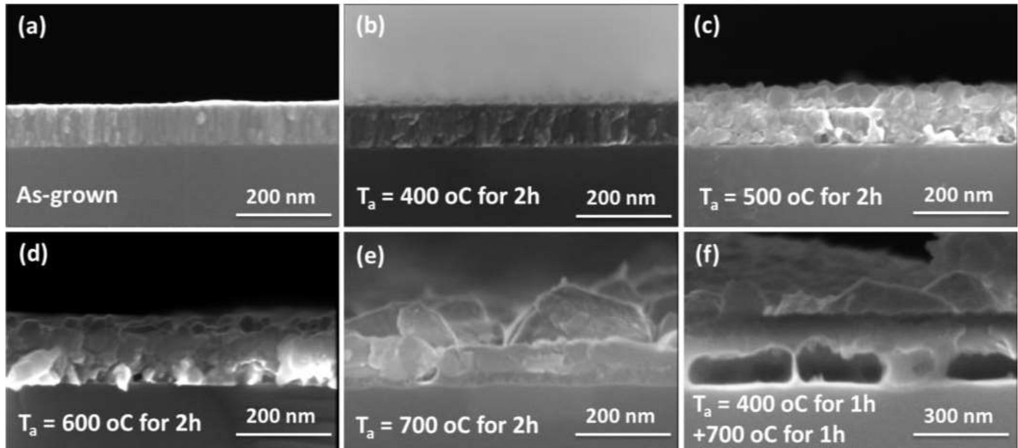

Figure 7.11: *Cross-sectional SEM micrographs of Ni-Mn-Ga film annealed at different temperatures.*

Figures 7.10 and 7.11 present top-view and cross-sectional SEM micrographs of the Ni-Mn-Ga films. The as-deposited film is homogeneous with a grain size of about 20nm. The film morphology and grain size become rougher and larger as the annealing temperature increases. Grain size is about 25, 60, 50, 50, and 60 nm for the film annealed by the one-step process with a change in temperature from 400-700 °C and the two-step process, respectively. Notably, the stripes, a typical signature of the twin boundaries, are observed in the films annealed at 500, 600, and 700 °C, as shown in the insert in Figure 7.10 (e). The interface between the annealed film and the substrate is fairly poor as delamination occurred due to the high temperature processes.

In order to achieve better film morphology and grain, the annealing time is increased to 4h. Figure 7.12 shows a top-view and cross-sectional SEM images for a 500nm-thick film annealed at 650°C for 4h. It is clearly shown that the film annealed at 650 °C for 4h is homogenous with larger grains of 100-150 nm. Stripes are also observed that indicate the presence of twin boundaries of the martensite phase.

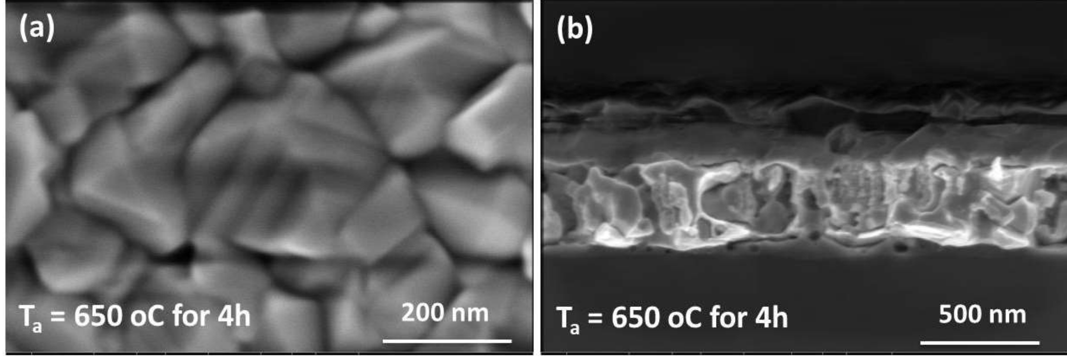

Figure 7.12: *(a) Top-view and (b) cross-sectional SEM micrographs of 500nm-thick Ni-Mn-Ga films annealed at 650 °C for 4h in high vacuum.*

XPS was performed to study the composition of Ni-Mn-Ga films annealed at 650c°C for 4h, as shown in Figure 7.13. Table 2 summarizes the atomic concentrations of C, Ni, Mn, Ga, O, and Si presented in the sample.

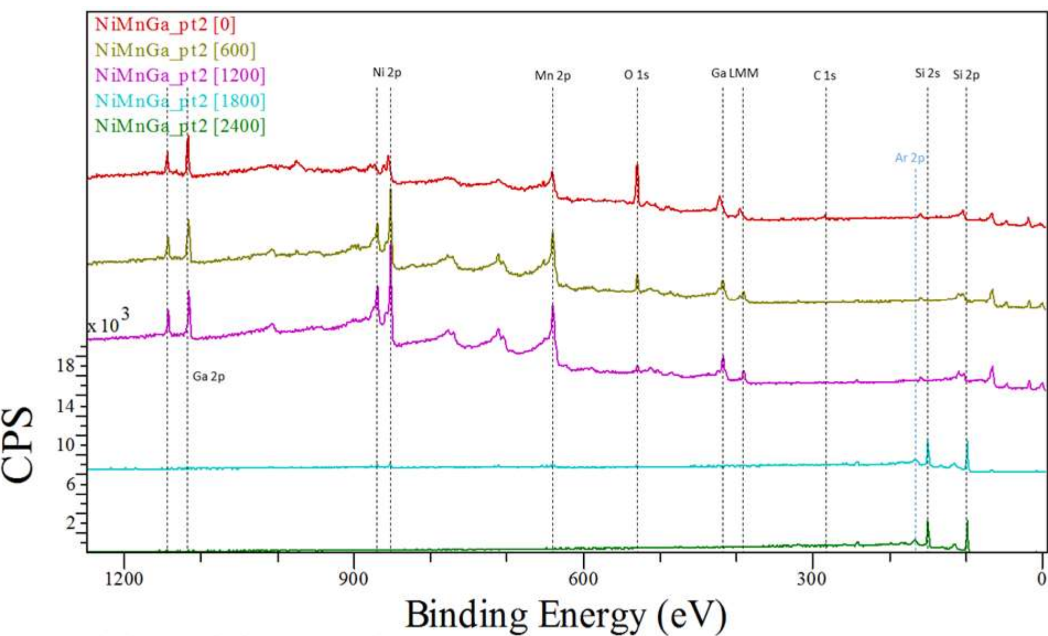

Figure 7.13: *The in-depth XPS profile of Ni-Mn-Ga film annealed at 650 °C for 4h on the surface and after sputtering for 600, 1200, 1800 and 2400 s.*

It can be seen that the films are strongly oxidized on the surface with 47.9 at.% of oxygen presence in the film. After sputtering, no significant amount of oxygen is detected in depth. It is noteworthy that the film composition varies depending on the film thickness. The compositions of Ni, Mn and Ga are 54.80, 21.94 and 23.26 at.% after 600 s of sputtering, respectively. These change to 60, 18.76, and 21.24 at.% after 1200 s of sputtering. Moreover, as compared to the starting target, in $Ni_{45}Mn_{27.5}Ga_{27.5}$, the percentage of Ni increases, while percentages of Mn and Ga decrease. It has been reported that Mn and Ga exhibit a high evaporation rate compared to Ni due to the high temperature post-annealing process [9]. The loss of Mn and Ga cause an increase in the percentage of Ni in the film. Also, after 1800 s of sputtering, we noticed a transition zone with the presence of nickel in the silicon/silicon oxide interface, which could be due to the atomic interdiffusion of nickel in silicon. We will come back to this observation in the next section about diffusion barriers.

Table 7.2: *The elemental compositions of Ni-Mn-Ga film annealed at 650 °C for 4h analyzed after different sputtering times.*

Sputtering time (s)	C (at.%)	Ga (at.%)	Mn (at.%)	Ni (at.%)	O (at.%)	Si (at.%)
0	14.5	10	10.9	16.7	47.9	0
600	0	23.26	21.94	54.80	-	0
1200	0	21.24	18.76	60	-	0
1800	0	0	0.1	4.1	2.9	92.8
2400	0	0	0	0	0	100
ACI Ni-Mn-Ga **sputtering target**	-	27.5	27.5	45.0	-	-

The VSM measurements were carried out to study the magnetic properties of the Ni-Mn-Ga film annealed at 650 °C for 4h, as presented in Figure 7.14. Figure 7.14(a) shows the typical ferromagnetic behavior of the film measured at 300, 175 and 5 K. The temperature dependence of magnetization measurements is carried out for two constant values of magnetic field DC bias, as shown in Figure 7.14 (b). The martensitic transformation transition is at about 50 K. On application of a small external magnetic field of 5 mT, the magnetic moment of the films shows a drop below 50 K. As explained before, this is possibly due to an initial loss of FM ordering caused by the presence of antiferromagnetic short-range ordering. With a stronger field of 5 T, this feature vanishes and keeps increasing below the transformation temperature. The slight increase in magnetic moment below the transformation temperature is observed only in Ni-Mn-Ga alloys. In all other alloys, the magnetization in the martensitic state is lower than in the austenitic state [5].

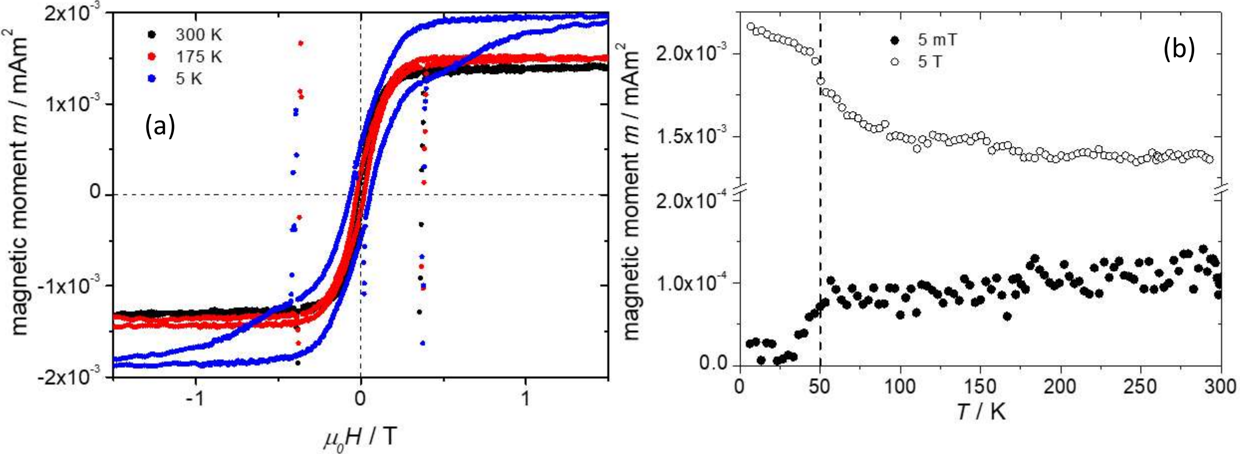

Figure 7.14: *Magnetization measurements for the Ni-Mn-Ga film annealed at 650 °C for 4h in a high vacuum (10^{-6} mbar), (a) against the applied DC magnetic field, and (b) against the sample temperature.*

7.1.2.2. Effect of co-sputtering

As pointed out above, the loss of Mn and Ga, and possibly also nickel interdiffusion in the silicon substrate, caused by the high temperature post-annealing leads to a deviation in the composition of the annealed film compared the desired composition. In this section, an additional Mn target is used to compensate the manganese loss, thus tailoring the film composition. The Mn and Ni-Mn-Ga targets are sputtered simultaneously in the same PVD reactor. We call it co-sputtering. The sputtering DC power is fixed at 100 W for the Ni-Mn-Ga target, whereas the RF magnetron power for the Mn target varies from 10 to 30 W with intermediate values.

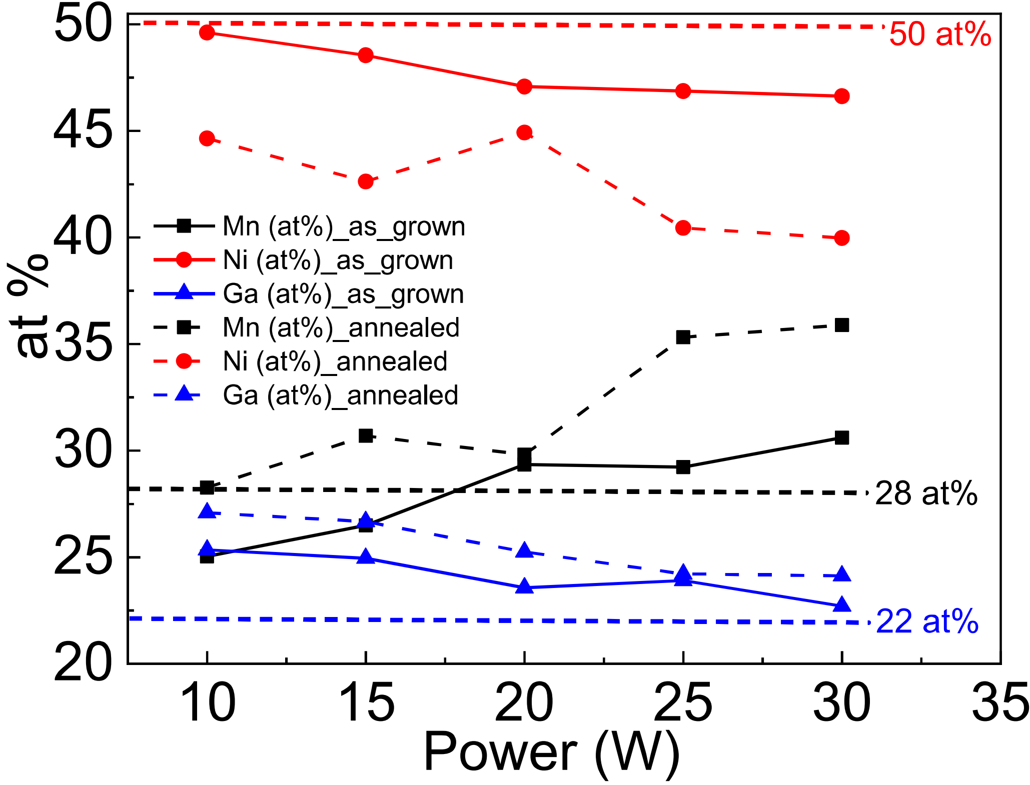

Figure 7.15: *The elemental composition identified by EDX of Ni-Mn-Ga films versus the sputtering power of the Mn target. The dashed black, blue and red lines indicate the desired composition of Ni-Mn-Ga film at 50, 28 and 22 at% for Ni, Mn and Ga, respectively, to get the ferromagnetic shape memory effect at room temperature.*

Figure 7.15 shows a dependence of the film composition on the RF power for both as-grown film and film annealed at 650°C for 4h. In general, increasing the RF power of Mn target increases the percentage of Mn, meanwhile the percentages of Ni and Ga gradually decrease. The optimal RF power for Mn target is found between 15-25 W, by which point the film composition approaches the desired composition.

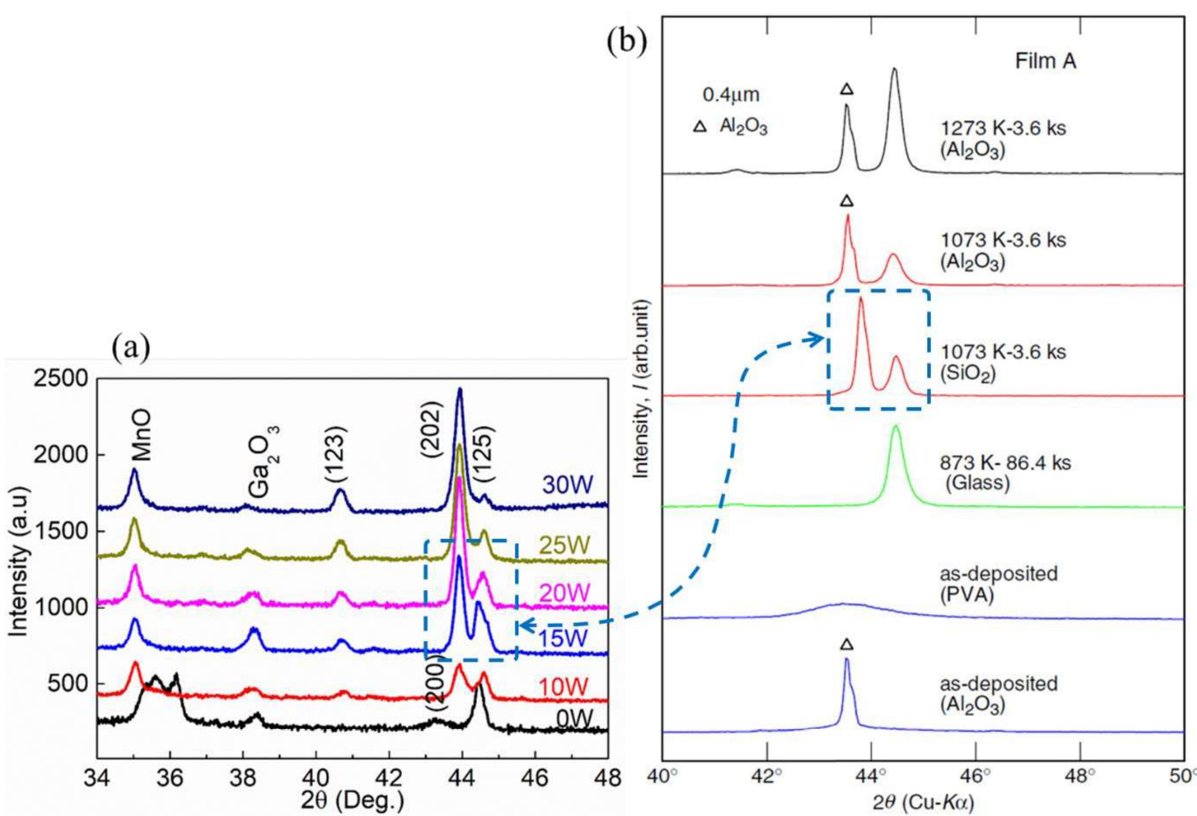

***Figure 7.16**: (a) XRD patterns of Ni-Mn-Ga films synthesized by different powers of Mn target.(b) Results reported by V. A. Chernenko et al* [8].

To get the ferromagnetic shape memory effect at room temperature, a composition of $Ni_{50}Mn_{28}Ga_{22}$ must be achieved, taking into account the valence electron concentration (e/a) definition (see Figure 7.6). XRD patterns of Ni-Mn-Ga films in Figure 7.16(a) show typical diffraction patterns for Ni-Mn-Ga alloys between 43-45°, as well as an oxide phase, as MnO and Ga_2O_3 are also detected. We note that a value of 15 W for the sputtering power of the Mn target induced diffraction peaks similar to the ones obtained by V. A. Chernenko et al., who optimized the processing of thin film deposition of the Ni-Mn-Ga material [8].

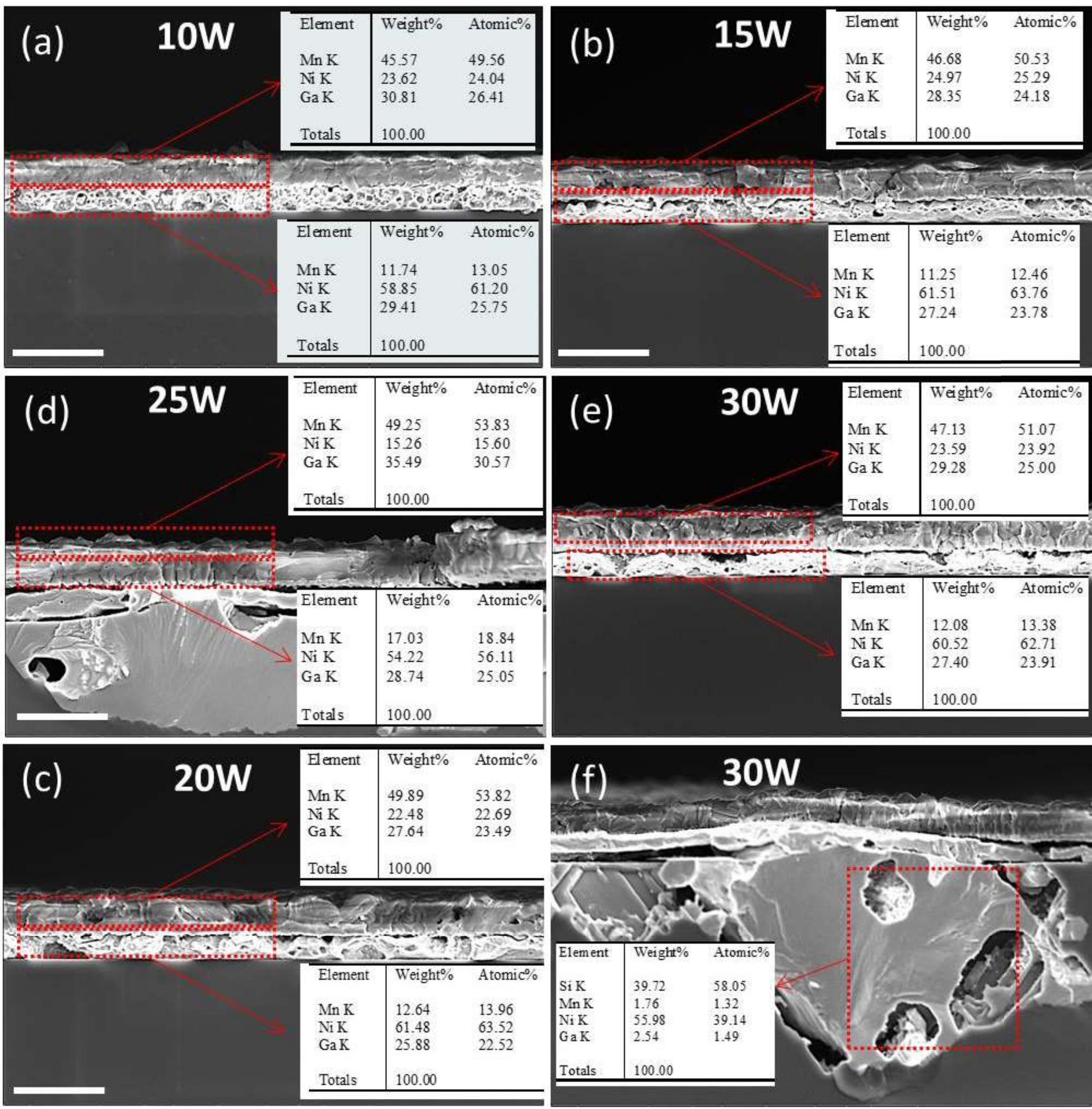

Figure 7.17: *Cross-sectional SEM micrograph and inserted EDX acquisition in cross-section configuration. The scale bar is 1 µm.*

The cross-sectional analysis made by SEM confirmed the in-depth anisotropy of our films. Annealed films exhibit a clear separation with a different elemental composition in the two layers, as pointed out by the local EDX analysis in Figure 7.17. For all co-sputtered films with different RF powers in the manganese target, the percentage of Mn in the top layers is dominant and is less in the lower layer, while the percentage of Ni displays an opposite trend, i.e. more Ni is present in the lower layer than the top one. The percentage of Ga is less fluctuated. Moreover, it is noted that a remarkable amount of Ni is diffused into silicon substrate, as shown in Figure 7.17(f), causing a loss of Ni in the films. This observation confirms the atomic interdiffusion trend for nickel suggested previously in Table 2.

7.1.2.3. Effect of diffusion barrier layers

The films grown directly on silicon substrates show a severe diffusion of Ni into the substrate and cause the layer separation and delamination. We need to find a way to maintain uniformity in the atomic composition of the film in depth. To prevent these issues, several diffusion barrier layers were deposited by ALD, PE-ALD or PVD, such as: 50nm-thick Al_2O_3 (ALD), 40nm-thick HfO_2 (ALD), 100nm-thick Pt (PVD), and 150nm-thick AlN (PE-ALD) films. Then, co-sputtering is used with a power of 20W applied to the Mn target, and 100 W to the Ni-Mn-Ga ternary target.

Figures 7.18 and 7.19 show top-view and cross-sectional SEM micrographs of the film grown on the different barrier layers. It can be seen that film morphologies are quite rough, composed of small grains with a size of about 50-60 nm. The layer separation is still observed in the film grown directly on Si, while the films grown on Si coated with a diffusion barrier layer appear quite homogeneous in the cross-section, as presented in Figure 7.19.

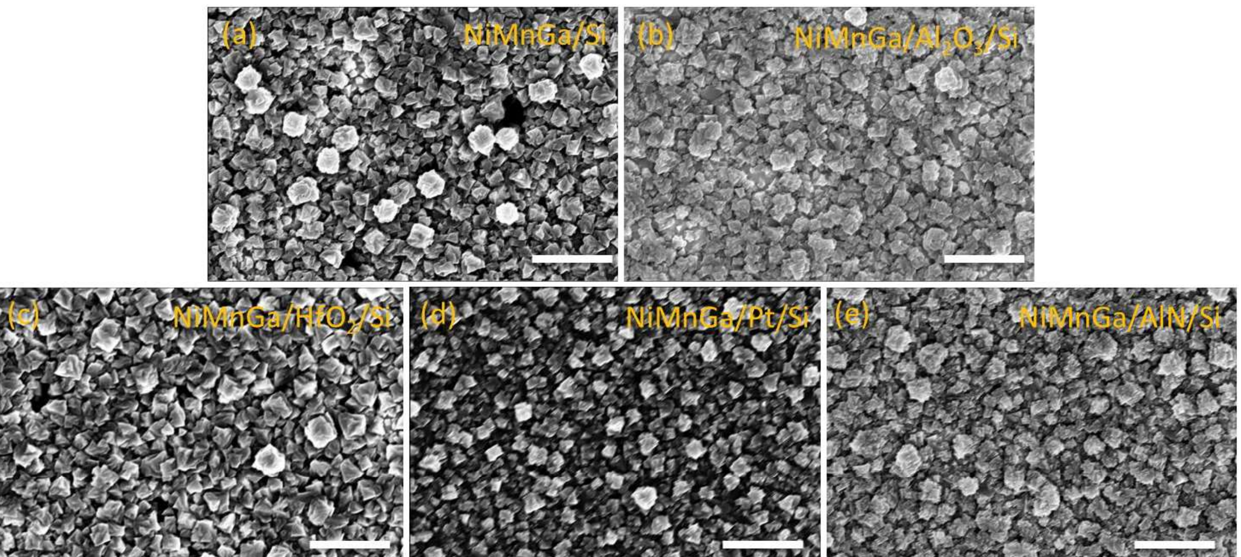

Figure 7.18: *Top-view SEM images of 500nm-thick Ni-Mn-Ga films on silicon substrate (a) and coated with different diffusion barrier layers (b) 50nm-thick Al_2O_3, (c) 40nm-thick HfO_2, (d) 100nm-thick Pt, and (e) 150nm-thick AlN films. The scale bar is 200 nm.*

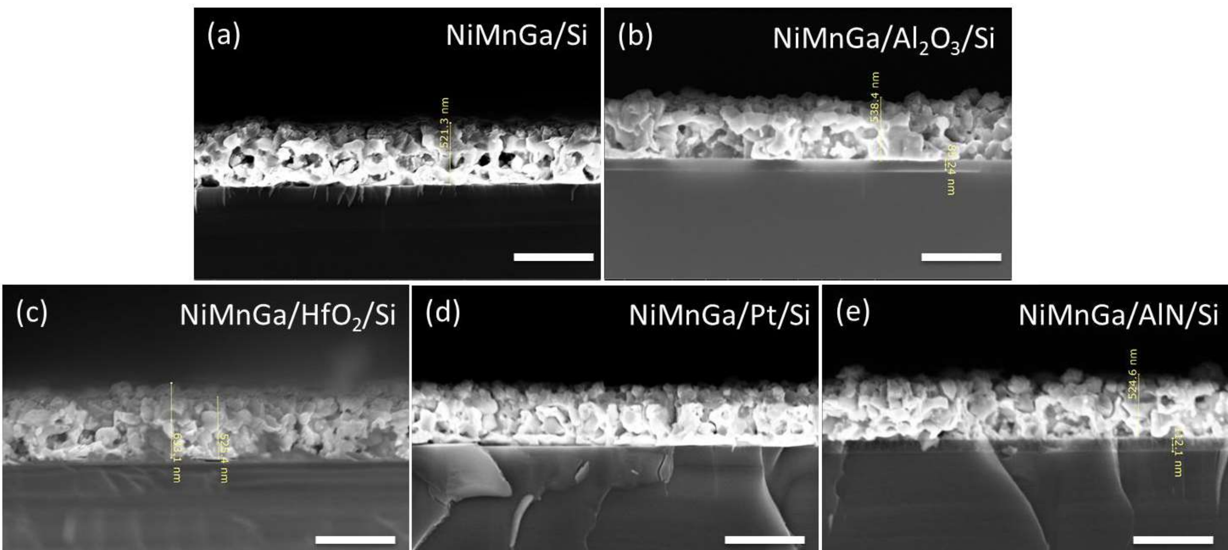

Figure 7.19: *Cross-sectional SEM micrographs of 500nm-thick Ni-Mn-Ga films on a silicon substrate (a) and coated with different diffusion barrier layers, (b) 50nm-thick Al_2O_3, (c) 40nm-thick HfO_2, (d) 100nm-thick Pt, and (e) 150nm-thick AlN films. The scale bar is 500 nm.*

The film stoichiometry was studied by performing local EDX in the top-view configuration, as shown in Figure 7.20. The use of some diffusion barrier layers is quite helpful to prevent Ni diffusion, showing a higher Ni concentration of about 48 at.% compared to the one grown on Si (47 at%). Changes in the concentration of Mn and Ga are also observed. There is a higher Mn presence in the films grown with diffusion barriers, except for the AlN case. However, the films grown on Pt, Al_2O_3 layers presented a severe delamination after the post-annealing stage, which may be due to weak adhesion between these layers and the Si substrate.

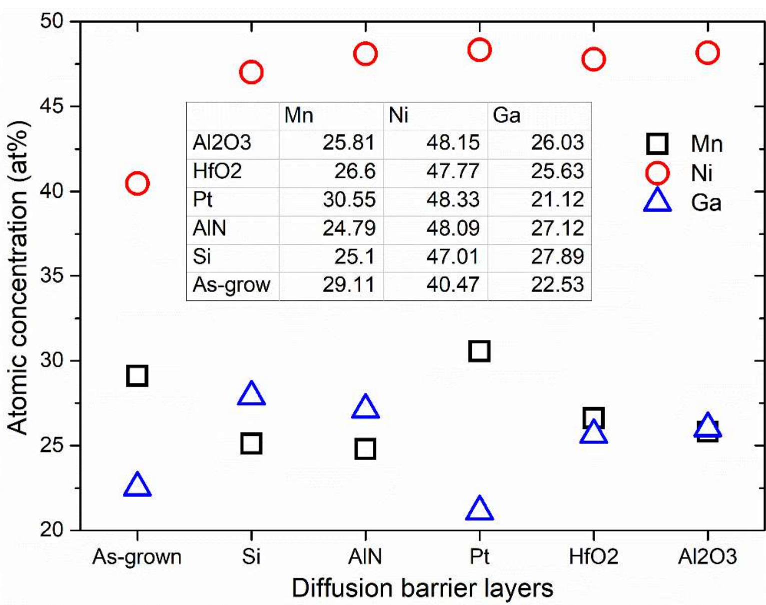

	Mn	Ni	Ga
Al2O3	25.81	48.15	26.03
HfO2	26.6	47.77	25.63
Pt	30.55	48.33	21.12
AlN	24.79	48.09	27.12
Si	25.1	47.01	27.89
As-grow	29.11	40.47	22.53

Figure 7.20: *The elemental composition of the Ni-Mn-Ga annealed films with a different diffusion barrier layer collected by EDX.*

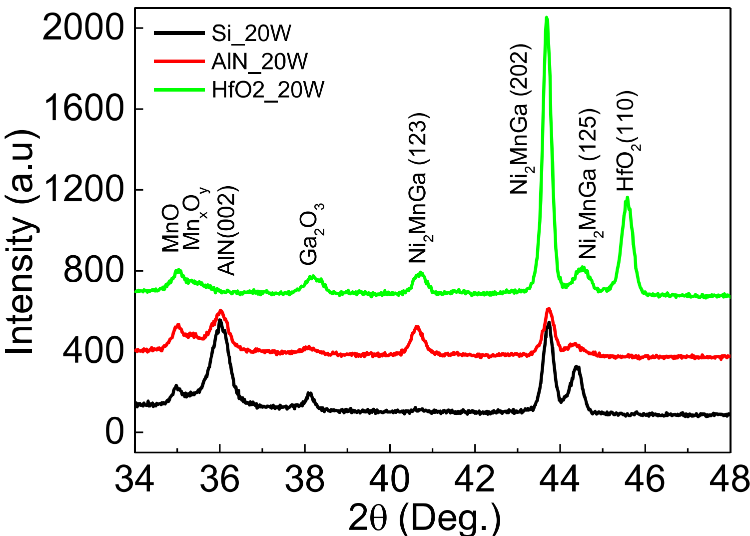

Figure 7.21: *XRD pattern of Ni-Mn-Ga films on two different diffusion barrier layers without delamination observed after the post-annealing stage. The pristine silicon sample as a supporting substrate is also illustrated as a reference without a diffusion barrier.*

Figure 7.21 presents the XRD data of the films grown on Si, AlN- and HfO_2-coated Si substrates. Besides the Ni-Mn-Ga peaks observed at around 40.8°, 43.8° and 44.5°, some peaks of manganese oxides and Ga_2O_3 are also detected. It is interesting to note the presence of the Ni_2MnGa(123) diffraction peak only for the samples with a diffusion barrier. This refers to (123) plane with cubic structure [10]. In the next steps of this study, we kept the AlN thin layer as a diffusion barrier to maintain the stoichiometry in the depth of the Ni-Mn-Ga layer. This is also of practical experimental interest because it is done by a similar PE-ALD process as the process for the top AlN piezoelectric layer detailed in Chapter 5. The effect of the use of reduction H_2 gas during the post-annealing process for the films grown on Si and AlN/Si samples was also investigated to avoid the oxidation of the Ni alloy film as observed on the XRD spectrum in Figure 7.21 for Mn_xO_y and Ga_2O_3 presence.

For the magnetization measurements by VSM, we observed that the signal level of the too thin layer (~ 100nm) of Ni-Mn-Ga is drowned in the background noise. Hence, in order to increase signals of magnetization measurements, 2.5µm-thick films were grown on Si and AlN-coated Si. Figures 7.22, 7.23 and 7.24 present magnetization measurements at different temperatures and the temperature dependence of magnetization for the films grown on Si and AlN/Si annealed in H_2 environment, as well as the film on Si annealed in high vacuum. All three films exhibit a ferromagnetic behavior at different measurement temperatures (300, 60, 50, and 5K); no significant change in magnetic moment is observed at high and low temperatures. The saturation moment of the films annealed in the H_2 environment is slightly higher compared to the film annealed in high vacuum. It is about 0.9 mAm^2 for the films annealed in H_2 environment and 0.6 mAm^2 for the films annealed in high vacuum. This may be due to a lower occurrence of manganese oxide phases in the films when films are annealed in the reduction gas environment.

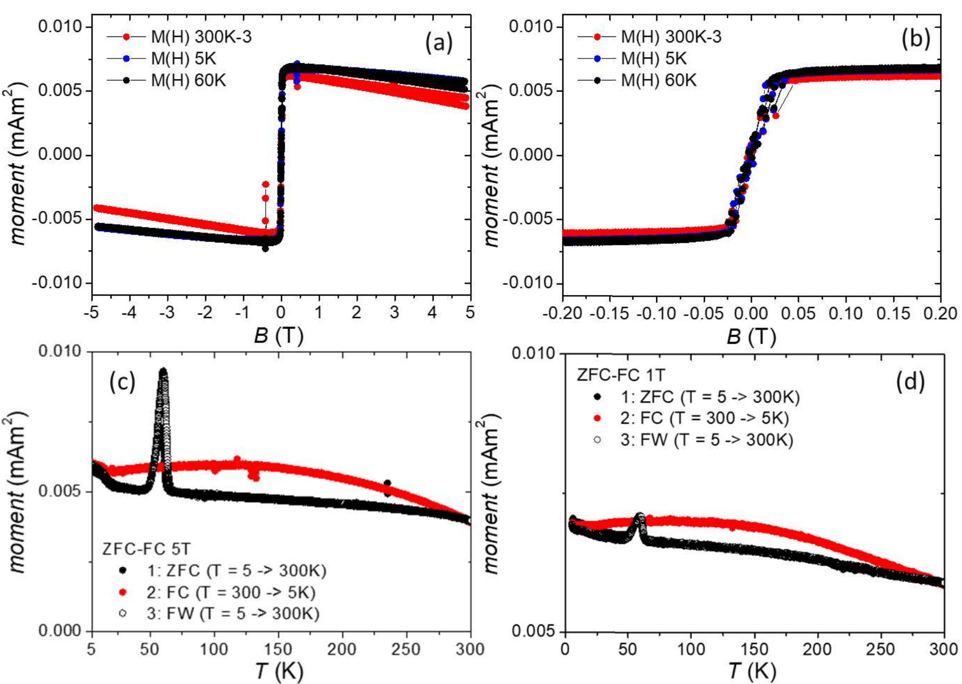

Figure 7.22: *Magnetization measurement of 2.5µm-thick Ni-Mn-Ga film on Si post-annealed in high vacuum. (a) Magnetization curve with the moment measurement against the magnetic field, with (b) a detailed view around 0 Tesla. (c) Evolution of the magnetic moment against the sample temperature with a constant DC bias of 5 Tesla. (d) Evolution of the magnetic moment against the sample temperature with a constant DC bias of 1 Tesla.*

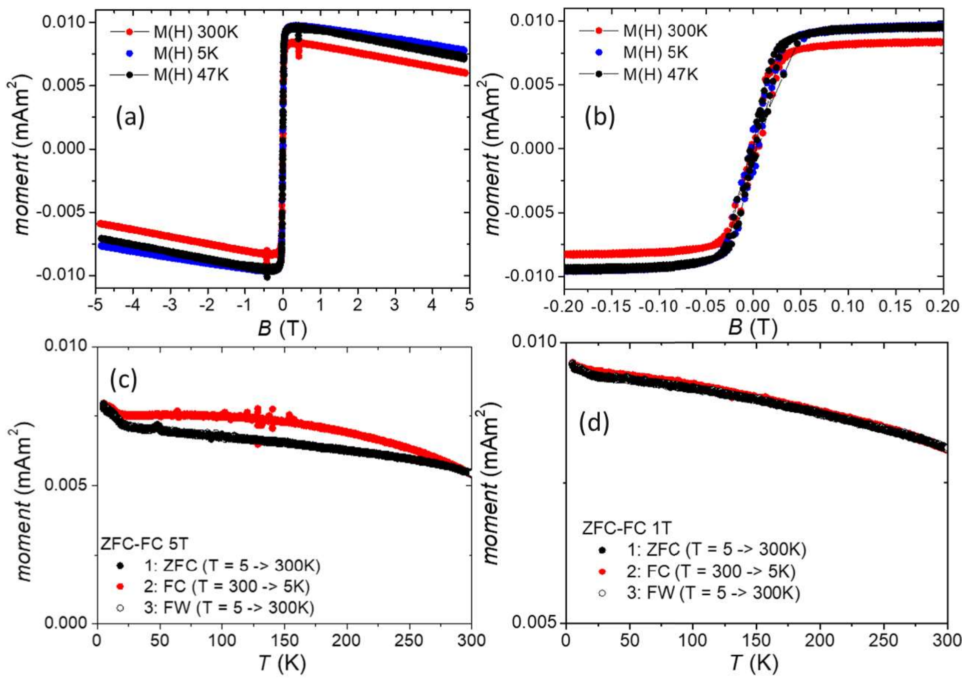

Figure 7.23: *Magnetization measurement of 2.5µm-thick Ni-Mn-Ga film on Si post-annealed in an H_2/Ar environment.*

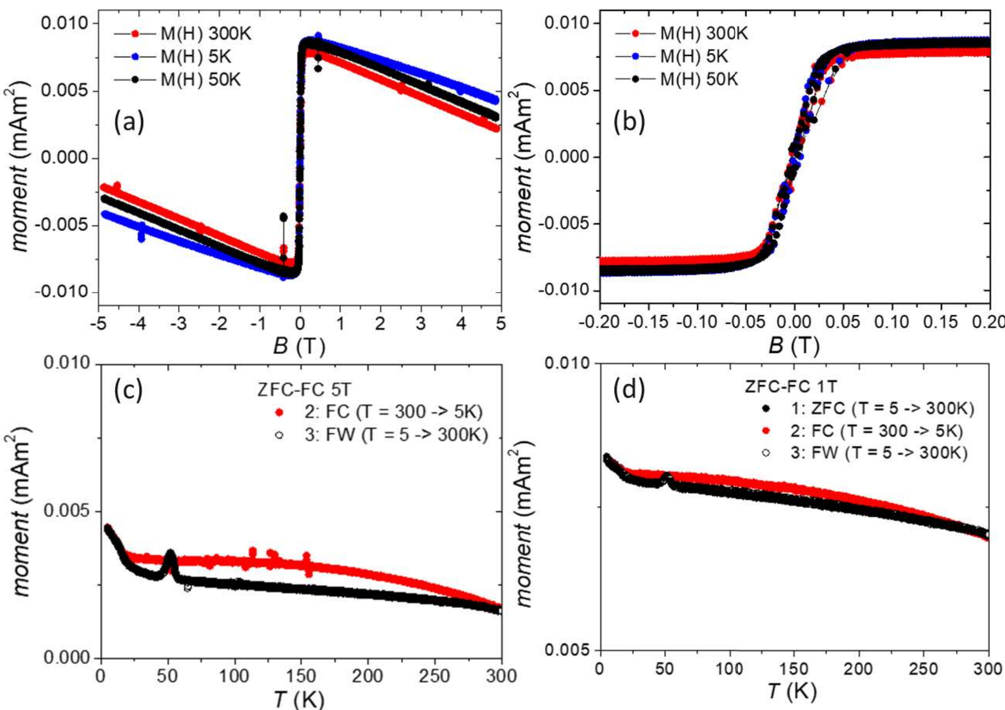

Figure 7.24: *Magnetization measurement of 2.5µm-thick Ni-Mn-Ga film on AlN-coated Si post-annealed in H_2/Ar environment.*

The temperature dependence of magnetization, M(T), was also tested. ZFC (zero-field cooling), FC (field cooling) and FW (field-warming) sequences were carried out. In general, FC curves increase with a decreasing temperature. More interesting features are observed in ZFC curves where there is an occurrence of a cusp at around 50 K. This feature is more profound on the application of a higher field (5 T) and is more dominant in films annealed in high vacuum. The appearance of a cusp in ZFC curves is similar to spin-glass-like magnetic materials [11], however, a cusp in the ZFC of these materials only occurs after applying a small magnetic field such as 0.01 mT for $SrRuO_3$, 0.005 mT for $La_{0.5}Sr_{0.5}CoO_3$ compounds [11]. This feature has never before been observed in Ni-Mn-Ga alloys.

7.1.2.4. Temperature dependence of X-ray diffraction measurement

To study the martensitic transformation expected in the Ni-Mn-Ga films for obtaining a high mechanical strain effect during austenitic/martensitic phase transition, the temperature dependence of X-ray diffraction (T-XRD) was analyzed in the 2.5µm-thick Ni-Mn-Ga film grown on AlN-coated silicon substrates. Preliminary results are shown in Figures 7.25, 7.26 and 7.27.

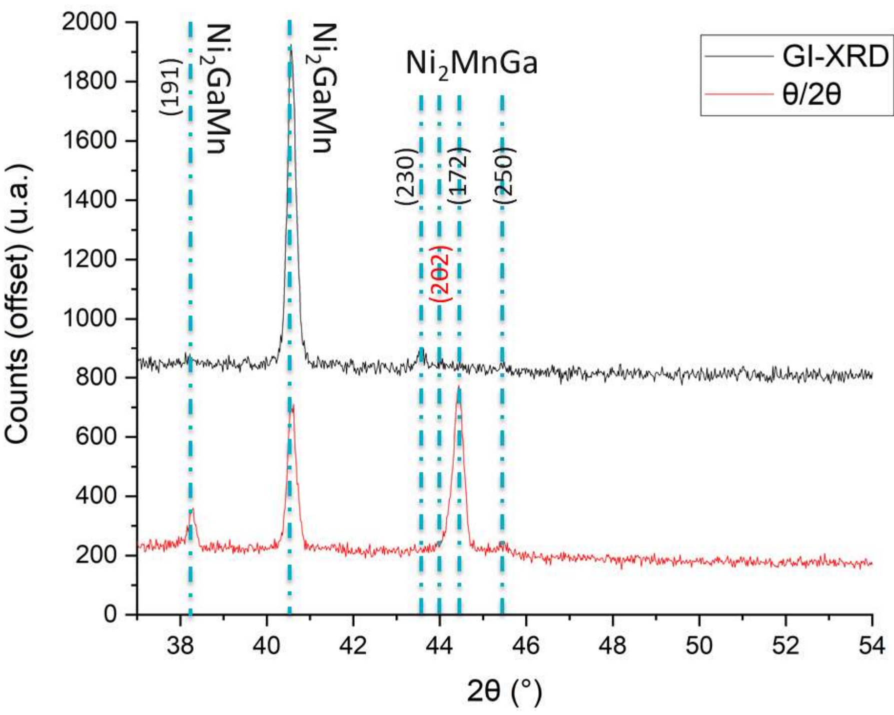

Figure 7.25: *XRD data measured in the air atmosphere in a grazing incidence (GI-XRD) (ω = 3.5°) and θ/2θ locked-couple configurations.*

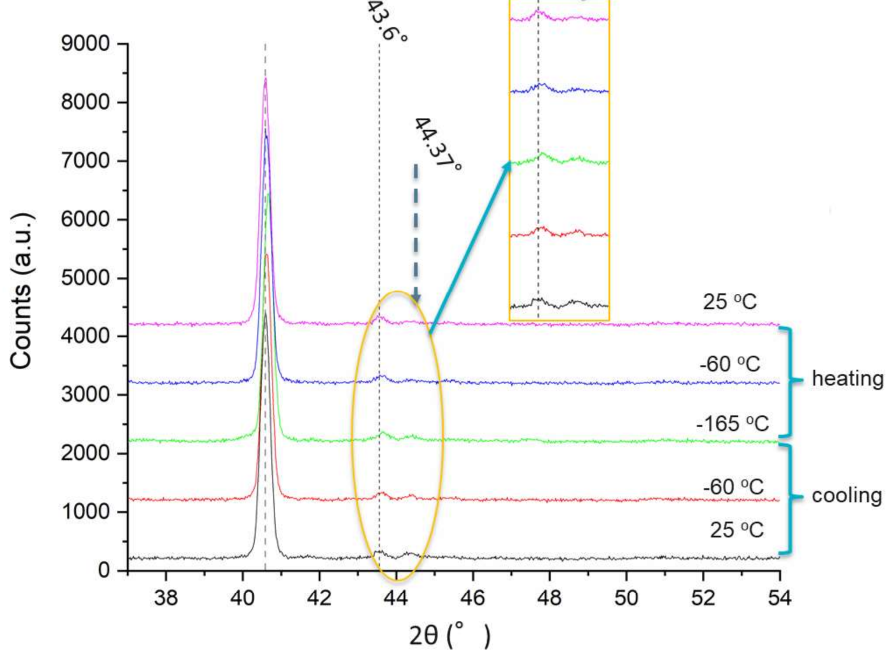

Figure 7.26*: GI-XRD (ω = 3.5°) measurements below room temperature as the following sequence 25 → -60 → -165 → -60 → 25 °C.*

The measurements were performed in a primary vacuum at low temperatures (down to -165 °C) using liquid nitrogen, while high temperature measurements (up to 130 °C) were carried out in an

Ar atmosphere to prevent film oxidation. Figure 7.25 presents the XRD data of the Ni-Mn-Ga film measured by GI (grazing incidence) (more sensitive to top surface structure) and θ/2θ locked-couple (averaging the diffraction signals from the in-depth structure of the film) configurations. Two dominant peaks are identified, which are at a 40.5° referring (123) plane with a cubic structure; the peak at 44.37° is assigned to the (172) diffraction peak of the martensitic phase [10]. The spectra do not change much when changing the temperature from 25 °C to – 165 °C except that one could distinguish a tiny change of the peak at 2θ = 44.37°, as shown in Figure 7.26. This peak can be attributed to a martensitic (172) diffraction pattern, but here we are at the detection limit of the XRD detector to confirm this diffraction peak.

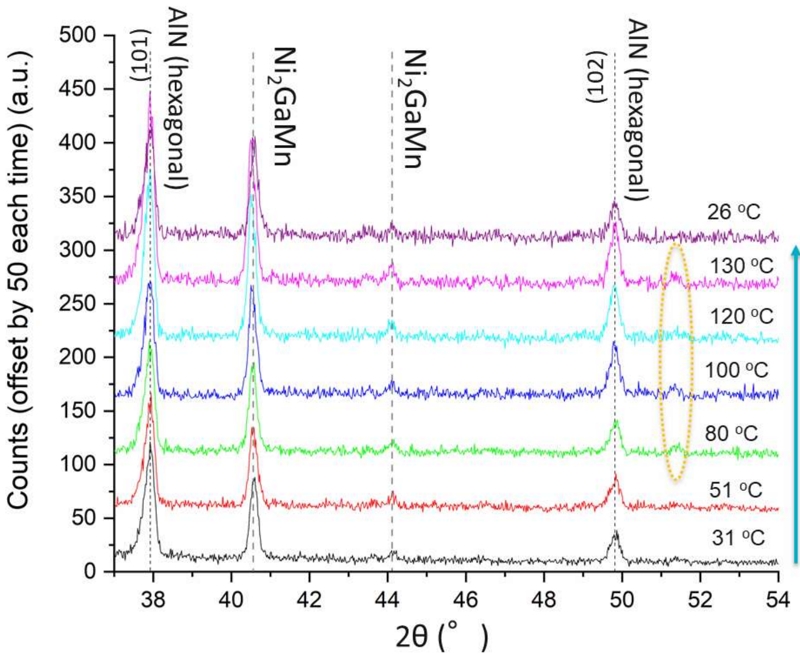

***Figure 7.27**: GI-XRD (ω = 3.5°) measurements above room temperature as the following sequence 31 → 51 → 80 → 100 → 120 → 130 → 26 °C.*

In high temperature measurements from room temperature to 130 °C, the occurrence of a peak is observed at around 51.5 ° and this could belong to cubic phase $L1_2$ (002) relating to the appearance of an austenitic phase. The temperature dependence of XRD measurements shows interesting and promising features to confirm the phase transition we could expect at a temperature higher than 300K as claimed in the literature. However these features are quite weak and are caused by the strong absorption of Ar gas (for the measurements at high temperatures) and the detection of the sensitivity limit of our XRD detector. A similar analysis in a synchrotron facility may provide a better resolution and a clear confirmation that our experimental process achieved Ni-Mn-Ga thin films with a significative ferromagnetic shape memory alloy effect working at temperatures higher than 300K for applications in magnetoelectric (ME) devices.

7.1.3. Conclusion

In summary, we have successfully grown Ni-Mn-Ga films on an Si substrate, as well as on different diffusion barriers to solve inhomogeneity issues of the films. The effect of the post-annealing process was carefully investigated and optimized at 650 °C for 4 h. The 500nm-thick film exhibits the martensitic transformation at around 50 K, as presented in the magnetization characterizations by VSM. The co-sputtering was introduced in order to compensate the Mn loss during post-annealing. The optimal power of the Mn target was found to be 15, and 20 W by which the film stoichiometry can be tuned to the desired $Ni_{50}Mn_{28}Ga_{22}$ film so that the martensitic transition temperature can be achieved above room temperatures. We introduced innovative diffusion barriers, such as Pt, Al_2O_3, HfO_2, AlN between the film and Si substrate in order to reduce both the Ni diffusion into Si and the layer separation. Magnetization measurements were performed on co-sputtered samples with the diffusion barrier showing that all films exhibit a ferromagnetic behavior. A cusp was observed in the ZFC curve, and was particularly clear in the 2.5µm-thick film grown directly on Si. The origin of the cusp is not clear. The feature is quite similar to a spin-glass-like magnetic property, however, it can only occur on application of a small magnetic field. The preliminary results of the temperature dependence of X-ray diffraction measurements show interesting and promising features occurring at temperatures higher than room temperature. A synchrotron facility is needed to obtain better signal and resolution and confirm this trend. Meanwhile, small-angle neutron scattering (SANS) measurements are scheduled to study magnetic properties of those samples against different DC magnetic field biases and different sample temperatures to highlight the phase transition inducing giant strain.

7.2 AlScN film as a promising replacement of AlN film

Another way to improve the magnetoelectric transducing efficiency of our composites relies on the increasing of the piezoelectric response of the AlN layer. Recently, extensive studies on the high piezoelectric response of Scandium Aluminum Nitride (ScAlN) alloy thin films, which is at least 500% greater than AlN [12,13], suggest a promising candidate for magnetoelectric composites. M. Akiyama and co-workers [12] observe[14]d that the d_{33} gradually increases when increasing Sc concentration from 0 to 43%. At an Sc concentration of 43%, the alloy films exhibit a peak d_{33} of 24.6 pCN^{-1}, which then sharply drops as Sc concentration increases (Figure 7.28(a)).

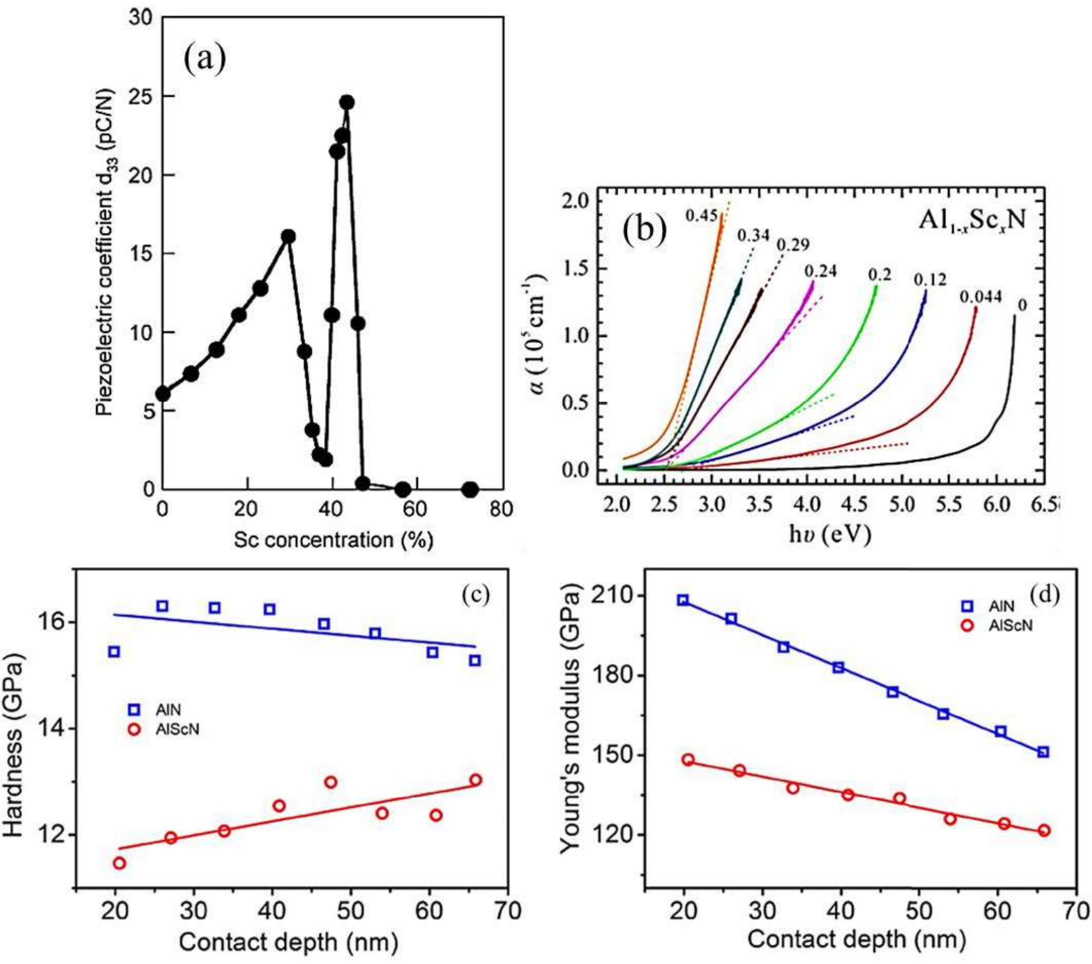

Figure 7.28: *Dependence of (a) piezoelectric coefficient* d_{33} [12]*, (b) the optical absorption as function of photon energy of* $Sc_xAl_{1-x}N$ *alloys at different Sc concentrations* [15]*, (c)-(d) comparison of the hardness and Young's modulus of AlN and* $Sc_xAl_{1-x}N$ *(x = 0.27)* [14].

The dependence of the piezoelectric coefficient d_{33} of $Sc_xAl_{1-x}N$ alloys on Sc concentration is strongly correlated to its corresponding crystal structures. The crystal structures are in a purely hexagonal phase below 41%. In contrast, above 46%, the crystal structure changes to a cubic phase. Between 42 and 45%, both hexagonal and cubic phases coexist. These observations are similar to $Sc_xGa_{1-x}N$ alloys. Using quantum mechanical calculations, R. Tasnadi and his colleagues [16] discovered that the anomalous piezoelectric response in wurtzite $Sc_xAl_{1-x}N$ alloys is intrinsic, and comes from a strong change in the response of the internal atomic coordinates to a strain and the pronounced softening of the C_{33} elastic constant.

Moreover, the softening effect was observed in $Sc_xAl_{1-x}N$ alloys as compared to AlN. Figures 7.28 (c) and (d) present the hardness and Young's modulus of $Sc_xAl_{1-x}N$ film with x = 0.27 and AlN film [14]. The hardness and Young's modulus of AlN are about 15.5 GPa and 210 GPa, whereas those of ScAlN film are approximately 11.5 GPa and 149.4 GPa, which are significantly lower than those of AlN film.

An example of the dependence of the optical bandgap in Sc concentration is shown in Figure 7.28(b). As can be seen, the bandgap gradually decreases as Sc concentration increases. By adding Sc, the AlN possibly changes from an insulating to a semiconducting material. An open question remaining is how Sc concentration affects electrical resistivity and leakage current, and the piezoelectric response of the ScAlN film. Indeed, a balance exists between the benefit of increasing the piezoelectric coefficient with Sc doping, and at the same time, the occurrence of a deleterious effect, also concerning the increase of the leakage currents in the material. In the end, the question is open concerning this advantageous or disadvantageous balance.

We did several experiments in order to grow AlScN thin film by PE-ALD, based on our existing process for pure AlN. It has not yet been successful because we encountered some technical issues for the use of a specific hot source canister for the Scandium precursor in the ALD chamber. However, this experiment is a priority for the future activities of the group.

7.3 Resonant structures

Besides upgrading the performances of the film materials of the ME composite, another strategy consists of the use of mechanically resonant structures, such as a cantilever (Figure 7.29). Greve et al. [17] reported a giant ME coefficient in $(Fe_{90}Co_{10})_{78}Si_{12}B_{10}$-AlN thin film composite of 737 $V.cm^{-1}.Oe^{-1}$ at a resonance frequency of 753 Hz, which is more than 200 times greater than the value measured out of resonance at 100 Hz. An ME coefficient of about 160 $V.cm^{-1}.Oe^{-1}$ at the 1st bending mode anti-resonance frequency of 1.7 kHz in a laminated composite cantilever structure consists of a single crystal fiber composite (SFC) bonded with Ni [18]. Annapureddy and co-workers [19] reported a giant ME coefficient of 1'330 $V.cm^{-1}.Oe^{-1}$ at 100 Hz in a cantilever made of $Pb(Mg_{1/3}Nb_{2/3})O_3$-$Pb(Zr,Ti)O_3$ piezoelectric single crystal macro-fiber composite mounted with a highly textured magnetostrictive Fe-Ga alloy.

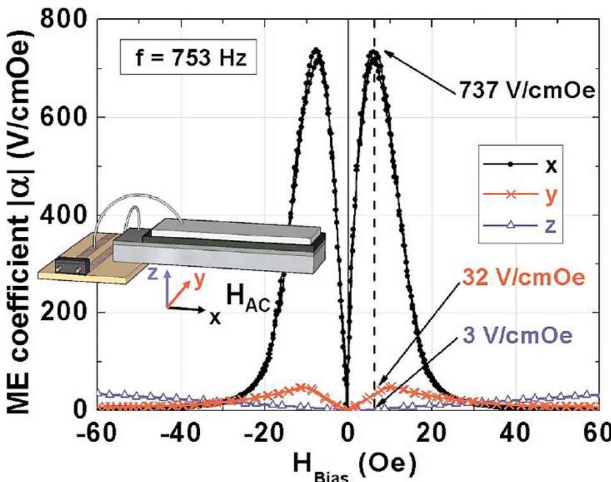

Figure 7.29: *The ME coefficient of a cantilever with a 1.75 µm FeCoBSi and 1.8 µm AlN film measured at resonance frequency of 753 Hz* [17]*. Here 'x', 'y', and 'z' denote the magnetic field direction.*

The resonant structures show great potential for enhancing the ME coefficient. In this section, millimeter-size cantilevers made of AlN film deposited on Ni foils are designed to tune the mechanically resonant frequency to 100 Hz. The relationship between the resonance frequency and cantilever dimensions is given by the following equation [17]:

$$f_n = \frac{1}{4\pi}\frac{\lambda_n^2}{L_1^2}\sqrt{\frac{\hat{E}_1 h_1^3}{3(\sum_n \rho_n h_n)}}$$

Here, n is the mode order, λ_n is a dimensionless parameter, L and h are the length and thickness of the cantilever, and ρ is the density of the material. For the substrate material, the index is $n = 1$, whereas for films on the cantilever, $n = 2, 3, \ldots$. $\hat{E}$ is the effective Young's modulus with $\hat{E} = E/(1-\upsilon^2)$. Here, υ is the Poisson's ratio.

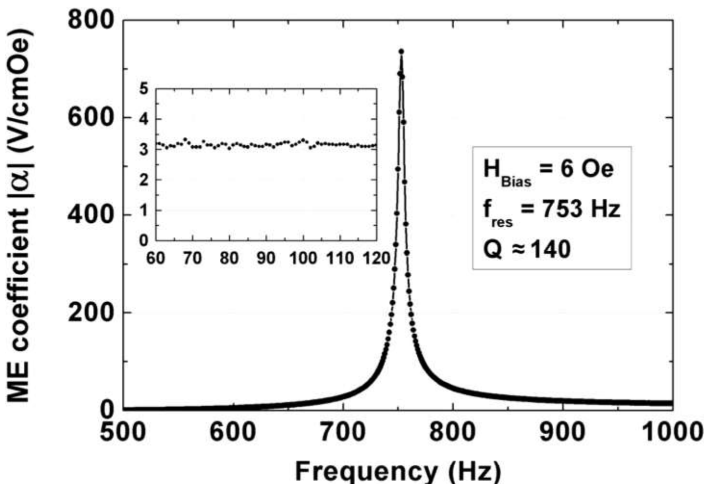

Figure 7.30: *The ME coefficient of a cantilever with a 1.75 µm Metglas film and 1.8 µm AlN film dependent on the frequency with a fixed magnetic field bias and drive field* [17].

An example of the frequency dependence of the ME coefficient is presented in Figure 7.30 [17]. A quality factor Q is usually used to evaluate the quality of the resonance structure. Generally, the higher the Q, the better the performance of devices. The definition of the Q factor is given below:

$$Q = \frac{f_0}{\Delta f}$$

Where f_0 is the resonance frequency, and Δf is the resonance width or full-width half-maximum.

Using the in-house LIST cleanroom facilities, our group has already worked on the processing of the MEMS structure, with cantilevers integrating the piezotronics ZnO strain gauge processed by ALD. Figure 7.31 illustrates these cantilever structures, which were successfully developed in our group [20]. Hence, this development combined with our knowledge of magnetoelectric processing pave the way for forthcoming realizations of the integration of ME composites in MEMS structures.

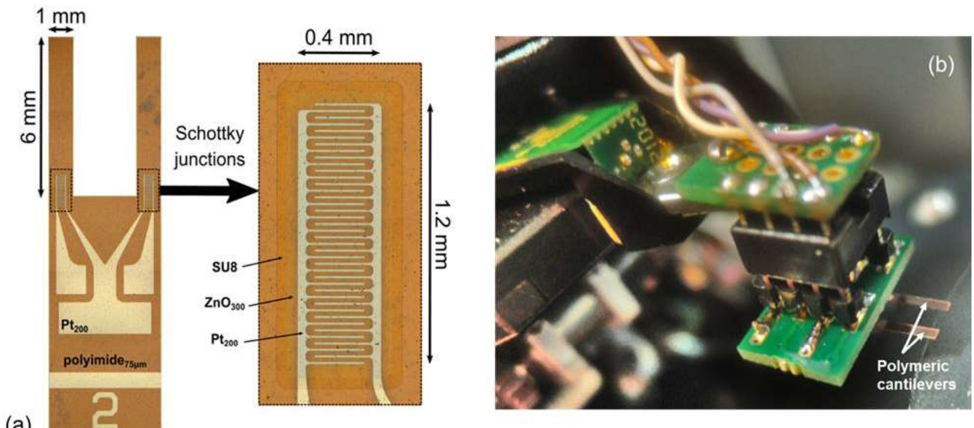

Figure 7.31: *(a) Top view representation of cantilevered structures integrating a piezotronic strain microsensor made of ZnO thin layers by ALD. The dashed lines represent a zoom on the interdigitated electrodes; (b) Integration of a piezotronic strain microsensor into the AFM nose. The sensors are bonded on the PCB and represented upside down on the picture, with the polymeric cantilevers positioned and clamped at the edge of the PCB* [20].

7.4. References

(1) Faran, E.; Shilo, D. Ferromagnetic Shape Memory Alloys-Challenges, Applications, and Experimental Characterization. *Exp. Tech.* **2015**. https://doi.org/10.1111/ext.12153.

(2) Sozinov, A.; Likhachev, A. A.; Lanska, N.; Ullakko, K. Giant Magnetic-Field-Induced Strain in NiMnGa Seven-Layered Martensitic Phase. *Appl. Phys. Lett.* **2002**. https://doi.org/10.1063/1.1458075.

(3) Kiefer, B.; Lagoudas, D. C. Magnetic Field-Induced Martensitic Variant Reorientation in Magnetic Shape Memory Alloys. *Philos. Mag.* **2005**. https://doi.org/10.1080/14786430500363858.

(4) Kaufmann, S.; Niemann, R.; Thersleff, T.; Róßler, U. K.; Heczko, O.; Buschbeck, J.; Holzapfel, B.; Schultz, L.; Fáhler, S. Modulated Martensite: Why It Forms and Why It Deforms Easily. *New J. Phys.* **2011**. https://doi.org/10.1088/1367-2630/13/5/053029.

(5) Planes, A.; Mãosa, L.; Acet, M. Magnetocaloric Effect and Its Relation to Shape-Memory Properties in Ferromagnetic Heusler Alloys. *J. Phys. Condens. Matter* **2009**. https://doi.org/10.1088/0953-8984/21/23/233201.

(6) Chernenko, V. A. Compositional Instability of β-Phase in Ni-Mn-Ga Alloys. *Scr. Mater.* **1999**. https://doi.org/10.1016/S1359-6462(98)00494-1.

(7) Jin, X.; Marioni, M.; Bono, D.; Allen, S. M.; O'Handley, R. C.; Hsu, T. Y. Empirical Mapping of Ni-Mn-Ga Properties with Composition and Valence Electron Concentration. *J. Appl. Phys.* **2002**. https://doi.org/10.1063/1.1453943.

(8) Chernenko, V. A.; Ohtsuka, M.; Kohl, M.; Khovailo, V. V.; Takagi, T. Transformation Behavior of Ni-Mn-Ga Thin Films. In *Smart Materials and Structures*; 2005. https://doi.org/10.1088/0964-1726/14/5/012.

(9) Heczko, O.; Thomas, M.; Buschbeck, J.; Schultz, L.; Fähler, S. Epitaxial Ni-Mn-Ga Films Deposited on SrTi O3 and Evidence of Magnetically Induced Reorientation of Martensitic Variants at Room Temperature. *Appl. Phys. Lett.* **2008**. https://doi.org/10.1063/1.2883961.

(10) Chernenko, V. A.; L'vov, V. A.; Khovailo, V. V.; Takagi, T.; Kanomata, T.; Suzuki, T.; Kainuma, R. Interdependence between the Magnetic Properties and Lattice Parameters of Ni-Mn-Ga Martensite. *J. Phys. Condens. Matter* **2004**. https://doi.org/10.1088/0953-8984/16/46/020.

(11) Joy, P. A.; Anil Kumar, P. S.; Date, S. K. The Relationship between Field-Cooled and Zero-Field-Cooled Susceptibilities of Some Ordered Magnetic Systems. *J. Phys. Condens. Matter* **1998**. https://doi.org/10.1088/0953-8984/10/48/024.

(12) Akiyama, M.; Kamohara, T.; Kano, K.; Teshigahara, A.; Takeuchi, Y.; Kawahara, N. Enhancement of Piezoelectric Response in Scandium Aluminum Nitride Alloy Thin Films Prepared by Dual Reactive Cosputtering. *Adv. Mater.* **2009**. https://doi.org/10.1002/adma.200802611.

(13) Mertin, S.; Heinz, B.; Rattunde, O.; Christmann, G.; Dubois, M. A.; Nicolay, S.; Muralt, P. Piezoelectric and Structural Properties of C-Axis Textured Aluminium Scandium

Nitride Thin Films up to High Scandium Content. *Surf. Coatings Technol.* **2018**. https://doi.org/10.1016/j.surfcoat.2018.01.046.

(14) Wang, W. B.; Fu, Y. Q.; Chen, J. J.; Xuan, W. P.; Chen, J. K.; Wang, X. Z.; Mayrhofer, P.; Duan, P. F.; Bittner, A.; Schmid, U.; Luo, J. K. AlScN Thin Film Based Surface Acoustic Wave Devices with Enhanced Microfluidic Performance. *Journal of Micromechanics and Microengineering*. 2016. https://doi.org/10.1088/0960-1317/26/7/075006.

(15) Deng, R.; Evans, S. R.; Gall, D. Bandgap in Al1-XScxN. *Appl. Phys. Lett.* **2013**. https://doi.org/10.1063/1.4795784.

(16) Tasnádi, F.; Alling, B.; Höglund, C.; Wingqvist, G.; Birch, J.; Hultman, L.; Abrikosov, I. A. Origin of the Anomalous Piezoelectric Response in Wurtzite ScxAl1-XN Alloys. *Phys. Rev. Lett.* **2010**. https://doi.org/10.1103/PhysRevLett.104.137601.

(17) Greve, H.; Woltermann, E.; Quenzer, H. J.; Wagner, B.; Quandt, E. Giant Magnetoelectric Coefficients in (Fe90 Co 10)78 Si12 B10 -AlN Thin Film Composites. *Appl. Phys. Lett.* **2010**. https://doi.org/10.1063/1.3377908.

(18) Ryu, J.; Kang, J. E.; Zhou, Y.; Choi, S. Y.; Yoon, W. H.; Park, D. S.; Choi, J. J.; Hahn, B. D.; Ahn, C. W.; Kim, J. W.; Kim, Y. Do; Priya, S.; Lee, S. Y.; Jeong, S.; Jeong, D. Y. Ubiquitous Magneto-Mechano-Electric Generator. *Energy Environ. Sci.* **2015**. https://doi.org/10.1039/c5ee00414d.

(19) Annapureddy, V.; Na, S. M.; Hwang, G. T.; Kang, M. G.; Sriramdas, R.; Palneedi, H.; Yoon, W. H.; Hahn, B. D.; Kim, J. W.; Ahn, C. W.; Park, D. S.; Choi, J. J.; Jeong, D. Y.; Flatau, A. B.; Peddigari, M.; Priya, S.; Kim, K. H.; Ryu, J. Exceeding Milli-Watt Powering Magneto-Mechano-Electric Generator for Standalone-Powered Electronics. *Energy Environ. Sci.* **2018**. https://doi.org/10.1039/c7ee03429f.

(20) Joly, R.; Girod, S.; Adjeroud, N.; Nguyen, T.; Grysan, P.; Klein, S.; Menguelti, K.; Vergne, C.; Polesel-Maris, J. Polymeric Cantilevered Piezotronic Strain Microsensors Processed by Atomic Layer Deposition. *Sensors Actuators A Phys.* **2020**, *315*, 112280. https://doi.org/https://doi.org/10.1016/j.sna.2020.112280.

8

Summary and outlooks

We have presented the developments of several tasks and in the end, developed an operational magnetoelectric transducer, with potential new ways of investigating to improve performances. We addressed the main challenge of the mechanical energy transfer in layers composites from the magnetostrictive layer to the piezoelectric one by means of different deposition techniques based on ALD and PVD. Although presenting a lower piezoelectric coefficient, the use of piezoelectric materials after thin film deposition, such as wurtzite crystals (e.g. AlN, ZnO, GaN), represents a substantial advantage with respect to the simplification of the fabrication of ME microdevices with materials compatible with cleanroom facilities. In particular, aluminum nitride (AlN) thin film with its excellent dielectric properties has paved the way for piezoelectric applications with its excellent integration capabilities. It represents the best alternative for piezoelectric MEMS-CMOS fabrication without the need for poling. We proposed the use of plasma-enhanced ALD (PE-ALD) to obtain conformal and fully active piezoelectric thin films made of AlN. The thin film growth was done at 250°C, a significantly lower deposition temperature than most piezoelectric materials deposition. In comparison to ceramic lead zirconate titanate (PZT) processed at high temperatures (above 650°C), or even to piezoelectric polymers (PVDF-based) difficult to process in thin and conformal layers while exhibiting very poor piezoelectric coefficients. Subsequently, magnetoelectric composites composed of aluminum nitride (AlN) films with conventional magnetostrictive foils of nickel, iron, and cobalt were obtained, and the performance of these composites was demonstrated by magnetoelectric and output power density measurements. The developments of these different bricks to obtain an ME device have induced more detailed experimental studies to understand the fundamentals of the innovative processes we proposed.

Chapter four dealt with the first challenge, which was to visualize the feasibility of the use of zinc oxide (ZnO) thin films as a piezoelectric layer in the magnetoelectric composite. Two main issues needed to be addressed so that a piezoelectric response can be achieved. The first was to tailor the crystalline orientation of ZnO thin film to the highly preferred (002) orientation, and the second was to increase the resistivity of ZnO thin film. To do that, we proposed the approach of adding gaseous O_2 after the diethyl zinc (DEZ) pulse during ALD cycles. The O_2 pulse time was varied between 1, 3, and 5 seconds at a constant deposition temperature of 180 °C. The effect of deposition temperature was studied by altering it from 100 to 200 °C while the O_2 pulse time was fixed at 1 second. It was found that using O_2 gas during ALD profoundly affected the properties of ZnO thin films. The crystalline structure was highly tuned from random orientations to a polar (002)-preferred orientation in the presence of O_2 gas. The electrical resistivity of the films synthesized under the O_2 conditions showed a significant increase of 3–4 orders of magnitude compared to the film grown without O_2 gas. Moreover, the electrical properties and optical properties strongly correlated to the electronic properties and chemical composition of ZnO thin films. Indeed, the highest resistivity and the largest band gap were found on the ZnO thin film

grown with oxygen gas at 100 °C, due to it having the lowest oxygen deficiency compared to other samples. The intensity ratio of the near band edge emission to the deep-level emission peak was able to be increased by applying an adequate pulsing of oxygen gas during the process. The preferentially (002)-oriented film was attributed to the stabilization of the polar surfaces under the O_2 environment and its lowest surface energy. To understand what happened during ALD growth under the presence of O_2 gas, ^{18}O-labelled isotopic water as a precursor instead of the conventional one was used to track the origin of oxygen atoms in ZnO film during growth from two different sources. Several analysis techniques were used to characterize the ZnO films such as *in situ* QCM during ALD growth, XPS, D-SIMS and ToF-SIMS. D-SIMS and XPS results have proven that additional oxygen species are present in the ZnO films when gaseous O_2 is added in the ALD process. However, oxygen gas does not play a catalyzer role. The detection of $Zn_xO_yC_2H_5^-$ ions by ToF-SIMS accompanied by the *in situ* QCM characteristics suggests a new chemical reaction mechanism in the ZnO thin films grown with O_2 gas presence. Monoethyl zinc reacts further with O_2, leading to the positive mass changes during the O_2 and water pulses by the respective formation of ethylperoxy radicals and ethylhydroperoxide chains in the bulk of the film. The monitoring of the $^{18}O/^{16}O$ ratio along the depth of the film revealed the evolution of the chemical contribution of the water precursor and gaseous O_2 during the ALD growth. It showed that, when coupling the water precursor with gaseous O_2 in the ALD process, the gaseous O_2 contribution of the oxygen atoms in the chemistry of the thin film continuously increases during the growth process.

However, the leakage current in ZnO thin films was still very high, thus piezoelectric characterization was not accessible. Alternatively, AlN is the best substitution for ZnO, because of the similarities in structural and piezoelectric properties. Moreover, AlN is an insulating material with a wide bandgap of 6.3 eV, which ensures a high resistivity in AlN thin film.

Chapter five addressed the optimization of AlN thin film growth by plasma-enhanced atomic layer deposition (PE-ALD) at a low temperature of 250 °C. The variation of plasma time and post-annealing processes were applied for AlN thin film growth processes at 180°C in order to obtain (002) preferred orientation, however with no success. Also, we investigated ways of post-annealing at high temperatures and the use of a buffer layer made of wurtzite ZnO, but without convincing results on the structural properties of AlN thin films for a piezoelectric response. By increasing the original deposition temperature of 250 °C in concomitance with variation of the purging time after trimethylaluminum (TMA) pulse, (002) preferred orientation was achieved. The films obtained presented a high purity with a carbon level of 1 at.%, an oxygen amount of 6-9 at.% and an Al/N stoichiometric ratio of close to one. In addition, the effective transverse piezoelectric $e_{31,f}$ coefficients were evaluated. The measurements showed a strong correlation between the film texture and the piezoelectric response; i.e. the highest value of the effective transverse piezoelectric $e_{31,f}$ coefficient of 0.37 C/m^2 was achieved on the AlN film grown at 250 °C and 30 s with the highest texture coefficient TC(002) of 2.75 along the c-axis orientation.

In **Chapter six**, magnetoelectric composites were fabricated by coating 550nm-thick AlN layers on nickel, iron, and cobalt foils. The film crystal properties and the interface between the films and the foils were carefully investigated by high-resolution transmission electron microscopy. It was found that a transition layer of amorphous Al_xO_y/AlO_xN_y was formed between the films and the foils. The evolution of the crystallinity of the AlN film was studied, showing that the film was amorphous at the interface and significantly improved during the ALD growth. A strong self-biased magnetoelectric coefficient was achieved in AlN/Ni composites. Namely, the maximum magnetoelectric coefficient of AlN/Ni composites with Ni foil thickness of 7.5, 15, and 30 µm

correspondingly was 3.3, 2.8, and 3.1 $V.cm^{-1}Oe^{-1}$ measured at an off-resonance frequency of 46 Hz and at a zero-bias DC magnetic field. In addition, the magnetoelectric effect was studied in composites made of 550nm-thick films grown on 12.5µm-thick Fe and 15µm-thick Co foils. The maximum magnetoelectric coefficients of AlN/Fe and Al/Co composites were 0.32 and 0.12 $V.cm^{-1}.Oe^{-1}$, respectively, and were characterized at 46 Hz with a AC magnetic field amplitude of H_{AC}= 8.5 Oe with a bias field (H_{dc}) of 6 and 200 Oe. In particular, an energy harvester based on an AlN/Ni magnetoelectric composite was demonstrated. A RMS power density of 75 nW/cm^3 was produced on a load resistance of 200 kΩ off resonance. Resonance structures introduced in Chapter seven would be one way of increasing the power density at a specific frequency.

In **Chapter seven**, several potential approaches were introduced in order to upgrade the magnetoelectric coupling and performance of thin film magnetoelectric composites. Ni-Mn-Ga Heusler alloy film is a potential candidate with a ferromagnetic shape memory effect with capabilities of giant magnetoelastic effects (up to a few %) compared to a magnetostrictive layer limited to tens of ppm of strain induced by a magnetic field. Ni-Mn-Ga films were successfully grown on an Si substrate, as well as on different diffusion barriers. The effect of the post-annealing process was carefully investigated and subsequently optimized at 650 °C for 4 h. The 500nm-thick film showed a martensitic transformation at around 50 K, as seen in the magnetization. The co-sputtering was used in order to compensate the Mn loss during the post-annealing. The optimal power of the Mn target was found to be 15 and 20 W at which the film stoichiometry can be tuned close to the desired $Ni_{50}Mn_{28}Ga_{22}$ film in order to obtain the ferromagnetic shape memory effect at room temperature and above, taking into account the valence electron concentration (e/a) definition, with the giant magnetostrain induced by an external magnetic field. Different diffusion barriers such as Pt, Al_2O_3, HfO_2, AlN were introduced between the film and Si substrate in order to reduce the Ni diffusion into Si and to maintain the homogeneity of the atomic composition in the depth of the film. Magnetization measurements were performed on co-sputtered samples with the diffusion barrier showing that all films exhibited ferromagnetic behavior, even at room temperature. A cusp at 50 K was observed in ZFC curve, and was particularly clear in the 2.5µm-thick film grown directly on Si. The origin of the cusp is not clear. The feature is quite similar to the spin-glass-like magnetic property, however, it can only occur on application of a small magnetic field. The preliminary results of the temperature dependence of x-ray diffraction measurements show interesting and promising features, occurring at higher temperatures above room temperature, concerning the effective phase switch of the thin film alloys. A synchrotron facility is needed to obtain a better signal and resolution to confirm this feature of the ferromagnetic shape memory alloy effect. Meanwhile, small-angle neutron scattering (SANS) measurements are scheduled to study the magnetic properties of those samples. In addition, the AlScN compound and the use of a resonance structure were introduced as promising approaches by which to increase the magnetoelectric effect in the composites. Although AlScN thin film is a potential replacement for AlN thin film because of a significant enhancement in piezoelectric properties, a question remains about the counterpart of the bandgap decreasing and leakage currents by the Sc concentration. Several experiments have been performed in order to grow AlScN thin film by PE-ALD. It is not yet successful because of some technical issues that occurred. However, this candidate is a priority for upcoming activities.

Outlooks:

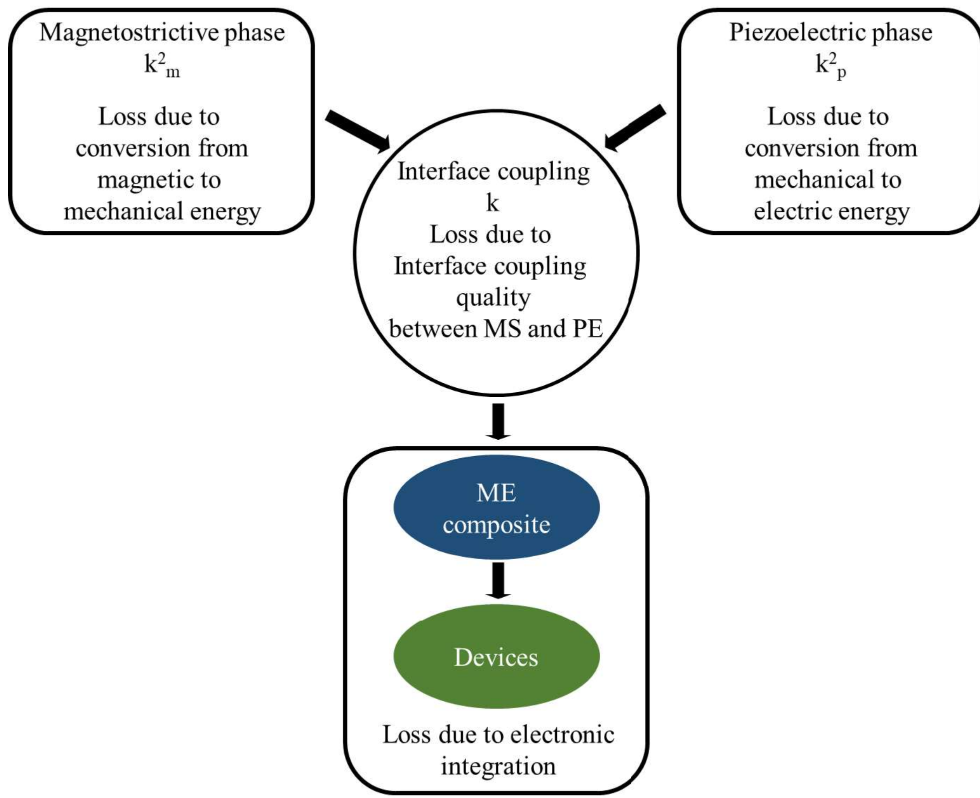

To discuss the outlook, let us first consider the possible losses in the conversion efficiency of magnetic energy to electric energy. There are four possible losses, corresponding to four elements:

(i) The loss in the magnetostrictive layer due to the conversion of magnetic energy to mechanical energy. The magnetomechanical coupling factor k_m is used to evaluate the conversion property.

(ii) The loss in the piezoelectric layer due to the conversion of mechanical energy to electric energy. The electromechanical coupling factor k_p, is used to evaluate the conversion property.

(iii) In thin film magnetoelectric composites, losses can occur due to the low-quality interface between the two layers.

(iv) Finally, we have to consider loss due to impedance matching and electronic integration for energy harvesting and sensing applications.

To avoid losses (i) and (ii) relating to material properties, low-loss single crystals are recommended[1–4]. For instance, a PMN-PZT single crystal microfiber was designed and tested. Using textured/single crystal magnetostrictive materials combined with single piezoelectric crystals is expected to further improve magnetoelectric coupling. Some compounds, such as Alfenol (Fe-Al) and Galfenol (Fe-Ga) or Ni-Mn-Ga Heusler alloy thin films are promising due to their good ductility and magnetomechanical coupling. However, the uses of the single crystals or textured perovskite piezoelectric materials face a challenge for making a high-quality interface between the piezoelectric and magnetostrictive materials due to high-temperature processes. Loss (iii) is related to fabrication methods and can be diminished by choosing a relevant technique. In this thesis, the ALD technique with its conformal coating profile emerges as an efficient and

promising method by which to design magnetoelectric composites with a high-quality interface. Therefore, the optimal approach for obtaining high-response ME composites should be to choose advantageous materials, in terms of quality and fabrication methods. A combination of AlScN thin films grown by PE-ALD and Ni-Mn-Ga films, and their integration into MEMS structures, such as resonance cantilevers, are promising approaches to minimize the losses and thus achieve high-performance devices [5], as shown in Section “7.3: Resonance structures” in Chapter 7.

References

(1) Ryu, J.; Priya, S.; Uchino, K.; Kim, H. E. Magnetoelectric Effect in Composites of Magnetostrictive and Piezoelectric Materials. *Journal of Electroceramics*. 2002. https://doi.org/10.1023/A:1020599728432.

(2) Yang, Z.; Zu, J. Comparison of PZN-PT, PMN-PT Single Crystals and PZT Ceramic for Vibration Energy Harvesting. *Energy Convers. Manag.* **2016**. https://doi.org/10.1016/j.enconman.2016.05.085.

(3) Downing, J. R.; Na, S. M.; Flatau, A. B. Compressive Pre-Stress Effects on Magnetostrictive Behaviors of Highly Textured Galfenol and Alfenol Thin Sheets. *AIP Adv.* **2017**. https://doi.org/10.1063/1.4974064.

(4) Annapureddy, V.; Palneedi, H.; Hwang, G. T.; Peddigari, M.; Jeong, D. Y.; Yoon, W. H.; Kim, K. H.; Ryu, J. Magnetic Energy Harvesting with Magnetoelectrics: An Emerging Technology for Self-Powered Autonomous Systems. *Sustain. Energy Fuels* **2017**. https://doi.org/10.1039/c7se00403f.

(5) Joly, R.; Girod, S.; Adjeroud, N.; Nguyen, T.; Grysan, P.; Klein, S.; Menguelti, K.; Vergne, C.; Polesel-Maris, J. Polymeric Cantilevered Piezotronic Strain Microsensors Processed by Atomic Layer Deposition. *Sensors Actuators A Phys.* **2020**, *315*, 112280. https://doi.org/https://doi.org/10.1016/j.sna.2020.112280.

Annex

A1: Estimation of the interface coupling factor k in ME composites

The general idea of estimation of the interface coupling is following three steps: (i) consider the device as a strain sensor, (ii) based on the output voltage on the piezoelectric layer induced by a magnetic field to calculate the strain, and (iii) the interface k factor in AlN/Ni composite can be roughly estimated as a division between the strain induced in the AlN layer and strain in Ni layer induced by magnetic field.

Conversion of Voltage output to Strain

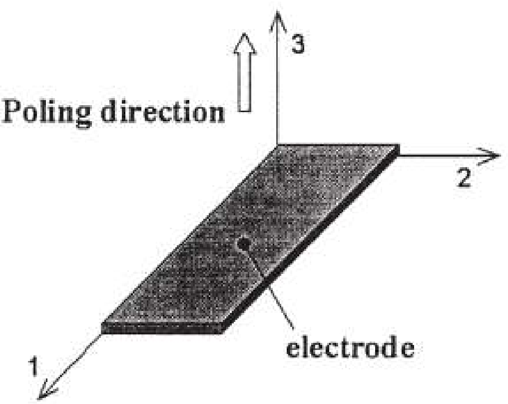

Figure A.1: Piezoelectric sheet [1].

A parallel plate capacitor is a general way to treat a typical piezoelectric sheet, whole capacitance is given as below [1]:

$$C_p = \frac{e_{33} l_c b_c}{t_c} \quad \text{(Eq. A1)}$$

where l_c, b_c, and t_c are the length, width, and thickness of the sensor, respectively. And is the permittivity of the piezoelectric material.

The relationship between charge q and voltage generated V_c across the electrodes of the capacitor is expressed as [1]:

$$V_c = \frac{q}{C_p} \quad \text{(Eq. A2)}$$

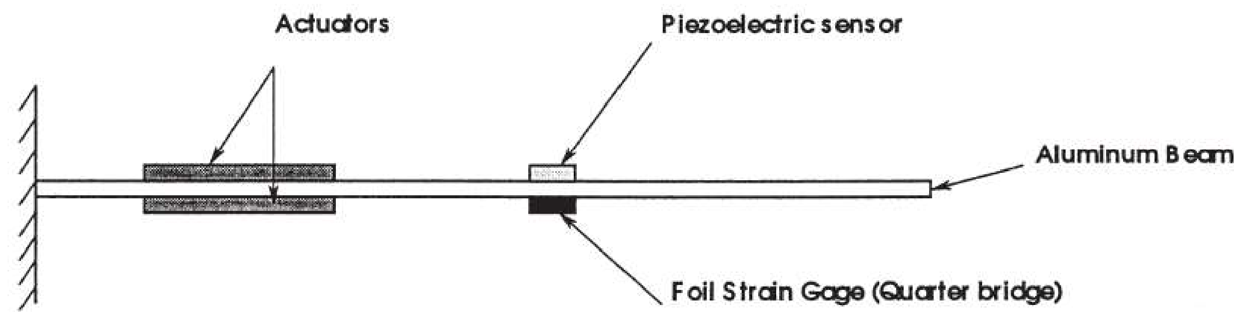

Figure A2: Calibration setup [1].

Considering only the effect of strain along the 1-direction ε_1, the voltage generated by the sensor can be expressed as [1]:

$$V_c = \frac{d_{31} Y_c b_c}{C_p} \int_{l_c} \varepsilon_1 dx \quad \text{(Eq. A3)}$$

Assuming the value of ε_1 to be averaged over the gage length and defining a sensitivity parameter:

$$S_q = d_{31} Y_c b_c l_c \quad \text{(Eq. A4)}$$

where Y_c is the Young's modulus of the piezoelectric material:

The relationship between strain and voltage generated by the sensor is then given by [1]:

$$\varepsilon_1 = \frac{V_c C_p}{S_q} \quad \text{(Eq. A5)}$$

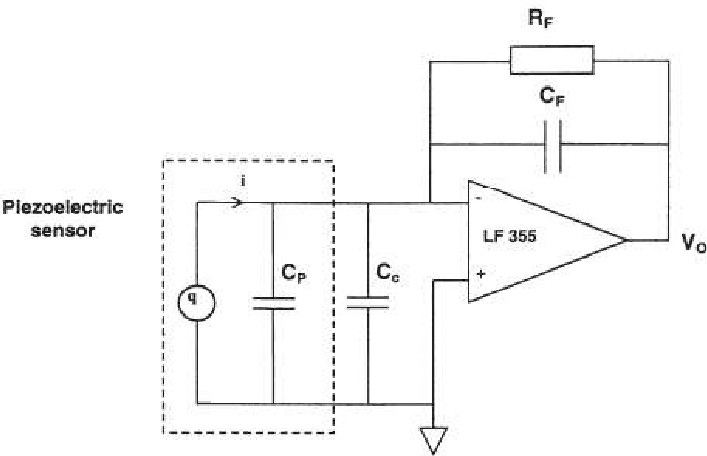

Figure A3: Charge amplifier circuit [1].

The output of the piezoelectric sensor has to be passed though some signal conditioning electronics to precisely measure the voltage generated by the sensor. The signal conditioning circuit is shown in figure A3. Here the piezoelectric sensor is modelled as a charge generator in parallel with a

capacitance, C_p, equal to the capacitance of the sensor [1]. The C_c is the parasitic capacitance. The charge generated by the sensor is transferred onto the feedback capacitance, C_F.

The quantity is defined as the circuit sensitivity, which represent the output voltage per unit strain input, as given below [1]:

$$S_q^* = \frac{d_{31} Y_c b_c l_c}{C_F} \qquad \text{(Eq. A6)}$$

There are two correction factors needed to be considered: (i) due to Poisson's ratio effect K_p, and (ii) due to the shear lag effect $K_b = l_{eff} b_{eff}$. The value of is very close to unity, the shear lag effect can be neglected without significant error [1].

From equations Eqs. 5-6 and taking into account of the two correction factors K_b and K_p, the final conversion relation from output voltage to longitudinal strain is given [1]:

$$\varepsilon_1 = \frac{V_0}{K_p K_b S_q^*} \qquad \text{(Eq. A7)}$$

Estimate the interface k factor in AlN/Ni composite.

Assuming the parameters of AlN layer in AlN/Ni composite are the same as the values from literatures, as given in table A1. The interface k factor in AlN/Ni composite can be roughly estimated as a division between the strain induced in the AlN layer ε_1 and strain in Ni layer induced by magnetic field ε_2. It is calculated about 0.3 for AlN/Ni composite.

Table A1: parameters of AlN and Ni layers, and AlN/Ni composite:

Parameters	Y_c (GPa) AlN layer)	e_{33} (AlN layer)	d_{31} (pm/V) (AlN layer)	Poisson's ratio (AlN layer)	Strain in Ni layer	V_{Output} in Al/Ni (mV)	Area (cm^2)	t_{AlN} (nm)
	243.5	9.1	-2	0.25	-3.0×10^{-6}	1.5	0.09	500
References	2	2	2	2	3			

A2: Materials properties

Table A2: the structure, lattice constants, Young Modulus, Poisson's ratio, and thermal expansion coefficient (TEC) of ZnO, AlN, Ni, Co, Fe, and Ni_2MnGa. Except for the TEC, other parameters of those materials were cited from the Materials Project (https://materialsproject.org/). The IDs are mp-2133 (ZnO), mp-661 (AlN), mp-23 (Ni), mp-54 (Co), and mp-13 (Fe).

Materials	Crystal structure	a (nm)	c (nm)	Young modulus (GPa)	Poisson's Ratio	TEC at 300K ($\times 10^{-6}$ / K)
ZnO	Hexagonal	0.329	0.531	130	0.36	4.45 [4]
AlN	Hexagonal	0.312	0.502	194	0.24	$\Delta c/c$ = 5.3 $\Delta a/a$ = 4.2 [5]
Ni	FCC	0.248		198	0.29	13.3 [6]
Co	Hexagonal	0.250	0.403	212	0.29	13.8 [7]
Fe	FCC	0.246		182	0.32	11.7 [7]
Ni_2MnGa	FCC [8]	0.583 [8]		107 [8]	0.38 [8]	15 [9]

References:

(1) Sirohi, J.; Chopra, I. Fundamental Understanding of Piezoelectric Strain Sensors. *J. Intell. Mater. Syst. Struct.* **2000**. https://doi.org/10.1106/8BFB-GC8P-XQ47-YCQ0.

(2) Song, X.; Fu, R.; He, H. Frequency Effects on the Dielectric Properties of AlN Film Deposited by Radio Frequency Reactive Magnetron Sputtering. *Microelectron. Eng.* **2009**. https://doi.org/10.1016/j.mee.2009.03.036.

(3) Klokholm, E.; Aboaf, J. The Saturation Magnetostriction of Thin Polycrystalline Films of Iron, Cobalt, and Nickel. *J. Appl. Phys.* **1982**. https://doi.org/10.1063/1.330930.

(4) Gadzhiev, G. G. The Thermal and Elastic Properties of Zinc Oxide-Based Ceramics at High Temperatures. *High Temp.* **2003**. https://doi.org/10.1023/B:HITE.0000008333.59304.58.

(5) Yim, W. M.; Paff, R. J. Thermal Expansion of AlN, Sapphire, and Silicon. *J. Appl. Phys.* **1974**. https://doi.org/10.1063/1.1663432.

(6) Souder, W. H.; Hidnert, P. Thermal Expansion of Nickel, Monel Metal, Stellite, Stainless Steel, and Aluminum. *J. Franklin Inst.* **1922**. https://doi.org/10.1016/s0016-0032(22)90687-8.

(7) Technologies, A. *Material Expansion Coefficients*; 2007.

(8) Sakon, T.; Adachi, Y.; Kanomata, T. Magneto-Structural Properties of Ni_2MnGa Ferromagnetic Shape Memory Alloy in Magnetic Fields. *Metals*. 2013. https://doi.org/10.3390/met3020202.

(9) Buchelnikov, V. D.; Khovailo, V. V.; Takagi, T. The Thermal Expansion Coefficient and Volume Magnetostriction of Heusler Ni_2MnGa Alloys. *J. Magn. Magn. Mater.* **2006**. https://doi.org/10.1016/j.jmmm.2005.10.192.

List of publications

Peer-viewed journal articles

1. **Tai Nguyen**, Philipp Bender, Sebastjan Glinsek, Yves Fleming, Noureddine Adjeroud, Patrick Grysan, Didier Arl, Mélanie Emo, Jaafar Ghabaja, Andreas Michels, and Jérôme Polesel-Maris, “A strong magnetoelectric coupling in thin-film composites made of AlN films and magnetostrictive foils”, under revision in ACS Applied Materials and Interfaces.
2. **Tai Nguyen**, Nathalie Valle, Jérôme Guillot, Noureddine Adjeroud, Brahime El Adib, Mael Guennou, Didier Arl, Raoul Joly, Jean-Nicolas Audinot, Yves Fleming, and Jérôme Polesel-Maris, “Elucidating the growth mechanism of ZnO films by Atomic Layer Deposition with Oxygen Gas via isotopic tracking”, accepted in RSC Journal of Materials Chemistry C. DOI: 10.1039/d0tc05439a.
3. Raoul Joly, Stéphanie Girod, Noureddine Adjeroud, **Tai Nguyen**, Patrick Grysan, Sébastien Klein, Kevin Menguelti, Christèle Vergne, Jérôme Polesel-Maris, “Polymeric cantilevered piezotronic strain microsensors processed by Atomic Layer Deposition”, Sensors and Actuators A 2020, 315, 112280.
4. **Tai Nguyen**, Noureddine Adjeroud, Sebastjan Glinsek, Yves Fleming, Jérôme Guillot, Patrick Grysan, and Jérôme Polesel-Maris, “A film-texture driven piezoelectricity of AlN thin films grown at low temperatures by plasma-enhanced atomic layer deposition”, APL Materials 2020, 8, 071101.
5. **Tai Nguyen**, Noureddine Adjeroud, Mael Guennou, Jérôme Guillot, Yves Fleming, Anne-Marie Papon, Didier Arl, Kevin Menguelti, Raoul Joly, Narciso Gambacorti, Jérôme Polesel-Maris, “Controlling electrical and optical properties of zinc oxide thin films grown by thermal atomic layer deposition with oxygen gas”, Results in Materials 2020, 6, 100088.

Conference proceeding

1. **Tai Nguyen**, Noureddine Adjeroud, Sebastjan Glinsek, Yves Fleming, Jérôme Guillot and Jérôme Polesel-Maris, "Strong Magnetoelectric Effects of 2–2 Composites Made of AlN Films Grown by Plasma-Enhanced Atomic Layer Deposition on Magnetostrictive Foils for Energy Harvesting Applications," 2020 IEEE 33rd International Conference on Micro Electro Mechanical Systems (MEMS), Vancouver, BC, Canada, 2020, pp. 578-581.
2. **Tai Nguyen**, Noureddine Adjeroud, Sebastjan Glinsek, Jérôme Guillot and Jérôme Polesel-Maris, "Low temperature growth of piezoelectric AlN films by plasma enhanced atomic layer deposition and magnetoelectric coupling with nickel for energy harvesting applications," 2019 19th International Conference on Micro and Nanotechnology for Power Generation and Energy Conversion Applications (PowerMEMS), Krakow, Poland, 20.

List of contributions

CHAPTER 4

Article 1:

"*Controlling electrical and optical properties of zinc oxide thin films grown by thermal atomic layer deposition with oxygen gas*", in Results in Materials 6, 100088 (2020) (DOI: 10.1016/j.rinma.2020.100088)

Contributions:

Tai Nguyen: Methodology, experiments (ALD processes, characterizations), manuscript writing - original draft.

Noureddine Adjeroud: Methodology, experiments (ALD processes). Mael Guennou: Photoluminescence analysis and data interpretation, review & editing. Jérôme Guillot: XPS analysis and data interpretation, review & editing. Yves Fleming: XRD and pole figure analysis and data interpretation, review & editing. Anne-Marie Papon: TEM cross section and diffraction analysis and data interpretation, review & editing. Didier Arl: SEM analysis and data interpretation, review & editing. Kevin Menguelti: experiments (ALD processes, samples preparation). Raoul Joly: experiments (ALD processes), review & editing. Narciso Gambacorti: TEM data interpretation. Jérôme Polesel Maris: Project manager, supervisor, ALD experiments, data analysis, funding acquisition, manuscript writing, review & editing.

Article 2:

"*Elucidating the growth mechanism of ZnO films by Atomic Layer Deposition with Oxygen Gas via isotopic tracking*", accepted in RSC Journal of Materials Chemistry C. DOI: 10.1039/d0tc05439a.

Contributions:

Tai Nguyen: Methodology, experiments (ALD processes, characterizations), data acquisition and analysis, manuscript writing - original draft.

N. Valle: Methodology, experiments (SIMS), data analysis and interpretation, review and editing. J. Guillot: XPS analysis and data interpretation, review & editing. J. Bour: ToF-SIMS acquisition and analysis. N. Adjeroud: Methodology, experiments (ALD processes). Y. Fleming: XRD experiments and data analysis interpretation, review & editing. M. Guennou: Photoluminescence analysis and data interpretation, review & editing. J. Audinot: Methodology, experiments (HIM-SIMS), data analysis, and interpretation. B. Adib: Experiments (SIMS), data analysis. R. Joly: Experiments (ALD processes, characterizations). D. Arl: SEM analysis and data interpretation, review & editing. G. Frache: ToF-SIMS analysis. Jérôme Polesel Maris: Project manager, supervisor, ALD experiments, data analysis, funding acquisition, manuscript writing, review & editing.

CHAPTER 5:

Article 3:

"*A film-texture driven piezoelectricity of AlN thin films grown at low temperatures by plasma-enhanced atomic layer deposition*", in APL Materials 8(7), 71101 (2020). (DOI: 10.1063/5.0011331).

Contributions:

Tai Nguyen: Methodology, experiments (ALD processes, characterizations), manuscript writing - original draft.

N. Adjeroud: Methodology, experiments (ALD processes). S. Glinsek: 4-PB characterization, review & editing. Yves Fleming: XRD and pole figure analysis and data interpretation, review & editing. Jérôme Guillot: XPS analysis and data interpretation, review & editing. Jérôme Polesel Maris: Project manager, supervisor, ALD experiments, data analysis, funding acquisition, manuscript writing, review & editing.

CHAPTER 6:

Article 4:

"*Low-temperature growth of AlN films on metal foils by plasma-enhanced atomic layer deposition for high-magnetoelectric-response thin-film composites*", under revision in ACS Applied Materials and Interfaces.

Tai Nguyen: Methodology, experiments (ALD processes, characterizations), manuscript writing - original draft.

Y. Fleming: XRD analysis and data interpretation, review & editing. P. Bender: magnetic measurements, review & editing. N. Adjeroud: Methodology, experiments (ALD processes). P. Grysan: AFM, review & editing. D. Arl, M. Emo and J. Ghabaja: TEM observations and data interpretation, review & editing. A. Michels: magnetic measurements, review & editing. Jérôme Polesel Maris: Project manager, supervisor, ALD experiments, data analysis, funding acquisition, manuscript writing, review & editing.